Lipidomic interrogation of Neonatal Progeroid Syndrome, Farber's Disease, and Spinal Muscular Atrophy with Progressive Myoclonic Epilepsy

Graeme Stephen Vaughn McDowell

A thesis submitted to the University of Ottawa in partial fulfillment of the requirements for the PhD degree in Biochemistry

Department of Biochemistry, Microbiology, and Immunology

Faculty of Medicine

University of Ottawa

Abstract

Spinal Muscular Atrophy with Progressive Myoclonic Epilepsy (SMA-PME), Farber Lipogranulomatosis (FL), and a rare variant form of Neonatal Progeroid Syndrome (NPS) are three monogenetic rare disorders caused by pathogenic variation in genes encoding lipid modifying proteins. FL and SMA-PME are caused by loss of function mutations in *ASAH1*, encoding the acid ceramidase (aCDase) enzyme. It is not, however, known how aCDase deficiency can produce either the isolated neurological symptoms of SMA-PME or the predominantly systemic symptoms of FL. Further, a recently identified variant form of NPS has been attributed to variants in *ANO6*, encoding a dual function calcium-activated chloride channel and glycerophosphoserine (GPS) scramblase. Here, it is not known how *ANO6* mutation causes the premature aging phenotype that defines NPS. To address these questions, I sought to elucidate pathogenic changes in lipid metabolism that associate clinical phenotype. I show here that the different patient mutations in *ANO6* cause a non-physiological gain of channel function and either a loss or gain of scramblase function depending on the variant expressed. Both variants, however, alter GPS metabolic homeostasis suggesting a common mechanism of action. To provide *in vivo* insight, I characterized a novel mouse model based on our NPS patient genetics, showing extremely low penetrance of disease symptoms in terms of live births yet confirming that affected animals show impaired GPS metabolism in affected organs. Next, I characterized the clinical presentation of six new patients with SMA-PME and identified distinct sphingolipid metabolic fingerprints in FL and SMA-PME cells. I show that FL is defined by a hypometabolic sphingolipid phenotype with cellular and molecular features of a classic lysosomal storage disorder. By contrast, SMA-PME has a hypermetabolic sphingolipid phenotype with features of non-classic lysosomal trafficking disorders. To provide clinical insight, I assessed the potential of enzyme replacement therapy, demonstrating a rescue of sphingolipid metabolism in SMA-PME patient cells. Together, this thesis identified changes in the cellular and tissue

lipid profiles of patients with ANO6-NPS, SMA-PME, or FL, elucidating some of the lipid-centric pathomechanisms of these diseases.

Acknowledgements

"Je n'ai fait celle-ci plus longue que parce que je n'ai pas eu le loisir de la fair plus courte"/ "I have made this longer than usual because I have not had the time to make it shorter" – Blaise Pascal

When I started this journey many years ago, I often imagined where in life I'd be when I got to writing this section of my thesis. Suffice it to say, I could never have guessed how life has panned out to get me where I am today. I would not have made it here without the support and encouragement of countless people, some of which I'd like to acknowledge directly.

First, I would like to extend my deepest and sincerest thanks to my supervisors, Dr. Steffany Bennett and Dr. David Dyment. Thank you, Stef, for all your you've done over the last [redacted] years. Without your guidance, enthusiasm, attention to detail, and endless support, there is no world where I could have finished this. You pushed me to be better than I dreamed I could be and trusted me even when I couldn't. Thank you, David, for bringing the clinical side to my experience in my PhD. Your expertise, demeaner, and perspective, helped me see the bigger picture, and gave me the drive to seek the answers I found, presented here. Thank you both for everything.

I'd like to thank the Bennett lab members, past and present, for all the support, laughs, music, and companionship that kept me sane throughout the years. A special thanks to Dr. Hongbin Xu, Dr. Yun Wang, Dr. Irina Alecu, Dr. Matthew Granger, Dr. Stephanie Fowler, Mark Akins, Graeme Taylor, and Thao Nguyen-Tran, for your help in training me, running samples for me, and helping me be the best I can. An extra thank you to Danielle Robinson MD, and Sneha Gupta, for being fantastic students and for all of the hard work you both did, be it long hours in the mouse room, tissue culture hood, or at the computer. I would also like to thank my advisory committee, Dr. Diane Lagace, Dr. Alex Mackenzie, and Dr William Stanford, for their guidance and insight throughout my PhD project.

I cannot adequately express my gratitude to my family for their constant and undying love and support. Mom and Dad, thank you for always being there to listen, give advice, read manuscripts, or chat about whatever was happening, be it with school or not. Without you I wouldn't have made it through this. Thank you to Karin, Kris, Wes, Marcus, Dani, Althea, Emma, and Adam, for all the joyous family times we've had. I look forward to many more at the upcoming wedding and beyond!

To my friends: you all have a special place in my heart; I love you all. From boardgames, D&D, online gaming marathons, live streams, late night chats, to hikes, bike rides, triathlons, martial arts, archery tag, gym sessions, pool sessions, skating, skiing, ultimate, singing, or even just sitting at a pub with a pint, you kept me sane and kept me with a glimmer of work-life-balance. A special thank you to Kim, Glo, Larry, Drew, O.C.T.R.T.A, Paolo and Marina and Riko, C-Team, Shayna, Dan, Oren, Bryan, Tonal, Dungeons and Deranks, the Wildemount+Tortall crew, Camille, Kelly, Kurt, Bowie, and the rest of the Archery community, Robin, Scott, Kelly, Angie, Laeti, Nicholas, Cynthia, Christina, Sarah, Josh, all the group chats I dare not mention by name, and to anyone I haven't named, thank you for all the chats, hangouts, adventures, good times, shoulders to lean on… I couldn't have done it without you.

Perhaps, most importantly, to the patients and their families, thank you for your participation in this work. You are the reason I did this, and without you, this work has no meaning. I dedicate this work to you.

And finally, I would like to thank you, dear reader. Perhaps one day, one of you will find the cures we so desperately need.

Table of Contents

Abbreviations

Please note: The abbreviations listed below are re-defined at first instance in each chapter.

A4GALT	α-1,4-galactosyltransferase
AB	Antibody buffer
aCDase	acid ceramidase
ACER	Alkaline ceramidase gene
$AdPLA_2$	adipose specific PLA_2
AlkCDase	alkaline ceramidase
ANOVA	Analysis of variance
ASAH1	N-Acylsphingosine Amidohydrolase 1
ASAH2	N-Acylsphingosine Amidohydrolase 2
ANO1-6	Anoctamin 1-6
ANO6-NPS	ANO6-determined rare variant of NPS
APGAR	Appearance, Pulse, Grimace, Activity, and Respiration medical assessment for newborns
B4GALT6	β-1,4-galactosyltransferase 6
BATL	Bayesian Annotations for Targeted Lipidomics
BBK	Beam Break test
BME	β mercaptoethanol
Bp	Base pair
BSA	Bovine serum albumin
C1P	Ceramide-1-Phosphate
CAD	Collision gas
Cas9	CRISPR associated protein 9
cat#	catalogue number
CDase	ceramidase
Cer	Ceramide
Cer(d18 :1)	Ceramide
Cer(d18 :0)	Dihydroceramide
Cer(t18 :0)	Phytoceramide
Cer(OH)	Hydroxylated ceramide
CerS	Ceramide Synthase
CERT	ceramide transfer protein
CGT	Ceramide galactosyltransferase
CHEO	Children's hospital of Eastern Ontario
CHO-M	Chinese hamster ovary cells
CID	collision-induced dissociation
CK	ceramide kinase
CNS	Central nervous system
CoA	Coenzyme-A
COL3A	Collagen type III alpha
CoV	Compensation voltage
Cps	Counts per second

CRISPR	Clustered Regularly Interspaced Short Palindromic Repeats
CRM	Charge residue model
CTRL	Control
CUR	Curtain gas
Cy3/5	Cyanide 3/5 dye
DC	Direct current
DES	Dihydroceramide desaturase
DistC	Distance Correlation measure
DMEM	Dulbecco's Modified Eagle's Medium
D-MEM/F-12	Dulbecco's Modified Eagle's Medium: Ham's Nutrient Mixture 12
DMS	Differential ion mobility spectrometry
DMSO	Dimethyl sulfoxide
DTT	Dithiothreitol
EC50	Effective concentration 50
EEG	Electroencephalogram
EGFP	Enhanced green fluorescent protein
EM	Electron Microscopy
EMG	Electromyography
ePBS	extraction PBS
EPI	Enhanced product ion
ER	Endoplasmic Reticulum
ERT	Enzyme replacement therapy
ESI	Electrospray Ionization
FA	Formic Acid
FACS	fluorescence activated cell sorting
FBS	Fetal Bovine Serum
FCS	Fetal calf serum
FD	Farber Lipogranulomatosis or Farber disease
FDA	US Food and Drug administration
FDR	false discovery rate
FL	Farber's Lipogranulomatosis or Farber disease
G1P0	Gravida 1 Para 0; a woman who is pregnant for the first time
GALC	Galactosylceramidase
GalCer	Galactosylceramide
GalSph	Galactosylsphingosine
GAPDH	Glyceraldehyde-3-phosphate dehydrogenase
Gb3Cer	Globotriaosylceramide
GBA1	β glucocerebrosidase
GCS	Glucosylceramide Synthase
GDD	Global developmental delay
GLA	α-galactosidase A
GLB1	β-galactosidase
GlcCer	Glucosylceramide
GlcSph	Glucosylsphingosine

GPA	Glycerophosphatidic acid
GPC	Glycerophosphocholine
GPE	Glycerophosphoethanolamines
GPLs	Glycerophospholipids
GPS	Glycerophosphoserine
GPS(O)	Alkyl-acyl-glycerophosphoserine
GPS(O)-PAF	Alkyl-acetyl-glycerophosphoserine
GPS(P)	Alkenyl-acyl-glycerophosphoserine
GS1	Ion Source Gas 1/Nebulizer Gas
GS2	Ion Source Gas 2/Heated Gas
GTC	generalized tonic-clonic seizure
HBSS	Hanks' balanced salt solution
HexCer	Hexosylceramide
HexSph	Hexosylsphingosine
HGPS	Hutchinson-Gilford progeria syndrome
HPLC	High performance liquid chromatography
HRP	Horseradish peroxidase
IBS	Illustrator for Biological Sequences
i.d.	Internal diameter
IDA	Information-dependent acquisition
IEM	ion-evaporation model
IPA	Isopropanol
IPSC	Induced Pluripotent Stem Cells
IRX1	Iroquois Homebox 1
KO	Knockout
LacCer	Lactosylceramide
LAMP-1	Lysosomal-associated membrane protein 1
LB	Lysogeny broth
LC	Long chain
LE	Late Endosomes
LIT	linear ion trap
LMNA	Laminin A/C Gene
LPC	lysophosphocholine
LPCAT3	lysophosphocholine acyltransferase 3
LPEAT1	lysophosphoethanolamine acyltransferase 1
$LPLA_2$	lysosomal PLA_2
LPS	lysophosphoserine
LPSAT	lysophosphoserine acyltransferase
LPS(O)	Alkyl-linked lyso glycerophosphoserine
LPS(P)	Alkenyl-linked lyso glycerophosphoserine
LSD	Lysosomal Storage Disorder
M	Mitochondria
M6P	Mannose-6-Phosphate

M6PR	Mannose-6-Phosphate Receptor
MALDI	matrix-assisted laser desorption/ionization
Mo	Mouse
MPS	Mucolipidosis (Type I, II, II, or VI)
MR	Magnetic resonance
MRI	Magnetic resonance imaging
MRM	Multiple selected reaction monitoring
MS	Mass spectrometry
MS/MS	Tandem mass spectrometry
MT	Microtubule
MTA	material transfer agreement
MUFA	Monounsaturated fatty acid
m/z	mass to charge ratio
N	Nucleus
nCDase	Neutral ceramidase (protein)
ND	Not determined
NIH	National institute of Health
NPS	Neonatal Progeroid Syndrome
NR	Not reported
OF	Open field
OMIM	Online Mendelian Inheritance of Man
pA	Pico amps
PBS	Phosphate buffered saline
PBST	Phosphate buffered saline with Tween-20
PC	phosphocholine
PEMT	Phosphoethanolamine Methyl Transferase
pF	Pico farad
PIS	Precursor Ion Scan
PISD	phosphatidylserine decarboxylase
PLA	phospholipase A
PLA_1	Phospholipase A1
PLA_2	Phospholipase A2
PME	Progressive myoclonic epilepsy
POLR3	RNA Polymerase III Complex gene
PS	Glycerophosphoserine
PSD	Phosphoserine Decarboxylase
PS(O)	Alkyl-acyl-glycerophosphoserine
PS(O)-PAF	Alkyl-acetyl-glyceropohosphoserine
PS(P)	Alkenyl-acyl glycerophosphoserine
$PS\text{-}PLA_1$	Serine specific Phospholipase A1
PSS1	Phosphatidylserine synthase 1
PSS2	Phosphatidylserine synthase 2
PtPr	Product to precursor ratio
PUFA	Polyunsaturated fatty acid
PVDF	Polyvinylidene fluoride/polyvinylidene difluoride

Q	Quadrupole
Rb	Rabbit
RF	Radio frequency
rhAC	Recombinant human acid ceramidase
RIPA	Radioimmunoprecipitation assay buffer
ROI	Region of interest
RPM	Revolutions per minute
RT	Retention time
RT-PCR	Reverse transcription polymerase chain reaction
S1P	Sphingosine-1-phosphate
SD	Standard deviation
SDS	Sodium Dodecyl Sulfate
SDS-PAGE	Sodium dodecyl sulfate polyacrylamide gel electrophoresis
SEM	Standard Error of the Mean
SFA	Saturated fatty acid
sgRNA	Single guide RNA
SK	Sphingosine kinase
SLs	Sphingolipids
SM	Sphingomyelin
SMA	Spinal muscular atrophy
SMA-PME	Spinal Muscular Atrophy with Progressive Myoclonic Epilepsy
SMase	sphingomyelinase
SMN	Survival motor neuron (protein)
Sn	stereospecifically numbered
SNHL	sensorineuronal hearing loss
SNP	single nucleotide polymorphism
Sph	Sphingosine
Sph(d18:1)	Sphingosine
Sph(d18:0)	Sphinganine
$sPLA_1$	secreted PLA_1
$sPLA_2$	secreted PLA_2
SPT	serine palmitoyl transferase
SRM	Selected Reaction Monitoring
SubQ	subcutaneous
sV	Secretory Vesicle
SepV	Separation Voltage
T-test	Student’s t-test
tcPBS	tissue culture phosphate buffered saline
Ter	Stop codon
TFA	trifluoroacetic acid
TLC	thin layer chromatography
TMEM16F	transmembrane protein 16 F, also known as Anoctamin 6
UCSC	University of California at Santa Cruz

US	United States
USA	United States of America
V	volts
VLC	Very long chain
WES	Whole exome sequencing
WRNPS	Wiedemann-Rautenstrauch Neonatal Progeroid Syndrome
WRS	Wiedemann-Rautenstrauch Syndrome
ZMPSTE24	Zinc Metallopeptidase STE24
ZT	Zeitgeber time

List of Figures

List of Tables

Chapter 1 : General Introduction

1.1 Rare Monogenetic Diseases

1.1.1 What defines a rare disease?

Rare diseases are an emerging health imperative, both nationally and internationally. Defined as, severe, progressive, degenerative, life-threatening, or chronically debilitating disorders[1, 2], their impact on families and our health care systems is often overlooked due to low prevalence by diagnosis. The definition of "low prevalence" is variable, with no international consensus over the threshold for classifying a disease as rare. Indeed, a disease considered rare in one ethnic population can be common in another ethnic population. For example, with respect to Tay Sachs disease, carrier prevalence is 1 in 250-300 in the general population[3], with an incidence of 1 in 320,000 births[4], yet among disaggregated Jewish populations carrier frequency is estimated to be as high as 1 in 29, with an incidence of 1 in 3500 live births[5]. Thus, "rare" is community/population specific. In Europe, the European Medicines Agency deems a disease with a prevalence of fewer than 1 in 2000 people as rare; whereas the Taiwan Department of Health deems a prevalence of fewer than 1 in 10,000 as rare[2]. In Canada, while there is no official definition, Health Canada has been operationally using the cut-off of fewer than 5 in 10,000 Canadians to define a rare disease[1]. None of these definitions distinguish community/population-specific attributes yet in the Canadian context, Tay Sachs Disease, for example, is highly prevalent in persons of Cajun ancestry in Quebec and Louisiana USA, possibly as a result of a single common ancestral couple from France[6-8]. Key to novel therapeutic strategies, a large proportion of these rare diseases, estimated at 7000 as a result of their ancestral origin, have a genetic origin, which contrasts with more prevalent diseases, which are influenced more by environmental factors and numerous small-effect genetic variants[9]. As of 2013, approximately 50% of the genes responsible for these 7000 monogenic rare diseases have been identified[10]. Moreover, a large proportion, between 65 and 75%, of rare diseases are pediatric with onset in childhood[2].

Rare diseases have a significant healthcare burden, both in Canada and globally given combined prevalence of all disorders. Estimates of the frequency of individual rare diseases range between 5,000 and 8,000 either nationally or globally, with the most cited figure greater than 7,000 rare diseases[1, 11]. Haendel *et al* in 2020, using the Monarch Disease Ontology, calculated there to be more than 10,000 rare diseases globally to date[9]. With such a large number of rare diseases, this translates into a surprisingly high proportion of the population. Estimates suggest that approximately 1 million Canadians, or 2-3% of the population[1] are living with a rare disease. Globally, it has been estimated that over 400 million people are affected by a rare disease, 30 million of whom are in Europe, and 25-30 million are in the United States of America[11, 12]. These statistics emphasize that while each disease itself is rare, collectively they are common. Between one-half and two-thirds of those living with rare diseases are children[1], and one-third of children suffering from a rare disease will die before their fifth birthday[12]. This translates to an enormous impact on years of potential life lost and, more importantly, human tragedy[1]. Approximately 50% of patients suffering from a rare disease do not have an accurate diagnosis for their condition[1, 9] and for those that do get a diagnosis, this often takes years[12]. Without a diagnosis, patients can feel abandoned and hopeless. Unfortunately, even where a diagnosis is available, this does not guarantee treatment, as there is no approved treatment for 95% of rare diseases[1, 12]. There is urgent need to address this deficit one disease at a time.

Perhaps the greatest burden on families and the healthcare system is the lack of available treatments, and where an approved treatment is available, the expense prohibits application and hope. Orphan drugs, often candidates to treat rare diseases[13], are expensive to produce, and, due to the small patient pool, are priced accordingly. For example, in 2017 it was estimated that the total sales of orphan drugs was $125 billion. While impressive, this is approximately a mere 15.9% of all prescription non-generic drugs[14]. To stimulate the development of treatments, the US passed the Orphan Drug Act in 1983. This measure aimed to incentivise the pharmaceutical industry to develop and market new drugs to treat rare diseases

by reducing barriers for their creation and increasing funding to realize this objective. Since the act was passed, the FDA has approved 744 orphan drugs, representing an approximate 15.8-fold increase in therapeutic options prior to this legislation being passed[14]. While these developments are promising, there is still the need to develop more diagnostic tools and therapies for rare diseases, both newly discovered and previously known[9]. However, there are some unique challenges associated with studying rare diseases that will need to be overcome.

1.1.2 Challenges of Studying Rare Diseases

The mantra of "collectively common, individually rare" explains the crux of the rare disease challenge. Due to the variety, the variability in their presentation, and the sheer number of rare diseases, most clinicians are unlikely to have experience with recognizing or managing the majority of conditions[9]. This contributes to the high percentage of patients who do not have a correct diagnosis and explains why diagnoses can take years to obtain[14, 15]. In many cases, our basic knowledge of each disease, including its cause, natural course, and mechanism[11] are not well characterized or known, and thus not available to clinicians, reducing their ability to diagnose their patients. There are Canadian centers of rare diseases, where clinicians and researchers collaborate on a specific set of rare diseases[16] (e.g., Ehlers-Danlos Syndrome Clinic University Health Network[17]), but these centres are fairly dispersed, and patients who do not live close to such a center may not benefit.

Clearly, there is a need for more study and better dissemination of study results, but there are challenges facing researchers attempting to study rare diseases. In terms of fundamental science research, the small number of patients and the variability of these patients makes these diseases challenging to classify and identify; even if the genetic determinant for a disease is known, it is possible that these diseases have variable presentations or severities, making it harder to verify that patients are suffering from the same disorder with the same genetic determinant (as described in Chapters 3, 4, and 5 for in this thesis). This becomes especially important when trying to find the root cause of the disease. Technologies

such as whole exome sequencing (WES) have revolutionized the field, but there is still a need for multiple patients to verify genetic findings[10]. Moreover, there are few model systems for the vast majority of rare diseases. I sought to address this challenge for a rare variant of neonatal progeroid syndrome (NPS) in Chapter 2.

For natural histories, similar problems exist. The geographic dispersal of patients and potential study participants severely hampers the recruitment of a large enough sample for studies to be sufficiently powered. Furthermore, the logistical challenge of bringing sick and geographically dispersed patients to centers for trials, or else bringing the researchers to the patients, is difficult and expensive[11]. Another challenge faced by researchers is the lack of biomarkers and agreement on clinical endpoints[11]. To this end, in Chapter 3 of this thesis, I review the natural history of 6 "unpublished" Spinal Muscular Atrophy with Progressive Myoclonic Epilepsy (SMA-PME) patients and compare them to 24 individuals previously reported[18]. Again, the small number of patients, and the lack of models make studying accurate clinically relevant biomarkers challenging for non-clinical researchers, which then is translated to the inability for clinical researchers to track disease progression during intervention trials. A final challenge for both fundamental and clinical research is the comparative lack of funding, in part due to the lack of general awareness of these rare conditions. This also poses a challenge for incentivising pharmaceutical companies to fund drug development.

1.2 Lipidomics of rare diseases

In this thesis, I seek to elucidate the metabolic underpinnings of three monogenetic rare paediatric diseases genetically determined by mutations in a) *ANO6* encoding a phospholipid scramblase responsible for regulating glycerophosphoserine content at the inner and outer leaflets of the plasma membrane (resulting in a variant form of NPS) and b) *ASAH1* encoding the lysosomal acid ceramidase

responsible for ceramide degradation (resulting in either Farber's Lipogranulomatosis (FL) or SMA-PME). Background on each rare disease will be provided in each chapter. Here, in this general introduction, I review basic lipid biology of the lipid classes affected by these mutations and the summarize the technical nature of lipidomic approaches employed in this thesis.

1.2.1 Lipid structure and nomenclature

Lipids are possibly the largest class of biomolecules, present in every cell in the body and estimated to be comprised of up to 100,000 different molecular species[19]. They are often defined as biomolecules that are insoluble in water but soluble in organic solvents. A more modern and specific definition is that lipids are hydrophobic or amphipathic small molecules that originate entirely (or in part) by carbanion-based condensations of thioesters – including fatty acyls, glycerolipids, glycerophospholipids (GPLs), sphingolipids (SLs), saccharolipids, and polyketides – and/or by carbocation-based condensations of isoprene units – such as in prenol lipids and sterol lipids[20]. These categories are the eight general classes of lipids[20, 21]. Each class differs in structure, and the molecular species within each class have subtle structural variations that impact form and function[22]. GPLs and SLs are the two most abundant classes and diverse molecular species make up the structural members of cell membranes[23]. Both GPLs and SLs consist of three core building blocks: GPLs consist of a glycerol backbone, a phosphate linked headgroup that can be further esterified to choline, ethanolamine, serine, or inositol, and up to two hydrocarbon chains (Figure 1.1). SLs consist of a sphingoid base, a headgroup, and a fatty chain (Figure 1.2).

There are 20 subclasses of GPL defined by their headgroups[21]. Three are depicted in Figure 1.1. The simplest GPL is defined by glycerophosphatidic acid – the phosphate headgroup has no further modification. The other subclasses are defined by which moiety is conjugated to the phosphate group; for example, glycerophosphoserine (GPS) contains a serine esterified to the phosphate group. In mammals, the phospho-headgroup is conjugated at the *sn-3* position of the glycerol moiety (Figure 1.1).

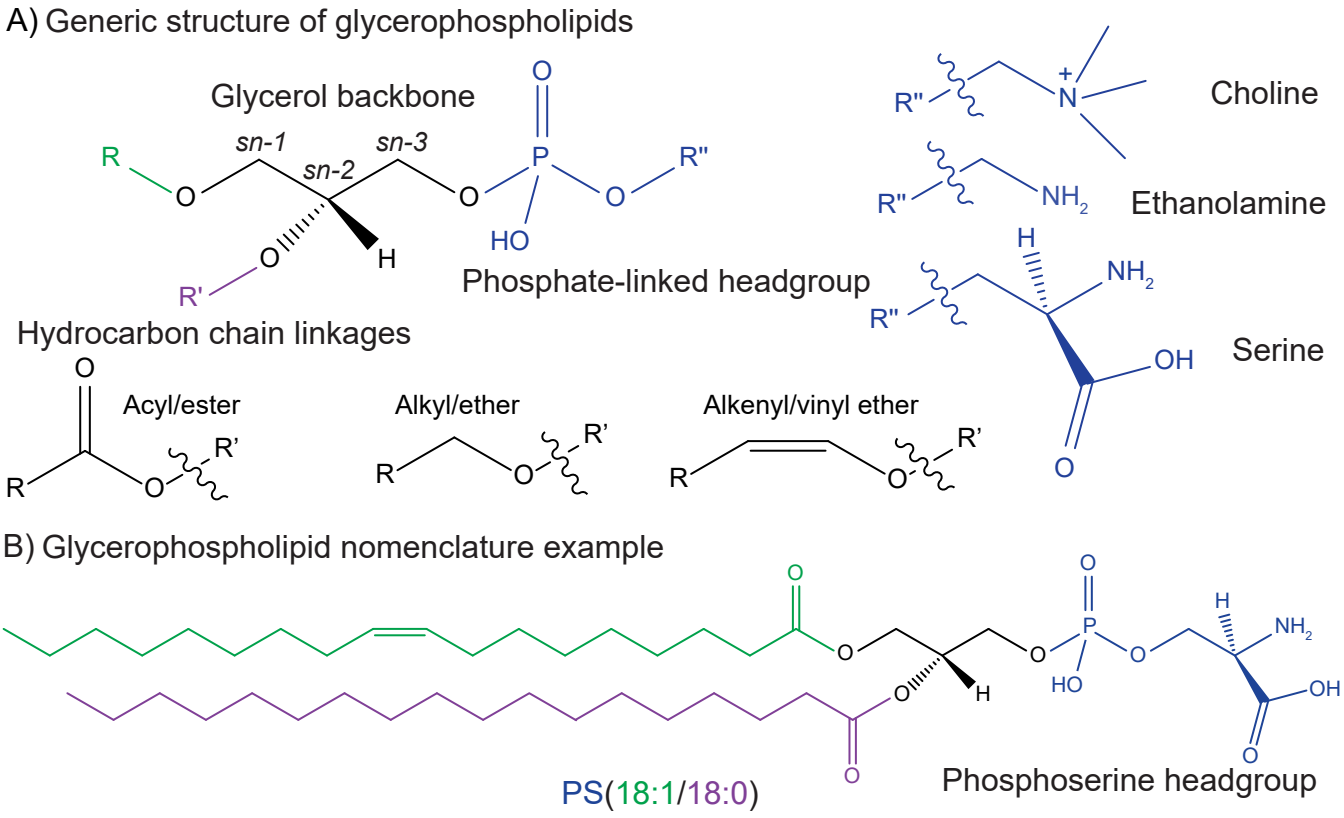

Figure 1.1 Structural characteristics of glycerophospholipids (GPLs). Schematics depict generic (A) and molecular (B) structures of GPLs. A) Generic GPL structure (left). The glycerol backbone is depicted in black, with *sn* positions labelled. The phosphate-linked headgroup is shown in blue, with acylated hydrocarbon chains at the *sn*-1 position in green (R) and the *sn*-2 position in purple (R'). Three linkages to the glycerol backbone are possible at *sn*-1 and *sn*-2 (acyl/ester, alkyl/ether, and alkenyl/vinyl ether) depicted below. R" in blue represents the phosphate-linked headgroup. Three of the possible glycerophospholipid headgroups are depicted (right), choline for glycerophosphocholine, ethanolamine for glycerophosphoethanolamine, and serine for glycerophosphoserine. B) Schematic of glycerophosphoserine PS(18:1/18:0) demonstrating how the nomenclature refers to the molecular structure. Name elements are coloured to match structural elements. In both nomenclature and structural figure, the phosphoserine headgroup is in blue; the glycerol backbone is in black; the *sn*-1 acyl-hydrocarbon chain is in green with :1 indicating the degree of unsaturation; the *sn*-2 acyl-hydrocarbon chain is in purple. If linkages had been ether, an O- would precede the hydrocarbon; if vinyl ether a P- would precede the hydrocarbon. Abbreviations: PS, glycerophosphoserine.

The hydrocarbon chains are located at the *sn-1* and *sn-2* positions of the glycerol, and are conjugated by either an ester bond, an ether bond, or a vinyl-ether bond, known as acyl, alkyl, or alkenyl bonds, respectively (Figure 1.1). If modified by a hydroxyl group at either the *sn*-1 or *sn*-2 positions, the lipid is known as a *lyso* GPL. In this thesis, the lipid nomenclature used describes the molecular identity of GPLs as follows: GPC and LPC refer to a lipid with a phosphocholine head group. GPS and LPS refer to a lipid with a phosphoserine head group. O- indicates an ether linkage; P- indicates a vinyl ether linkage; no designation refers to an ester linkage to the glycerol backbone. Thus, PS(18:1/18:0) refers to a GPS molecular species with a hydrocarbon chain of 18 carbons long with one unsaturation acylated at the *sn*-1 position and a hydrocarbon chain of 18 carbons long with no unsaturations at the *sn*-2 position.

SLs are classified by their headgroups, the sphingoid base backbone, and their N-acyl hydrocarbons, for which there are many subclasses, including the sphingoid bases (with an OH in place of the hydrocarbon), ceramides (Cer), phosphosphingolipids, and glycosphingolipids[21]. The simplest of these classes, the sphingoid base, is also the backbone of the other subclasses. Sphingoid bases consist of a hydrocarbon and an amide group (Figure 1.2). The individual combinations of hydrocarbon chain length and number of unsaturations determines the specific subclass of this sphingoid base. For example, a sphingoid base with 18 carbons and 0 unsaturations is also known as sphinganine, whereas if there is one unsaturation at the 4-5 carbon bond in the trans configuration, this is referred to as sphingosine (Sph). Further, the sphingoid base, due to the substrates involved in the *de novo* synthesis (described in section 1.2.3) can have between one and three hydroxy groups on carbons 1, 3 and 4, with the most prevalent structures consisting of two hydroxy groups, one on carbon 1, and one on carbon 3 (Figure 1.2). If a sphingoid base has a fatty chain acylated to the nitrogen of the amine, it becomes a member of the Cer class. The specific subclass of Cer is determined by the sphingoid base used to generate it. For example, Cer is formed from Sph, whereas dihydroceramide is formed from sphinganine. From Cer, other SL classes are generated by adding a headgroup to the oxygen on carbon 1 of the sphingoid base. Addition

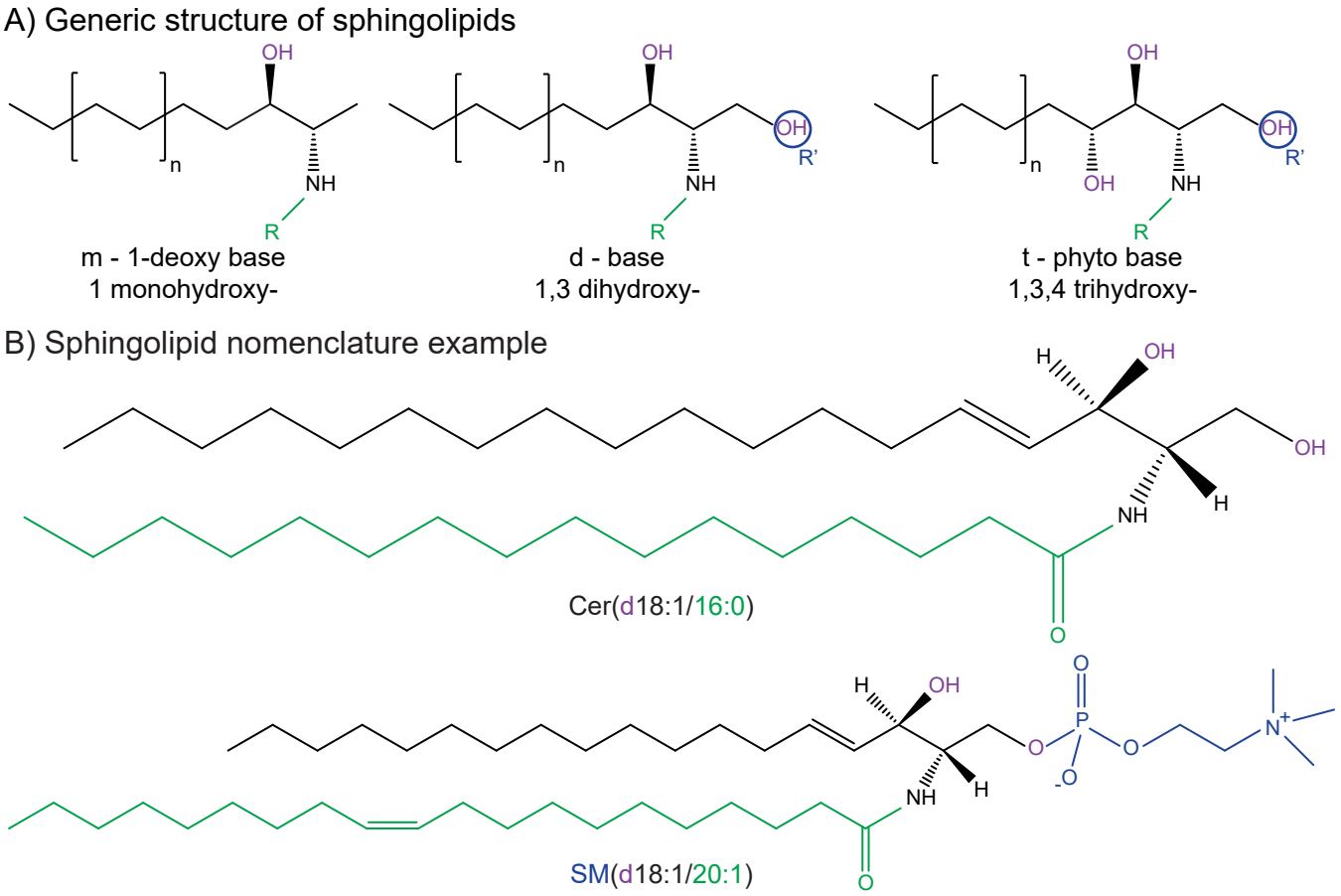

Figure 1.2 Structural characteristics of sphingolipids (SLs). Schematics depict generic (A) and molecular (B) structures of SLs. A) Generic SL structures depicting the three sphingoid base backbones. Hydrocarbons defining the sphingoid base are in black. The core structures of a 1-monohydroxy sphingoid base is depicted on the left, a 1,3-dihydroxy sphingoid base is depicted in the center, and a 1,3,4 trihydroxy sphingoid base is depicted on the right. The circle (blue) indicates the R' OH group that can be modified into other headgroups in complex SLs. R represents the N-acyl chain defining the molecular species, and is depicted in green. B) Schematics of two SLs, a ceramide (top, wherein R' is OH and R is a 16:0 hydrocarbon), and a sphingomyelin (bottom, wherein R' is a phosphocholine headgroup and R is a 20:1 hydrocarbon). Structural elements and nomenclature are coloured, with backbone in black, dihydroxy oxygens in purple, the N-acyl chain in green, and for sphingomyelin, the headgroup in blue. C) Schematics of generic glucosylceramide (GlcCer) and galactosylceramide (GalCer). The structural element distinguishing these stereoisomers, the position of the hydroxy group on the 4th carbon in the sugar ring, is circled in red, with GlcCer on the left and GalCer on the right. Abbreviations: Cer, Ceramide; SM, Sphingomyelin; GlcCer, glucosylceramide; GalCer, galactosylceramide.

of a phosphocholine headgroup produces sphingomyelin (SM), a subclass of phosphosphingolipids, whereas conjugating Cer with one or more sugar moieties results in a glycosphingolipid. In this thesis, the lipid nomenclature used describes the molecular identities of SLs as follows: first the subclass is denoted by the headgroup, second, details of the sphingoid base, including the number of hydroxy groups, the carbon chain length, and number of unsaturations is recorded, and finally the carbon chain length and number of unsaturations in the N-acylated fatty chain, if it is present. Thus, Cer(d18:1/16:0) refers to a Cer with a sphingoid backbone of a hydrocarbon chain that is 18 carbons long, with one unsaturation and two hydroxy groups, and an N-acyl chain that is 16 carbons long, with no unsaturations (Figure 1.2). SM(d18:1/20:1) refers to an SM with a sphingoid base that is 18 carbons long, with 1 unsaturation, and 2 hydroxy moieties, and is N-acylated by a hydrocarbon chain that is 20 carbons long, with 1 unsaturation (Figure 1.2).

1.2.2 GPS metabolism

In this thesis, Chapter 2 will examine the impact of *ANO6/Ano6* mutation on GPS metabolism *in vitro* in human cells and *in vivo* in a mouse model, while Chapters 3, 4, and 5, will examine the impact of *ASAH1* mutations on sphingolipid metabolism in human cells. Both of these classes of lipids contain/are formed from serine metabolism, and the basic metabolism of these species is reviewed below.

In mammalian cells, GPS is generated via headgroup exchange mechanisms, starting with GPC or GPE[24] (Figure 1.3A). This process is calcium-dependent and occurs through the actions of one of two GPS synthases, located in the endoplasmic reticulum (ER), primarily within the mitochondria-associated membrane fraction of the ER suggesting close contact between both organnelles[25]. Phosphatidylserine synthase 1 (PSS1) exchanges the choline from GPC with serine, and phosphatidylserine synthase 2 (PSS2) exchanges the ethanolamine from GPE with serine[24, 26]. To date, no enzyme has been identified in mammalian cells that directly synthesizes GPS from CDP-diacylglycerol and serine, as is the

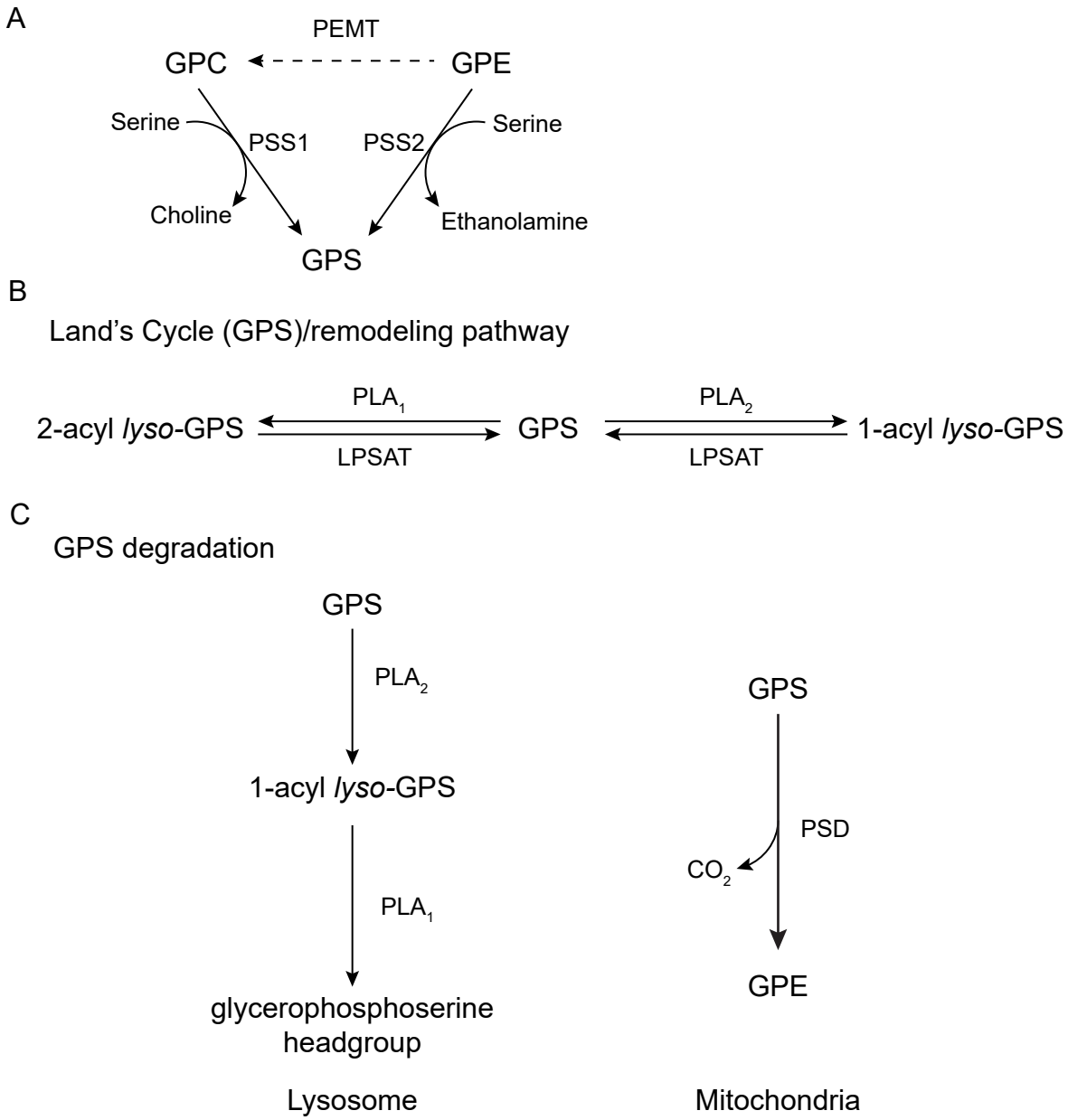

Figure 1.3 Glycerophosphoserine metabolism pathways. A) Synthesis of GPS occurs via headgroup exchange with either GPC or GPE, via the actions of PSS1 or PSS2 in mammals. B) GPS-specific Land's Cycle remodeling pathway. GPS is modified into 1-acyl *lyso*-GPS via the actions of GPS-permissive PLA_2s and can be reacylated by lysophosphoserine acyltransferases (LPSATs). GPS can also be converted into a 2-acyl *lyso*-GPS through the actions of GPS-permissive PLA_1s and again remodelled back to GPS by subsets of LPSATs. C) GPS degradation occurs in two pathways in mammalian cells. In the lysosome, GPS is first degraded by a GPS-specific PLA_2, resulting in 1-acyl *lyso*-GPS. This *lyso*-GPS is then acted upon by a PLA_1, resulting in a glycerophosphoserine headgroup with no acyl-chains (left). In the mitochondria (right), GPS is decarboxylated to GPE via the action of PSD. Abbreviations: CO_2, Carbon dioxide; GPC, glycerophosphocholine; GPE, glycerophosphoethanolamine; GPS, glycerophosphoserine; LPSAT, lysophosphoserine acyltransferase; PEMT, phosphoethanolamine methyl transferase; PLA_1, phospholipase A_1; PLA_2, phospholipase A_2; PSD, phosphoserine decarboxylase; PSS1, phosphatidylserine synthase 1; PSS2, phosphatidylserine synthase 2.

mechanism in yeast and prokaryotes[24]. Although PSS1 and PSS2 have different substrate specificities they do show redundancy, as mice lacking either *Pss1*, or *Pss2*, are viable and fertile[25, 27], although some male *Pss2*$^{-/-}$ mice do display reduced fertility. Loss of both *Pss1* and *Pss2* is lethal[27], indicating that GPS is necessary for survival. Once synthesized in the ER[28], GPS is primarily transported to the plasma membrane, but can also be found in Golgi, endosomes, ER, and mitochondrial membranes[29]. Transport is through vesicular transport[28], or by lipid transfer proteins[30] concentrating at membrane contact sites (reviewed by Lenoir *et al*.[31]). Once at the plasma membrane, GPS can be further modified via the Land's cycle (Figure 1.3B).

GPS, like other GPLs, can remodelled, following *de novo* synthesis, through Land's cycle metabolism (Figure 1.3B). The Land's cycle consists of two steps: hydrolysis and acyl remodelling. In the hydrolysis step, phospholipase A (PLA) 1 or 2 enzymes hydrolyse one of the acyl-linked chains from the GPS. The PLA_2 superfamily alone is composed of five specific categories of enzymes subdivided into 15 groups and multiple subgroups (reviewed by Burke and Dennis[32]). PLA_1 enzymes hydrolyse the *sn*-1 chain from a GPL resulting in a 2-acyl *lyso*-GPL[33], and PLA_2 enzymes hydrolyse the *sn-2* chain from GPLs resulting in a 1-acyl *lyso*-GPL[34]. GPS are hydrolyzed at the *sn*-1 position by GPS-specific secreted PLA_1 ($sPLA_1$) and PS-PLA_1[35]. Multiple $sPLA_2$s hydrolyze the acyl-linked hydrocarbon at the *sn*-2 position, including lysosomal PLA_2 (Group XV $LPLA_2$) which shows activity towards GPS under acidic conditions, and the adipose specific PLA_2 (Group XVI $AdPLA_2$) show higher activity for the anionic GPS family[34]. *Lyso*-GPS can, in turn, be remodelled back to GPS, by lysophosphoserine acyltransferases (LPSAT). LPSATs are part of a larger family of lysophospholipid acyltransferases, all of which catalyze the transfer of the acyl group from an acyl-CoA to a *lyso*-GPL resulting in a GPL. Each has different substrate specificity. For example, the lysophosphoethanolamine acyltransferase 1 (LPEAT1) was found to have similar activity levels towards glycerophosphoethanolamines (GPEs) as well as GPSs, but not towards glycerophosphocholines (GPCs)[36]. By utilizing a variety of acyl-CoAs, rapid changes in the diversity of

species at the plasma membrane can be achieved, for example, lysophosphocholine acyltransferase 3 (LPCAT3) shows LPSAT activity and can utilize Acyl-CoAs with 18:1, 18:2, or 20:4 chains[36].

GPS is degraded in two distinct pathways (Figure 1.3C). GPS can be recycled to the lysosome, where it undergoes sequential degradation by phospholipases. Typically, a PLA_2 will first hydrolyse GPS, and then a PLA_1 with 1-acyl *lyso*-GPS activity, such as the PS-PLA_1, will hydrolyse the remaining acyl chain resulting in a GPS headgroup and a free fatty acid[37]. The second pathway occurs in the mitochondria. There, GPS species are decarboxylated by phosphatidylserine decarboxylase (PISD), resulting in GPE and carbon dioxide[24].

1.2.3 SL metabolism

Sphingolipids (SLs) are a class of lipids consisting of an N-acylated hydrocarbon and a sphingoid backbone (Figure 1.4). SL metabolism is a complex network of highly regulated reactions, with ceramide (Cer) at the center[38]. Cers are produced through *de novo* synthesis and remodelling pathways. They are modified to a large number of complex SLs through modification pathways. Finally, constituent structural components recycled through the salvage pathway (Figure 1.4).

De novo Cer synthesis pathway is initiated and occurs in the ER (Figure 1.4). The first, and rate-limiting, step of the process occurs when serine palmitoyl transferase (SPT) condenses serine and palmitoyl-CoA into 3-keto-dihydrosphinganine[38]. While SPT does have substrate preferences – it preferentially catalyzes the condensation between palmitoyl-CoA and serine, ultimately resulting in the 18-carbon chain backbone (sphingosine or d18:1) which is the most prevalent in mammalian tissue – it can also utilize other acyl-CoAs resulting in atypical sphingoid bases[39-42]. Similarly, SPT can also utilize other amino acids, mostly alanine or glycine, which results in the atypical SLs, 1-deoxy-sphingolipids, or 1-deoxymethyl-sphingolipids, respectively[39, 40, 43]. 3-keto-dihydrosphinganine is rapidly reduced by 3-

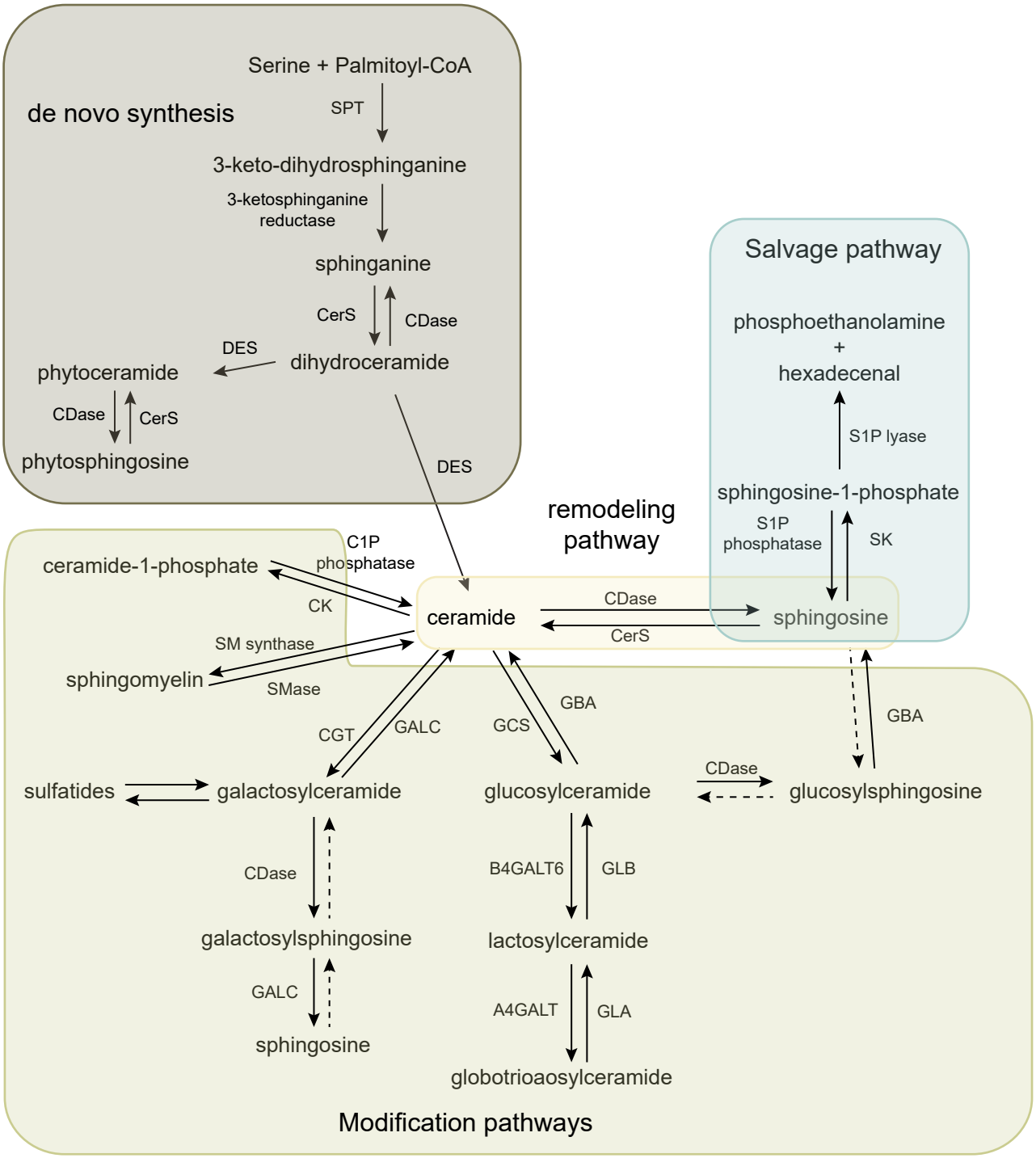

Figure 1.4 Sphingolipid metabolism pathways. Sphingolipid metabolism is comprised of the *de novo* synthesis pathway, the ceramide remodeling pathway, the modification pathway, and the salvage pathway. The *de novo* synthesis pathway begins with the condensation of serine and palmitoyl-CoA, and results in the generation of ceramide, or phytoceramide. The ceramide remodeling pathway occurs between ceramide and sphingosine, potentially resulting in ceramides with different N-acyl chains. The modification pathways begin with ceramide, and results in the generation of sphingolipids with more complex headgroups, but the same N-acyl chain conjugated to the backbone. The salvage pathway begins with sphingosine, and results in the degradation of the backbone, resulting in phosphoethanolamine and hexadecenal. Abbreviations, A4GALT, α-1,4-galactosyltransferase; B4GALT6, β-1,4-galactosyltransferase 6; C1P phosphatase, ceramide-1-phosphate phosphatase; CDase, ceramidase; CerS, ceramide synthase; CGT, ceramide galactosyltransferase; CK, ceramide kinase; DES, dihydroceramide desaturase; GALC, galactosylceramidase; GBA, β-glucocerebrosidase; GCS, glucosylceramide synthase; GLA, α-galactosidase A; GLB, β-galactosidase; S1P, sphingosine-1-phosphate; S1P lyase, sphingosine-1-phosphate lyase; S1P phosphatase, sphingosine-1-phosphate phosphatase; SK, sphingosine kinase; SM, sphingomyelin; SMase, sphingomyelinase; SM synthase, sphingomyelin synthase; SPT, serine palmitoyl transferase.

ketosphingaine reductase, which results in the production of sphinganine (Sph(d18:0)). Sphinganine is then N-acylated by the action of ceramide synthases (CerS) proteins producing dihydroceramide (Cer(d18:0/X:Y)). The CerS proteins are a family of integral membrane proteins, there are six members in mammalian cells, and they are located in the ER and Golgi. Each of the CerS enzymes has fatty-CoA preference, reviewed by Tidhar and Futerman[43]. Interestingly, the CerS proteins are not restricted to sphinganine as a substrate, as they can also N-acylate sphingosine. Dihydroceramide, once produced, is then desaturated by dihydroceramide desaturase (DES). There are multiple DES enzymes, with DES1 introducing the 4,5-double bond to dihydroceramide resulting in Cer (Cer(d18:1/X:Y)), and DES2 is responsible for the addition of a 4-hydroxyl group, generating phytoceramide[40] (Cer(t18:0/X:Y)) (Figure 1.3). After the action of DES, forming Cer or a phytoceramide, the sphingoid base of the lipid is not modified further.

Once Cer has been generated, various modification pathways can occur, generating more complex SLs. Most of these modification pathways occur by adding, or modifying, a headgroup to Cer, and many of these synthesis steps occur in the Golgi apparatus. To facilitate this, Cer is transported from the ER to the Golgi either by ceramide transfer protein (CERT), or by vesicular transportation[38]. Once in the Golgi apparatus, Cer can be modified by a variety of pathways generating different SLs. A phosphocholine headgroup from a GPC can be transferred to a Cer by the action of sphingomyelin (SM) synthase, resulting in a SM and a diacylglycerol. Cer can also be phosphorylated by ceramide kinase (CK), resulting in Ceramide-1-Phosphate (C1P), a potent signaling molecule. Apart from phosphate containing modifications, Cer can be conjugated with different sugar headgroups, forming glycososphingolipids. The simplest of these are the hexosylceramides (HexCers), which are Cers conjugated either to a galactose resulting in galactosylceramide (GalCer) following the action of ceramide galactosyltransferase (CGT), or a ceramide conjugated to glucose, resulting in glucosylceramide (GlcCer) due to glucosylceramide synthase (GCS). GalCer is the basis for the sulfatide family of

glycososphingolipids. GlcCer is further modified by the addition of a galactose by β-1,4-galactosyltransferase 6 (B4GALT6), resulting in lactosylceramide (LacCer), which is a branch point for further glycososphingolipid families, forming the sugar backbone of a large variety of other species, for example, gangliosides, or the globotriaosylceramides (Gb3Cer). Gb3Cer is synthesized by α-1,4-galactosyltransferase (A4GALT), which conjugates a galactose onto LacCer. All of these modifications can be reversed through further metabolic pathways, most of which occur in the endo-lysosomal network. SM can be hydrolysed back into Cer by one of the sphingomyelinases (SMase), identified by their pH optima as either acid, neutral, or alkaline SMases[38], and C1P can be dephosphorylated back into Cer by C1P phosphatase. The glycososphingolipids are recycled back to Cer via the action of sequential hydrolysis reactions, removing the sugar moieties from the reducing end of the oligosaccharide chain[41]; Gb3Cer is hydrolysed to LacCer by α-galactosidase A (GLA), LacCer is hydrolysed to GlcCer by β-galactosidase (GLB1), and GlcCer is hydrolysed to Cer by β-glucocerebrosidases (GBA1, GBA2). GalCer, by contrast, is hydrolysed to Cer by galactosylceramidase (GALC). There is evidence showing that the N-acyl chain from both GlcCer and GalCer can be hydrolysed by acid ceramidase (aCDase)[44, 45], resulting in the production of glucosylsphingosine (GlcSph) and galactosylsphingosine (GalSph) respectively. The glucose or galactose moiety from GlcSph and GalSph can be hydrolyzed by GBA1 or GALC, resulting in sphingosine (Sph), which can enter the remodelling pathway, or the salvage pathway.

The Cer remodeling pathway (Figure 1.4), is a smaller pathway, compared to the variety of the modification pathways, but is no less important. In the remodeling pathway, the N-acyl chain from Cer is hydrolysed, resulting in Sphingosine (Sph) and a free fatty acid. This process is catalyzed by one of the ceramidase proteins (CDase), identified by their pH optima; aCDase, neutral ceramidase (nCDase), and the three alkaline ceramidases (alkCDase 1, 2, or 3). Each of the CDases resides in different cellular compartments, aCDase is localized to the lysosome, but has also been found localized in the nucleus[46], nCDase is primarily localized to the plasma membrane, but can also localize to the Golgi and

mitochondria[47], and alkCDase 1 is primarily localized to the ER, alkCDase 2 is localized to the Golgi, and alkCDase 3 when overexpressed is localized to both the ER and the Golgi apparatus[48]. The produced Sph can then be remodelled into Cer, N-acylated by one of the six CerS.

Alternatively, the Sph produced by the remodeling pathway, or by the deglycolysis of GlcSph or GalSph, can enter the salvage pathway. The salvage pathway results in the recycling of sphingosine into component parts. It begins with the phosphorylation of Sph into sphingosine-1-phosphate (S1P) via sphingosine kinase (SK), which, like C1P, is a potent signaling molecule. S1P can be dephosphorylated back to Sph by S1P phosphatases, or it is metabolized into phosphoethanolamine and hexadecenal, by S1P lyase[49].

Taken together, SL metabolism is a highly complex and regulated network of pathways and metabolites and is essential for the proper functioning of cells.

1.2.4 Targeted lipidomics

Advances in mass spectrometry have enabled, for the first time, lipids to be identified at the molecular level. I review here the technical underpinnings of targeted lipidomics used in this thesis to assess GPS and SL metabolism in three rare diseases.

In simple terms, mass spectrometry is a technique wherein electric and magnetic fields influence the trajectory of charged particles in a vacuum. The interaction between the ions and these fields depends on each particle's mass-to-charge ratio (m/z), and thus the trajectory of the particle depends on its m/z[50, 51]. Only charged particles can be influenced by these electromagnetic fields, and so all molecules must be ionized prior to mass spectrometry analysis, and the ions must be in the gas phase to be analyzed. Therefore, mass spectrometers must accomplish a few things: they must ionize the samples, they must bring the samples to the gas phase if they are not already in vapour form, and then they must measure

the m/z of the produced ions[50]. Modern mass spectrometers include three main components: the ion source, where analytes are ionized and volatized; the mass analyzer(s) that separate the ions according to their m/z; and the detector, which records an induced charge, or the current produced when an ion interacts with it[52] (Figure 1.5). Mass spectrometry analyses can also include further processing steps, such as the inclusion of prior separation (for example, with high performance liquid chromatography, HPLC), or with separation steps occurring after ionization but before the entry into the mass analyzers (for example, ion mobility also known as differential ion mobility spectrometry (DMS)). While there are many different types of mass spectrometer, whether classified by the ion source or by the number and type of mass analyzers, I will only discuss the principles of the system used in subsequent chapters of this thesis. I thus describe high-performance liquid chromatography, electrospray ionization, tandem mass spectrometry (HPLC-ESI-MS/MS). I will also briefly discuss DMS as an orthogonal separation step to HPLC in the mass spectrometry pipeline[53], forming our HPLC-ESI-DMS-MS/MS mass spectrometry analytical work flow used to discriminate between GlcCer and GalCer at the molecular level.

1.2.5 HPLC

In this thesis, I employed reverse phase HPLC wherein samples containing a mixture of analytes are separated based on their hydrophobicity (Figure 1.6). In reverse phase HPLC, samples are carried by the mobile phase through a column containing the stationary phase, and the speed that the analytes travel through the column, and thus into the mass spectrometer, is governed by the equilibrium between the adsorption and desorption the analytes have with the stationary phase (aka retention). This speed is referred to as retention time – referring to the amount of time individual species withing a given lipid extract are retained on the column prior to elution[52]. The difference in this speed enables analytes of different hydrophobicities to be separated. More hydrophilic lipids elute first and more hydrophobic lipids are retained for longer periods of time on the column, eluting later. The mobile phase is liquid and

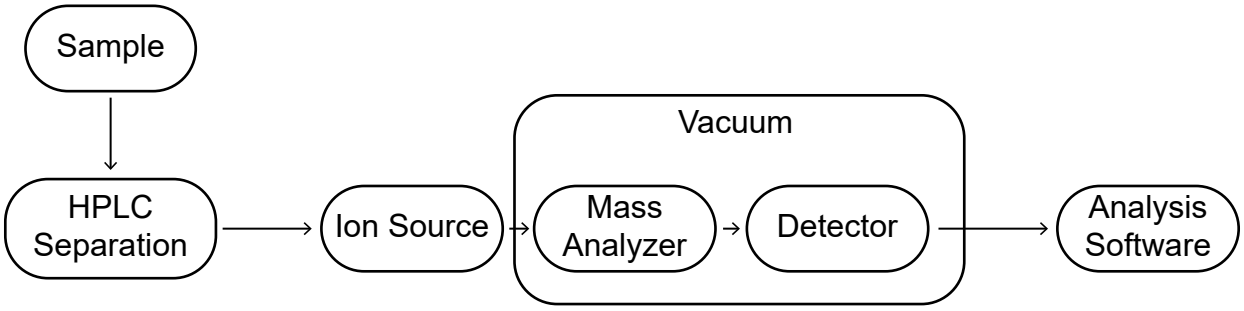

Figure 1.5 Lipidomic workflow. Samples are separated via HPLC separation (see Figure 1.6), and then ionized in the ion source (see Figure 1.7), to form a vapourized spray of ions in the gas phase. The ions then enter the mass analyzer(s) (see Figure 1.9) under vacuum, where they are separated by their mass to charge ratio (m/z) and detected in the detector. The recorded mass spectra are then processed by user's analysis software of choice.

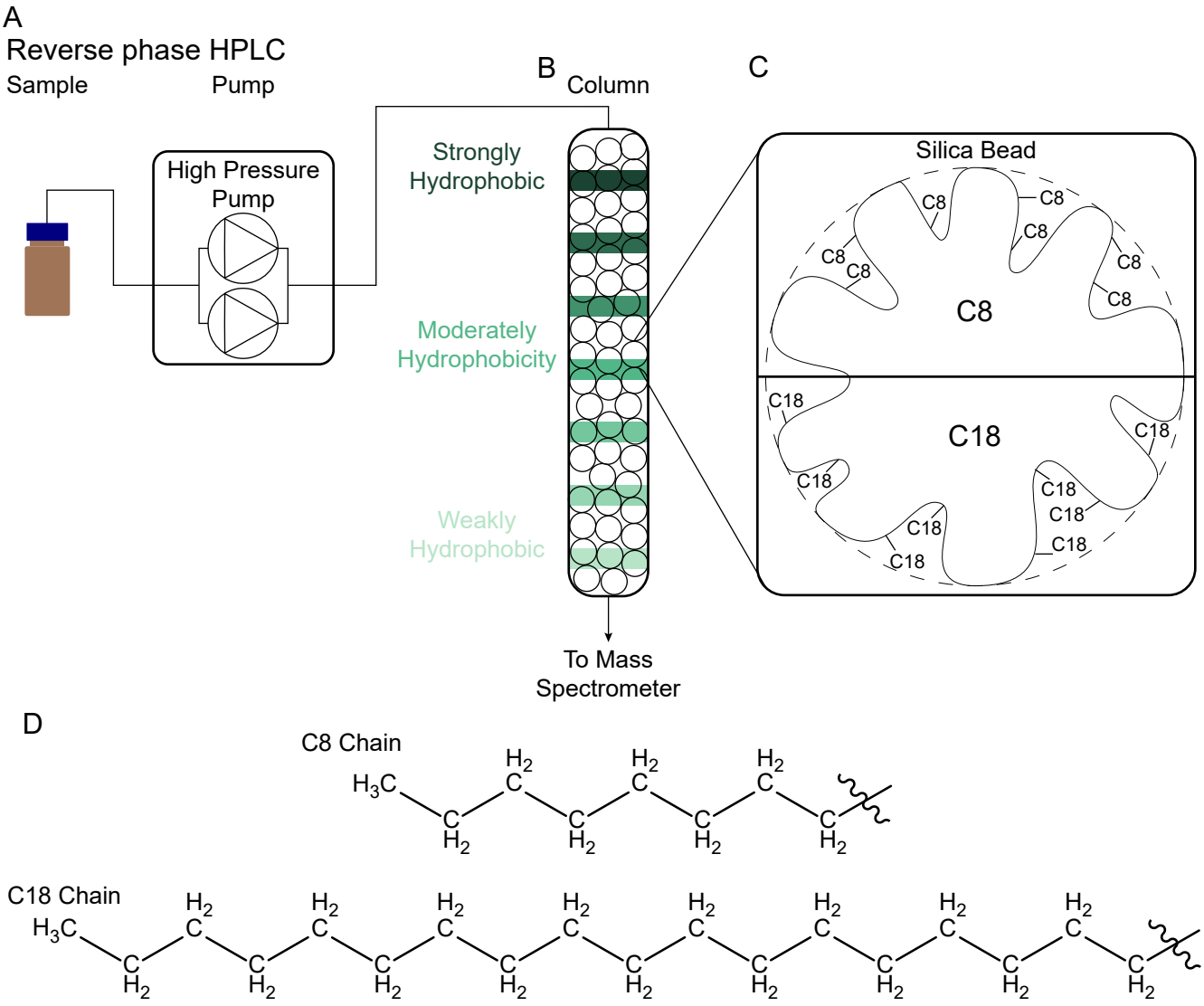

Figure 1.6 Reverse phase HPLC schematic. Schematic diagram of reverse-phased high performance liquid chromatography (HPLC). A) liquid sample is injected into the HPLC system, where a high pressure pump forces the sample through the column. A binary pump is depicted, which allows for the creation of a gradient in the hydrophobicity of the mobile phase. B) The sample mixture is pumped through the column, which consists of a capillary containing the stationary phase. C) The stationary phase consists of porous silica beads with hydrophobic moieties conjugated on them. D) These hydrophobic components consist of carbon chains of either 8 or 18 carbons long and are situated within the pores of the beads. Due to the hydrophobicity of the stationary phase, more hydrophobic components of the sample mixture adhere to the apex of the column, whereas weakly hydrophobic components travel further down the column. Increasing the hydrophobicity of the mobile phase allows for the more hydrophobic components to elute from the column, and into the mass spectrometer.

the stationary phase is solid, generally in the form of particles or beads. In reverse phase HPLC separations, the stationary phase is non-polar, frequently porous silica beads modified by hydrocarbon chains (Figure 1.6 C, D). The mobile phase is polar[54], commonly water, alcohol, and acetonitrile[55]. In HPLC the sample within the mobile phase is pumped through the column with pressure (speed) influencing retention time (Figure 1.6A,B). As the sample is pumped through the column, the different analyte molecules interact with the stationary phase, slowing their progress through the column. In reverse phase analyses, the more hydrophobic the analyte is, the more strongly it interacts with the stationary phase, and thus the longer it is retained on the column[55, 56] (Figure 1.6).

The mobile phase can either be isocratic, where the solvent remains at a constant concentration throughout the course of the separation, or can be a gradient, where the composition of the solvent is changed during the separation[57]. By using a gradient approach, the changing polarity of the solvent changes the equilibrium balance between adsorption and desorption of the analyte molecules, allowing for the more tightly adsorbed analytes to elute off the column[57]. In reverse phase experiments, for example, throughout the course of the experiment the polar solvent is mixed with progressively higher concentrations of non-polar solvent, causing the strongly hydrophobic analytes to interact less strongly with the stationary phase, allowing them to elute off the column. Trifluoroacetic acid (TFA) or formic acid (FA) are commonly added to the mobile phase, to reduce pH to ~1.5-2.2[58] and ensure lipids are protonated thus charged for detection by the mass analyzers.

1.2.6 Electrospray Ionization

The first component of a mass spectrometer is the ion source. The ion source performs two main functions in HPLC-ESI-MS/MS. First, the ion source vaporizes the sample. Second, and more importantly, the ion source exploits the deprotonation enabled by the mobile phase to impart a charge to

the analyte molecules. Mass analyzers can only detect charged ions. Lipidomics has been realized through advances in ionization technology including the development of 'soft' ionization methods that do not fragment analyte molecules to their constituent electrons, rather partially fragments analytes allowing structural moieties that define individual lipid species to be detected. The two most utilized soft ionization techniques are electrospray ionization (ESI), which ionizes liquid samples into the gas phase[59]; and matrix-assisted laser desorption/ionization (MALDI), which ionizes solid sample into the gas phase. A description and explanation of MALDI is beyond the scope of this thesis, but a recent review of it can be found by Zhu *et al*[60].

A summary of the ESI process is provided in Figure 1.7. To transform lipid in liquid to gas phase, liquid lipid ions first accumulate at the tip of the ESI capillary[50, 52]. To assist the desolvation process and increase the ionization efficiency of the electrospray process, volatile organic solvents, or compounds that increase conductivity such as formic acid are often added to the mobile phase solution[52]. The surface tension of the analyte-containing solution causes a drop to form at the tip of the capillary. A high voltage is applied between the capillary and the mass analyzer sample plate[61], and this causes charge separation at the tip of the capillary which acts against the surface tension[50, 61]. For example, in positive ion mode, the capillary is an anode while the sample cone is a cathode. The electric field is produced by the generation of a potential difference between the capillary and the opposing MS inlet [62] (Figure 1.7). When the voltage applied at the capillary and the surface tension of the liquid within are at equilibrium, the drop becomes cone-shaped, named the Taylor cone (Figure 1.7), after Sir Geoffrey Taylor who characterized the properties of this cone[50, 59]. An increase in the electric potential at the capillary causes a spray of liquid droplets to be expelled from the Taylor cone into the space between the capillary and the mass analyzer inlet, forming the aerosolized electrospray[50, 52, 59] (Figure 1.7). If a positive voltage is applied at the capillary and a negative voltage at the sample inlet, the droplets are positively charged referred to as positive ion mode. Flipping the charges, i.e., negatively charged capillary and positively

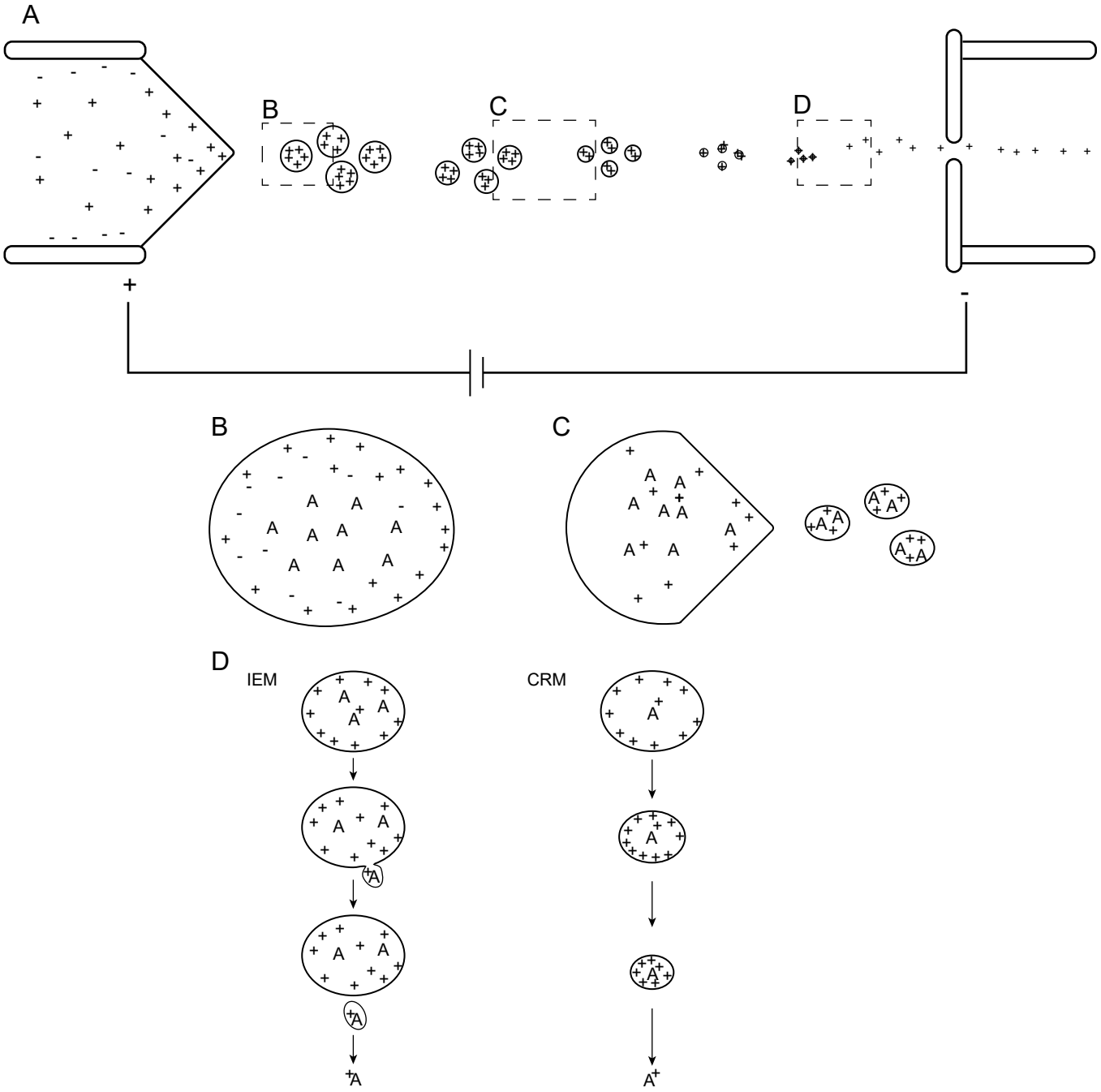

Figure 1.7 Electrospray ionization. A) The liquid sample containing the analyte mixture is pumped through the column to the end of the capillary, which has a strong voltage applied across it. In positive ion mode, there is a positive charge at the capillary tip, and a negative charge at the mass spectrometer inlet. The analytes form the Taylor cone and are released into the space between the capillary and the inlet to the mass spectrometer. B) Droplets are released into the space between the capillary and the orifice. Droplets form an oblong globoid shape with the analyte molecules generally in the middle, with the charge at the surface of the droplet. Depicted is the positive surface charge in positive ion mode. C) Due to desolvation, the droplet size shrinks, effectively increasing the charge density of the droplet. Eventually, a second Taylor cone forms, and smaller droplets are released. D) Summaries of the two theories of the last charge transfer to the analyte molecules. Both the Ion Evaporation Model (left), and the Charge Residue Model (right) result in charged individual analyte ions. Abbreviations: A, analyte molecule; A+, analyte ions (positive ion mode); CRM, Charge residue model; IEM, Ion Evaporation model; +, positive charge; -, negative charge.

charged sample inlet, generates negative ions, or negative ion mode[52].

Once the droplets leave the Taylor cone, they undergo extensive solvent evaporation (termed desolvation) assisted by the addition of a drying gas such as N_2 and higher temperatures, which results in a decrease in the solvation shell and thus size of the droplets[61, 63]. These droplets, while under the external electric field, form an elongated shape, even becoming pointed at both poles of the droplets[50] (Figure 1.7). The reduction in the solvation shell effectively increases the charge density of the droplets, until Coulombic charge repulsion overcomes their surface tension, at the Rayleigh instability limit, and the droplets become unstable[50]. The charge density aggregates at the pointed ends of the droplet, forming the Taylor cone, and expelling smaller droplets, approximately 10% of the size of the original[59] (Figure 1.7). These daughter droplets undergo further desolvation, and the process repeats. Once the droplets are sufficiently small, analyte ions are released into the gas phase and are brought into the mass analyzer.

This last step is controversial in that there are two mechanistic models: the ion-evaporation model (IEM), and the charge residue model (CRM)[59] (Figure 1.7D). In IEM, the analyte is charged, typically from protonation assisted by an organic acid as reviewed above[64]. Once the droplet containing this analyte ion reaches a small enough radius, the charge density on its surface becomes sufficient to make it energetically favourable for the ion to be expelled from the droplet[50, 52, 59]. The ion travels beyond the droplet surface until it is fully released. Any remaining solvent ions are dried by the heat and the carrier gas, resulting in an analyte ion entering the mass spectrometer[52].

In CRM, the droplets continue to undergo evaporation and fission cycles until they reach a point where, on average, there is one or fewer than one analyte molecule per droplet. When the last solvent molecules are evaporated from the analyte molecule, the excess charge of the droplet is transferred to the analyte molecule, and these ions are released to the gas phase. For much of this process, the analyte molecules are not affected by the changing charge at the surface of the solvent droplet, until the charge

is passed onto them. It is generally accepted that low molecular weight ions are brought to the gas phase via IEM, whereas larger ions form via CRM[50, 52, 59].

1.2.7. DMS

Following ionization, a second dimension of separation can be applied to discriminate between lipid stereoisomers. HPLC represents the first dimension of analyte separation, based on hydrophobicity. Yet there are multiple isomers (lipids with the same molecular formula but different structure) that will elute with identical retentions times, notably in this thesis GlcCers and GalCers (Figure 1.2). Their separation requires a second dimension, or orthogonal separation[53, 65].

DMS is an orthogonal separation technique, occurring between the ion source and the mass spectrometer sampling orifice, where gas phase ions are separated based on their mobility in high and low electric fields in a carrier gas at atmospheric pressure[56, 65, 66]. The ions travel through a gap in two parallel plates towards the mass analyzer, carried by a neutral/inert gas such as N_2 (Figure 1.8). During this flight path, the ions are subjected to an electric field perpendicular to the direction of the carrier gas flow. This electric field is generated by a high-voltage radio frequency asymmetric box wave (Figure 1.8), with a maximum amplitude called the separation voltage (SepV)[65]. As the electric field is applied perpendicularly, the analyte ions drift off axis towards the walls of the plates, ultimately leaving the flight path towards the mass analyzer[66, 67] (Figure 1.8). The ions within this asymmetric field are affected differently by the oscillating field based on their collision cross-section, giving the ions different pathways through the field, and allowing them to be separated[50, 56, 67]. A counterbalancing DC voltage, called the Compensation Voltage (COV), is applied across the DMS cell, and when tuned properly, the overlapping SepV and COV values will correct the trajectory of ions with a specific collision cross-section, allowing specific structures to pass into the mass analyzer. This forms the basis of the separating

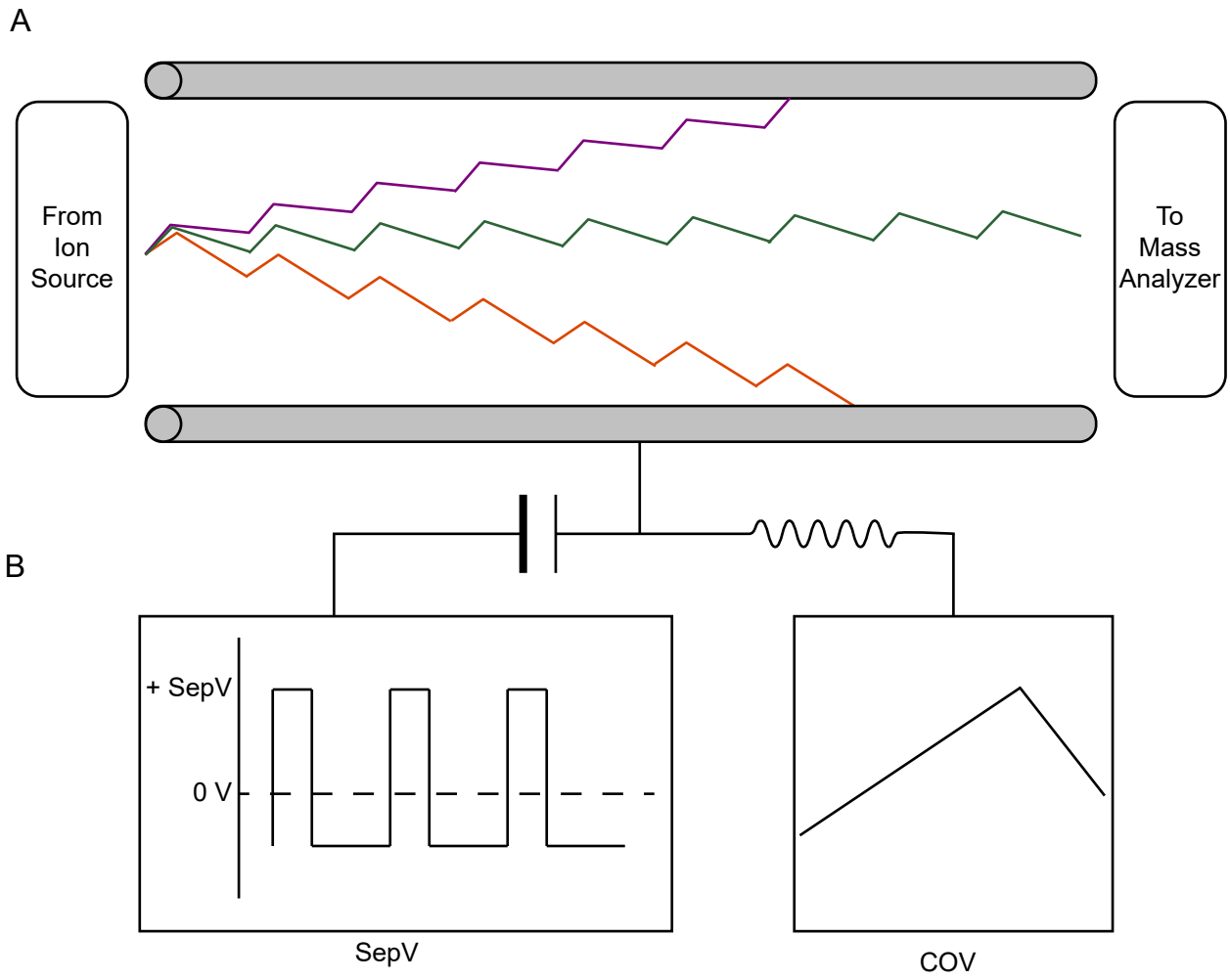

Figure 1.8: Schematic of Differential Mobility Spectrometry. A) Following HPLC separation and ionization, ions travel through the DMS cell in modifier gas, and the trajectories of these ions are influenced by the electric fields applied perpendicularly, as they divert from the path to the analyzer, represented by the coloured traces. The DMS cell is tuned such that only specific species can travel through and reach the analyzer, represented by the green trace. B) The perpendicular electric field applied across the DMS cell consists of the separation voltage (SepV) and the compensation voltage (COV). The SepV (left) is defined by an asymmetric box wave with maximum amplitude tuned by the experimenter. The COV (right) is a counterbalancing DC voltage which acts to correct the trajectory of the ions. Abbreviations: COV, compensation voltage; SepV, separation voltage.

function of DMS, which only allows for ions with identical retention times yet different ion mobilities to be directed by the SepV and COV electric fields[56]. To further enhance the separation of DMS, volatile chemical modifiers can be added to the carrier gas. Interactions between the modifiers and the analyte ions can cause shifts in the necessary COV values to separate that specific compound and can often shift the COV from isomeric or isobaric compounds[65]. The effectiveness of the chemical modifier depends on the gas-phase properties of the modifier, and the binding between the ion and the modifier.

DMS separates ions within the electric field generated in the DMS cell based on their collision cross-section, which is determined, in part, by their structural characteristics. Stereoisomers are species with the same atomic makeup, and the same atomic connectivity, but differ in the spatial arrangement of these atoms. For example, HexCers refer to the mixture of GlcCers and GalCers, which differ in their stereochemistry at carbon 4 (Figure 1.2C), with the hydroxyl group being in either the equatorial (GlcCer) or axial (GalCer) position. Reverse phase HPLC separation is driven by the hydrophobicity of these lipids, which cannot separate the retention time of GlcCer or GalCer stereoisomers; however, their different stereochemistry results in differential mobility within the DMS cell, enabling DMS to separate both GlcCer and GalCer glycosphingolipids[53, 56].

1.2.8 Quadrupole Mass Analyzers

Following ionization and, if applied, further separation by ion mobility, the analyte ions are directed into the mass analyzers. The mass analyzers filter the ions by their m/z and then pass these ions to the detector. This thesis employed a quadrupole analyzer, consisting of four conducting rods arranged in parallel within a vacuum, with a space in the middle permitting ion passage. The opposing pairs of rods are electrically connected to each other (Figure 1.9). In the first quadrupole (Q1) and the third quadrupole

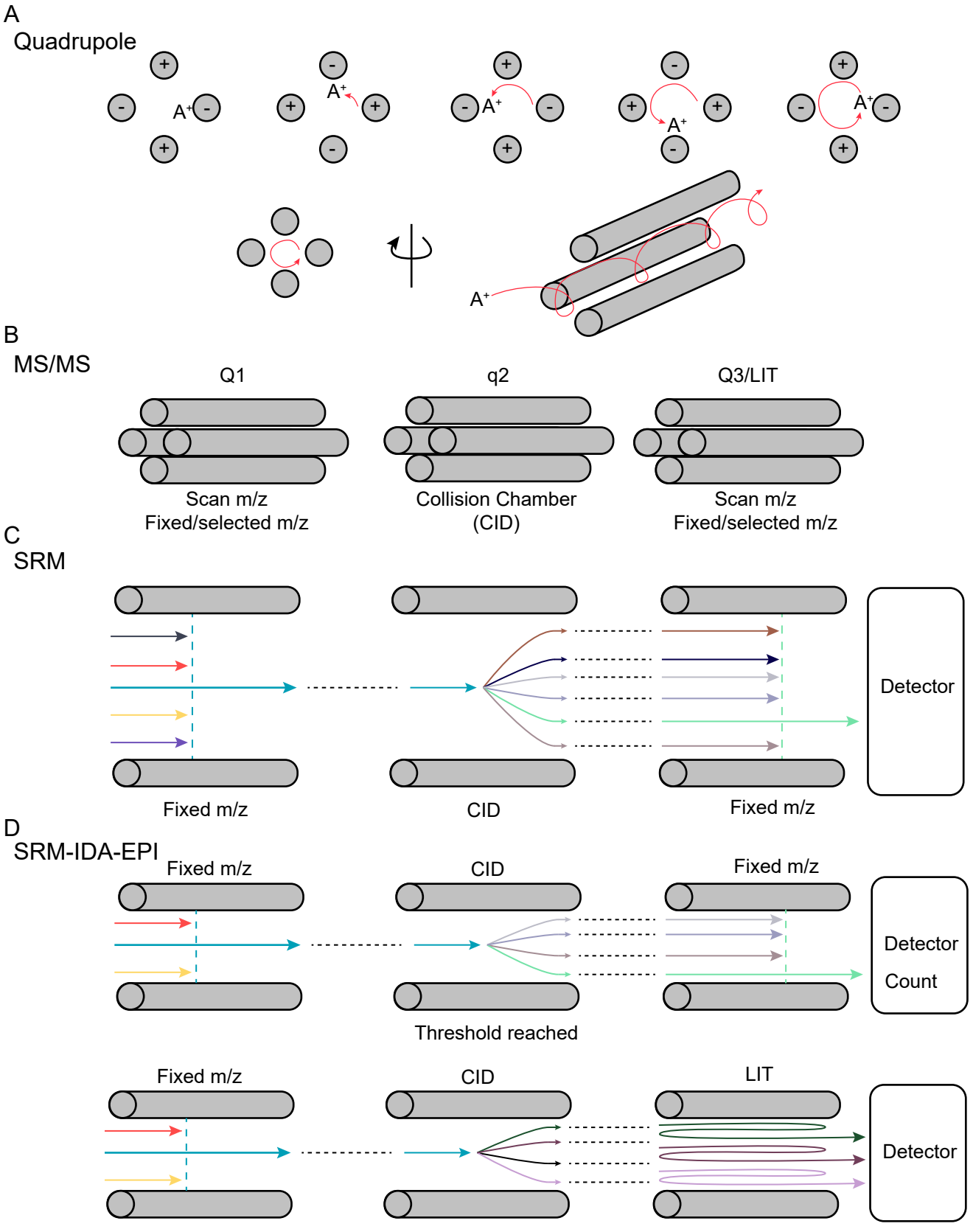

Figure 1.9 Triple quadrupole mass analyzers. For details, see next page.

Figure 1.9 Triple quadrupole mass analyzers

A) Schematic of the trajectory of an ion with a selected for m/z within Q1 (the first quadrupole). In positive ion mode, the analyte is positively charged, and thus drifts towards the negatively charged quadrupole. The basic trajectory of the analyte is depicted in red. B) The triple quadrupole, tandem MS/MS setup. Quadrupole 1 (Q1) and Quadrupole 3 (Q3) either scan through a specified m/z range or are set to a fixed m/z. Quadrupole 2 (q2) is set as a collision-induced dissociation (CID) chamber to fragment the precursor ions filtered in Q1 before passing these product ions to Q3. C) Selected reaction monitoring (SRM) method for MS/MS. Q1 is set to a fixed m/z, and any analytes with that m/z pass through to q2 where they are fragmented, and a specific fragment is selected for and measured in Q3. D) SRM-information dependent acquisition (IDA)-enhanced product ion (EPI) scan mode method for MS/MS experiments. First, an SRM scan is performed, and the presence of a designated production ion (filtered by a specific m/z) striking the detector is counted. Once a preset threshold is reached, the EPI scan mode is triggered, where Q3 is used as a LIT, trapping all fragments transmitted from q2 to the detector to enable structural identification. Abbreviations: CID, collision-induced dissociation; LIT, linear ion trap; m/z, mass to charge ratio; Q1, first quadrupole; q2, second quadrupole/collision cell; Q3, third quadrupole; SRM, single reaction monitoring; SRM-IDA-EPI, single reaction monitoring-information dependent acquisition-enhanced product ion scan.

(Q3), an electric field is applied to the quadrupoles, with a radio frequency (RF) voltage being applied to one pair of rods, and an equal amplitude, but out of phase, RF voltage to the other pair of rods. In the second quadrupole, collision with an inert gas is initiated (described below). The RF frequency forms an alternating current, and the potentials oscillate as the ions travel through the quadrupole. Hence, one pair of rods begins with a set positive voltage, then alternates between positive and negative voltages, whereas the other pair begins with a set negative voltage, and alternates between negative and positive voltages (Figure 1.9) The amplitude of these voltages is the same. A positive or negative DC offset voltage is set among the pairs of rods, such that one pair has a positive DC offset voltage and the other has a negative DC voltage[57]. The RF and DC voltages generate an electric field that acts on the trajectory of the ions as they travel through the quadrupole (Figure 1.9). The alternating RF voltage generates an oscillating field that causes the ions to follow a complex trajectory to reach the detector at the end of the analyzer (Q3). Briefly, in positive ion mode, cations enter each quadrupole and travel through to the other end. The cations drift towards the negatively charged rods and are repelled from the positively charged rods. But before the cations can contact the rod, the polarity switches, and the ions are now repulsed from the rod, and drift towards the center, being attracted to the now negatively charged rods. This alternating RF voltage focuses ions with the desired m/z into the center of the quadrupole, and this continues until the analyte cations reach the end of the quadrupole[52, 56]. It is the interplay between the oscillating RF voltage and the static DC voltage allows for the quadrupole to act as a mass filter. When a certain RF/DC voltage is specified, only ions with a specific m/z ratio can travel through the quadrupole[50]. This works because ions with a m/z below the specified value are deflected by the oscillating RF voltage into an unstable trajectory which ultimately results in the ions contacting one of the rods, being discharged, and thus not reaching the detector at the end of the quadrupole[68]. Ions with an m/z higher than the specified value are less affected by the RF voltage, but instead are influenced by the DC voltage, so drift towards rods with the opposite charge to that of the ion, i.e., towards the negative voltage rods in positive ion mode. As

with the low m/z ions, these heavier ones have an unstable trajectory and they are not detected. Thus, the strength of the RF and DC voltages applied to the rods determine which ions (aka the specified m/z) achieve a stable trajectory and thus reach the end of the quadrupole. By adjusting the RF/DC voltages, the quadrupole filters for different m/z ions. Finally, quadrupoles can act in two modes. They can be set to transmit a single m/z through to the detector (Fixed or Selected), or they can scan through a specified m/z range (Scan)[69].

In this thesis, I used a QTRAP 5500 mass spectrometer wherein the linear ion trap (LIT) can operate as a linear ion trap or a third quadrupole. LITs resemble quadrupoles in having four parallel rods connected electrically as described above, but they are different in that they also contain a pair of electrodes on the ends, which can apply electric and magnetic fields to trap ions[69, 70]. The ions are trapped radially within the quadrupole, and axially by the electrodes on the end. By adjusting the RF and DC fields, ions can be ejected from the LIT and detected. Due to the configuration of the LIT, it can act as either an ion trap or a quadrupole[69]. The main advantage of using an LIT is that by trapping ions, we can effectively increase the signal of these ions, improving the detection of low-density ions and we can identify all charged fragments following threshold detection of the diagnostic ion (described below).

1.2.9 Tandem Mass spectrometry

Tandem mass spectrometry or MS/MS refers to systems with two or more mass analyzers operated in sequence to increase the flexibility of the system[71]. A tandem quadrupole mass spectrometer often contains three quadrupole analyzers in sequence so is called a triple quadrupole, with the first and third acting as mass analyzers, and the second acting as a collision cell (Figure 1.9B). In a typical triple quadrupole MS/MS experiment, precursor ions are selected in the first quadrupole (Q1), either in fixed or scan mode, and are then transmitted to the collision chamber (q2) where they undergo fragmentation

via collision-induced dissociation (CID). CID results when the ion collides with an inert gas such as nitrogen, resulting in the fragmentation of the precursor (intact ion) into smaller product ions. Here, the bond energies of the molecule are fragmented according to the collision gas being used and the energy applied to the collision chamber[69, 71]. The product ions are then transmitted into the third quadrupole (Q3), which either selects for a specific fragment ion m/z, or scans through the range of fragment ion m/z levels and sends these ions to the detector. Both Q1 and Q3 can be set to either scan or fixed m/z modes in various combinations. Selected Reaction Monitoring (SRM) refers to the mode in which both are set to a specific m/z. This MS/MS mode results in high specificity detection of a particular analyte (Figure 1.9C).

If Q3 is a LIT then when the LIT function is enabled, all the fragments generated in q2 are trapped and scanned in the LIT, increasing the sensitivity and resolution of these fragments. In this thesis, this functionality is used for the SRM-information dependent acquisition-enhanced product ion (SRM-IDA-EPI) experiments I used to structurally identify lipids by assessing all fragments generated from a given precursor ion at a given retention time and then using these fragments to provide unambiguous molecular identification. These MS/MS experiments have two steps. In the first, an SRM method is used, wherein a specific mass transition is monitored, and the presence of the fragment monitored in Q3 is counted when it reaches the detector. Once a specified threshold of counts is reached within a pre-set time-limit, the second step of the experiment is triggered. In the second step, an EPI scan is performed, wherein the same precursor ion is selected for in Q1; in q2 this ion is fragmented, using a collision energy different than that of the SRM scan to further fragment the ion beyond its "weakest" linkage into multiple constituent fragments; these fragments are then trapped in the LIT. The complete repertoire of product fragment ions are then ejected from the LIT and detected, providing a mass spectrum that allows for detailed structural determination of the precursor ion[72] (Figure 1.9D).

1.2.9 Multichannel electron multiplier/high-energy dynode

The final element of a mass spectrometer is the detector whose role it is to detect the ions that pass through the mass analyzer(s), and then convert ion intensities into a digital signal that is recorded to produce a mass spectrum. Perhaps the most common ion detector is the electron multiplier and the related channel electron multiplier. In these detectors, the ion stream leaving the mass analyzer strikes a surface which can be coated ceramics, copper beryllium plates, or other metals or semi conductors, resulting in the release of electrons from that surface[56]. If an electrode behind the plate where these secondary electrons are emitted is held at a positive potential, the emitted electrons are drawn to the electrode[56]. Upon striking the electrode, progressively more electrons are emitted, and further electrodes, held at progressively higher potentials, continue to draw those electrons to them. This results in a significant amplification of signal, up to the order of 10^5 to 10^6, and this current is digitized in an analog-to-digital converter and a mass spectrum is generated from the digitized signal[56, 73, 74]. Electron multiplier detectors are composed either of discrete electrode plates, as described above, or they contain a single continuous surface. This continuous surface is commonly made of glass coated with a semiconductive substance, often with a bent or spiralized shape. Secondary ions are attracted to the end of the detector, but due to its curved or spiral shape, many collisions occur that generate more secondary electrons, resulting in a signal amplification similar to that of the discrete electrode plate electron multiplier. When these continuous electron multipliers are miniaturized, a single tube is too small to be effective, so many of these tubes are placed in an array to form a multichannel electron multiplier. A single multichannel array results in a drop in signal amplification power, however, so two or more arrays are sandwiched together and their amplification outputs summed together, resulting in similar signal strength[56].

To summarize, this introduction has reviewed the overarching intent and challenges associated with studying rare diseases, the focus of this thesis on rare diseases involving aberrant lipid metabolism, and the technology and methodology used to study lipid metabolism at the molecular level (aka lipidomics).

1.3 Rationale, Hypotheses, and Specific Aims

The overall objectives of this thesis are to 1) generate and phenotype a preclinical model of variant form Neonatal Progeroid Syndrome (NPS) caused by variants in the GPS scramblase gene *ANO6,* 2) identify metabolic differences that discriminate Farber lipogranulomatosis (FL) and Spinal Muscular Atrophy with Progressive Myoclonic Epilepsy (SMA-PME) caused by mutation in the acid ceramidase gene *ASAH1,* and 3) assess whether the metabolic defects in SMA-PME could be rescued *in vitro*. My overarching objective was to identify the lipid-centric pathomechanisms of these diseases to enable cause-directed therapeutic targeting. I hypothesized that: a) the *Ano6* variants identified in a rare variant form of NPS would result in aberrant GPS metabolism associated with early cellular senescence and that animals born with mutations in *Ano6* equivalent to those found in human patients would recapitulate symptoms of NPS (variant form); b) SL metabolism would differ in FL and SMA-PME patients given distinct disease presentations yet common genetic determinants in *ASAH1* mutation and that these distinct sphingolipid fingerprints would mechanistically explain the differential presentations of patients exhibiting "pure" or “mixed” disease ; and c) treating SMA-PME patient fibroblasts with recombinant enzyme, as enzyme replacement therapy, would normalize this SL profile *in vitro*, providing proof of principal of potential therapeutic intervention. To test these hypotheses, I proposed four specific aims:

1. Identify functional biochemical and lipidomic changes in engineered and primary cells with patient mutations in *ANO6* (Chapter 2) and establish whether a novel CRISPR/Cas9 *ANO6*:c.1414G>C mouse model of the rare variant form of NPS associated with ANO6 recapitulated the human disease presentation (Chapter 2)
2. Define the natural history of SMA-PME thereby identifying the primary clinical features of the disorder and the extent of mixed Farber’s and SMA-PME presentation (Chapter 3)

3. Elucidate the metabolic signatures distinguishing FL from SMA-PME using primary patient fibroblast cultures (Chapter 4)
4. Use these SMA-PME patient fibroblasts to test the capacity of enzyme replacement therapy to normalize the sphingolipidome *in vitro* (Chapters 3 and 5).

Chapter 2 : Disruption of glycerophosphoserine metabolism is linked to an *ANO6*-associated rare variant form of Neonatal Progeroid Syndrome

Graeme S.V. McDowell[1*], Filippo Beleggia[2,3,*], Danielle T. Robinson[1*], Sebastian Albrecht[4,5,6,*], Maria Schotik[2,7,8,9,*], Susanne Brodeser[8], Yasemin Alanay[10], Tim M. Strom[11], Irina Alecu[1], Mark Akins[1], Graeme P. Taylor[1], Greg O. Cron[12,] Heather Hare[13], Thomas Meitinger[11], Kym Boycott[13], Thomas J. Jentsch[4,5,6], Bernd Wollnik[2,9], David A. Dyment[13†], Steffany A.L. Bennett[1,12†,]

[1]Neural Regeneration Laboratory, Ottawa Institute of Systems Biology, uOttawa Brain and Mind Research Center, Department of Biochemistry, Microbiology, and Immunology, Centre for Catalysis Research and Innovation, Department of Chemistry and Biomolecular Sciences, University of Ottawa, Ottawa, ON, Canada; [2]Institute of Human Genetics, University of Cologne, Cologne, Germany; [3]Institute of Human Genetics, University Clinic Düsseldorf, Düsseldorf, Germany; [4]Leibniz-Institut für Molekulare Pharmakologie (FMP), Berlin, Germany; [5]Max-Delbrück-Centrum für Molekulare Medizin (MDC), Berlin, Germany; [6]NeuroCure Cluster of Excellence, Charité Universitätsmedizin, Berlin, Germany; [7]Institute for Developmental Biology, University of Cologne, Cologne, Germany; [8]Cologne Excellence Cluster on Cellular Stress Responses in Aging-Associated Diseases (CECAD), University of Cologne, Cologne, Germany; [9]Institute of Human Genetics, University of Göttingen, Göttingen, Germany; [10]Pediatric Genetics Department, Istanbul, Turkey; [11]Institute of Human Genetics, Neuherberg, Germany; [12]Ottawa Hospital Research Institute, University of Ottawa, Ottawa, ON, Canada, [13]Department of Genetics, Children's Hospital of Eastern Ontario Research Institute, University of Ottawa, Ottawa, ON, Canada

*These authors contributed equally to this work

[†]Correspondence: sbennet@uottawa.ca (SALB); ddyment@cheo.on.ca

2.1 Objective of Study

The objective of this study was to identify functional, biochemical, and lipidomic changes *in vitro* associated with a rare variant form of NPS attributed to pathological variants in the *ANO6* gene and then to validate a preclinical animal model based on patient mutation. In this study, most of the *in vitro* work was performed by co-first author FB and is credited in all figure captions, representing ~50% of the paper. Co-first author GSVM performed 10% of the *in vitro* experiments, all of the lipidomics, and *in vivo* experiments representing ~50% of the paper. All data are included with full credit to both co-first authors.

2.2 Author Contributions

GSVM, FB, BW, BW, DAD and SALB conceived and designed the experiments and analyzed all data. LC-ESI-MS/MS was performed by GSVM and IA. Cell culture experiments were performed by GSVM, FB, SA, MS, and MA. Electrophysiology was performed by FB, SA, and MS. Behavioural phenotyping was performed by GSVM, DTR, MA, GPT, and GOC. SB, YA, TMS, HH, TM, KB, TJJ contributed reagents/materials/analysis tools: GOC, SS, GPT. GSVM, FB, SA, MS, BW, DAD, and SALB wrote the paper.

2.3 Abstract

The objective of this study was to identify lipidomic and biochemical changes that occur within a rare form of NPS, where the genetic determinant are variants in the Anoctamin 6 (*ANO6*) gene. First, to study the effect of patient mutations on this protein in human cells, we generated HEK293 cells expressing the mutant ANO6 proteins, and show that variants result in a non-physiological gain of

channel function and opposing variant-gain or loss of GPS scramblase function. To determine the effect of these mutations in an *in vivo* model, we generated the first mouse model of ANO6-based NPS using the murine equivalent to patient mutations. In this model, we demonstrate low pathological penetrance, restricted to females, most often resulting in embryonic lethality. However, common to both the human patient fibroblasts and the mouse model, were disruptions in GPS metabolism. Together, these data indicate that the pathogenic effects of these *ANO6* variants are a dysregulated GPS lipidome resulting in the clinical presentation of the disease, however returning the aberrant lipid metabolism could provide an avenue for treatment for this disease in human patients.

2.4 Introduction

Wiedemann-Rautenstrauch Neonatal Progeroid Syndrome (NPS, OMIM 264090) is a lethal autosomal disease characterized by intrauterine and postnatal growth retardation[75, 76]. Neonates present at birth with a progeroid appearance, prominent scalp veins, and malar hypoplasia[77-79]. Children fail to thrive, exhibiting multiple features associated with premature aging including sparse hair, hip dysplasia, and generalized lipoatrophy with paradoxical fat accumulation in the suprabuttock region[77-79]. Death in first decade of life results from the accelerated aging of multiple systems culminating in sepsis, respiratory failure, cardiac complications, and pnemonia[80]. NPS is linked to loss of function mutations in *POLR3* RNA polymerase III complex subunit genes; however, these mutations are not detected in all NPS patients[81-83]. For example, Hutchinson-Gilford progeria (HGPS, OMIM 176670), resulting from autosomal dominant mutations in the *LMNA* gene, partially phenocopies NPS but with a later developmental onset. In 2012, Kiraz *et al*[84] described a variant case of NPS detected at birth in an individual with a non-pathogenic c1698C>T, heterozygous (p.His566His) *LMNA* gene variation, thus distinct from HGPS. We describe here a second individual with a similar progeroid phenotype at birth

lacking any *LMNA* or *POLR3* gene variants. Onset and clinical presentation were consistent with a diagnosis of NPS, but this individual survived into early adulthood until death from cor pulmonale.

We performed whole exome sequencing of both the Kiraz patient[84] and the proband identified in this study, identifying *de novo* mutations in the *ANO6,* also known as *TMEM16F*, gene (anoctamin 6, MIM:608663, GeneBank: NM_001025356.3) in both individuals. *ANO6* is one of ten anoctamin genes ubiquitously expressed in all eukaryotes[85, 86]. The protein family is defined by their ten transmembrane-spanning helical domains[87-89]. While initially identified as calcium-activated chloride channels[90-92], most anoctamin proteins are now recognized to be non-selective ion channels that further act as phospholipid scramblases (reviewed in[87, 93]). Phospholipid scramblases, like flippases and floppases, facilitate the translocation of phospholipids between the inner and outer leaflets of the plasma membrane bilayer. Unlike flippases and floppases, scramblases are ATP-independent and bidirectional, thus they can move phospholipids between the inner and outer membrane leaflets against the concentration gradient[94-97]. ANO6 protein is a calcium-activated scramblase that can translocate glycerophosphoserines (GPS), glycerophosphocholines (GPCs), glycerophosphoethanolamines (GPEs) and sphingomyelins (SMs) between membrane leaflets of the lipid bilayer with preference for GPS[98].

GPS lipids are defined by a glycerol backbone, two hydrocarbon chains at the *sn*-1 and *sn*-2 positions attached to the glycerol backbone by ester, ether, or vinyl ether linkages, and a phosphoserine head-group at the *sn*-3 position. The length and degree of unsaturation of the *sn*-1 and *sn*-2 hydrocarbon chains define the molecular identity of each GPS while the phosphoserine headgroup renders all GPS lipids negatively charged at physiological pH[99]. GPS lipids are not synthesized *de novo* rather are remodeled from GPCs and GPEs through exchange of the choline or ethanolamine head-group for serine by the actions of phosphatidylserine synthase 1 and 2 respectively[24]. Both enzymes localize to the endoplasmic reticulum where GPS are first produced then transported to other membrane compartments. Although GPS lipids comprise only 3-10% of the lipid content of the plasma membrane[100, 101], their asymmetric distribution

between the inner and outer plasma membrane leaflet is essential for normal cellular homeostasis (reviewed in[102]). While ATP-dependent flippases act to maintain a higher concentration of GPS at the inner (cytosolic) leaflet of the plasma membrane (reviewed in [103]), scramblases (i.e., ANO6) can reverse this distribution by translocating GPS from the intracellular to the extracellular leaflet following calcium activation initiating apoptosis[104-109], ferroptosis [109], bone mineralization[102, 110, 111], and blood clotting[112-115].

Here, we identify gain-of-function mutations in the phospholipid scramblase *ANO6* as a novel cause for segmental progeroid phenotypes. We show that the expression of mutant proteins disrupts GPS composition and symmetry at the plasma membrane results in a premature cellular aging phenotype *in vitro*. Using CRISPR/Cas9-generated mutant mice, we further show *in vivo* that the penetrance of this rare variant form of NPS is exceedingly low with the majority of carriers asymptomatic. Affected embryos die *in utero* but rare survivors phenocopy patient systems and manifest systemically the GPS disruptions detected in patient fibroblasts.

2.5 Materials and Methods

2.5.1 Human Subjects and whole-exome sequencing

Primary dermal fibroblast lines were derived from punch biopsies from two NPS patients by informed consent from their families according to CHEO REB #11/04 E research ethic board approval. ANO6 mutations/variants were confirmed by exome sequencing in each cell line as we have described[116].

2.5.2 Cell cultures

Primary fibroblasts were grown in DMEM, supplemented with 10% FCS (Biochrom AG), 1% PenStrep and 0.3% Amphotericin B. Cells were grown in a humidified incubator at 5% CO_2 and 37°C.

HEK293 ANO6 knockout (KO) cell lines were generated using CRISPR/Cas9 genomic editing as described[117]. Briefly, targeting sequences for disrupting *ANO6* in HEK293 cells were obtained using the UCSC Genome browser tool at http://www.genome-engineering.org/crispr and cloned into the px330 single plasmid system[117]. Cells were co-transfected with px330 containing the sgRNA sequences ANO6_sgRNA2: GACAGAAGGTACCGTTCATTAGGG, ANO6_sgRNA4: GTAACTGAAGCGATGATCAATAGG and pEGFP-C1 using Lipofectamine 2000. Two days post transfection, single EGFP positive cells were FACS-sorted into 96 well plates with preconditioned DMEM. Genomic target sites of the clones were amplified by PCR and cloned into pcDNA3.1. Nine to fifteen alleles per clone were checked for sequence alterations using Sanger sequencing. Loss of transcript was assessed by RT-PCR. Total RNA was isolated using the NucleoSpin RNA kit (Macherey-Nagel) and reverse-transcribed using Superscript II reverse transcriptase (Invitrogen) and Oligo-dT primers (Invitrogen). cDNA was amplified using Phusion DNA polymerase (ThermoFisher). Primer pairs were ANO6RT_fwd1: ACGCACCATGGGAGGTGTTATG and ANO6RT_rev1: ACTGACGGCGGAATTTGCAATC detecting a 387 bp amplicon of ANO6; ANO6RT_fwd2: CAGCTTTCCCACTCCATGATTGC and ANO6RT_rev2: TGGTCACCACAGCCAGAATTGC detecting a 1488 bp amplicon of ANO6. GAPDH was used as a loading control amplified with the primer pairs: GAPDH_fwd: ACAGTCAGCCGCATCTTCTT and GAPDH_rev: GTTAAAAGCAGCCCTGGTGA detecting a 127 bp amplicon.

In subsequent activity experiments, HEK293 ANO6 KO cells were transfected with wild-type (WT), G472R, or ΔI611 cDNA3.1 constructs N-terminally tagged with EGFP, 3xFlag, or mCherry as indicated using Lipofectamine 2000 on glass coverslips or 6 cm dishes. The WT, G472R, and ΔI611 cDNAs were generated by standard mutagenesis. Human *ANO6* cDNA was obtained from Open Biosystems (BC098410.1). The mismatch L837 in this cDNA was mutated back to the WT NM_001025356.2 sequence using overlapping PCR primers: *ANO6*-L837F_fwd:

CCAAGCTGGCTTTTATCATTGTCATG and *ANO6*-L837F_rev: CAATGATAAAAGCCAGCTTGGCTGC. This DNA sequence was further mutagenized by PCR to obtain the G472R and ΔI611 mutations using the primers: *ANO6*-G472R_fwd: CAGTTATTAGGATCATTGTC, *ANO6*-G472R_rev: CAATGATCCTAATAACTGAAGC, *ANO6*-ΔI611_fwd: GACAATAATGGGAGGAAAAGC, and *ANO6*-ΔI611_rev: CTCCCATTATTGTCAGCTGAG.

2.5.3 Protein localization

For immunolocalization, HEK293 ANO6 KO cells were grown on glass coverslips and transfected at 50% confluency with pcDNA-3xFlag-ANO6 constructs. Forty-eight hrs post transfection cells were fixed with pre-cooled methanol at -20°C for 10 min and washed extensively with ice-cold 10 mM phosphate buffer containing 154 mM NaCl (1x PBS). Fixed cultures were incubated with monoclonal mouse anti-M2 Flag (1 µg/ml, Sigma Aldrich, F1804) in antibody buffer (0.1% Triton X-100, 3% BSA in 1xPBS) for 2 hrs at room temperature, followed by 1 hr incubation with Alexa Flour 555-Goat anti-Mouse IgG (2 µg/ml, Thermo Fisher A-21424**)** in antibody buffer. For cell surface biotinylation, 48 hrs post-transfection cultures were washed with ice-cold 1x PBS) and incubated with 1 mg/ml Sulfo-NHS-SS-Biotin (Thermo Fisher) in 1x PBS at 4°C for 30 min. Unreacted Sulfo-NHS-SS-Biotin was quenched by addition of 50 mM glycine in 1xPBS. Cells were lysed in protein lysis buffer containing 50 mM Tris-HCl pH 7.4, 150 mM NaCl, 1% NP-40, 0.25% sodium deoxycholate, 4 mM Pefabloc SC (Carl Roth) and complete protease inhibitor cocktail (Roche). The lysate was cleared from insoluble material by centrifugation for 10 min at 4°C and 20.000 g. 10% input was removed for Western blotting and the remaining lysate was incubated with equilibrated Streptavidin Agarose resin (Pierce) in protein lysis buffer for 1 hr at 4°C. Protein was eluted from the beads by incubation with denaturing buffer containing 50 mM Tris-HCl pH 6.8, 2% SDS, 10% glycerol, 0.2% bromophenol blue and 0.2% DTT at 55 °C for

10 min. Western blotting was performed with monoclonal anti-M2 Flag (2 µg/ml, Sigma Aldrich F1804), monoclonal AC74 anti-β-Actin (1 µg/ml, Sigma Aldrich, A2228) and HRP-goat Anti-Mouse IgG (100 ng/ml, Jackson Immuno Research 115-035-003).

2.5.4 Electrophysiology

For patch-clamp recordings HEK293 cells were grown in a 12-well plate and transfected with 2 µg DNA per well when cells reached 80% confluency using the calcium phosphate precipitation method[118] and grown for 24-48 hrs at 37°C before measurements. Transfected cells were plated on glass coverslips coated with Poly-L-Lysine (Sigma-Aldrich) at least two hours ahead of recordings. Borosilicate glass patch pipettes were fire polished and had resistances between 3-5 MΩ. The standard pipette solution contained 100 mM Cs-methanesulfonate, 40 mM CsCl, 1 mM $MgCl_2$, 1.5 mM Na_2ATP, 5 mM EGTA and 10 mM HEPES and different concentrations of $CaCl_2$: 5.62 mM (250 µM free Ca^{2+}), 5.25 mM (80 µM free), 4.95 mM (10 µM free), 4.90 mM (3 µM free), 4.34 mM (1 µM free), 3.78 mM (0.5 µM free) or 1.9 mM (0.1 µM free). The solutions' pH was adjusted to 7.2 using CsOH and osmolarity to 305 mOsm/kg using sucrose. Free calcium concentrations were calculated using http://maxchelator.stanford.edu/CaMgATPEGTA-NIST.htm. Bath solution contained 150 mM NaCl, 1.5 mM $CaCl_2$, 1 mM $MgCl_2$, 10 mM HEPES and 10 mM Glucose. pH was adjusted to 7.4 using NaOH and osmolarity to 325 mOsm/kg using Sucrose. Data were acquired with an EPC-10 double amplifier and patchmaster software and analyzed using fitmaster software (HEKA).

2.5.6 Annexin V assay for PS exposure

ANO6 wild-type (WT) or KO HEK293 cells were transfected at 50% confluency with pcDNA-EGFP-ANO6 constructs using Lipofectamine 2000. For monitoring the kinetics of PS exposure 48 hours post

transfection $1*10^5$ cells were collected in HEPES buffer containing 2.5 mM Calcium, 140 mM NaCl, 1/100 Annexin V-Cy5 (BD Pharmingen) and 1 µg/ml Propidium iodide (Invitrogen). Immediately before measurement 10 µM A23187 (Sigma-Aldrich) was added to the cells which were immediately inserted into a BD LSRFortessa flow cytometer. For end-point measurement of PS exposure $1*10^5$ cells were incubated at 37°C in 50 µl HEPES buffer containing 2.5 mM Calcium, 140 mM NaCl and the indicated A23187 concentration for 20 min. The reaction was quenched by addition of 450 µl ice-cold HEPES buffer containing 2.5 mM Calcium, 140 mM NaCl, 1 µg/ml Propidium iodide and 1/100 Annexin V-Cy5. Cells were kept on ice for a maximum of two hours before insertion into a BD LSRFortessa flow cytometer. Data were analyzed using FlowJo v10 software. Only clearly Propidium iodide-negative cells were selected to exclude dead cells and cells with low membrane integrity.

2.5.7 Generation of Ano6 G495R Mutant Mice

All experiments were approved by the Animal Care Committee of the University of Ottawa and performed in strict accordance with the ethical guidelines of experimentation of the Canadian Council for Animal Care. In total, 152 male mice, and 133 female mice were used in this study. CRISPR/Cas9 endonuclease-mediated double-strand breaks followed by homology directed repair and guide RNA with sequence GGATCGGGTCTGTCCCGTTG targeted to chromosome 15:9577878 was performed at the Toronto Centre for Phenogenomics generating p.G495R replacement in exon 13. This mutation in C57Bl/6N mice corresponds to our human p.G472R determinant. $Ano6^{+/G495R}$ founders were provided to us at 2 months of age. Mice were found to be fecund and bred well. $Ano6^{G495R/G495R}$, $Ano6^{+/G495R}$, and $Ano6^{+/+}$ littermates were maintained by filial breeding of $Ano6^{+/G495R}$ male and female mice. All mice were genotyped for their mutant Ano6 status at weaning, or at time of phenotypic characterization for our pre-weaning groups, using digital droplet PCR. At weaning, mice were separated by sex, but not genotype, group-housed, and maintained on a 12:12 hour light: dark cycle with Zeitgeber time 0 (ZT) set

to 6:00 AM. Mice were fed a normal chow diet (Envigo, Teklad Global 18% Protein Rodent Diet, 2018) *ad libitum*.

2.5.8 Genotyping

PCR reaction mixtures were prepared in a total volume of 22 µL containing 11 µL Supermix for probes without uDTP (Bio-Rad, cat #186-3023), 4.18 µL nuclease free water, 0.22 µL Restriction enzyme MseI (New England BioLabs, cat# R0525L), 5.5 µL DNA (2 ng/µL concentration, extracted from ear or tail tissue samples using Qiagen DNEasy Blood and Tissue kit) and 1.1 µL probe and primer mixture. Primer mixture contained forward and reverse primers at a final concentration of 10 µM, and wild-type LNA and em1 (SNP) LNA probe at 5 µM. Forward primer had sequence 5'-GCTGTCCGTGTTCATCGTATT-3', reverse primer had sequence 5'-CTGATGATGGAGGCTGTGATG-3', wild-type LNA probe was an oligonucleotide with 5' fluorophore HEX, 3' quencher IowaBlack FQ, with sequence 5'-HEX-CCAA+C+G+GGA+CA-IowaBlack FQ-3', and em1 SNP probe had 5' fluorophore FAM, 3' quencher IowaBlack FQ with sequence 5'-FAM-CCAA+C+C+GGA+CA-IowaBlack FQ-3'. All primers and probes were purchased from Integrated DNA Technologies (Coralville, Iowa). 20 µL of PCR reaction mixture was transferred to a sample well in a disposable droplet generator cassette (Bio-Rad, cat# 1864008). 70 µL of droplet generation oil (Bio-Rad, cat# 1863005) was loaded into the oil well for each channel, and the cassette loaded into a QX200 Droplet Generator (Bio-Rad, cat # 1864002). The droplets were then transferred to a 96-well Eppendorf skirted Plate (Eppendorf, cat # 951020362). Droplet PCR reactions were run on a C1000 Touch Thermal Cycler, incubating the plates at 95^{o}C for 10 minutes, followed by 49 cycles 95^{o}C for 30 seconds, followed by 53^{o}C for 60 seconds then 72^{o}C for 60 seconds. Following the last cycle, the reaction was incubated at 98^{o}C for 10 minutes. The temperature ramp increment was 2^{o}C/second ramp speed for all steps. Plates were read on a QX200 Droplet reader using Quantasoft (Bio-Rad, version

1.6.6.0320). At least two wells of confirmed WT DNA, WT/SNP DNA, SNP/SNP DNA and non-template control were included on each plate as controls. Each well was read using the QX200 and analyzed for emission in the HEX or FAM wavelengths. One-dimensional amplitude plots displaying measured HEX and FAM amplitudes for each droplet were analyzed using the controls to set threshold values. Wells that contained equal counts for both WT and SNP probes were considered WT/SNP, wells that had twice the WT signal and little-to-no detectable SNP signal were considered WT/WT, and the SNP/SNP was the converse of WT/WT. Wells with fewer than 12,000 droplets were not included. Each sample was run in at least duplicate, and if neither duplicate had ≥ 12,000 droplets, the sample was re-run at a later date.

2.5.9 Phenotyping

2.5.9.1 Length and weight

Mouse length and weight measurements were taken once a week, from weaning (at 3 weeks of age) until 25 weeks of age. Length was measured from anus to nose tip, excluding tail length. Mouse weights were measured using a digital scale (Ohaus, CS 200 portable compact scale). To collect pre-weaning measurements, two separate cohorts were used, measuring the weight and lengths of pups at 7 or 14 days after birth. Due to the amount of handling involved, the pups were sacrificed immediately prior to measurements.

2.5.9.2 Footpad length and area

Mouse footprints were taken at weaning, and once a month thereafter. To collect footprints, non-toxic paint (Crayola, cat #54-1205) was applied to their left front and hind paws via cotton swabs (AMG Medical Inc., cat #018-435, lot 93072). The whole paw was placed on a piece of paper, and the paw was gently pressed down using a malleable scapula, leaving a paw print on the page. This was repeated until

the prints were no longer visible on the page as a dilution series. The paw prints were inspected, and if fewer than two showed high enough quality for measurement, more paint was applied, and the process repeated until at least two complete paw prints were taken. Footprints were scanned, and the length and area were measured using ImageJ (National Institute of Mental Health, Maryland USA)[121]. Pre-weaning paw measurements were obtained from the sacrificed pre-weaning 7- and 14-day pup cohorts post sacrifice.

2.5.9.3 MRI Acquisition

MRI was performed with a General Electric / Agilent MR901 7T small-animal scanner, in combination with a SA Instruments Inc physiological monitoring/warm-air delivery system and VetEquip isoflurane anesthesia system. Full-body coronal MR images of each anesthetised mouse were obtained with a 2D multi-slice, multi-phase T1-weighted fast gradient echo pulse sequence with repetition time of 3.8 ms, echo time 1.6 ms, flip angle 60°, bandwidth 63 kHz, field of view 10.5 x 5.3 cm^2, matrix 128×64×22, and spatial resolution of 0.8×0.8×1.0 mm^3, 15 phases. The total time for isoflurane induction, positioning, MRI adjustments, and scanning was 5 minutes per animal.

2.5.9.4 MRI-body fat analysis

For each mouse, an MRI index of body fat content (percent of voxels identified as fat) was calculated using threshold-based segmentation[122, 123]. MRI analysis was performed using ImageJ v1.49 (National Institute of Health, USA)[121]. Each MRI image was a hyperstack of 15 scans at each of 22 z-slices. For each slice, the average intensities of scans 3-15 were calculated using the Z Project Average Intensity option in ImageJ. To ensure reproducibility, a macro was developed to consistently recreate these steps (S1 Appendix). To calculate the total, subcutaneous and visceral fat percentages, the whole body, subcutaneous, and visceral fat regions were traced in ImageJ by hand for each slice. The areas of the regions were recorded and summed over the 22 z slices. Subcutaneous, visceral, and total body fat

percentages were calculated separately. The subcutaneous and visceral fat distinction on MR imaging was based on previous studies[123, 124].

2.5.9.5 Behavioural phenotyping procedures

To assess the impact of the ANO6 G495R mutation on the psychomotor abilities of these mice, WT (+/+) mice (11 males, 15 females), heterozygous (+/G495R) mice (18 males, 16 females) and homozygous mutant (G495R/G495R) mice (9 males, 10 females) were tested using a battery of behavior tests (Figure 2.1) at one and three months of age. All animals were allowed to acclimatize to the testing room for one hour prior to any behavioural assessment.

2.5.9.5.1 *Open Field*

Behavioural indices of relative levels of basic motor function were assessed by the open field test. The open field arenas were white acrylic boxes measuring approximately 45 cm long on each side and 45 cm tall. The light level in the middle of each of the arenas was 300 ± 10 lux. Each mouse was placed in the lower left corner of one of the open field arenas and given ten minutes to explore. The animal's exploration was recorded by a video camera (Panasonic, WV-BP334) mounted above the arenas, and the movements tracked and analyzed using Ethovision (Noldus, v11.5). After a ten-minute trial, mice were returned to their home cage. Distance moved over the ten-minute trial was calculated.

2.5.9.5.2 *Grip Strength*

The Grip Strength test was used to measure the maximum peak force of the animal's grip. For this test, the animal was allowed to acclimatize to the base plate of the force meter (Chantillion DFE II, Columbus Instruments) for 30 seconds, and the vertical grid attached to the force meter for 20 seconds. After acclimatization, the animal was held and allowed to grab the grid with its front paws. The animal was held at the base of the tail and while still gripping the grid, was moved so its body was horizontal. The mouse was gently pulled backwards off the grid and the force meter measured the animal's maximum grip before letting go. Each animal was tested for six trials before being returned to its home cage. The

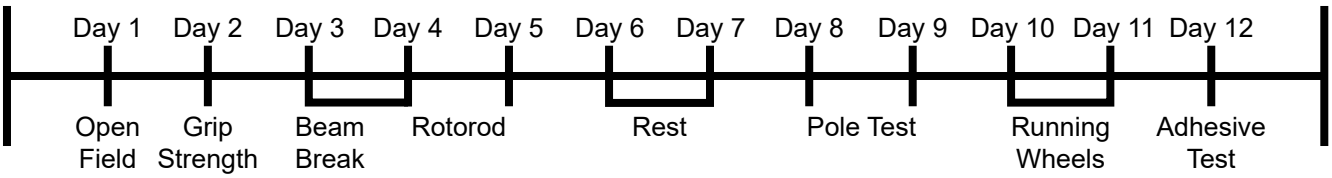

Figure 2.1: Behaviour paradigm for animal studies. Schematic depicting the timeline for the battery of behaviour tests. Testing lasted 12 days, with a two-day rest period for the animals halfway through testing. Single-day tests performed were the open field test, grip strength test, and adhesive test, rotorod and pole-tests were performed twice, on consecutive days, beam-break test was performed overnight leading into rotorod test, and the home-cage running wheel test was performed for a 26-hour period over one full night-day cycle.

peak force in gram force was recorded for each trial. After all animals were tested, the mass of each animal was recorded to standardize grip strength to body mass.

2.5.9.5.3 *Beam-break*

The Beam Break test was used to measure general motor ability in the animals. Each mouse was housed singly in a cage where its movements could be measured using infrared beams, for the duration of the experiment. Each time the animal passed through one of the infrared beams, a photocell analyzer recorded the beam break. The mice were placed in the cage at ZT 10 (two hours prior to lights turning off) and were measured while they habituated to the new cages. The mice were then tracked overnight until ZT 2 (two hours after the lights turn on), giving a total of 16 hours under observation, covering their active cycle.

2.5.9.5.4 *Rotorod*

The rotorod test was used as a test of motor coordination and endurance. The animals were placed on a textured and rotating rod of approximately 3 cm diameter facing the direction of the rod's rotation. If the animals turned around on the rod prior to the start of the trial, they were picked up and placed facing the correct direction once. The rod rotated at a steadily accelerating rate (from 1 to 45 RPM over 150 seconds), and the time the animal stayed on the rod was measured, up to a maximum of 300 seconds. If an animal grabbed onto the rod and completed a full rotation without falling, this was considered a failed trial, and the experimenter ended the trial for that mouse. Each animal was tested for three trials, on two consecutive days. The mice rested for 60 ± 5-minutes between trials on a day. The time to fall, the distance travelled, and the maximum rotational speed reached were recorded.

2.5.9.5.5 *Pole test*

The pole test was used as a test of motor coordination and agility. Each animal was placed at the top of a rough surfaced vertical pole (diameter approximately 1 cm, height approximately 48 cm) with the head facing upwards. To complete a trial, the mouse was required to turn on the pole to face downward

and climb down the pole to the bottom. Time to turn on the pole and time to descend were recorded. Mice were tested over a total of three trials per day, for two consecutive days.

2.5.9.5.6 *Running wheels*

Voluntary exercise was recorded using running wheels. The animals were placed in individual cages with access to a running wheel (Med Associates, ENV-044) mounted on a base with a wireless transmitter. Each revolution in a 30 second period was transmitted to a hub, connected to a computer that tracked all the wheels simultaneously. The mice were measured for 26 hours, starting at ZT 10, giving the animals two hours prior to the lights turning off to habituate to the wheels before their active cycle, and were monitored until ZT 12 (when the lights turn off) the next day, allowing for monitoring for a full light: dark cycle. Following the trial the mice were returned to their home cages.

2.5.9.5.7 *Adhesive tape removal test*

The adhesive tape test was used to assess manual dexterity. Each animal was habituated for at least 60 seconds in a transparent, bedding-free shoebox cage. A piece of adhesive tape (Nexcare 3M first aid tape) of equal size was applied to the hairless part of each forepaw. The animal was placed back in the cage and observed for up to 120 seconds by two observers located on opposite sides of the cage. Each observer scored the time for the mouse to react to, and then to remove the adhesive tape. Each mouse underwent five trials for this test, and for trials beyond the first round, the 60-second habituation time was not applied. The order of placing the adhesive tape (right or left forepaw first) was randomized. The order of testing animals within each cage was randomized for the first round, with subsequent rounds maintaining the same order. The order of each cage to be tested was random.

2.5.10 Lipid extraction and collection

Dorsal thoracic skin and heart (separated into right ventricle and left ventricle with septum) were collected from two-month old females. Lipids were extracted from these tissues using a modified Bligh and Dyer protocol described previously[125-128]. Briefly, heart tissue samples were added to ice cold

acidified methanol (2% acetic acid; Fisher, A38-212, in methanol; Fisher, cat# BP1105 (v/v)) in a Kimble 10-ml glass threaded tube (VWR, cat# 21020-640), and homogenized using a tissue tearer (985370; BioSpec, Bartlesville, OK, USA). To ensure complete homogenization of tissue samples, each sample was then sonicated using a probe sonicator (Fisher Scientific, 60 Sonic Dismembrator Sonicator) for 10 seconds, three times at speed setting 10. Following sonication, 380.1 pmol of PS(12:0/13:0) (Avanti Polar Lipids, cat# LM-1300) was added to act as internal standard. 0.1M Sodium Acetate (Sodium Acetate; Sigma, cat# S-2889, LC/MS grade water; J.T. Baker, cat# 9831-03) was added to complete the aqueous phase. To collect the lipids from skin, shaved skin samples were added to a 10 mL glass Kimble tube containing 0.1M sodium acetate and homogenized using a tissue grinder. To ensure complete homogenization of tissue samples, each sample was then sonicated using a probe sonicator for 10 seconds, three times, at speed setting 10. Following homogenization, acidified methanol was added, along with 380.1 pmol of PS(12:0/13:0) to act as an internal standard, completing the aqueous phase. For both tissue types, lipids were extracted by addition of chloroform (Fisher, cat# C298) to a ratio of 1.6 : 2 : 1.9 Sodium acetate : acidified methanol : chloroform (v/v/v). The organic phase was collected, and the aqueous phase successively back-extracted using chloroform three times. The organic phases were collected and pooled. Samples were dried under a constant stream of nitrogen gas. Dried lipid extracts were re-dissolved in ethanol (Commercial Alcohols, cat# P016EAAN), and stored under nitrogen gas in amber glass vials (Chromatographic Specialities, cat# C779100AW) and kept at -80^{o}C.

2.5.11 HPLC-ESI-MS/MS

GPS was quantified by high performance liquid chromatography electrospray ionization tandem mass spectrometry (HPLC-ESI-MS/MS), using an Agilent 1290 Infinity II LC and a triple quadrupole-linear ion trap mass spectrometer QTRAP 5500, equipped with a Turbo V ion source (AB SCIEX, Concord, Canada). Nitrogen was used as curtain gas, collision gas, and ion source gas 1 and 2. Samples were

prepared for HPLC injection by diluting lipid extract with solvent A2 (Isopropanol (Fisher, cat# A416-4): Methanol (Fisher, cat#BP1105-4): LC/MS grade water (5:1:4; v/v/v) with 0.2% Formic Acid (Fisher, 56302), 10 mM Ammonium Acetate (OmniPur, 2145), and 5 µM phosphoric acid (Honeywell Fluka, Cat# 40779-10 MMol)), and an external standard mixture containing 2.62 pmol of PS(17:0/14:1) (Avanti LM-1304), PS(17:0/20:4) (Avanti LM-1302), and PS(21:0/22:6) (Avanti LM-1303), respectively, in ethanol. HPLC separation was achieved on a 100 mm x 250 µm (i.d.) capillary column packed with ReproSil-Pur C_{18} beads (particle size of 3 µm and pore size of 120Å, Dr A. Maish, Ammerbruch, Germany) with 5 µl sample injections by an autosampler maintained at 4^{o}C with a flow rate of 10 µl/min. The binary solvent gradient consisted of Solvent A2 and Solvent B2 (Acetonitrile (J.T. Baker, cat#9829-03): Isopropanol (1:1; v/v) with 0.2% formic acid, 10 mM ammonium acetate, and 5 µM phosphoric acid). Gradient elution started with 20%B2, ramping to 50% B2 over five minutes, and then to 80% B2 over the next 15, finally ramping to 100% B2 within the next minute. The gradient remained at 100% B2 for the next 19 minutes, then over the next minute dropped to 5% B2, for 4 minutes, before rising again to 20% B2 where it stayed for the remainder of the run to re-equilibrate the column.

Data acquisition for quantification was performed in positive ion mode using multiple selected reaction monitoring (MRM) monitoring multiple transitions with a difference between the product and precursor ions of m/z 185, representing the neutral loss of a phosphatidylserine headgroup. Molecular identities were determined using BATL[129] and verified by performing HPLC-MRM information-dependent acquisition (IDA)-enhanced product ion (EPI) experiments, in which MRM was used as a survey scan to identify target analytes, and an IDA of EPI spectra was acquired in the linear ion trap. The IDA method triggered EPI scans following analysis of MRM signals with dynamic background subtraction from the survey scan. The IDA criteria were set to select the one-to-three most intense peaks, and intensity threshold set to exceed 1000 cps. The EPI experiment operated in positive-ion mode, scanning mass range from *m/z* 200-1000 at a scan rate of 10,000 Da/s with dynamic fill in the ion trap.

Two collision energies were applied, 35 eV and 50 eV with collision energy spread of 15 eV, to ensure a broad coverage of fragmentation for both low *m/z* and high *m/z* species. Following acquisition, the EPI spectra were examined for structural determination of the lipid species present in the samples. The identities, m/z and retention times of the identified lipid species were added to the library. Instrument control and data acquisition were performed with Analyst software (v 1.6.2, AB SCIEX). Processing of quantitative MRM data was performed using MultiQuant software (v 3.0.2, AB SCIEX). For quantification, raw peak areas were corrected for extraction efficiency, and instrument response by normalization to standards added at time of extraction. Lipid abundances were expressed as pmol equivalents of PS(12:0/13:0) per mg tissue, or per 1E6 cells.

2.5.12 Statistical Analysis

GraphPad Prism version 10.0.2 (GraphPad Software, San Diego CA) was used for all statistical analyses. Alpha values of $p \leq 0.05$ were deemed significant for assessment of main and interaction effects. Changes in groups were assessed by two-way ANOVA followed by Holm-Šídák *post-hoc* tests adjusting the alpha levels for multiple comparisons as indicated. Repeated measures analysis was performed where warranted. Mendelian ratios were determined via chi-square analyses. Kaplan-Meier survival curves were compared using log-rank Mantel-Cox analysis.

2.6 Results

2.6.1 Identification of a variant form of NPS in two probands from unrelated families

2.6.1.1 NPS Patient 1

The clinical presentation of NPS Patient 1 was described previously by Kiraz *et al.* (2012)[84]. Briefly, this female patient was born at term to healthy non-consanguineous parents. Birth weight, length, and

occipitofrontal head circumference were below 3rd percentile. She had an abnormal (characteristic progeroid) appearance with micrognathia, large eyes, prominent scalp veins, and sparse hair (Figure 2A, left). She had natal teeth, partial syndactyly on the second and third toes, craniosynostosis, mild osteoporosis, lack of subcutaneous fat with paradoxical accumulation of fat around the buttocks, and bilateral renal pelvicalyceal ectasia. She had normal mental development, no signs of cardiac disease, and no signs of ophthalmological alterations. Motor skills were delayed and movements slow. X-rays of the extremities showed thin, long bones and osteoporotic changes. Sequencing the *LMNA* gene showed no sequence variants likely to cause laminopathies, but had a c1698C>T (p.His566His) heterozygous variation on the *LMNA* gene.

2.6.1.2 NPS Patient 2

This female patient was born to a healthy 27-year-old woman on her first pregnancy (G1P0). There were no teratogenic exposures or maternal illness, though the pregnancy was complicated by poor fetal growth, ultimately resulting in a Caesarean section at 34 weeks, due to intrauterine growth restriction and fetal distress. The patient's birthweight was 1.46 kg (10th percentile), head circumference was 29 cm (3rd-10th percentile), and length was 40 cm (< 10th percentile). Newborn screening was performed, and the patient's APGAR scores were 5 at 1 minute and 9 at 5 minutes. The patient stayed in hospital for 1 month for prematurity and low birthweight. During her admission, she was noted to have an enlarged anterior fontanelle, prominent scalp veins, and little to no scalp hair. The patient had an aged appearance of the face and hands. She had eruption of primary dentition early at 3 months. There were no other concerns in early life with the exception of a breath holding spell at 8 months of age, and her unique appearance for which she was referred to the Genetics department at CHEO. She had normal developmental milestones. She excelled in school and attended a local college. There were no hospital admissions or surgeries. A review of symptoms was unremarkable. She did have a history of

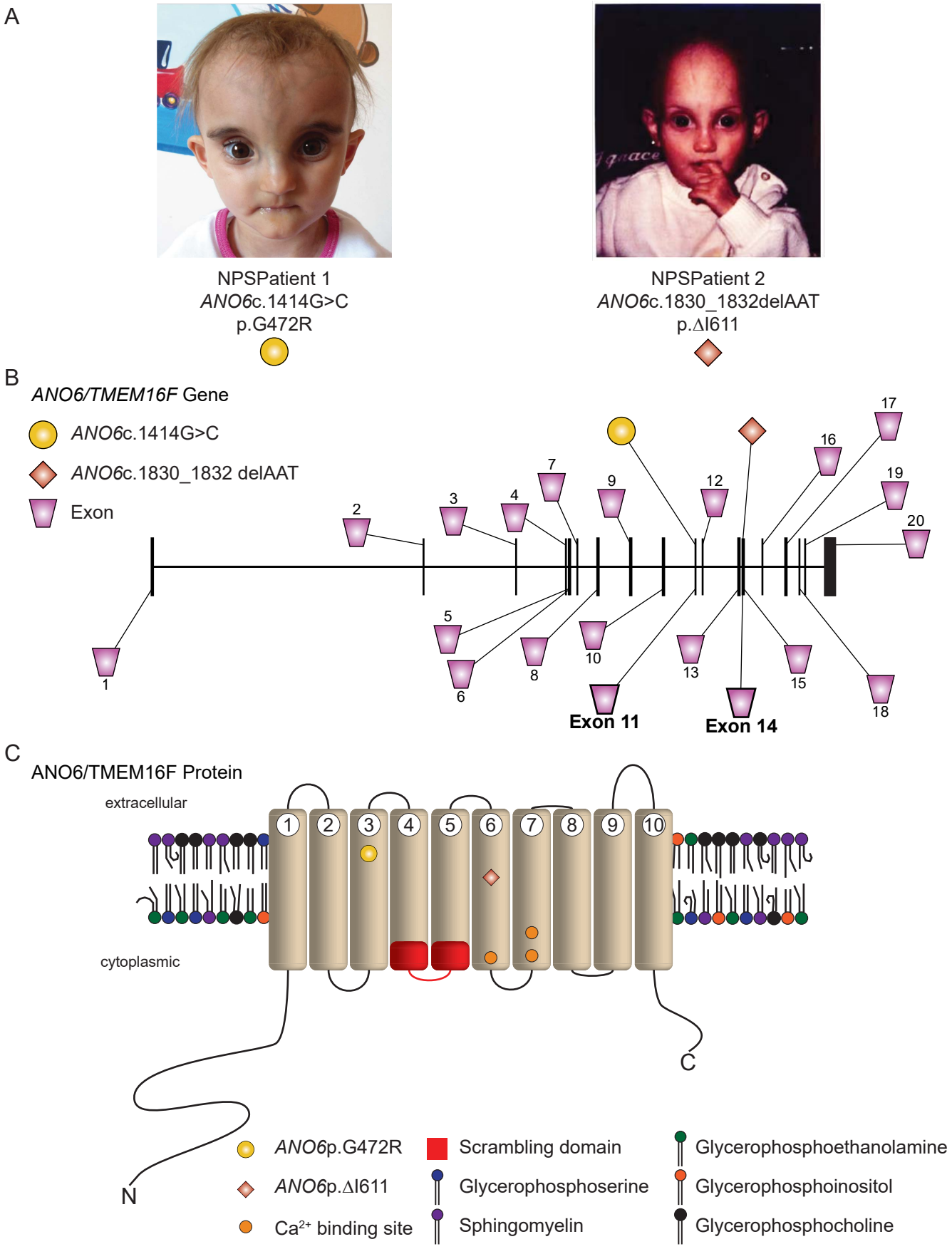

Figure 2.2: *ANO6* mutations identified as disease-causing mutations in Neonatal progeroid syndrome (NPS) patients. A) Photographs of the two NPS patients, and their ANO6 mutations identified. Photos show evidence of progeroid appearance: sparseness of hair, prominent scalp veins, and a reduction in subcutaneous fat. B) Schematic diagram (created in IBS[130]) of the *ANO6* gene, showing the structure of the gene with patient mutations indicated. Exons are drawn to scale, mutation locations within exon 11 and 14 displayed. C) Cartoon schematic of ANO6 protein embedded in a plasma membrane. N-terminus and C-terminus are indicated, and the ten transmembrane loops are numbered. Scrambling domain and calcium binding sites are indicated. Distribution and size of lipids in plasma membrane are not to scale. Predicted protein outcome of patient mutations is indicated on the 3rd and 6th transmembrane loops.

menorrhagia. At age 13 she developed a worsening syncope and at 16 had significant exercise intolerance. She was diagnosed with a severe right-sided cardiomyopathy and pulmonary hypertension at age 19 and died due to cardiac arrest at age 20. An autopsy showed evidence of chronic cor pulmonale and the right ventricle showed concentric hypertrophy. There was no evidence of any coronary atherosclerosis. Microscopy of the lung tissue showed prominent muscular thickening of arteries and arterioles with widening of the space between internal and external elasticas. There was also evidence of plexiform lesions in keeping with a plexogenic arteriopathy. Skin biopsies from the extremities showed a thinning of her epidermis, while the dermis showed mild fibrosis. The patient's family history was unremarkable. There was one healthy brother, and her parents were non consanguineous. Parents were of Scottish/Ukranian and English origin. There was no history of genetic conditions or congenital anomalies in the family.

An assessment was performed when the patient was 19 years old. She was 155 cm (10^{th} percentile) for height and 55 kg (50^{th} percentile) for weight. Head circumference was 52 cm (3^{rd} percentile). She was noted to have a high-pitched voice, and thin, sparse hair. She had prominent scars from chickenpox on her forehead. She had enophthalmos and a tightness of the skin on her nose and ears though otherwise normal development. She had a short philtrum and a retrusion of her upper jaw (Figure 2.2A, right). Chin was prominent and grooved. Her hands and feet were "tiny" with prominent varicosities and an aged appearance. Hand lengths measured 14.1 cm and 14.6 cm (left and right, respectively, both < 3^{rd} percentile). Radiographs of her hands showed evidence of osteopenia. She had limited movement to small joints (3-5^{th} metacarpals) and dystrophic nails of both hands and feet. She had camptodactyly of the 5^{th} digits of her hand bilaterally and a single palmar crease in the left palm. She had a prominent sandal-gap and feet measured 20.5 cm and 20.7 cm (left, and right, both < 3^{rd} percentile). Limbs were proportionate. Skin on extremities was described as soft and velvety. There was a lack of subcutaneous fat in a stocking and glove pattern, and an excess of adipose tissue around her abdomen. Prior

investigations included a normal karyotype and sequencing *COL3A*, *ZMPSTE24* and *LMNA* genes showed no mutations.

2.6.1.3 Both patients harbour ANO6 variants

Patient 1 carried a *de novo* substitution in her *ANO6* gene, causing a missense mutation at position 472 (*ANO6*:c.1414G>C, p.G472R, NM_001025356), exchanging the conserved glycine for arginine (Figure 2.2B-C) and a non-pathogenic c1698C>T, heterozygous (p.His566His) *LMNA* gene variation. Patient 2 carried a *de novo* three base pair deletion in her *ANO6* gene at position 611 (*ANO6*:c.1830_1832delAAT, p.ΔI611, NM_001025356), causing the deletion of a conserved isoleucine (Figure 2.2 B,C) and a *de novo* substitution in the *IRX1* (Iroquois Homebox 1) gene, at a non-conserved site (p.A262V). Both patients were heterozygous for their indicated mutation. Given the phenotypic overlap of both patients, we identified these *de novo* variants in *ANO6* to be the cause of their variant form of NPS. Both mutations are located in transmembrane domains, in proximity to the scramblase domain (Figure 2.2C).

2.6.2 G472R and ΔI611 variants do not affect localization of ANO6 to the plasma membrane

To assess function of the ANO6 mutants in the absence of endogenous expression, we generated ANO6 KO HEK293 cells using CRISPR/Cas9. In two separate strategies, the N-terminus and the third transmembrane region of ANO6 were targeted (data not shown). We chose two clones in which mRNA levels were markedly reduced, attributed to nonsense-mediated RNA decay (data not shown). We transiently transfected these clones with Flag-tagged WT, G472R, or ΔI611 constructs to assess whether the variant protein could localize to the plasma membrane in absence of endogenous WT protein. Immunostaining indicated localization of all three ANO6 proteins to the plasma membrane (Figure 2.3A). We used cell surface biotinylation to assess cell surface protein levels. The ΔI611 variant was less

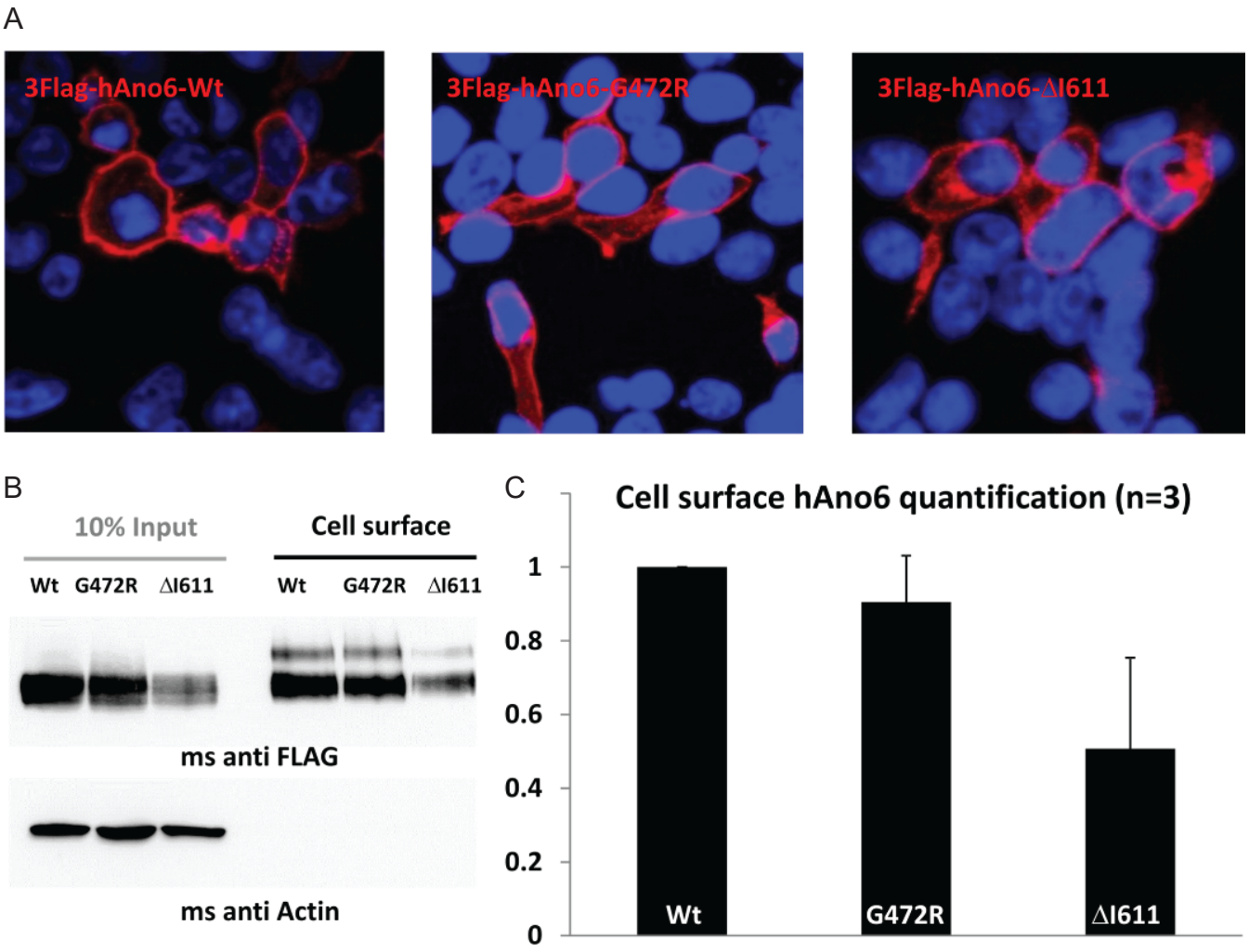

Figure 2.3: Mutant and wild-type ANO6 are expressed at the plasma membrane. Cassettes containing either FLAG-tagged ANO6 wild type (3Flag-hAno6-Wt), FLAG-tagged ANO6 with G472R mutation (3Flag-hAno6-G472R), or FLAG-tagged ANO6 with ΔI611 mutation (3Flag-hAno6-ΔI611) were expressed in HEK cells. A) Immunostained cells showing where the flag-tagged protein was expressed within HEK cells. Staining shows expression at the cell surface. B) Cells surface biotinylation was performed, cells were lysed, and the cell-surface and input fractions were separated using SDS-PAGE and proteins were measured using western-blotting. Protein with the FLAG tag were blotted for, and found at the cell surface, and 10% input of the cells. Actin was used as a control. C) Quantification of the western blot in (B). Bars represent mean intensity relative to wild-type ± SEM. These studies were performed by co-first author FB.

abundantly detected at the plasma membrane than WT or G472R, consistent with the lower overall expression of the 3xFlag-hANO6ΔI611 construct (Figure 2.3B, C).

2.6.3. Channel activity is increased in G472R and ΔI611 variants

We investigated the electrophysiological properties of the mutant ANO6 proteins, using a whole-cell configuration in KO HEK293 cells transiently transfected with EGFP-tagged WT, G472R, or ΔI611 constructs. Consistent with previous reports[131, 132], WT channels activated slowly in very high calcium concentrations (Figure 2.4A). Increasing calcium concentrations resulted in a faster time to peak activation for all three channels (Figure 2.4A). Given this lengthy activation, we next investigated whether smaller currents could be observed within shorter, physiologically relevant, periods of time (i.e., 5 min). Interestingly, the G472R variant channel appeared to produce currents independently of free Ca^{2+} suggesting gain of function; however, currents were very low (less than 100 pA/pF at +100 mV). In contrast, currents from ΔI611-expressing cells were observed instantaneously once free pipette calcium concentration reached 3 µM, further increased when calcium concentrations reached 10 µM, then decreased when higher calcium concentrations were applied (100 µM, Figure 2.4B). These instantaneously active currents, not detected in WT-expressing cells, were, however, restricted to strongly depolarized voltages.

To examine channel biology in more detail, we investigated the current/voltage relationship using 250 µM Ca^{2+} in the patch pipette. We applied a voltage ramp protocol from -100 mV to +100 mV and measured the instantaneous current and the steady-state current densities once achieved (Figure 2.4C). Cells expressing WT and both mutants displayed strongly outward rectifying currents (Figure 2.4C, D). The kinetics of activation by depolarization, determined by the ratio of the instantaneous and (pseudo-) steady state currents at +100 mV with 250 µM free Ca2+, were significantly faster in both variants compared to WT, with G472R being the faster overall (Figure 2.4E). The rectification index, calculated

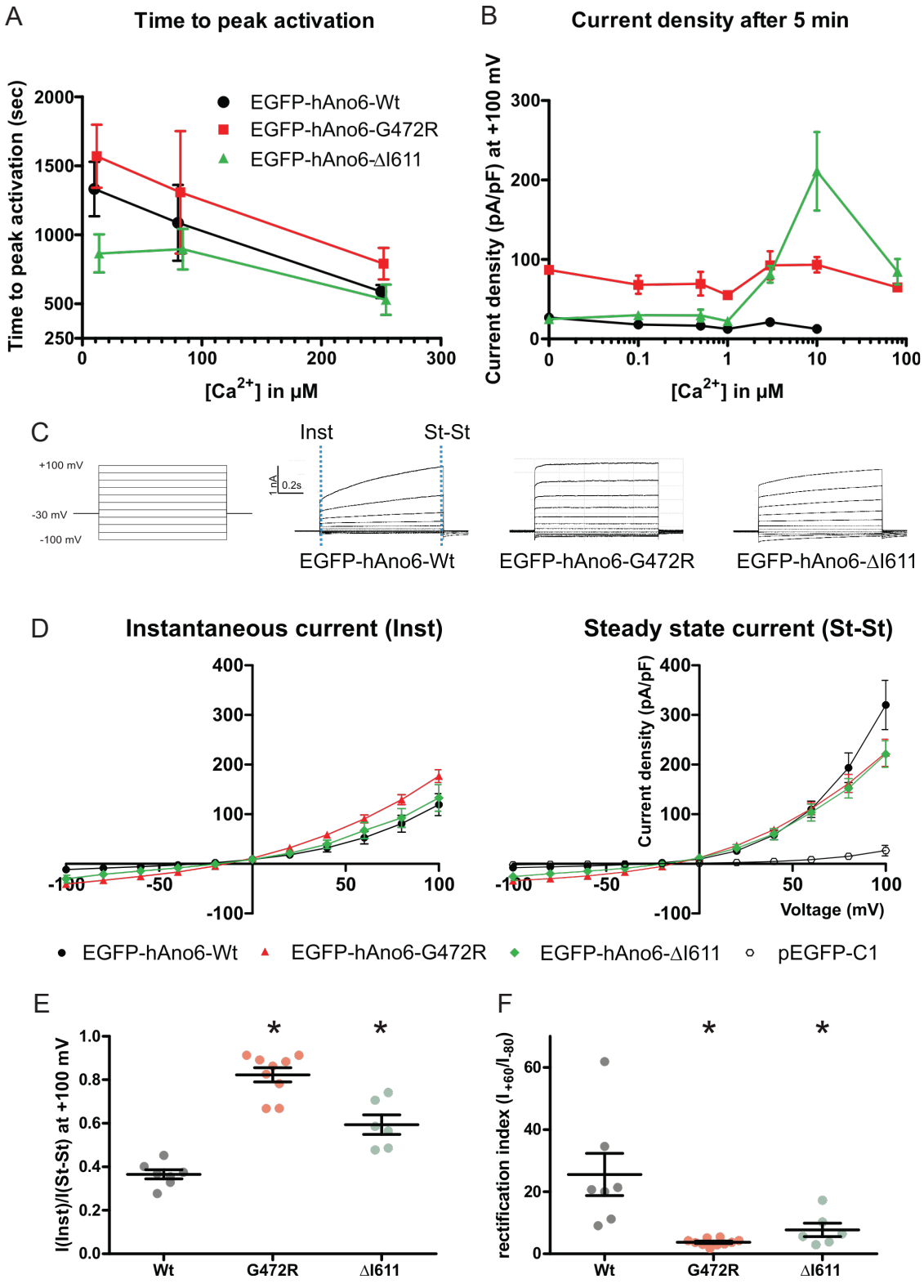

Figure 2.4: Patient mutations result in faster channel activation. Electrophysiological investigations of the mutant ANO6 constructs using a whole-cell configuration in HEK293cells. A) Channel activation by calcium. Data depict time of peak current activation ± SD vs free calcium concentration. B) Given non-physiological calcium concentrations in (A), smaller currents were assessed in whole cells. Data represent current density ± SD at various calcium concentrations after 1s +100 mV pulses 5 min after breaking into the cell. C) Applied voltage step protocol ranging from -100 mV to +100 mV in 20 mV increments and representative currents in whole-cell configuration. D) Current/Voltage curve displaying both the instantaneous and the (pseudo-)steady-state current densities ± SD. E) Calculation of activation kinetics as the ratio of instantaneous and (pseudo) steady state currents ± SD. F) Rectification index calculated as ratio between currents at +60 and -80 mV ± SD. Statistics were one-way ANOVA with Bonferroni post hoc analysis, *p<0.05 versus wild type. These studies were performed by co-first author FB.

as the ratio between currents at +60 and -80 mV, was significantly reduced in both variants compared to WT (Figure 2.4F). While indicative of a gain of channel function with respect to a shift in activation to more physiological conditions, variant currents at negative potentials were very low, slow and observed only at very strong depolarization pulses (+80 to 100 mV). Thus, this gain of function is unlikely to represent a disease promoting phenotype.

2.6.4 ANO6$^{\Delta I611}$ shows gain of GPS scramblase function while ANO6^{G472R} shows loss of GPS scramblase function

It has been proposed that the currents generated by ANO6 activation are secondary to the scrambling of phospholipids in the plasma membrane[14,15]. To examine the consequences of the two mutations on phospholipid scrambling, we first removed endogenous *ANO6,* generating HEK293 knockout cell lines using CRISPR/Cas9 gene editing. In two separate strategies, the N-terminus (ANO6$^{-/-}$ clone 2.5) and the third transmembrane domain (ANO6$^{-/-}$ clone 4.16) were targeted (Figure 2.5A) Both clones had premature stop codons on both alleles as verified by cloning and sequencing of the genomic DNA. Reverse transcription PCR showed a very strong decrease in Ano6 mRNA levels (Figure 2.5B), very likely due to nonsense-mediated RNA decay.

We assessed glycerophosphoserine (GPS) scramblase activity in these cells by flow cytometry using Cy5-labelled Annexin V, which binds to glycerophosphoserine (GPS) when exposed on the outside of the cell[133]. As expected, WT HEK293 cells showed increased Annexin V binding in response to the Ca^{2+} ionophore A23187 (Figure 2.6A). Neither HEK293 knockout clones exhibited any GPS scramblase activity (Figure 2.6B). Overexpression of both WT (Figure 2.6B) and mutant constructs rescued GPS scramblase activity in HEK293 knockout cell lines (Figure 2.7A). However, the plateau values reached were lower in G472R overexpressing cells suggesting either a loss of scramblase function or that

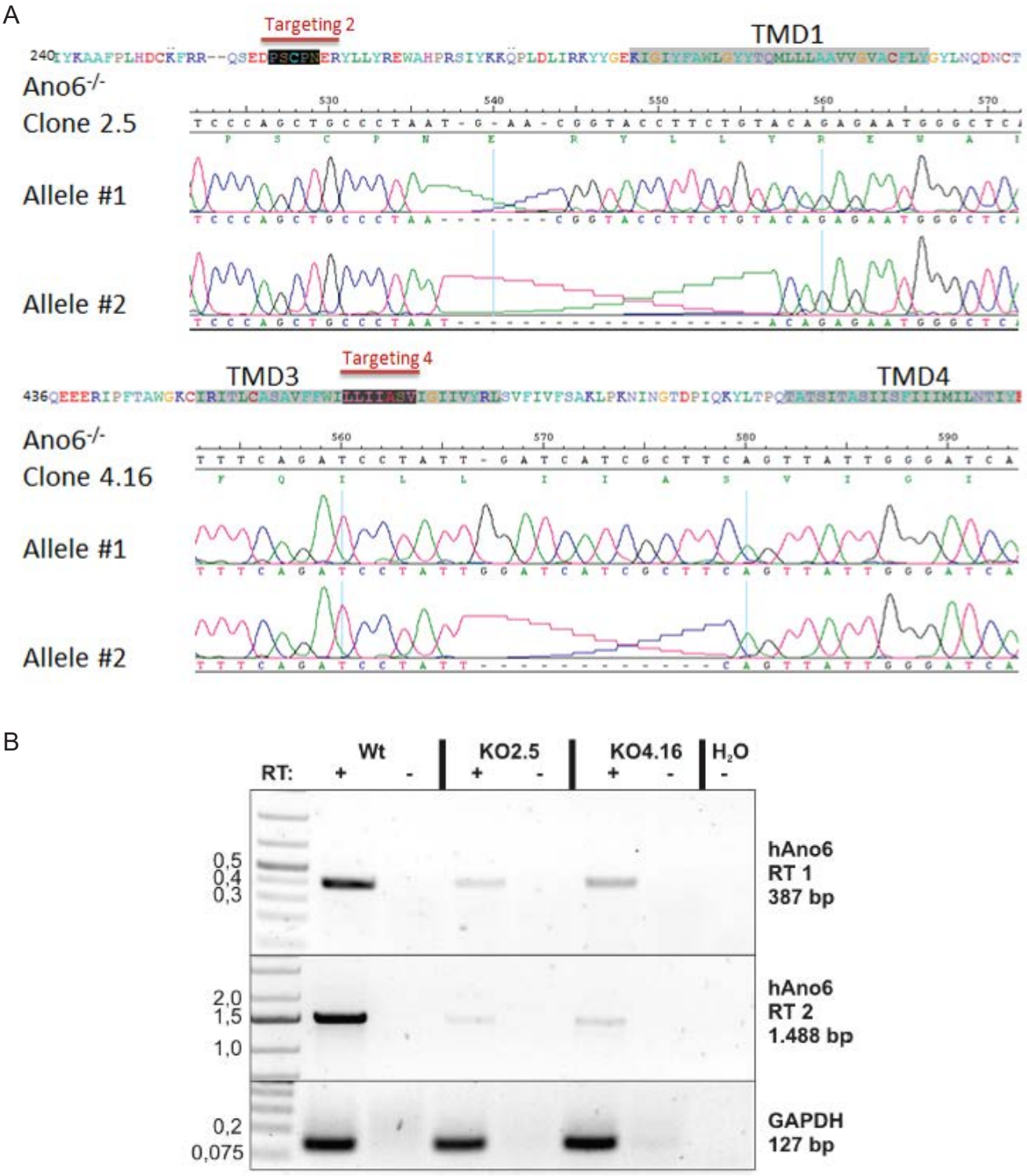

Figure 2.5: Generation of ANO6 knockouts in HEK293 cells. A) Knockout strategy with exemplary sequencing peaks. B) Reverse transcription PCR performed on the transfected HEK293 cells with knockout clones 2.5 and 4.16, using two sets of primers that are not affected by the targeted regions. GAPDH was used as a loading control. These studies were performed by co-first author FB.

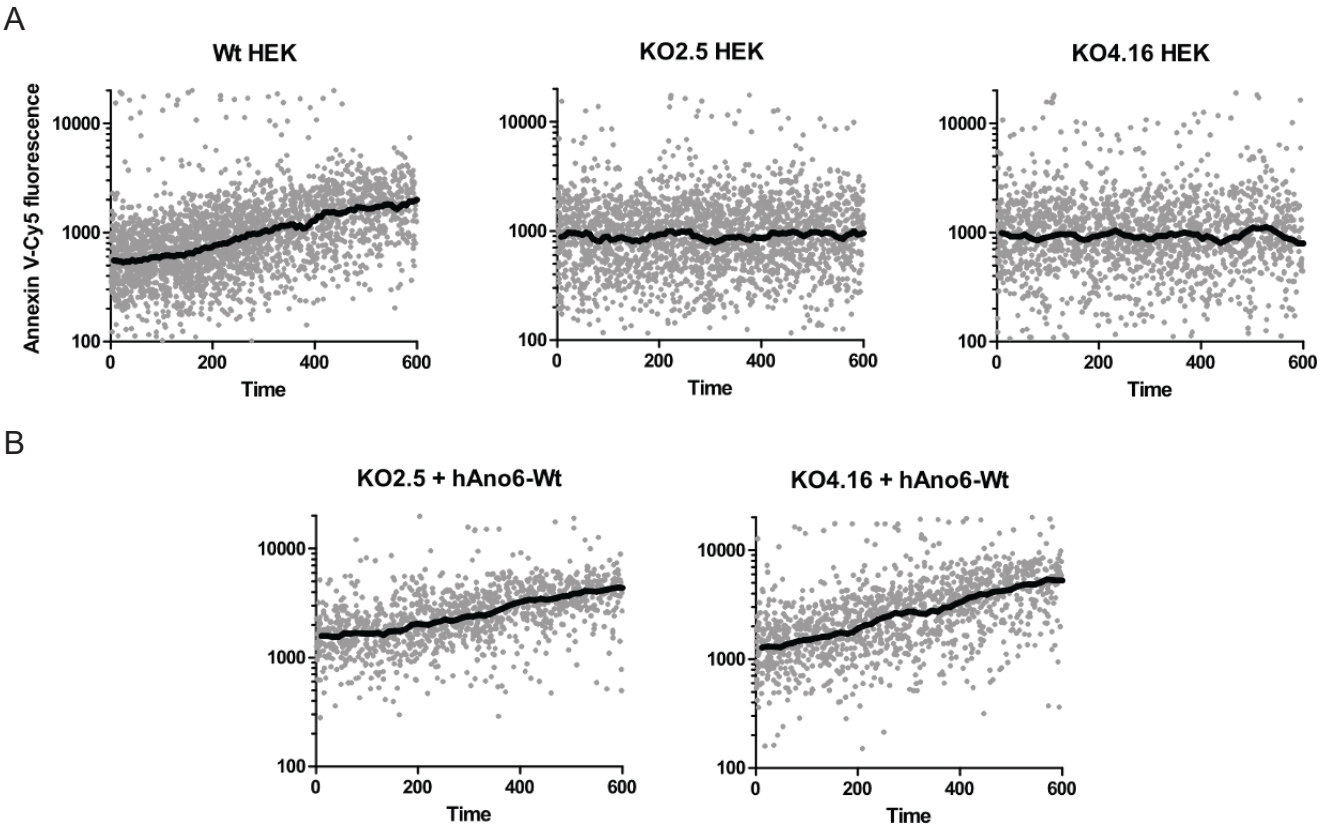

Figure 2.6: GPS Scrambling is abolished in ANO6 knockout cells, but rescued by overexpression of WT ANO6. Annexin V-Cy5 fluorescence measured over time following exposure to the Ca^{2+} ionophore A23187 via flow cytometry. Grey dots represent individual fluorescent events, and the black line shows the median fluorescence. A) Fluorescent traces of the wildtype HEK293 cells, and the two HEK 293 ANO6 knockout clones. B) Fluorescent traces of the two ANO6 knockout clones rescued by expression of wildtype ANO6. These studies were performed by co-first author FB.

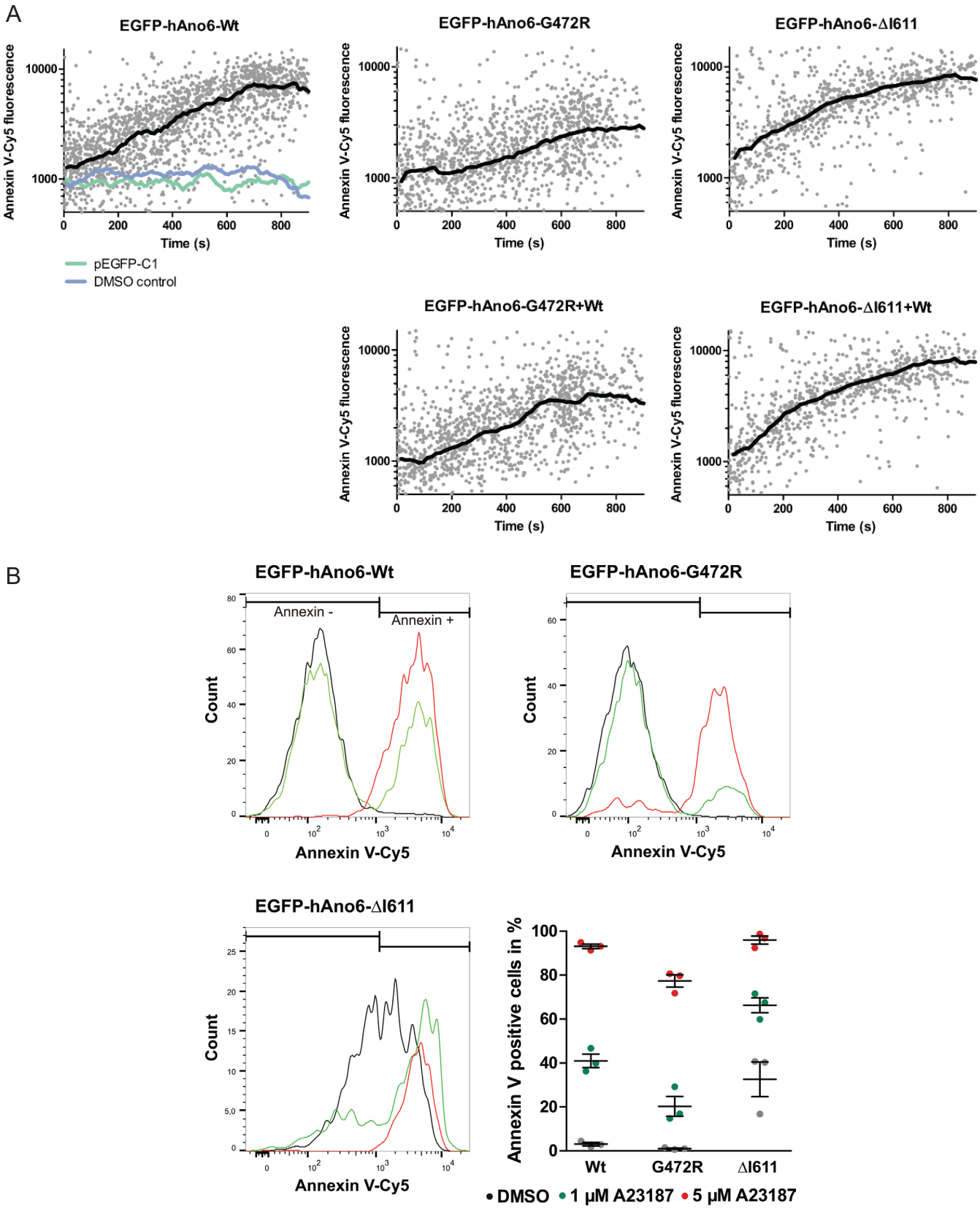

Figure 2.7: ANO6$^{\Delta I611}$ gain and ANO6^{G472R} loss of GPS scramblase function. A) Annexin V-Cy5 fluorescence measured over time following exposure to the Ca^{2+} ionophore A23187 via flow cytometry. Grey dots represent individual fluorescent events, and the black lines represent median fluorescence. Green line represents empty vector control, and the blue line represents effect of DMSO vehicle without A23187. B) Count of cells displaying Annexin V-Cy5 signal after treatment with 0 µM A23187 (black), 1 µM A23187 (green), or 5 µM A23187 (red). Percentage of Annexin V-Cy5 positive cells per condition and per concentration of A23187 ionophore (bottom right). These studies were performed by co-first author FB.

G472R expressing cells have less GPS in their plasma membrane thus GPS-exposed at plasma membrane in response to A23187. To establish whether calcium sensitivity is altered, we investigated scramblase activity at different concentrations of A23187 (Figure 2.7B). In the DMSO control, few cells transfected with WT or the G472R mutant were positive for Annexin V-Cy5 in the absence of A23187 (Figure 2.7B). By contrast, 32.6 ±7.9 percent of the ΔI611-transfected cells exhibited spontaneous scramblase activity in the absence of A23187 indicative of either a gain of function or an increase of GPS in their plasma membrane (Figure 2.7B). At 1 µM A23187, 41% of WT-expressing cells were positive for Annexin V-Cy5; 66% of ΔI611-transfected cells were positive for Annexin V-Cy5; while only 20% of G472R-expressing cells were positive for Annexin V-Cy5 (Figure 2.7B). These data are consistent with a gain of function in the ΔI611 mutant and a loss of function in the G472R mutant that could be attributed to a difference in GPS content at the plasma membrane.

2.6.5 Low disease associated penetrance of NPS-like symptoms in a murine model of the G472R NPS-associated variant

Taken together, our opposing *in vitro* data with respect to gain and loss of mutant scramblase function led us to hypothesize that NPS-variant pathogenicity was the result of impairments in GPS metabolism and not scramblase activity. However, our *in vitro* interrogation relied on the overexpression of NPS variants. To test whether GPS metabolism is disrupted *in vivo* and produces NPS features at physiological expression levels, we used CRISPR/Cas9 endonuclease-mediated double-strand breaks followed by homology directed repair and guide RNA with sequence GGATCGGGTCTGTCCCGTTG targeted to chromosome 15:9577878 to produce a p.G495R replacement in exon 13. This mutation in C57Bl/6N mice corresponds to the human p.G472R rare variant NPS-determinant (Figure 2.8).

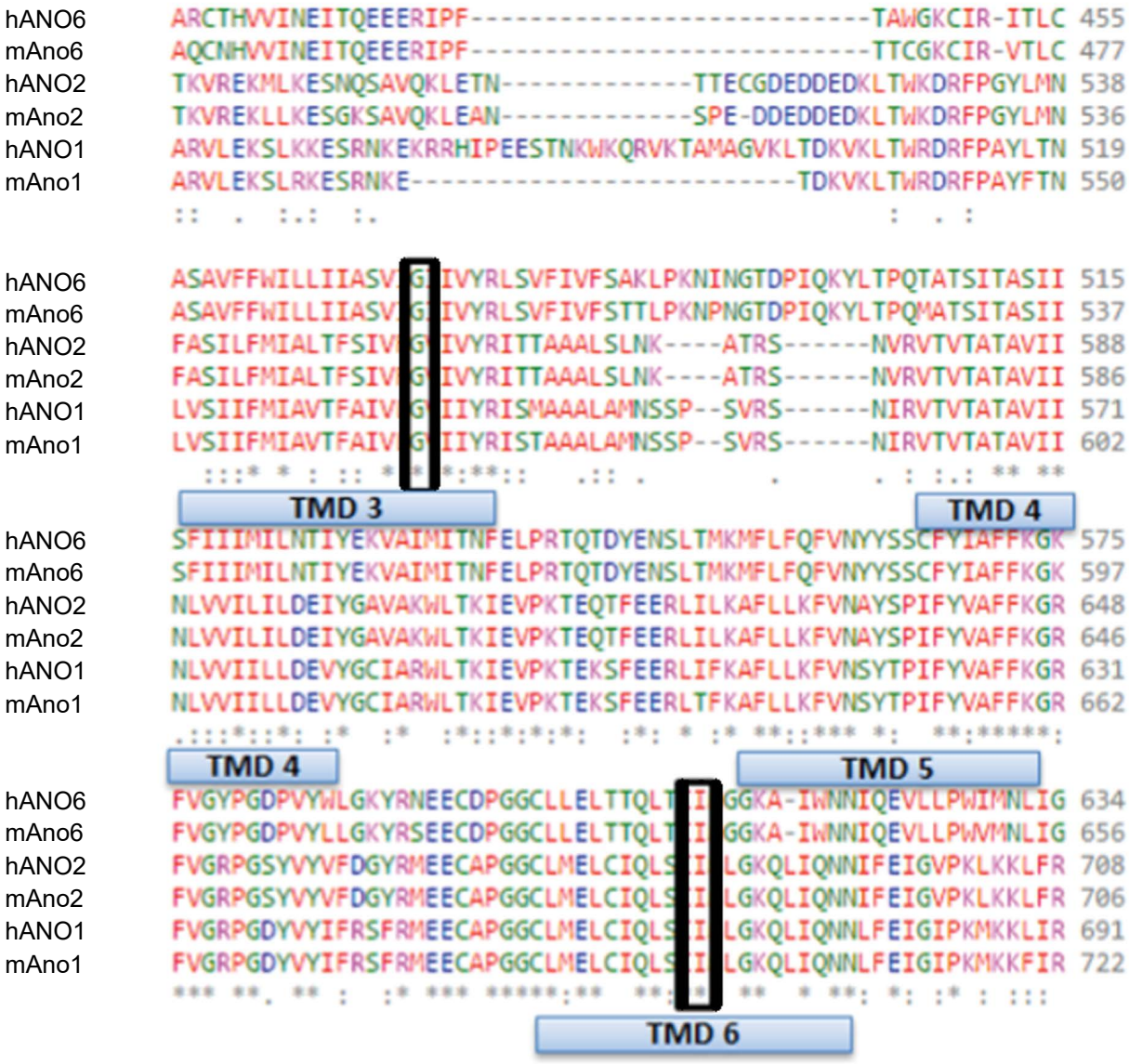

Figure 2.8: Patient mutations occur in highly conserved regions of ANO6. Sequence alignment of human and murine ANO6, ANO2, and ANO1 from human ANO6 residues 423 to 634. Mutations (surrounded by black boxes) locate to the transmembrane 3 and 6 domains and are found in highly conserved regions across species and anoctamin family members.

Table 2.1: Mendelian Ratios

	Total (n=304 with n=285 live births)						
	Males (n=152 live births)		Females (n=133 live births)		X^2 (p-value)		
	Observed	Expected	Observed	Expected	Total	Males	Females
ANO6$^{+/+}$	12.3% (n=35)	12.5%	17.5% (n=50)	12.5%	12.2 (p=0.032)	0.355 (p=0.8373)	12.8 (p=0.002)
ANO6$^{+/G495R}$	27.0% (n=77)	25%	19% (n=54)	25%			
ANO6$^{G495R/G495R}$	14.0% (n=40)	12.5%	10.2% (n=29)	12.5%			

We found that the vast majority of male and female Ano6$^{+/G495R}$ mice were viable and fecund. We traced a total of 304 progeny from heterozygote Ano6$^{+/G495R}$ X Ano6$^{+/G495R}$ matings from embryo to 220 days of age. A significant departure from the Mendelian ratio of live births was detected (Table 2.2). Significantly fewer heterozygous and homozygous female mice came to term representing 10% of all mice conceived (Table 2.2). Only a single female survived to 51 days of age with NPS-like features. No change in Mendelian genetics was detected in male births (Table 2.2). These data emphasized a low penetrance associated with embryonic lethality restricted to females.

Since patients were short stature, with low birth weight, small hands, and a lack of subcutaneous fat, we measured body weight, body length, the fore- and hind- paw length and area, and body fat content across all genotypes from birth to 32 weeks of age. In all but one female mouse brought to term, there was no difference in body weight or length (Figure 2.9A, B) or in fore or hind paw length or area (Figure 2.9C-E). There were no differences in total body fat assessed via MRI and no difference in the relative ratio of subcutaneous and visceral fat between genotypes (Figure 2.9G). We tracked the survival of these animals for up to 271 days. Consistent with the reduction in Mendelian birth ratios, viability was reduced by 10% in heterozygous and homozygous mutant mice compared to their wild-type littermates but not statistically significantly (Figure 2.9H). Taken together, these data indicated that viable Ano6$^{+/G495R}$ or Ano6 $^{G495R / G495R}$ do not display any gross phenotypic indicators of NPS.

In the absence of any gross physical changes in these mice, we assessed limb function. Because the human patients had smaller, and less dextrous hands and fingers, we tested the forepaw grip strength, agility, and manual dexterity of the animals. There were no differences in grip strength, normalized to bodyweight (Figure 2.10A), time-to-turn on the pole test as a marker of agility (Figure 2.10B), or manual dexterity as measured by the adhesive tape removal test (Figure 2.10C) between genotypes.

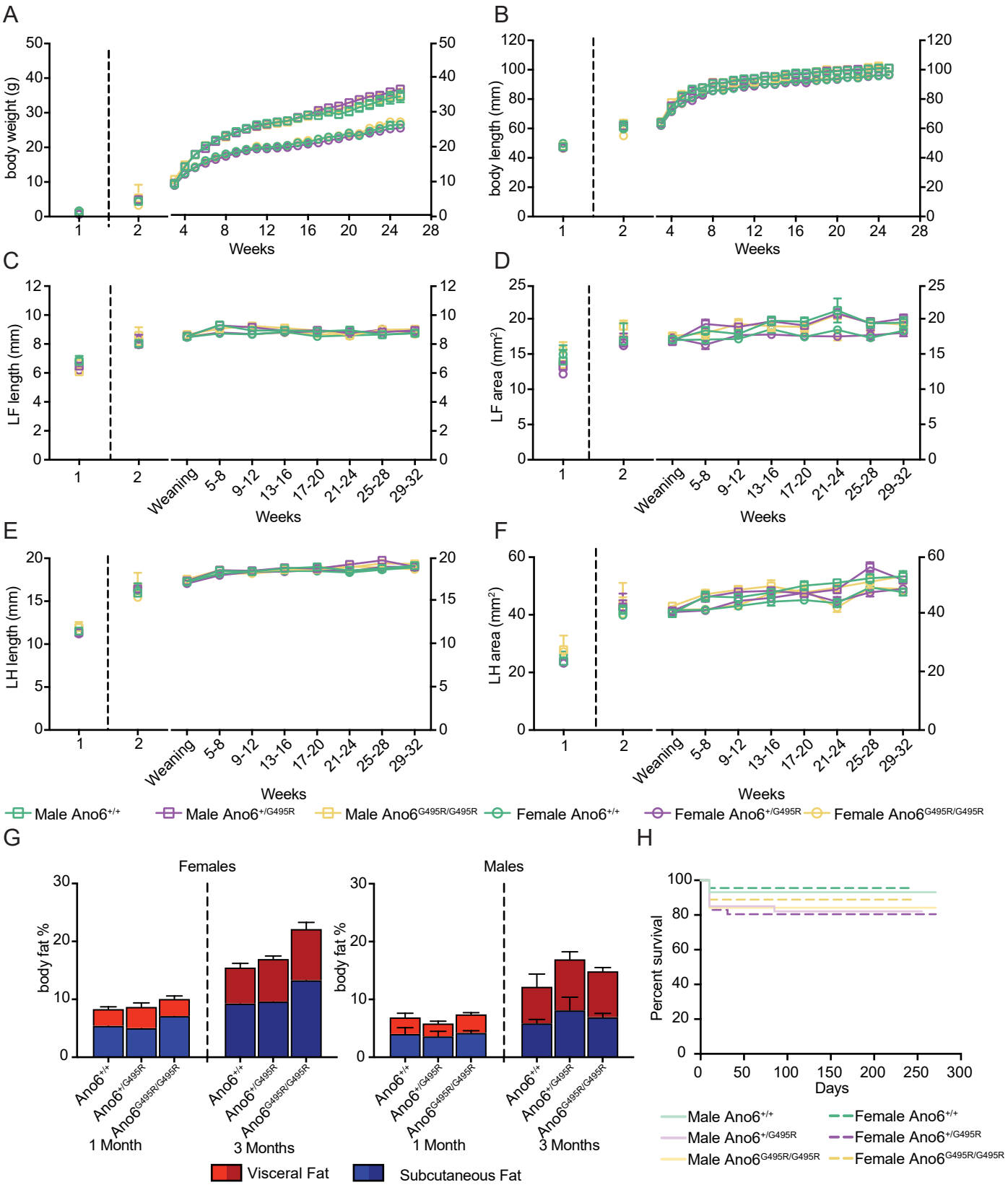

Figure 2.9: Surviving Ano6$^{+/G495R}$ and Ano6$^{G495R/G495R}$ mice studied showed no physical phenotypic alteration compared to Ano6$^{+/+}$ littermates. Physical measurements of mice born to heterozygous matings (A-F). A) Body-weight, and B) body length, were measured weekly from weaning to sacrifice. Separate cohorts were assessd for preweaning at one, and two weeks of age. C) Left forepaw length, D) left forepaw area, E) left hindpaw length, and F) left hindpaw area were measured monthly from weaning to 8 months of age. Data represent mean ± SEM of n = 3-47. Statistics were two-way ANOVAs. G) SubQ and visceral fat were measured at one month and three months of age in female (left) and male (right) mice. Data represent mean ± SEM of N = 3-4 per genotype and sex. Statistics were two-way ANOVAs. All main effects were not statistically significant. H) Kaplan-Meier survival curve of male and female mice assesed up to 270 days of age. Statistics were Log-rank (Mantel-Cox) Chi square 6.346 df = 5, p > 0.05. N = 29-77 mice per genotype and sex.

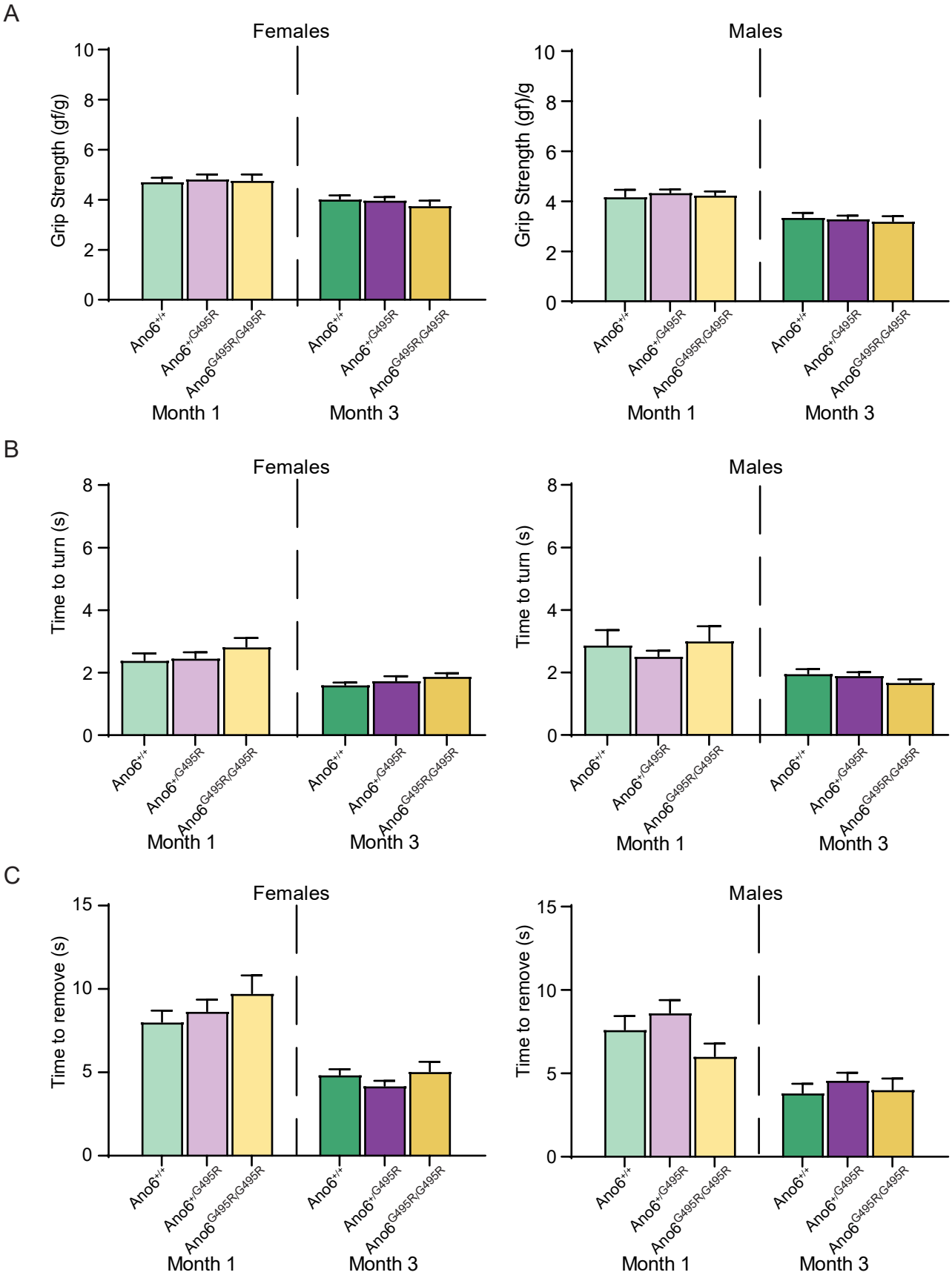

Figure 2.10: Surviving Ano6$^{+/G495R}$ and Ano6$^{G495R/G495R}$ mice do not have manual grip strength, agility, or manual dexterity deficits compared to wildtype littermates. A) Forepaw grip strength, B) agility, as determined by time-to-turn on the pole test, and C) manual dexterity, measured by the time to remove both pieces of adhesive tape during the adhesive test, as measured in female (left) and male (right) mice at one month of age with repeat testing at three months of age. Data represent mean ± SEM. Statistics were two-way ANOVA, $p > 0.05$. N = 9-18 mice per genotype and sex.

We tested the animals with a variety of voluntary and forced locomotive tests to determine if the p.G495R mutation recapitulated any motoric deficits observed in the NPS-variant patient. There was no difference in distance moved in the open field test (Figure 2.11A), voluntary running wheel activity (Figure 2.11B), baseline activity in their home-cages during the active period, using the beam-break apparatus (Figure 2.11C), or dexterity and locomotion assessed using the accelerating rotorod test

(Figure 2.11D).

A single affected female Ano6$^{+/G495R\text{-}NPS}$ mouse escaped embryonic lethality and was born live. She was smaller (Figure 2.12A) and had significantly reduced body-fat, both subcutaneous and visceral with the expected reduction in subcutaneous relative to visceral fat displayed by the patient (Figure 2.12B). Body weight and length was significantly reduced compared to her wild-type littermates (Figure 2.12C, D). Fore and hindlimb lengths and areas were reduced (Figure 2.12E-H). She died at 51 days of age, displaying a significantly shortened life-span compared to wild-type littermates (Mantel-Cox, Chi square = 9.502, df = 1, p = 0.0021) (Figure 2.12I).

2.6.6 GPS metabolism is disrupted in the affected female Ano6$^{+/G495R\text{-}NPS}$ but not unaffected Ano6$^{+/G495R}$ or Ano6$^{G495R/G495R}$ littermates

To address metabolic defects associating with phenotype, we compared the GPS lipidomes in skin and heart of unaffected and phenotypic littermates. There was no change in lipid abundance at the molecular level in unaffected Ano6$^{+/G495R}$ or Ano6 $^{G495R/G495R}$ littermates compared to Ano6$^{+/+}$ mice (Figure 2.13A, B). By contrast, a marked disruption in GPS homeostasis was evident in the affected female Ano6$^{+/G495R\text{-}NPS}$ mouse. In both skin and heart GPS lipidomes, we detected significant increases in 1-acyl lyso-GPS (LPS), 2-acyl LPS, and PS(O)-PAF metabolites and second messengers (Figure 2.14A, B). Homeostatic abundance of structural membrane lipids associated with the plasma membrane

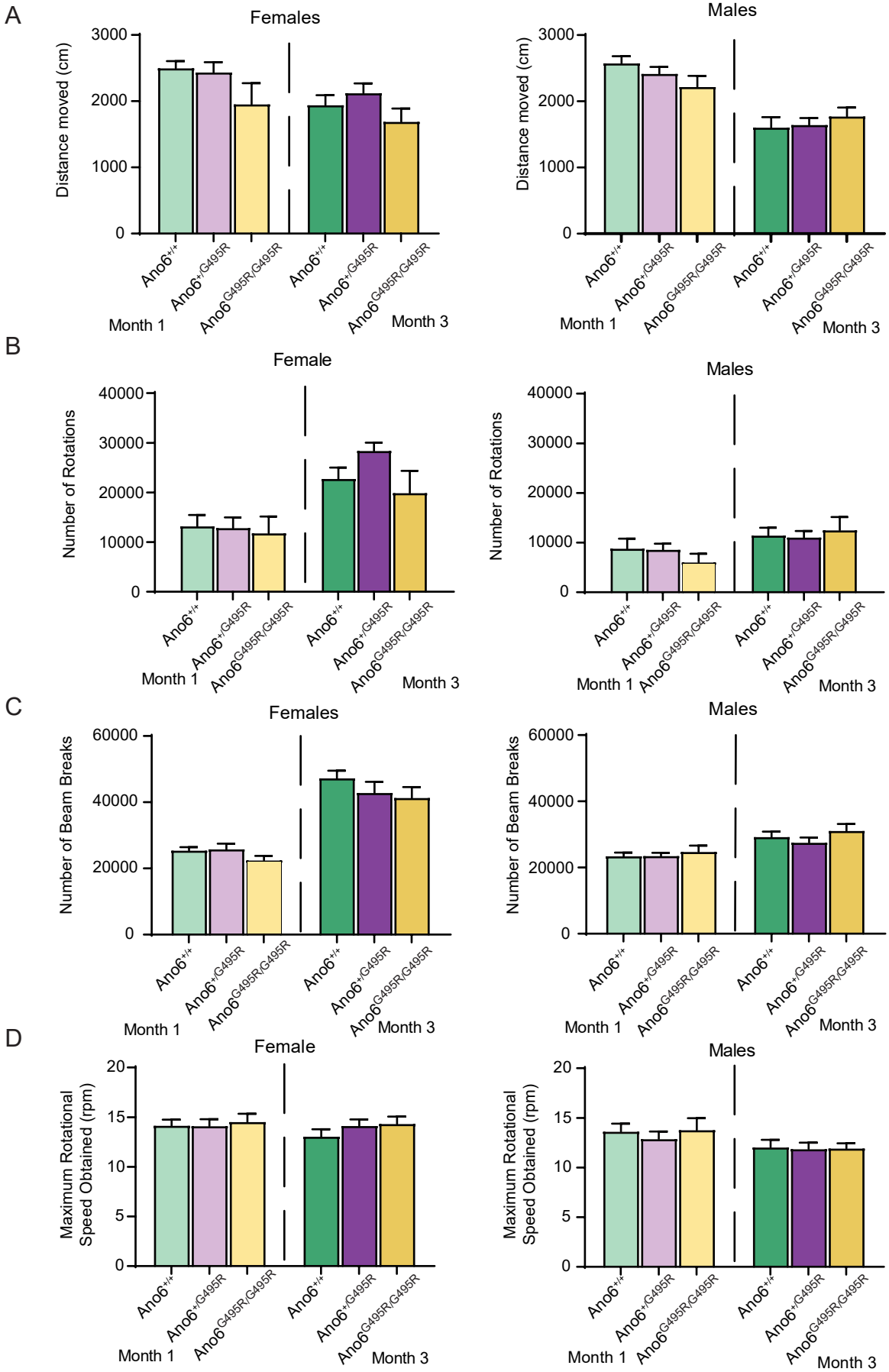

Figure 2.11: Ano6$^{+/G495R}$ and Ano6$^{G495R/G495R}$ mice do not display motoric deficits compared to wild-type littermates. Measurements for A) the distance moved as measured in the open field test over a 10 minute period trial as a measure for voluntary locomotion, B) the number of rotations over the active period once given free access to running wheels as voluntary locomotion, C) the home-cage activity using the beam break test, and D) the maximum rotational speed obtained by the animals on the accelerating rotorod test as a forced locomotive test, in female (left) and male (right) mice at one month, and tested again at three months of age. Data represent mean ± SEM, statistics were two-way ANOVA, $p > 0.05$. N = 9-18 per genotype and sex.

were differentially disrupted at the molecular level with significant decreases in GPS species with unsaturated fatty acyl groups at the *sn*-1 and *sn*-2 positions and significant increases in GPS species defined by polyunsaturated fatty acids at the *sn*-1 and *sn*-2 positions.

2.6.7 Levels of GPS second messengers and structural GPS accumulate in ANO6 ΔI611 patient fibroblasts

We asked whether fibroblasts derived from the patient with the ΔI611 exhibited a similar dysregulation in GPS metabolism (Figure 2.15). Unlike the skin and heart GPS lipidomes of affected female Ano6$^{+/G495R\text{-}NPS}$ mouse, there were no significant decreases in GPS abundances. Of the 33 species profiled, fourteen species were significantly elevated compared to control fibroblasts, specifically PS(16:0/16:0), PS(16:0/18:0), PS(16:0/22:6), PS(18:0/18:1), PS(18:1/20:0), PS(18:1/22:0), PS(18:1/22:1), PS(18:1/24:0), PS(18:1/24:1), PS(19:0/18:1), PS(20:1/20:3), PS(20:1/22:3), PS(20:4/20:4)|PS(18:2/22:6), and PS(20:4/22:5).

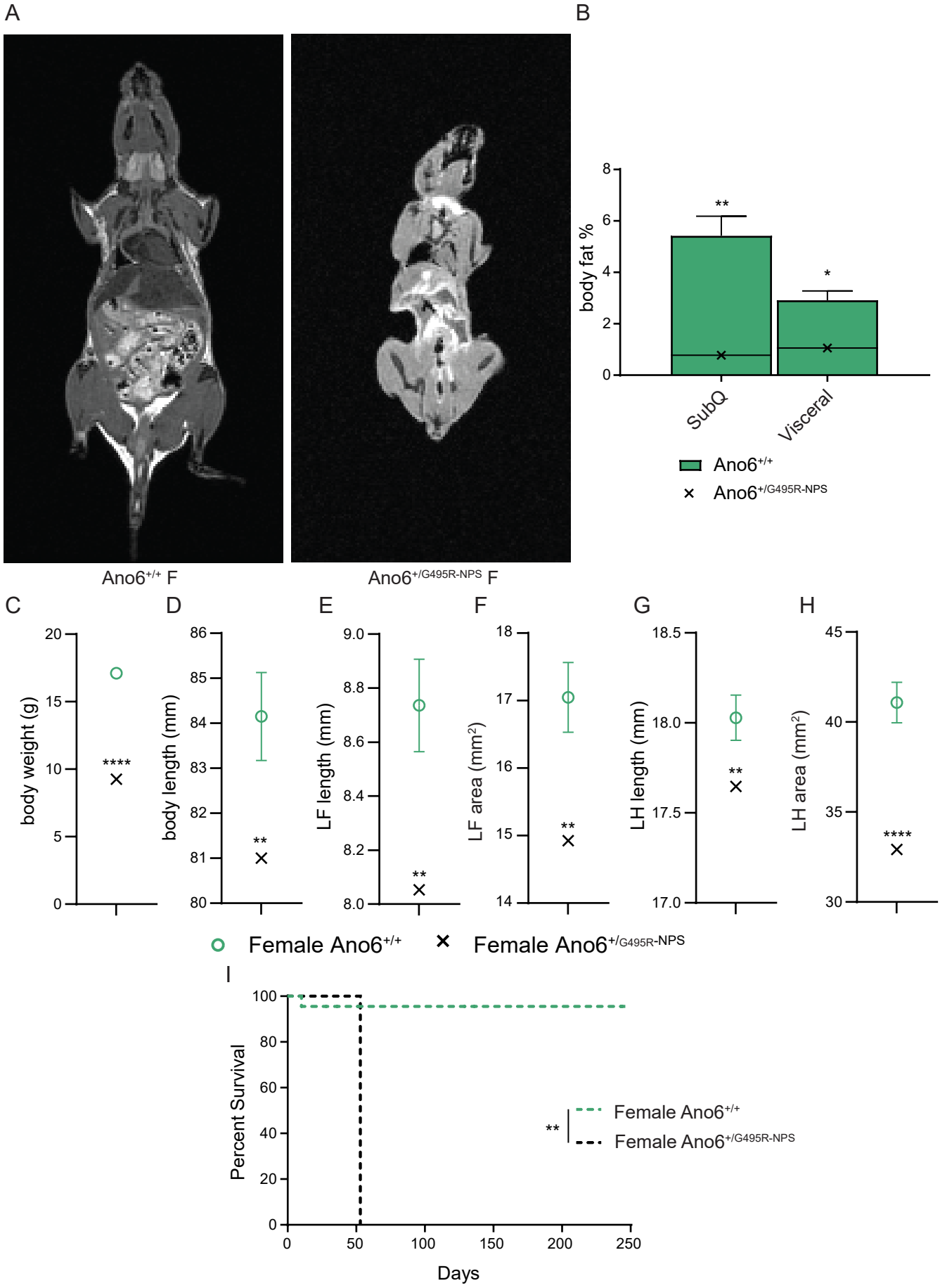

Figure 2.12: A single CRISPR/Cas9 *Ano6*:c.1414G>C mutant mouse born live displayed the NPS (variant) phenotype. For details, see next page.

Figure 2.12: A single CRISPR/Cas9 ANO6:c.1414G>C mutant mouse born live displayed the NPS (variant) phenotype.

A) Representative post-mortem T1 MRI image of a wild-type ($Ano6^{+/+}$) female (left) and the affected heterozygous ($Ano6^{+/G495R\text{-}NPS}$) female (right), taken at similar z slices. Percent bodyfat measured in these images were quantified in (B). B) Subcutaneous (SubQ) and visceral body fat percentages measured for $Ano6^{+/+}$ female mice, and the affected $Ano6^{+/G495R\ -NPS}$ mouse. Bars represent mean of n = 4 wildtype female mice ± SEM. Line represents affected animal's measured fat content. Statistics were one-sample t-test. C) Body weight, D) body length, E) left forepaw length, F) left forepaw area, G) left hindpaw length, and H) left hindpaw area of the affected $Ano6^{+/G495R\text{-}NPS}$ female compared to $Ano6^{+/+}$ female littermates. Affected mouse is represented by black X on graph. Green circles represent mean of n = 8-30 $Ano6^{+/+}$ female mice ± SEM. Statistics were one-sample t-test. I) Kaplan-Meier survival curves of the $Ano6^{+/+}$ females and the affected $Ano6^{+/G495R\text{-}NPS}$ female. Statistics are log-rank (Mantel-Cox) Chi square 9.502 df = 1. N = 50 female $Ano6^{+/+}$, N = 1 female $Ano6^{+/G495R\text{-}NPS}$.
Significance thresholds used were $*p \leq 0.05$, $**p < 0.01$.

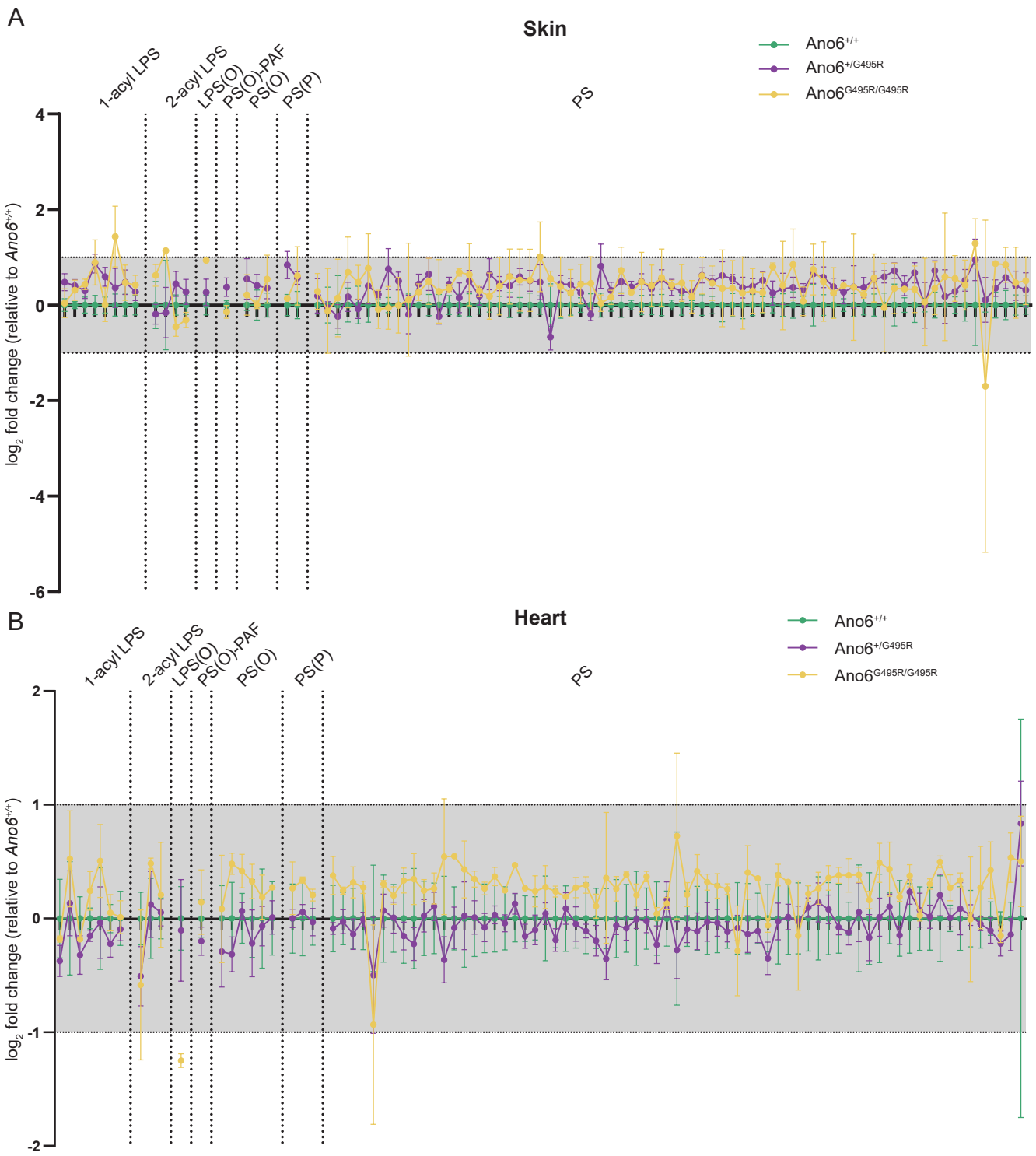

Figure 2.13: GPS skin and heart lipidomes are not significantly altered in unaffected Ano6$^{+/G495R}$ and Ano6$^{G495R/G495R}$ mice compared to wild-type littermates. A) Skin and B) heart lipidomes . Lipids are organized by subgroup from metabolites and second messengers to membrane structural lipids. Data represent $\log_2$ fold change relative to Ano6$^{+/+}$ mice ± SEM. Lipid abundances were assessed by HPLC-ESI-MS/MS. Statistics were one-way ANOVA on the pmol abundances per mg tissue wet weight for each species, $p > 0.05$. N = 3-5 female mice per genotype. Abbreviations: 1-acyl LPS, lyso-glycerophosphoserines with acyl-linked hydrocarbon chain at the *sn*-1 position; 2-acyl LPS, lyso-glycerophosphoserines with acyl-linked hydrocarbon chain at the *sn*-2 position; LPS(O), lyso-glycerophosphoserines with alkyl-linked hydrocarbon at the *sn*-1 position; LPS(P), lyso-glycerophosphoserines with alkenyl-linked hydrocarbon at the *sn*-1 position; PS(O)-PAF, alkylacetyl-glycerophosphoserines; PS(O), alkyl-acyl-glycerophosphoserine; PS(P), alkenylacyl-glycerophosphoserines; PS, glycerophosphoserines.

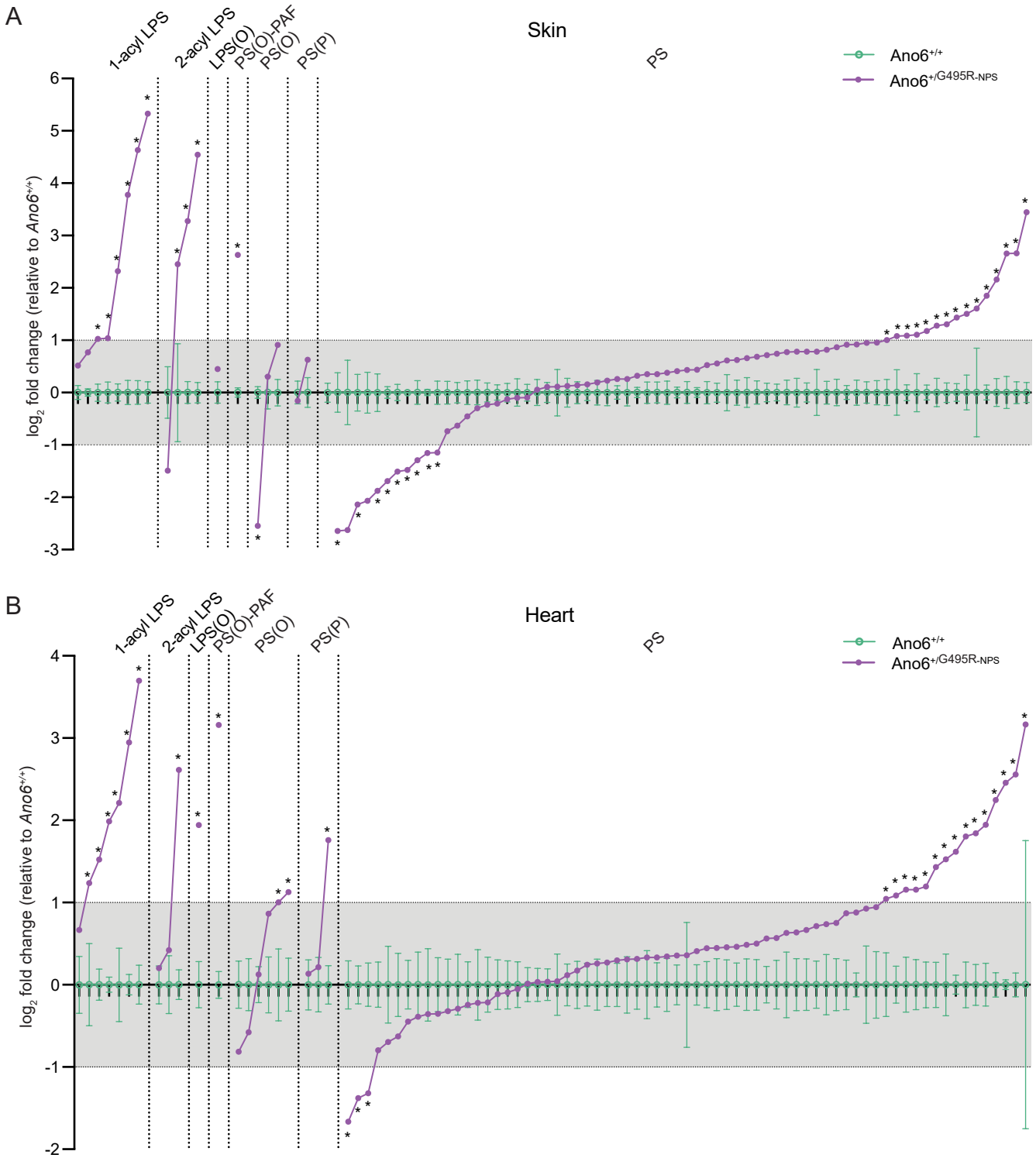

Figure 2.14: The GPS lipidome is dysregulated in the Ano6$^{+/G495R\text{-}NPS}$ mouse compared to wild-type littermates. A) Skin and B) heart lipidomes. Data represent $\log_2$ fold change of each GPS species detected in the Ano6$^{+/G495R\text{-}NPS}$ mouse relative to age-matched Ano6$^{+/+}$ wild-type littermates (n = 5). Lipid abundances were assessed by HPLC-ESI-MS/MS. Statistics were multiple one-sample t-tests, * $p \leq 0.05$, corrected for multiple comparisons using the method of Benjamini and Hochberg, with $q < 0.05$, on the pmol abundances per mg tissue wet weight. Abbreviations: 1-acyl LPS, lyso-glycerophosphoserines with acyl-linked hydrocarbon chain at the *sn*-1 position; 2-acyl LPS, lyso-glycerophosphoserines with acyl-linked hydrocarbon chain at the *sn*-2 position; LPS(O), lyso-glycerophosphoserines with alkyl-linked hydrocarbon at the *sn*-1 position; LPS(P), lyso-glycerophosphoserines with alkenyl-linked hydrocarbon at the sn-1 position; PS(O)-PAF, alkylacetyl-glycerophosphoserines; PS(O), alkyl-acyl-glycerophosphoserine; PS(P), alkenylacyl-glycerophosphoserines; PS, glycerophosphoserines.

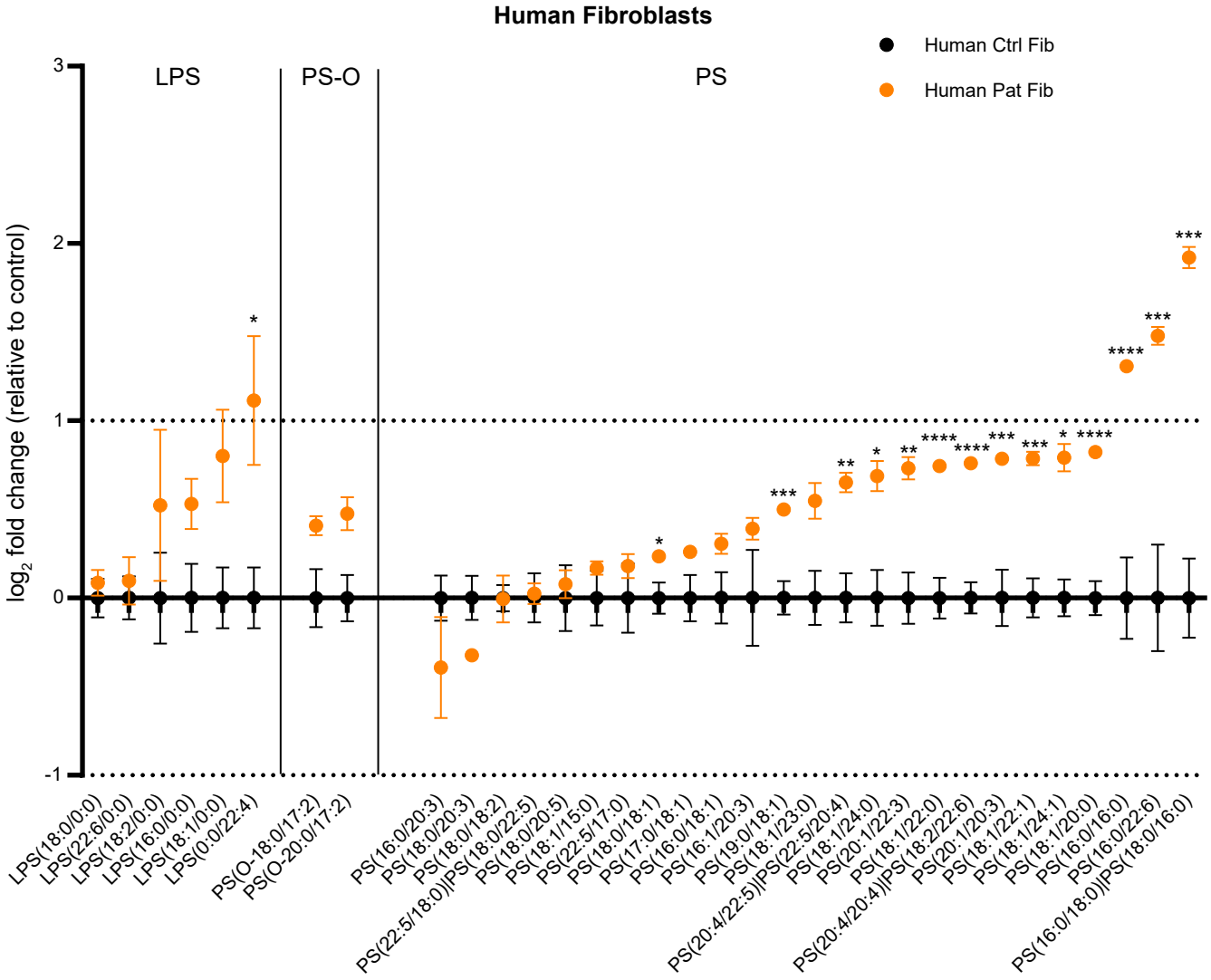

Figure 2.15 NPSPatient 2 with the ANO6$^{\Delta I611}$ mutation shows dysregulated GPS lipidome compared to controls. Data represent mean $\log_2$ fold change ± SEM. Statistics were Welch's t-test with false discovery rate (FDR) set at 1% using two-stage linear step-up FDR procedure of Benjamini, Krieger and Yekutieli[134] on pmol abundances per 1E6 cells between patient cells and control cells with . * q ≤ 0.05, ** q < 0.01, *** q < 0.001, **** q < 0.0001.

2.7 Discussion

In this chapter we describe the genetic underpinnings of a rare variant form of NPS and explored the biochemical consequences of these patient mutations on the ANO6 protein, in both human cells, and a novel mouse model of one of the variants. We show that the *ANO6* variants ΔI611 and G472R associated with NPS result in gain of channel function, but at non-physiological levels of calcium, and opposing gain or loss of GPS scramblase function depending on the variant. Thus, these protein functions do not conclusively associate with clinical phenotype. Using CRISPR/Cas9, we engineered a mouse model of the *ANO6*- G472R-NPS variant and demonstrate very low pathological penetrance that is restricted to females and results most commonly in embryonic lethality and rarely in phenotypic outcome consistent with NPS. The only defect common to the ΔI611 and G472R (G495R in mice) variant that associated with premature aging was a disruption in GPS metabolism, wherein GPS lipids defined by polyunsaturated fatty acids at the *sn*-1 and *sn*-2 position were aberrantly elevated in both patient fibroblasts and affected $ANO6^{+/\ G495R\text{-}NPS}$ tissues. Taken together, these data indicate that the pathogenic effects of these ANO6 variants are readily modified given that the majority of $ANO6^{G495R/+}$ animals are unaffected by restoration of GPS homeostasis.

In 2012, Kiraz et al[84] identified and described a patient who was diagnosed with a rare form of the neonatal progeroid syndrome. In this study, we identified a second patient that shared similar clinical features. Through whole exome sequencing, we identified heterozygous mutations in the *ANO6* gene, with no other overlapping gene variants common to both patients. Previously, mutations in *ANO6* have been identified in other diseases and conditions. Complete loss of ANO6 activity is associated with Scott Syndrome[135-137], and, in mouse models, results in bone mineralization and growth deficiencies[102, 110, 111]. Mutations resulting in gain of ANO6 activity, such as D409G[138, 139], Y563A[140], and I612A[140] induce cytotoxicity[140], accelerate Ca^{2+} dependent phospholipid scrambling, and/or increase Ca^{2+} channel sensitivity[140]. Our data suggest that none of these functions in ΔI611 or G472R carriers are likely to

represent a disease promoting phenotype given that the only common molecular impairment is a mild, non-physiological gain of channel function and either a loss (G495R) or a gain (ΔI611) of scramblase activity.

We do show that both variants significantly alter the cellular composition of GPS in patient cells and affected murine tissue with the accumulation of species defined by polyunsaturated hydrocarbons at the *sn*-1 and *sn*-2 common to both NPS-associated *ANO6* variants. The GPS species pathologically elevated are uniquely susceptible to Fenton-catalyzed oxidation reactions at the plasma membrane[141], generating oxidized and glyco-oxidized species[141] that, in turn, are expected to impair cell viability, delay differentiation, and accelerate cell senescence[142, 143].

Together, our *in vitro* and *in vivo* data identify a novel gain of function in GPS membrane modeling linked to NPS. The longer latency to death in *ANO6*-linked NPS affords a unique opportunity to improve outcome for affected patients with respect to risk of pulmonary hypertension and premature aging complications. Thus, for this rare disorder, identifying the metabolic modifiers that restore GPS lipid homeostasis in our unaffected mice will provide alternate approaches to treat these rare variant forms of premature aging and identify new therapeutic targets. Future studies will be required to fully explore the consequences of this metabolic dysfunction on cellular phenotype and capacity to restore function via metabolic rescue.

Chapter 3 : The Clinical Spectrum of SMA-PME and *In Vitro* Normalization of its Cellular Ceramide Profile

Michelle M. Lee MD[1*], Graeme S.V. McDowell MSc[2*], Darryl C. De Vivo MD[3], Daniel Friedman MD[4], Samuel F. Berkovic MD[5], Maria Spanou MD[6], Argirios Dinopoulos MD[6], Katheryn Grand MS[7], Pedro A. Sanchez-Lara MD[7], Michelle Allen-Sharpley MD, PhD[7], Jodi Warman-Chardon MD, MSc[8,12], Alexander Solyom MD[9], Thierry Levade MD, PhD[10], Edward H. Schuchman PhD[11], Steffany A.L. Bennett PhD[2†], David A. Dyment DPhil, MD[12†], Toni S. Pearson MBBS[1,3†]

*Joint first authors

[1]Department of Neurology, Washington University School of Medicine, St. Louis, MO, USA; [2]Neural Regeneration Laboratory, Ottawa Institute of Systems Biology, Department of Biochemistry, Microbiology and Immunology, University of Ottawa, Ottawa, ON, Canada; [3]Department of Neurology and Pediatrics, Columbia University Irving Medical Center, New York, NY, USA; [4]Department of Neurology, NYU, USA; [5]Department of Neurology, University of Melbourne, Australia; [6]Pediatric Neurology Division, 3rd Department of Pediatrics, Attikon University Hospital, Athens, Greece; [7]Department of Pediatrics, Cedars-Sinai Medical Center, Los Angeles, California, US; [8]Department of Medicine (Neurology), Ottawa Hospital Research Institute, Ottawa, ON; [9]Aceragen, Basel, Switzerland; [10]Laboratoire de Biochimie Métabolique, CHU Toulouse, INSERM U1037, Centre de Recherches en Cancérologie de Toulouse, Université Paul Sabatier Toulouse, France; [11]Department of Genetics and Genomic Sciences, Icahn School of Medicine at Mount Sinai, New York, NY; [12]Children's Hospital of Eastern Ontario Research Institute, Ottawa, ON, Canada.

3.1 Objective of study

In Chapter 2, I identified functional biochemical and lipidomic changes *in vitro* and *in vivo* associated with a rare variant form of NPS attributed to pathological variants in the *ANO6* gene. Penetrance of phenotype was variable (embryonic lethal or rare live births) in my CRISPR/Cas9 *ANO6*:c.1414G>C mouse model and I chose not to pursue identifying the genetic modifiers that rescued phenotype in non-manifesting carriers. Instead, I turned to the investigation of clinical and metabolic differences underlying Spinal Muscular Atrophy with Progressive Myoclonic Epilepsy (SMA-PME) and Farber Lipogranulomatosis (FL). Both disorders result from mutations in a lipid regulatory gene *ASAH1*. I sought first to compare and contrast the natural history of FL and SMA-PME focussing on describing

the 30 patients identified with SMA-PME world-wide as of October 2022 and provide proof of principle of potential success of enzyme replacement therapy (ERT).

3.2 Author Contributions

AS, EHS, SALB, DAD, TSP, MML and GSVM conceived and designed the experiments and study. GSVM and MML analyzed all of the data with input and guidance from TSP, DAD, and SALB. Cohorts and clinical history were provided by DCDV, DF, SFB, MS, AD, KG, PAS-L, MA-S, JW-C, DAD, and TSP. LC-ESI-MS/MS and cell treatments were performed and analyzed by GSVM. Enzyme assays were performed by TL. MML, GSVM, DF, SFB, MS, AD, KG, PAS-L, MA-S, SALB, DAD, and TSP drafted the published manuscript. All authors revised manuscript for intellectual content. This chapter was published in Annals of Clinical and Translational Neurology as Lee MM*, **McDowell GSV***, De Vivo DC, Friedman D, Berkovic SF, Spanou M, Dinopoulos A, Grand K, Sanchez-Lara PA, Allen-Sharpley M, Warman-Chardon J, Solyom A, Levade T, Schuchman EH, Bennett SAL, Dyment DA, Pearson TS (2022) The clinical spectrum of SMA-PME and *in vitro* normalization of its cellular ceramide profile. *Ann Clin Transl Neurol*, 2022 9:1941-1952. doi: 10.1002/acn3.51687. * indicates joint first authors.

3.3 Abstract

The objectives of this study were to define the clinical and biochemical spectrum of spinal muscular atrophy with progressive myoclonic epilepsy (SMA-PME) and to determine if aberrant cellular ceramide accumulation could be normalized by enzyme replacement. Clinical features of 6 patients with SMA-PME were assessed by retrospective chart review, and a literature review of 24 previously published cases was performed. Leukocyte enzyme activity of acid ceramidase was assessed with a fluorescence-based assay. Skin fibroblast ceramide content was assessed by high performance liquid chromatography, electrospray ionization tandem mass spectroscopy. Enzyme replacement was assessed using recombinant

human acid ceramidase (rhAC) *in vitro.* The six new patients showed the hallmark features of SMA-PME, with variable initial symptoms and age of onset. Five of six patients carried at least one of the recurrent SMA-PME variants observed in two specific codons of *ASAH1*. A review of 30 total cases revealed that patients who were homozygous for the most common c.125C>T variant presented in the first decade of life with limb-girdle weakness as the initial symptom. Sensorineural hearing loss was associated with the c.456A>C variant. Leukocyte acid ceramidase activity varied from 4.1%-13.1% of controls. Ceramide species in fibroblasts were detected and total cellular ceramide content was elevated by 2 to 9-fold compared to controls. Treatment with rhAC normalized ceramide profiles in cultured fibroblasts to control levels within 48 h. This study details the genotype-phenotype correlations observed in SMA-PME and shows the impact of rhAC to correct the abnormal cellular ceramide profile in cells.

3.4 Introduction

Spinal muscular atrophy with progressive myoclonic epilepsy (SMA-PME; OMIM 159950) is an autosomal recessive lysosomal storage disorder caused by pathogenic variations in *ASAH1*[144-146]. This gene encodes the enzyme acid ceramidase (aCDase), which catalyzes the breakdown of ceramides into sphingosine and free fatty acids in the lysosome[147]. SMA-PME is a rare condition and, to date, a total of 24 patients from 19 families have been reported in detail in the literature with confirmed pathogenic variation in *ASAH1*[116, 146, 148-161]. Reported patients commonly present with proximal weakness in mid-childhood, followed by progressive seizures and myoclonus[162]. Mortality may result from respiratory insufficiency in early adulthood or from complications of refractory seizures. The isolated neurological phenotype observed in SMA-PME contrasts with the predominant peripheral symptoms associated with Farber Lipogranulomatosis or Farber disease (FD; OMIM:22800). FD is also a result of pathogenic variation at *ASAH1* and is characterized by a clinical triad of joint disease presenting as arthritis and/or

contractures, subcutaneous nodules, and a hoarse voice secondary to laryngeal involvement[163]. Farber disease has a broad phenotypic spectrum ranging from rapidly progressive disease leading to death in the first years of life, to rarer forms characterized by slowly progressive adult-onset disease[164]. While peripheral symptoms predominate in Farber disease, there have also been neurological symptoms reported to occur in a subset of patients that includes seizures, hypotonia, and lower motor neuron disease that can show in the late stages of the disease[160, 165].

Here, we describe the clinical features of six patients with SMA-PME (four previously unpublished and two published with brief clinical data[166, 167]). We analyze the clinical features and relationship of genotype to phenotype in these 6 patients, and 24 previously reported[116, 146, 148-159]. We describe pathogenic nonsense, missense, or splice site variants in *ASAH1* in each patient combined with biochemical verification of aCDase loss of function either by the detection of elevated ceramide using high performance liquid chromatography, electrospray ionization, tandem mass spectrometry (HPLC-ESI-MS/MS) or by aCDase deficiency assessed through enzyme analysis. We further show that the cellular phenotype of increased ceramide profile can be normalized by treatment with recombinant human acid ceramidase (rhAC). These observations provide insights into the broad phenotypic spectrum observed in SMA-PME and provide *in vitro* evidence for the impact of rhAC as a potential treatment requiring further pre-clinical investigation.

3.5 Material and Methods

3.5.1 Standard protocol approvals, registrations, and patient consents

Six patients were enrolled by informed consent from their families and according to the following research ethics board approvals: CHEO REB #11/04E.

3.5.2 Participants

We report here six patients with SMA-PME and their genotypes. Clinical information was collected retrospectively. Additional literature reviews were performed for 24 previously reported cases with molecularly confirmed SMA-PME[116, 146, 148-159]. Criteria for inclusion were: an isolated neurological presentation, an adequate description of the clinical phenotype, and confirmed pathogenic variants in *ASAH1*. We excluded reports of cases that lacked clinical data[168] and historical reports of SMA-PME that lacked molecular confirmation. Because several transcripts have been used in the literature when describing variants in *ASAH1*, we have converted variants to nomenclature corresponding to the NM_177924.5 transcript[161].

3.5.3 Acid ceramidase activity and immunoblotting

Fibroblast cell lines were generated from a punch biopsy by standard methods. Leukocyte aCDase activity was assayed in patients and their parents. Lymphocytes were isolated from whole blood and aCDase activity was determined in the cell lysates using a fluorescence-based assay with minor modifications[169, 170]. Fibroblast aCDase activity before (0 h) and after rhAC treatment (24 and 48 h) was assayed in three patients compared to seven controls (age- and sex-matched) by HPLC-ESI-MS/MS as described below. Immunoblotting was performed as previously described[171]. Primary antibodies were rabbit anti-ASAH1α, 1/500 (gifted by Professor Konrad Sandhoff, Universität Bonn) and rabbit anti-ASAH1β, 1/400, Sigma, cat# HP005468). Secondary antibodies were HRP-Donkey anti-Rabbit IgG, 1:5000, (Jackson ImmunoResearch, cat# 711-035-152).

3.5.4 In vitro treatment with rhAC and HPLC-ESI-MS/MS analysis of cellular ceramide content

Primary fibroblasts were cultured in Dulbecco's Modified Eagle Medium: Ham's Nutrient mixture 12 (D-MEM/F-12) (Gibco, cat# 12400-016) supplemented with 10% fetal bovine serum (Sigma Aldrich, F0926), and 2 mM L-glutamine (Gibco, cat# 25030-081). Recombinant human acid ceramidase (rhAC) is derived from CHO-M cells transfected with a DNA plasmid vector expressing wild-type human aCDase. It was produced at a contract manufacturing facility and was provided under material transfer agreement (MTA) originated under Enzyvant and currently with Aceragen. Development for potential clinical use is continuing under Aceragen as ACG-801. Where treatment with rhAC is indicated, cultures were treated with 10 µg/mL of rhAC in complete media similarly to the work in Farber patient cells[172]. Media + rhAC was refreshed every 24 h. Lipids were extracted according to a modified acidified Bligh and Dyer lipid extraction previously described in detail[127, 128]. Briefly, cells were trypsinized, counted via hemocytometer, washed with phosphate buffered saline (BioShop, cat# PBS404), and pelleted. Pellets were resuspended in 0.1 mol/L sodium acetate (Sigma, cat# S-2889, in LC/MS grade water; J.T. Baker, cat# 9831-03), acidified methanol (2% acetic acid, Fisher, A38-212 in methanol; Fisher, cat# BP1105, (v/v)) was added, along with 235 pmol of Cer(d18:1/16:0-d31) (Avanti Polar Lipids, cat# 868516). Lipids were extracted by addition of chloroform (Fisher, cat# C298) to a ratio of 1.6:2:1.4 sodium acetate:acidified methanol:chloroform (v/v/v). The organic phase was collected, and the samples were back-extracted three times, with the organic phases being collected and pooled. Samples were dried under a constant stream of nitrogen gas. Dried lipid extracts were re-dissolved in ethanol, stored under nitrogen gas in amber glass vials (Chromatographic Specialties, cat# C779100AW) and kept at -80^{o}C until use.

Ceramide content was quantified by HPLC-ESI-MS/MS using an Agilent 1290 LC and a triple quadrupole-linear ion trap mass spectrometer QTRAP 5500 (AB SCIEX). HPLC separation was achieved on a 100 mm x 250 µm (i.d.) capillary column packed with ReproSil-Pur 120 C8 beads (particle

size of 3 µm and pore size of 120 Å, Dr. A. Maisch, Ammerbruch, Germany) with 5 µL sample injections by an autosampler maintained at 4°C with a flow rate of 10 µL/min. The binary solvent gradient consisted of LC/MS grade water with 0.1% formic acid (Fisher, 56302) and 10 mmol/L ammonium acetate (OmniPur, 2145) (solvent A), and acetonitrile (J.T. Baker cat# 9829-03)/isopropanol (Fisher, cat# A416-4) (5:2; v/v) with 0.1% formic acid and 10 mmol/L ammonium acetate (solvent B). Gradient elution started with 30% B, ramping to 100% B over 5 min. After 30 min at 100% B, the gradient dropped to 30% B over the course of a minute, where it remained for the time remaining in the run to re-equilibrate the column. Data acquisition was performed in positive ion mode using multiple reaction monitoring (MRM) monitoring the product ion of 264.3, corresponding to di-dehydrated d18:1 sphingosine backbone. Instrument control and data acquisition were performed with Analyst software (v. 1.6.2, AB SCIEX). Processing of quantitative MRM data was performed using MultiQuant software (v. 3.0.2, AB SCIEX). Ceramide abundances were expressed as pmol equivalents of Cer(d18:1/16:0-d31) per million cells. Percent activity, defined as the change in ceramide content at 0, 24, and 48 h following rhAC treatment, was expressed relative to untreated age- and sex-matched controls. Total ceramide content was analyzed statistically using a one-way ANOVA with Holm-Šidák post-hoc tests. Changes in the abundances of individual ceramide species were determined statistically by multiple *t*-tests with false discovery rate (FDR) set at 1% using two-stage linear step-up FDR procedure of Benjamini, Krieger and Yekutieli[134] without assuming consistent standard deviation. The change in percent activity was assessed 0-48 h after treatment with rhAC and time needed to correct ceramide levels determined by linear regression. Statistical analyses were performed using GraphPad Prism version 9.41 (GraphPad Software).

3.5.5 Data availability

Anonymized data not published within the article will be made available upon request from a qualified investigator(s).

3.6 Results

3.6.1 Case Reports

Patient 1 is a 21-year-old female, briefly reported previously at age 15 years[167], who presented with seizures, weakness, and involuntary movements at age 9 years. Her non-consanguineous parents were of South Asian ancestry. Following normal early childhood development, her reported first symptom was mild learning difficulties at age 7 years (Table 3.1). At age 9 years, she developed brief and sudden drop attacks, and separate episodes of eye rolling and staring. An EEG showed generalized epileptiform discharges and a diagnosis of myoclonic seizures was made. Treatment with sodium valproate was initiated. At age 10 years, she developed difficulty rising from the floor due to muscle weakness, "limb shaking," and torticollis (head turn to the left). At age 12 years, she developed generalized tonic-clonic seizures. Neurological examination at age 13 years revealed hypotonia and symmetrical, proximal upper and lower limb muscle atrophy and weakness with relatively preserved distal limb strength. Tendon reflexes were brisk with spread. Hoffman's sign was present bilaterally. She had cervical and foot dystonia. There were frequent brief, small amplitude multifocal jerks in the hands and arms at rest that increased with action, and in the legs upon standing, consistent with cortical myoclonus. Gait was independent, normal-based and steady. Her weakness progressed and she lost the ability to walk independently at age 14 years. At age 16-17 years, her seizure burden worsened and there was accompanying cognitive decline leading to homebound state. At age 21 years, she has severe generalized weakness and is tracheostomy- and ventilator-dependent due to chronic respiratory failure. Trio-exome

sequencing showed biallelic variants at *ASAH1*; c.536C>T (p.Thr179Ile) and c.124A>G (p.Thr42Ala) (Table 3.1).

Patient 2 was a 26-year-old male who presented at age 22 years with seizures, myoclonus, and weakness. His early childhood medical and developmental history were normal. At age 5 years he was diagnosed with sensorineural hearing loss (Table 3.1). At age 12 years, he began to have difficulty keeping up with peers in sports. He nonetheless continued to play sports until age 16 years. At age 15 years, he had his first generalized tonic-clonic seizure. After a second seizure, he was treated with phenytoin and then valproate. He was seizure-free until age 18 years, when he experienced a prolonged generalized tonic-clonic seizure after starting college. These continued every few weeks with subsequent daily staring spells. Mild cognitive difficulties (short term memory and processing speed impairments), limb myoclonus, and anxiety were apparent by age 18 years and progressed. He continued to experience dozens of myoclonic seizures per day that were refractory to medications. Placement of a vagal nerve stimulator at age 21 years did not improve seizure frequency. On examination at age 22 years of age, Montreal Cognitive Assessment (score 18/30) revealed impaired executive function, spatial construction, memory, and attention. He had mild proximal upper and lower limb weakness, prominent facial myoclonus, and myoclonus in both arms that worsened with action. Tendon reflexes were reduced in the arms, normal in the legs, and plantar reflexes were flexor. Gait was wide-based and unsteady. Between age 22 and 24 years, he had daily myoclonic and absence seizures and tonic-clonic seizures every 6 months. Despite mild cognitive impairment, he was able to complete college level courses online. At age 24 years, he required a wheelchair and 24-h support for activities of daily living. From age 25 to 26 years, he had multiple hospitalizations for aspiration pneumonia. He died at age 26 years due to respiratory failure. Sanger sequencing of *ASAH1* identified the splicing variants c.125+1G>A and c.456A>C (Table 3.1).

Table 3.1: Clinical characteristics of 6 patients with molecularly confirmed SMA-PME

ID	Sex	Onset age (yrs)	Initial symptom	Weakness onset age (yrs)	Seizure onset age (yrs)	Seizure types	EEG findings	Other features	Age at Last follow -up	*ASAH1* genotype [NM_177924.5]
1	F	7	Learning difficulties	10	9	GTC, myoclonic	Diffuse background slowing; 2.5-3 Hz focal spikes with maximum amplitude posteriorly, bursts of generalized spike-slow wave (age 16)	myoclonus , dystonia	21 years	c.124A>G (p.Thr42Ala), c.536C>T (p.Thr179Ile)
2	M	5	SNHL	12	15	GTC, absence, myoclonic	Frontal predominant, generalized spike and polyspike -wave discharges in runs of up to 15 seconds (age 21)	Myoclonus , cognitive decline, anxiety	Died at age 26 years	c.125+1G>A, c.456A>C
3	F	2	weakness	2	6	Atonic, myoclonic, absence	Abundant generalized 3-4 Hz spike and wave discharges in runs of up to 8 seconds during wakefulness, improving in sleep (age 10)	myoclonus	11 years	c.125C>T (p.Thr42Met)
4	M	3	Speech delay, SNHL	15	10	GTC, myoclonic	Generalized epileptiform activity with occipital predominance	Cognitive decline, hallucinati ons	Died at age 19 years	c.456A>C, c.918-2A>G
5	F	3	seizures	4	3	Atonic, myoclonic	Generalized complexes of spike and wave with frontal-central predominance. Rhythmic spike activity located in central region related with episodes of behavioral arrest with fear and scream	tongue fasciculati on, moderate SNHL	10 years	c.109C>A (p.Pro37Thr), c.410_411del (p.Tyr137Ter)
6	F	13	seizures	None reported	13	Myoclonic	Multiple episodes of epileptic myoclonus	Myoclonus , SNHL detected on audiology (asympto matic)	14 years	c.186G>A (p.Trp62Ter), c.456A>C

GTC: generalized tonic-clonic; SNHL: sensorineural hearing loss

Patient 3 is an 11-year-old female with a background history of sickle cell disease who presented at age 5 years with early-onset, progressive weakness. A maternal half-brother had died at age 9 years, with a diagnosis of a "spinal muscular atrophy-like illness" associated with seizures that had manifested initially with weakness at 2.5 years of age. Her first reported symptom, at age 2 years, was muscle weakness that caused falls and difficulty climbing stairs (Table 3.1). Neurological examination at age 5 years revealed age-appropriate speech and cognitive function. She had tongue fasciculations and limb-girdle weakness with milder distal limb weakness. Tendon reflexes were normal in the arms and brisk in the legs with bilateral ankle clonus. She had a waddling gait, and Gowers' sign was present. At age 6 years she developed myoclonic seizures characterized by brief head drops. By age 10 years progressive weakness led to impaired head control, inability to lift her arms above shoulder-height, and loss of independent ambulation. At age 10-11 years her seizures worsened; she developed frequent seizures with altered responsiveness, refractory to multiple medications (levetiracetam, valproic acid, lacosamide, perampanel) and regression of cognitive function. A gastrostomy tube was inserted at age 11 years and initiation of the ketogenic diet led to subsequent improvement in seizure frequency and duration, although multiple daily myoclonic seizures persisted. Exome sequencing at age 5 years identified a homozygous pathogenic variant in *ASAH1*; c.125C>T (p.Thr42Met) (Table 3.1).

Patient 4 was a 19-year-old male, briefly reported by Courage et al[166], who first presented at 3-4 years of age with speech delay (Table 3.1). He was found to have mild to moderate high frequency bilateral sensorineural hearing loss. Otherwise, his perinatal and early childhood medical and developmental history were normal. There were no significant concerns about his cognition though parents reflected post-diagnosis that he had lost some specific skills during childhood (for example, the ability to read the hands of a clock). At age 10 years, he presented with "muscle twitching" and was initially diagnosed with a tic disorder. The abnormal movements progressed in frequency (up to once every 30 s) and included head drops. An EEG at age 12 years demonstrated frequent generalized epileptiform activity

with an occipital emphasis, marked photosensitivity, and revealed the 'twitches' to be myoclonic jerks, leading to a diagnosis of progressive myoclonic epilepsy. He remained active in sports until age 15 years when leg weakness prevented athletic activities. Subsequent motor deterioration was rapid. He became fully wheelchair-dependent by age 16 years due to progressive proximal weakness and frequent falls, and developed recurrent tonic-clonic seizures at that age. Speech became slurred and, at age 18 years, he lost the ability to speak, coincident with onset of hallucinations and clear cognitive decline. Due to progressive weight loss and concerns for choking, and recurrent respiratory infections, a gastrostomy tube was inserted at age 18 and he required night-time non-invasive ventilation. His seizure burden became increasingly severe and he died at age 19 years due to status epilepticus. Exome sequencing identified the *ASAH1* variant, c.918-2A>G that is suspected to impact splicing, and the known splicing variant c.456A>C (Table 3.1).

Patient 5 is a 10-year-old female who first presented at age 3 years with frequent falls (Table 3.1). At age 4 years, episodes progressed to include head drops. EEG showed generalized spike-wave epileptic discharges with central-parietal predominance. Brain MRI was normal and a metabolic work up was non-diagnostic. At age 5.5 years, seizures occurred several times per day with tonic extension of upper limbs followed by a cry and expression of fear. On examination, she had tongue fasciculations, vertical downgaze palsy, distal myoclonus of the limbs, head tremor, lower limb hyperreflexia, and muscle weakness. A second brain MRI at age 6 years revealed generalized cerebral atrophy. At age 6.5 years she presented with myoclonic seizures and suspected lower motor neuron disease. Exome analysis revealed a paternally inherited heterozygous variant c.109C>A (p.Pro37Thr) in *ASAH1* (NM_177924.5) (Table 3.1). A second variant was not identified at that time. An EMG confirmed neuronopathy and enzyme activity of aCDase was significantly reduced in leukocytes (Table 3.2), confirming the diagnosis of SMA-PME. At last follow-up at age 10 years, she had significant muscle weakness, ptosis, and moderate sensorineuronal hearing loss. Her memory and cognition were preserved. She continued to experience

20-50 seizures per day with short myoclonic jerks, head drop, and episodes of behavioral arrest, refractory to multiple medications. Sequencing of *ASAH1* performed by the Care4Rare Canada Consortium subsequently identified a second, maternally inherited variant in *ASAH1*; c.410_411del (p.Tyr137Ter) (Table 3.1).

Patient 6 is a 14-year-old typically developing female who first presented at age 13 years with abnormal jerking movements of her legs and arms (Table 3.1; Table 3.3). Her prior medical history was unremarkable and she was initially diagnosed with tics by her primary physician. Neurologic examination demonstrated decreased muscle bulk and hyporeflexia in the upper extremities, and bursts of upper limb myoclonus. A brain MRI and nerve conduction study were both normal. An EEG demonstrated polyspike and wave discharges and multiple episodes of epileptic myoclonus, and she was diagnosed with juvenile myoclonic epilepsy. Treatment with levetiracetam was initiated, with a good response. An epilepsy next-generation sequencing panel revealed two pathogenic variants in *ASAH1*, c.186G>A (p.Trp62Ter) and the splicing variant c.456A>C, each inherited from an unaffected carrier parent (Table 3.1). EMG subsequently demonstrated chronic neurogenic changes of proximal and bulbar muscles. Audiology evaluation revealed sensorineural hearing loss, which was asymptomatic. Two of her three siblings have also inherited both pathogenic variants. At ages 13 and 11 years, both siblings are typically developing and asymptomatic, but did have evidence of high frequency hearing loss on audiology screening.

Clinical features of the 6 patients indicate a well-defined spectrum but broad phenotypic variability in terms of age at onset, individual symptom severity and outcome (Table 3.1; Table 3.3). Consistently observed features were: gradually progressive proximal limb weakness due to lower motor neuron involvement, myoclonic seizures, and persistent myoclonus that worsened with action and was typically most evident in the arms and hands. In all patients, symptom onset was in childhood-adolescence (age 2-13 years), but initial symptoms were variable with weakness (n=1), subtle cognitive dysfunction (n=1),

seizures (n=2), or sensorineural hearing loss (n=2). Loss of ambulation due to progressive weakness occurred during the second decade of life in 3 cases; two patients became unable to walk before age 10 years, and another had seizures only. Cognitive decline became apparent during the course of the disease for patients 1-4. Cervical and foot dystonia, not previously reported as manifestations of SMA-PME[161], were uniquely observed in patient 1.

Five of the six patients had previously reported pathogenic variants (Table 3.4)[116, 146, 148-161]. Patient 3 was homozygous for the most frequent SMA-PME variant, c.125C>T (p.Thr42Met). Alterations at the same codon at c.124A>G (p.Thr42Ala) and the adjacent nucleotide c.125+1 in Patients 1 and 2, respectively, suggest that this is an important locus for SMA-PME. Another recurrent variant, c.456A>C, was observed in Patients 2, 4, and 6. The splice variant within intron 11, c.918-2A>G, was previously reported in Patient 4, and in a patient with a mixed presentation of SMA and Farber disease[166, 173]. The c.410_411del (p.Tyr137Ter) variant in Patient 5 was previously reported in a patient with SMA without epilepsy who later developed systemic features of FD[159]. Two entirely novel variants were identified: *ASAH1*: c.109C>A (p.Pro37Thr) (in Patient 5), and *ASAH1*: c.186G>A (p.Trp62Ter) (in Patient 6) (Table 3.1).

Table 3.2: Acid ceramidase activity in leukocytes (nmol/mg/hour)

	Unrelated control	Patient	Mother	Father	Patient % of parent(s)	Patient % of control
Family 1		0.117	1.846	1.466	7.1	-
Family 2	-	0.110	1.551	1.331	7.6	-
Family 3	3.380	0.162	1.238	-	13.1	4.8
Family 5		0.225	4.919	6.039	4.1	

Table 3.3: Characteristics of patients with SMA-PME due to biallelic variation at *ASAH1*

Pt. no.*	Sex	Age of onset (yrs)	Reported first symptom	Weakness onset (yrs)	Seizure onset (yrs)	Seizure types	Other features	Age at death (yrs)	*ASAH1* variants [NM_177924.3]	Reference
7	F	3-5	weakness, falls	3-5	7	myoclonic	hand tremor	11	c.125C>T / c.125C>T	Zhou *et al*., 2012
8	F	3-5	weakness, falls	3-5	7	myoclonic	tremors	17	c.125C>T / c.125C>T	
9	M	3-5	weakness, falls	3-5	7	myoclonic	tremors	17	c.125C>T / c.125C>T	
10	F	4	weakness	4	12	absence, myoclonic, generalized	myoclonus, dysphagia	alive at 17	c.125C>T / c.125C>T	
11	F	5	weakness	5	12	absence, myoclonic, generalized	myoclonus, dysphagia	alive at 17	c.125C>T / c.125C>T	
12	F	5	weakness	5	10	absence, myoclonic	myoclonus	alive at 15	c.125C>T / gene deletion	
13	F	10	seizures, myoclonus	16	10	absence, atonic, GTC	myoclonus, sensorineural hearing loss, tremor	17	c.850G>T / c.456A>C	Dyment *et al*., 2014
14	F	3	weakness	3	7	absence, myoclonic, head drops	myoclonus, tremor	alive at 13	c.125C>T / c.125C>T	Giraldez *et al.,* 2015
15	F	6	slow gait, weakness	6	8	absence, myoclonic	myoclonus, postural tremor, ataxia, mild cognitive impairment	19	c.125C>T / c.125C>T	Rubboli *et al.,* 2015
16	F	2	weakness, clumsy gait	2	3	absence, myoclonic	myoclonus, nystagmus, involuntary movements, cognitive impairment	alive at 7	c.125C>T / c.223insC	
17	F	3	weakness	3	8	absence, myoclonic	myoclonus, resting tremor, nasal speech, dysphagia	alive at 14	c.177C>G / c.456A>C	
18	M	10	action tremor	>10	13	absence, myoclonic, atonic, GTC	myoclonus, sensorineural hearing loss	alive at 25	c.456A>C / c.886C>T	Gan *et al.,* 2015

Pt. no.*	Sex	Age of onset (yrs)	Reported first symptom	Weakness onset (yrs)	Seizure onset (yrs)	Seizure types	Other features	Age at death (yrs)	*ASAH1* variants [NM_177924.3]	Reference
19	F	4	weakness	4	6	myoclonic, head drop, generalized	eyelid myoclonia	alive at 11	c.125C>T / c.125C>T	Oguz Akarsu et al., 2016
20	F	3	weakness	3	-	-	postural tremor, myalgias, scoliosis	alive at 30	c.124A>G / c.124A>G	Filosto *et al.,* 2016
21	F	7	weakness	7	-	-	scoliosis	alive at 17	c.124A>G / c.124A>G	
22	M	3	weakness	3	not reported	myoclonic	facial tremor, myoclonus, sensorineural hearing loss	alive "late teens"	c.410A>G / c.456A>C	Kernohan *et al.,* 2017
23	F	10	weakness	10	11.5	myoclonic, tonic-clonic	action tremor, ataxia, cognitive impairment	alive at 13.5	c.125C>T / c.125C>T	Yildiz *et al.,* 2018
24	F	5	resting tremor	10	7	absence, myoclonic, atonic, GTC	weakness	alive at 13	c.125C>T / c.125C>T	Shervin Badv *et al.,* 2019
25	F	8	slow gait	14	-	-	weakness, postural tremor	alive at 24	c.77C>G / c.125+1G>A	Ame van der Beek, *et al.,* 2019
26	F	5	headaches, myoclonic seizures with head drops	5-9	5	myoclonic, atonic	weakness, dysphagia, cognitive impairment, bilateral optic atrophy, ataxia	alive at 11	c.1157G>A / c.1157G>A	Mahmoud *et al.,* 2020
27	F	10 mo	weakness	10 mo	not reported	myoclonic	not reported	alive at 3	c.1078A>G / c.1078A>G	
28	F	15 mo	weakness	15 mo	not reported	myoclonic	not reported	alive at 1.5	c.1078A>G / c.1078A>G	
29	M	neonate	weakness	neonate	no clinical seizures	na	GDD, subcutaneous nodules of interphalangeal joints. Developed contractures throughout. Scoliosis	13	c.458_459del / c.1226T>C and c.35G>C	Axente *et al.,* 2021

Pt. no.*	Sex	Age of onset (yrs)	Reported first symptom	Weakness onset (yrs)	Seizure onset (yrs)	Seizure types	Other features	Age at death (yrs)	*ASAH1* variants [NM_177924.3]	Reference
30	F	childhood	weakness	childhood	none	na	hoarse voice, ptosis, tongue atrophy, arthralgias, alopecia, lipid pneumonia	alive >45 years	c.124A>G / c.413A>T	Puma *et al.,* 2021

*Patients 1-6 are presented in Table 1

3.6.2 Literature review and phenotype:genotype correlations

We analyzed these genotypes and natural histories together with the 24 cases of SMA-PME previously reported in the literature from 19 families[116, 146, 148-159] (Table 3.3, Table 3.4). While the overall number of reported patients are few, there is some evidence of a genotype:phenotype correlation for specific recurrent variants that have been observed in at least 3 families (Table 3.4). Patients who were homozygous for the most common variant, c.125C>T (p.Thr42Met) (n=11, including Patient 3 in the current report), typically developed weakness in the first decade of life as the initial symptom, with one exception of a patient whose initial symptom was tremor (Table 3.3, Table 3.4). The splicing variant c.456A>C was associated with sensorineural hearing loss in 6 of 7 patients with this variant, including 3 of the patients in this series. It was the initial symptom in Patients 2 and 4, and was detected after diagnosis on audiology assessment in Patient 6. Initial symptoms were variable in this group (Table 3.4). A recurrent c.124A>G (p.Thr42Ala) variant was detected in four patients, three of whom did not develop seizures at all by ages 17, 30, and 45 years respectively (Table 3.3, Table 34). Reported clinical features in the fourth group without any recurrent variant (Table 3.4) were variable, with myoclonus or tremor in only 50%, although the small numbers preclude statistical comparison.

Table 3.4: Clinical characteristics by *ASAH1* genotype

	Homozygous or compound heterozygous for most frequent variant, c.125C>T (p.Thr42Met)	Carriers of c.456A>C	Carriers of c.124A>G (p.Thr42Ala)	Remaining genotypes
Number of patients	13 (11 homozygous)	7	4 (2 homozygous)	6
Age of onset – mean (range)	4.8 y (2-10 y)	6.7 y (3-13 y)	5.7 y (3-7 y)	3.2 y (0.8-8 y)
Initial symptom				
Weakness	Y (12/13)	Y (2/7)	Y (3/4)	Y (4/6)
Seizures	N	Y (2/7)	N	Y (2/6)
Myoclonus	Y (1/13)	Y (3/7)	N	Y (1/6)
Sensorineural hearing loss	N	Y (2/7)	N	N
Learning/developmental difficulties	N	Y (1/7)	Y (1/4)	N
Clinical features during disease course				
Weakness	Y (13/13)	Y (6/7)	Y (4/4)	Y (6/6)
Time from weakness onset to loss of ambulation	9.8 y (6-13 y; n=6)	9.8 y (1-15 y; n=4)	4 y (n=1) 3 patients remained ambulatory into adulthood	9 y (n=1)
Seizures	Y (13/13)	Y (7/7)	Y (1/4)	Y (5/6)
Onset age for seizures	8 y (3-12 y; n=13)	11.5 y (8-15 y; n=6)	9 y (n=1)	4 y (3 and 5 y; n=2)
Myoclonus	Y (13/13)	Y (7/7)	Y (2/4)	Y (3/6)
Hearing loss	NR (0/13)	Y (6/7)	NR (0/4)	Y (1/6)
Age at death	16.5 y (13-19 y; n=4)	20.7 y (17-26 y; n=3)	None have died	None have died
Mixed (FD) clinical course	N	N	Y (n=1)	Y (n=1)

Y = yes, N = No, NR = not reported

3.6.3 hAC processing, activity, and function

Human aCDase enzyme levels were assessed by immunoblotting of lysates extracted from fibroblasts derived from Patients 1, 2, and 4. In all three patients, levels of the β subunit (40 kDa) were reduced and levels of the α subunit were barely detectable compared to unrelated age and sex-matched controls (Figure 3.1). Cellular aCDase activity was assessed in leukocytes from Patients 1, 2, 3, and 5. Activity ranged from 4.1% to 13.1% compared to either unaffected carrier parents or unrelated controls (Table 3.2). aCDase function was further assessed in fibroblasts from Patients 1, 2, 4, and 5 by directly quantifying cellular ceramide content by HPLC-ESI-MS/MS. Total cellular ceramide content was significantly elevated in each patient confirming loss of aCDase function and thus pathogenicity of the *ASAH1* variants (Figure 3.2 A-D, left panel). In total, 18 different ceramide species with a d18:1 sphingosine backbone were detected. Abundances of 11 species were significantly elevated in patient 1 (Figure 3.2 A, right panel). All species were significantly elevated in patients 2, 4, and 5 regardless of N-acyl chain length or degree of unsaturation (Figure 3.2B-D, right panel).

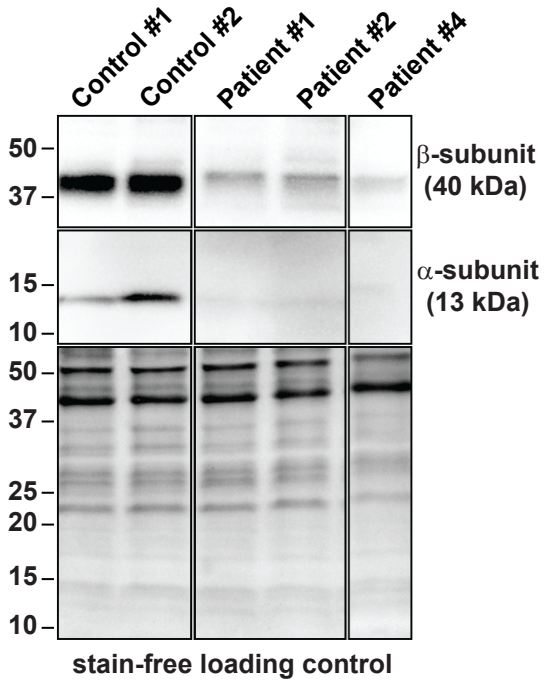

Figure 3.1. Assessment of aCDase enzyme processing by immunoblotting. Levels of the acid ceramidase α- and β-subunit are reduced compared to controls in Patient #1, #2, and #4. Loading controls are stain-free signal of total protein assessed using the PROTEAN TGX Stain-Free system.

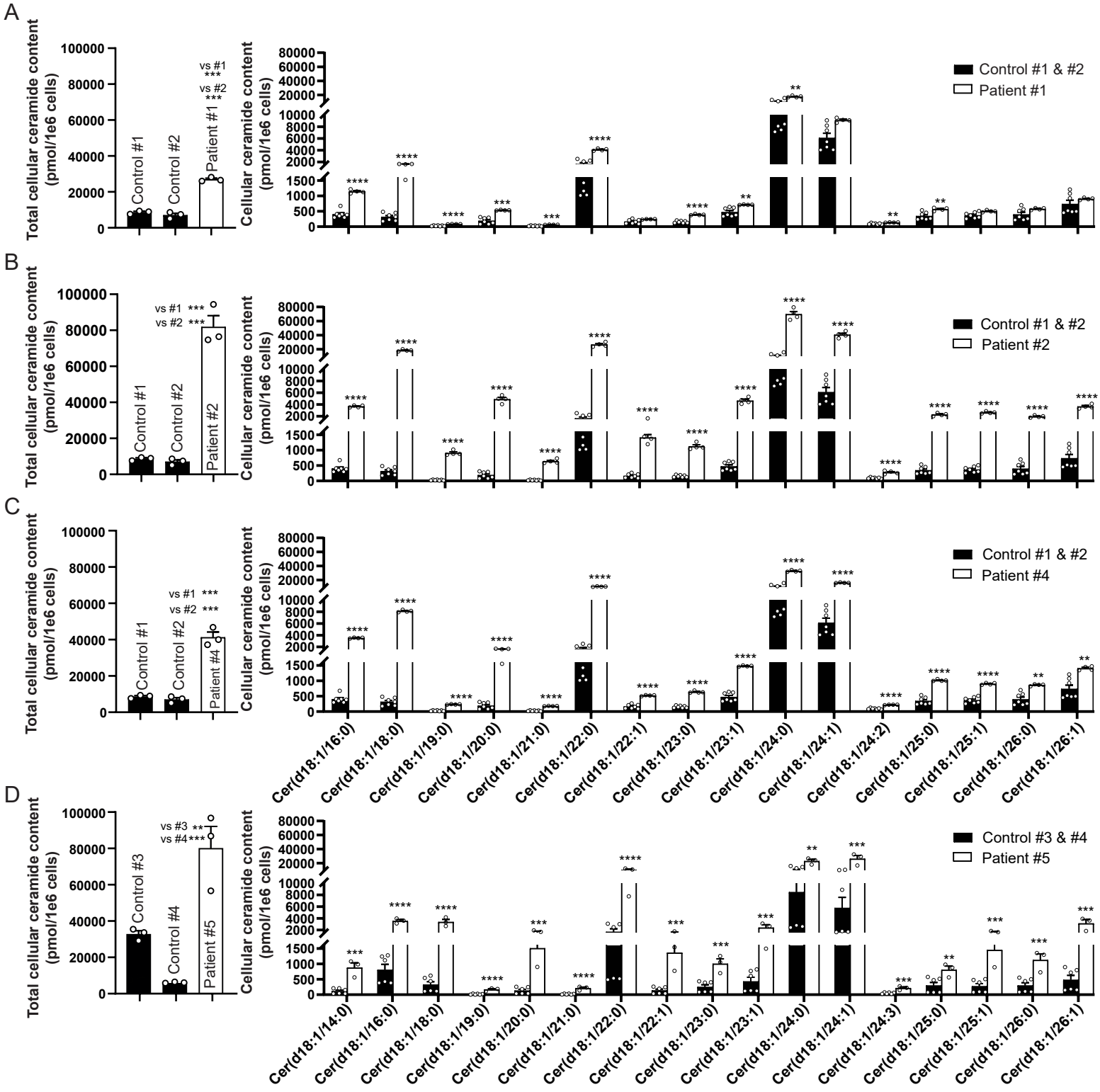

Figure 3.2. Molecular profiling by LC-ESI-MS/MS of fibroblast ceramides. Levels of the individual profiled ceramide species in controls and in (A) Patient #1, (B) Patient #2, (C) Patient #4, and (D) Patient #5. Data represent mean abundance (pmol/1E6 cells) ± SEM. In control cultures, data represent n=3-4 cultures from two different control (wild-type) biopsies. In patient cultures, data are n=4 cultures from the same patient. Statistics are multiple unpaired t-tests with Welch t-test correction and false detection rate of 1% according to Benjamini, Krieger, and Yeukuteli[134]. **q<0.01.

3.6.4 Rescue of the cellular phenotype by rhAC

To assess whether enzyme replacement therapy could normalize cellular ceramide levels in SMA-PME cells, dermal fibroblasts cultures from Patients 1, 2, and 4 were treated for 0, 24, 48 h with wild-type rhAC (10 µg/mL) (Figure 3.3). Administration of rhAC significantly reduced total ceramide abundance (Figure 3.3a). Assessment of the rate of change in activity indicated that 58 h of treatment would be required to completely correct ceramide levels *in vitro* (Figure 3.3b).

3.7 Discussion

SMA-PME remains an ultra-rare condition that now encompasses 30 reported patients with molecularly confirmed variation in *ASAH1*. Our series of 6 patients from different families, examined in the context of the 24 previously reported patients, illustrate the significant variability of symptom onset and progression of SMA-PME. Initial symptoms include weakness due to motor neuron disease, seizures, or myoclonus. These features, which may vary in the order of onset, constitute the core clinical features of this condition. The small-amplitude, twitchy movements of cortical myoclonus may mimic tremor, especially in the hands. This may explain the description of tremor in several previously reported cases (Table 3.3). In addition, sensorineural hearing loss was the presenting symptom in two of our patients, who both carried the c.456A>C variant.

The disease course of our 6 patients illustrate the clinical spectrum of this disorder, from which certain patterns of genotype:phenotype correlation emerge (Table 3.3, Table 3.4). First, individuals who are homozygous for the common recurrent c.125C>T variant characteristically present with proximal limb weakness during early childhood (between ages 2 and 6 years in all but one patient), followed within a few years by the development of seizures, and progressive motor and cognitive functional decline thereafter. The time from symptom onset to loss of the ability to walk ranged from 6 to 13 years in those

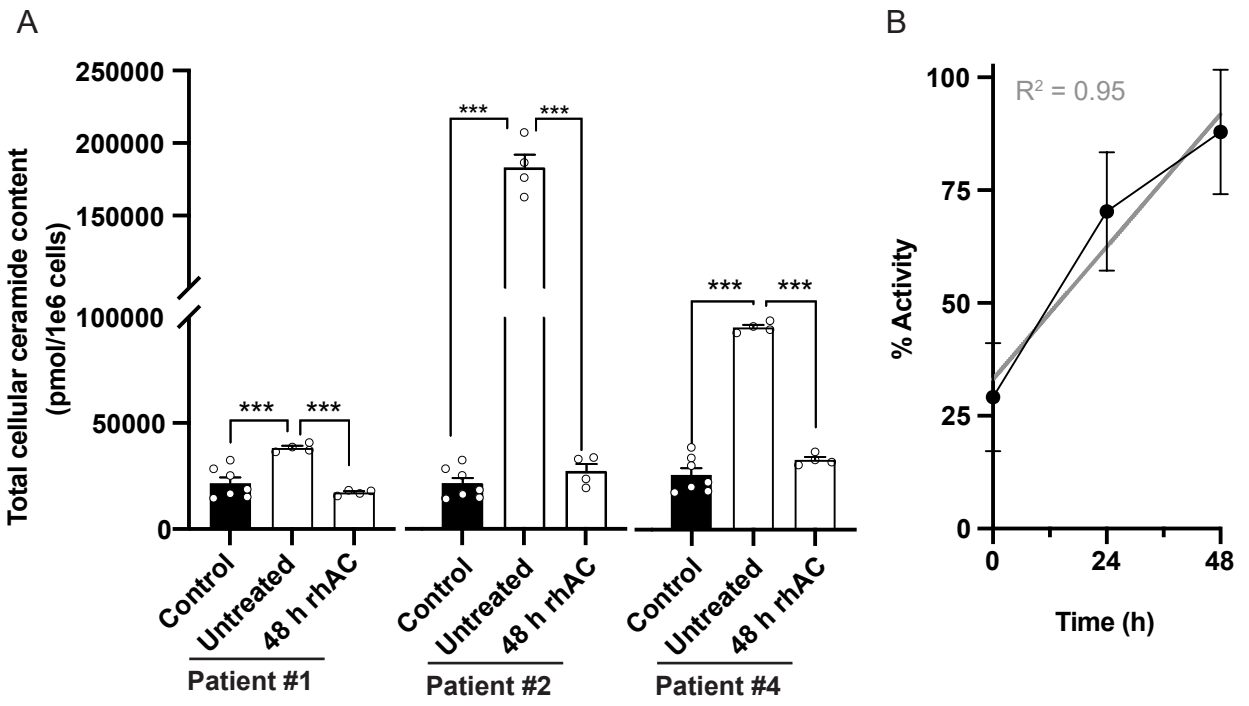

Figure 3.3. Loss of *ASAH1* function in fibroblasts of patient#1, #2, and #4 can be rescued by treatment with rhAC. (A) Total ceramide levels, quantified by LC-ESI-MS/MS, are significantly increased in fibroblast cultures of SMA-PME patients relative to control (wild-type *ASAH1*). Treatment for 48 h with wild-type rhAC (10 μg/mL) normalizes ceramide levels. Levels in all rhAC-treated cultures were comparable to control levels and significantly lower than in untreated cultures. Data represents mean ± SEM. In control cultures, data represent n = 3-4 replicate cultures from four different control (wild-type) biopsies. Note the controls compared to patient #1 and patient #2 are fibroblast cultures from a 26-year old male and a 9-year old female; controls compared to patient #4 were fibroblasts from a 6 year old male and a 7 year old male. In patient cultures, n = 4 replicate cultures from the same patient. Statistics are one-way ANOVA. *** $p < 0.001$, post-hoc Holm-Šidák correction for multiple comparisons. (B) The time required to correct ceramide levels in patient fibroblasts was determined by establishing the rate of change in percent activity at 0, 24, and 48 h following treatment with rhAC relative to all controls and performing linear regression. 58 h of treatment with 10 μg/ml rhAC would be required to normalize fully ceramide content *in vitro*.

reported, and the age of death was typically in the teen years. However, it should be emphasized that some individuals continued to walk independently and survived into their late teens and early 20s. Second, the recurrent heterozygous c.456A>C variant was associated with sensorineural hearing loss in 6 of 7 reported patients (3 in this series and 3 in the literature)[116, 150, 153, 166]. Hearing loss was the first symptom in 2 of our patients, presenting years before the onset of either seizures or weakness. The hearing of the last patient with this variant was not described in the report describing their symptoms[149]. Five of these seven patients experienced a later onset of seizures and weakness than patients homozygous for *ASAH1*, c.125C>T, p.Thr42Met, manifesting during the second decade of life. Further study will be required for definitive conclusions regarding any genotype:phenotype correlation.

There are only 6 published patients who do not carry at least one copy of the recurrent variants, and they show a higher degree of symptom variability than those with the recurrent variants (Table 3.3). For example, 2 siblings homozygous for c.1078A>G experienced onset of weakness at age 10 months[157], which is the youngest age of onset reported. Another patient without a recurrent variant carries a homozygous change at c.1157G>A[157]. This patient had optic atrophy, not previously associated with SMA-PME, in addition to weakness and seizures. Lastly, Patient 5 in the current series with a substitution at c.109C>A, p.Pro37Thr and a small deletion at c.410_411del, p.Tyr137Ter had an extremely early onset of intractable seizures at age 3 years that occurred prior to onset of weakness.

When we review the *genotypes* of the 24 reported cases and the current 6 cases, it becomes apparent that 20/30 (66%) carry at least one copy of the recurrent variants c.125C>T, p.Thr42Met, and c.124A>G, p.Thr42Ala or the immediately adjacent c.125+1 (thought to impact the splice at the exon 2 boundary[168]). When the other recurrent variant is considered (c.456A>C), 25/30 (83%) carry at least one of the variants at these two loci. The c.456A>C variant does not induce a p.Lys152Asn substitution, but rather alters exon splicing[116]. The other 3 variants located near exon/intron boundaries (c.125C>T, p.Thr42Ala, c.124A>G, p.Thr42Met and c.125+1) have not been assessed for their impact on splicing in lymphocytes,

and detection programs provide mixed results. Ceramidase activity has been reported for some, but not all, of the 24 cases in the literature[116, 146, 150, 152, 155, 156] and the activity was highly variable from 4.7% to 32% of controls. The enzyme activity of the four cases reported here (4.1-13.1%) was consistent with previous reports.

aCDase deficiency may present with isolated neurologic features (SMA-PME, predominant PME alone[116], SMA alone[152, 156]), isolated systemic features (forms of FD[160], progressive osteolysis[164], familial keloid scars[174]), or a combination[160]. The development of systemic symptoms in adulthood following childhood-onset SMA has been reported[158]. The pathophysiological mechanisms that underlie this phenotypic variability are not yet understood. Residual aCDase activity, while overall reduced in the *ASAH1* disease spectrum, does not correlate, entirely, with either SMA-PME or FD. Pathogenic variants in the α- and β- subunit of this enzyme also appear to occur in both disorders so an obvious effect of the protein subunit is not apparent. There are recurrent variants observed in Farber disease alone (c.998G>A, c.505T>C) as well as the previously mentioned recurrent variants in SMA-PME (c.125C>T, c.124A>G, c.456A>C). Importantly, the only published variants shared in both disorders are c.918-2A>G and c.410_411del, each observed in one patient in this series (Patients 4, and 5, respectively) and in one other individual with a mixed presentation of SMA and FD[159, 173]. This highlights the potential importance of the patients' genotype in predicting the clinical manifestations and disease course. Increasing knowledge on the biology of aCDase, particularly its catalytic mechanism and the importance of specific amino acid residues for its activation and function, should lead to improved understanding of how the dysfunction can result in such disparate presentations. The use of mass spectrometry to characterize the metabolomic signature in patients is a key means of understanding how phenotypes may be similar or differ from one another in a predictive fashion.

Management of SMA-PME is supportive and multidisciplinary with no curative treatments available. Alayoubi et al. generated a mouse model of systemic aCDase deficiency, and it has been shown that

aCDase enzyme replacement (either by direct injection or gene therapy with a lentivirus vector) leads to reduced cellular infiltrations, reduced ceramide in target tissues, and increased lifespans for Farber mice[172, 175]. Hematopoietic stem cell transplant has resulted in a resolution of the peripheral symptoms in some Farber patients, which is also a promising indication of the potential of enzyme replacement in human patients, but there does not appear to be an effect on CNS symptoms[176].

Our study is the first preclinical study to demonstrate the effects of recombinant enzyme replacement (currently in development as ACG-801) in cells from patients with an SMA-PME phenotype resulting from acid ceramidase deficiency, including demonstration that the ceramide accumulation in cultured fibroblasts can be rescued by treatment with rhAC. This has been performed with success in a mouse model of Farber disease[172]. Our work represents a preliminary study that requires replication and further preclinical study but does point to restoration of homeostasis by administration of wild-type enzyme over time. It is reasonable to expect that delivery of rhAC into the central nervous system will be required to be effective as a treatment for neurologic manifestations of aCDase deficiency although this will represent a significant obstacle to overcome given the enzyme's inability to cross the blood-brain barrier. The therapeutic window of opportunity to halt or even potentially reverse clinical progression in SMA-PME also remains to be determined.

Chapter 4 : Sphingolipid network and metabolic enzyme alterations are sufficient to distinguish Farber's Lipogranulomatosis from Spinal Muscular Atrophy with Progressive Myoclonic Epilepsy

Graeme SV McDowell[1], Mark Akins[1], Hongbin Xu[1], Irina Alecu[1], Yun Wang[1], Samantha Sherman[1], Sneha Gupta[1], Thao Nguyen-Tran[1,2], Wendy Mears[3], Muriel Mari[4,5], Samuel F. Berkovic[6], Maria Spanou[7], Argirios Dinopoulos[7], Jodi Warman-Chardon[8,9], Edward H. Schuchman[10], Toni S. Pearson[11,12], Fulvio M. Reggiori[4,5], Alexander Solyom[13], David A. Dyment*[3], and Steffany AL Bennett*[1,2]

[1]Neural Regeneration Laboratory, Ottawa Institute of Systems Biology, uOttawa Brain and Mind Research Centre, Department of Biochemistry, Microbiology, and Immunology, University of Ottawa, Ottawa, ON, Canada; [2]Department of Chemistry and Biomolecular Sciences, Centre for Catalysis Research and Innovation, University of Ottawa, Ottawa, ON, Canada; [3]Department of Genetics, Children's Hospital of Eastern Ontario Research Institute, University of Ottawa, Ottawa, ON, Canada; [4]Department of Biomedical Sciences of Cells and Systems, University of Groningen, University Medical Center Groningen, Groningen, The Netherlands; [5]Department of Biomedicine, Aarhus University, Aarhus, Denmark; [6]Epilepsy Research Center, Department of Medicine, University of Melbourne, Heidelberg, Victoria, Australia; [7]Pediatric Neurology Division, 3rd department of Pediatrics, Attikon University Hospital, Athens, Greece; [8]Department of Medicine (Neurology), Ottawa Hospital Research Institute, Ottawa, Ontario, Canada; [9]Children's Hospital of Eastern Ontario Research Institute, Ottawa, Ontario, Canada; [10]Department of Genetics and Genomic Sciences, Ichan School of Medicine at Mount Sinai, New York, NY, USA; [11]Department of Neurology, Washington University School of Medicine, St. Louis, Missouri, USA; [12]Departments of Neurology and Pediatrics, Columbia University Irving Medical Center, New York, New York, USA; [13]Aceragen, Basel, Switzerland.

* Joint corresponding authors: ddyment@cheo.on.ca (DAD); sbennet@uottawa.ca (SALB)

4.1 Objective of study

Having assessed the natural history of SMA-PME and identified relationships between genotype and the clinical presentation of SMA-PME, I investigated whether there were any metabolic differences that distinguished FL from SMA-PME. This work and that of Chapter 5 are being combined with studies performed by my lab colleagues using IPSC-derived neurons derived from these fibroblast lines and additional bioinformatic analyses prior to submission for publication. Only studies I was directly involved in are included in this thesis.

4.2 Author Contributions

GSVM, DAD, and SALB conceived and designed the experiments and analyzed all data. Reagents, materials, and/or tools were provided by AS and WM. Cohorts, samples, and clinical history were provided by SFB, MS, AD, JW-D, EHS, TSP, AD, and DAD. LC-ESI-MS/MS was performed by GSVM, HX, SS, TN-T, YW, and IA. Cell culture experiments were performed by GSVM and MA with SG. Electron microscopy was performed by MM and FMR with cell lines cultured and provided by GSVM.

4.3 Abstract

The objective of this study was to determine and define the metabolic signatures that differentiated SMA-PME from Farber Lipogranulomatosis (FL), caused by mutations in the same gene *ASAH1*. Sphingolipid metabolic profiles of fibroblasts collected from seven SMA-PME patients, three FL patients, and seven age and sex-matched controls were determined via high-performance liquid chromatography electrospray ionization tandem mass spectrometry. Both the FL and the SMA-PME patients showed characteristic accumulation of ceramides (Cers) and cerebrosides (HexCers), however examining sphingolipid species beyond Cers and HexCers revealed a unique metabolic fingerprint that

associated with disease phenotype. Performing metabolic pathway analysis and measuring levels of other sphingolipid metabolic enzymes revealed a hypometabolic response in FL, whereas SMA-PME displayed hypermetabolic responses. Further, using immunofluorescence and electron microscopy, these metabolic changes were shown to alter the subcellular accumulation of Cer. We found that Cer accumulated in the lysosome of FL cells and in vesicles fused to the plasma membrane in SMA-PME cells. Together, this study identifies metabolic differences between FL and SMA-PME that associate with disease presentation.

4.4 Introduction

Spinal Muscular Atrophy with Progressive Myoclonic Epilepsy (SMA-PME; OMIM 159950)[177] and Farber Lipogranulomatosis (FL; OMIM 228000)[178] are rare, autosomal-recessive childhood disorders, caused by pathogenic variations in the N-acylsphingosine amidohydrolase gene (*ASAH1*, MIM: 613468, GeneBank: NM_177924.5)[179, 180]. *ASAH1* encodes for acid ceramidase (aCDase, EC 3.5.1.23), one of five ceramidases capable of hydrolyzing ceramides (Cers) to a free fatty acid and a long chain sphingoid base (Figure 4.1)[181]. aCDase is unique in that it is the only family member that localizes to the lysosome and the only ceramidase that can hydrolyze both ceramides and cerebrosides (i.e., glucosylceramides and galactosylceramides, Figure 4.1)[44, 45, 182, 183].

Both SMA-PME and FL are aCDase deficiency disorders, yet clinical features are strikingly different. SMA-PME is an isolated neurological disorder presenting in late childhood/early adolescence after a symptom-free infancy[18, 162]. The first clinical symptom is often muscle weakness that progresses to immobility and respiratory insufficiency when muscles of breathing and swallowing are affected[18, 116, 145, 146, 153, 154, 177, 184]. Progressive myoclonic epilepsy develops either concurrently or shortly following the first clinical signs of motor neuron degeneration (typically at age 10-12 years)[162]. In addition to myoclonic epilepsy, absence and generalized tonic-clonic seizures are common. The seizures are

refractory to anti-epileptic treatments[162]. The disease lasts 5-10 years with tremor, hearing loss, and cognitive decline frequent co-morbidities. Individuals succumb to their refractory seizures or respiratory insufficiency in late adolescence to early adulthood (ages of 13-26 years)[18, 145, 146, 149, 154, 184]. By contrast, FL is an early onset disorder. Infants exhibit a triad of symptoms defined by subcutaneous nodules (lipogranulomas), arthritis and/or contractures, and vocal hoarseness secondary to laryngeal involvement[176, 178, 185]. The lipogranulomas consist of lipid-rich cells and tissue that localize to the joints of the phalanges, wrist, elbow, ankle, and over points of mechanical pressure resulting in joint deformation[176, 185]. Vocalization is affected when nodules spread to the larynx. Symptomatic infants have a weak cry and can develop dysphonia or aphonia over time[185]. Death occurs in early childhood as result of failure to thrive and nodule-mediated airway obstruction[176].

It is not known how aCDase deficiency can produce both isolated neurological (SMA-PME) or predominantly systemic (FL) symptoms with different age of onset. There is no clear association between enzymatic activity and disease features[18, 116, 146, 150, 153, 155, 156, 158, 160, 165, 173, 184, 186]. Cellular enzymatic activity ranges between 5-30% of wild-type in both SMA-PME and FL[18, 116, 146, 150, 153, 155, 156, 158, 160, 165, 173, 184, 186]. There are no reported *ASAH1* domains that show a clustering of variants discriminating SMA-PME or FL clinical phenotypes[160] although there is some evidence for genotype-phenotype relationships within a given disorder for specific symptoms[18]. While ultra-rare forms of FL have been reported with a slower progressive adult-onset disease[164], only two of these individuals exhibit the SMA-PME-like neurological symptoms of seizures, lower motor neuron disease, and hypotonia secondary to peripheral joint deformation[18, 166, 173]. There are two reported variants shared between SMA-PME and FL (c.918-2A > G and c.410_411del) but only one individual with these variants exhibits a mixed SMA-PME clinical presentation; the others exhibit either FL or SMA-PME features[18, 159, 173].

Given there is no clear genotype-phenotype association for SMA-PME and FL, we sought to identify the “metabolic modifiers” that are activated as a result of the loss of ASAH1 function that correlate with

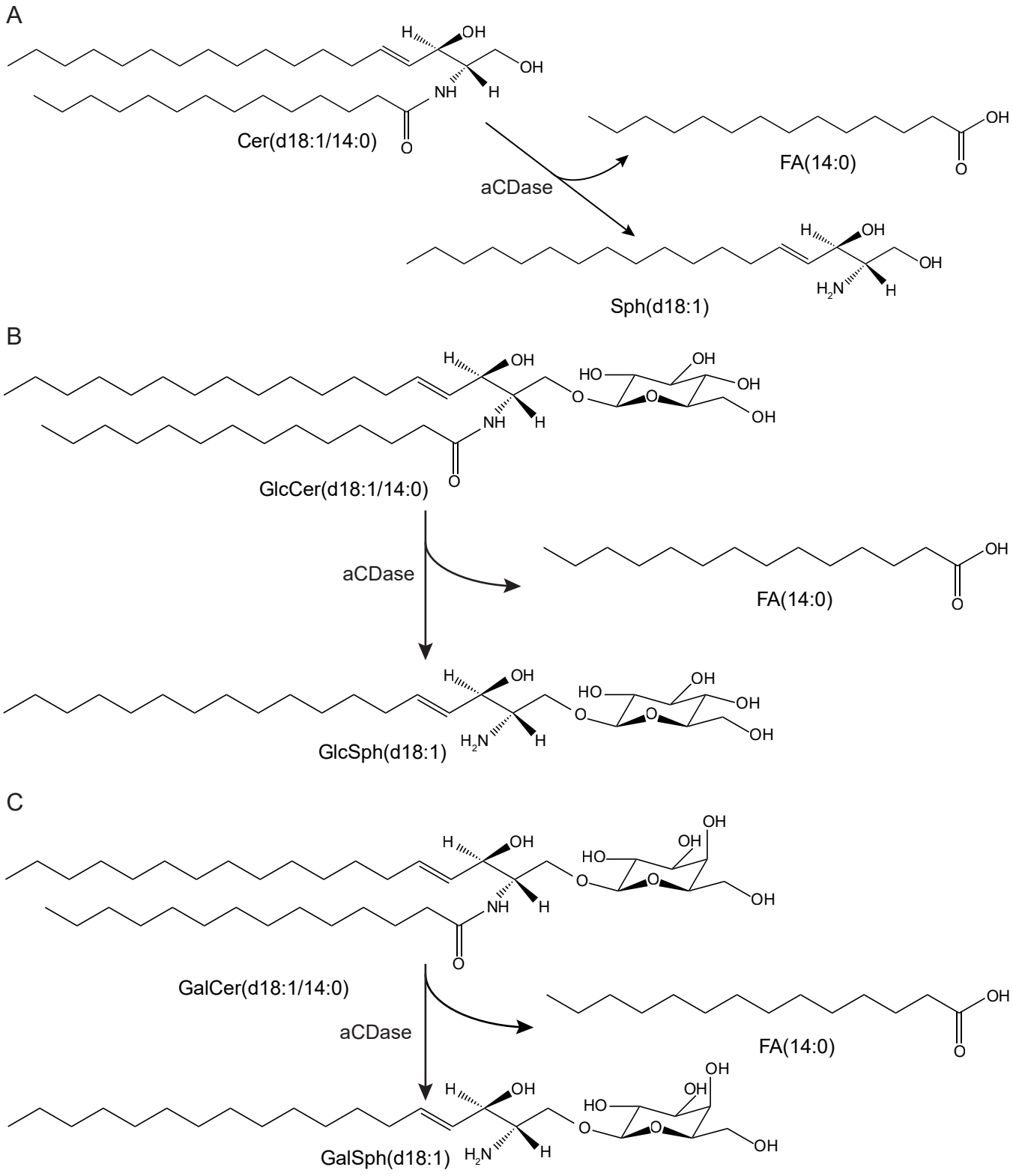

Figure 4.1: Acid Ceramidase Activity. aCDase hydrolyses A) Cers to Sph, B) GlcCers to GlcSph, and C) GalCers to GalSph by removing the N-acyl chain.

disease phenotype. We used unbiased lipidomic approaches to elucidate the changes in sphingolipid metabolism unique to each disorder *in vitro*. We show here that FL is a canonical lysosomal storage disorder wherein aCDase deficiency triggers a perfect storm of aberrant *hypo*metabolic compensatory changes in sphingolipid processing that work together to deplete sphingosine and resulting in the lysosomal accumulation of ceramides and cerebrosides. By contrast, we show here that SMA-PME is defined by compensatory *hyper*metabolic changes that elevate sphingosine and hexosylsphingosine and modulate ceramide and cerebroside levels leading to their accumulation not in the lysosome but at the plasma membrane. Together these data define new metabolic pathomechanisms that produce different cellular pathologies associated with the clinical presentation of SMA-PME and FL. This study identifies new metabolic targets for the potential treatment of SMA-PME and expands the concept of genetic modifiers to include metabolic modifiers that alter disease etiologies caused by the same genetic determinant.

4.5 Materials and Methods

4.5.1 Cell lines and exome sequencing

Primary dermal fibroblast lines were derived from punch biopsies from seven SMA-PME patients by informed consent from their families according to CHEO REB #11/04 E research ethic board approval. The natural history of these patients has been described in[18, 116, 153, 184]. FL (GM02314, GM02315, and GM05752) and seven fibroblast lines from apparently healthy controls (GM00038, GM05400, GM05757, GM00969, GM02912, GM03377, GM01651) were obtained from the Coriell Institute. *ASAH1* variants were confirmed by exome sequencing in each cell line as described previously[116]. Fibroblasts were maintained in Dulbecco's Modified Eagle's Medium/Ham's Nutrient Mixture 12 (D-MEM/F-12) (Gibco, cat# 12400-016) supplemented with 10% fetal bovine serum (Sigma Aldrich, cat# F0926), and 2 mM L-glutamine (Gibco, cat# 25030-081) at 37^{o}C in a 5% CO_2 environment.

4.5.2 Western immunoblotting

Protein collected from cells as previously described[187]. Briefly, confluent 10 cm^2 plates or 75 cm^2 flasks were washed with tcPBS and pelleted. Cell pellets were washed with tcPBS and resuspended in cold RIPA buffer (1% Nonidet P-40 (Sigma, cat# 74385-1L); 0.5% sodium desoxycholate (Fisher Scientific, cat# S285-100), 0.1% Sodium Dodecyl Sulfate (SDS, Invitrogen, cat# 15525-017) in extraction PBS (ePBS, 9.1 mM dibasic sodium phosphate, BioShop, cat# SPD307.1; 1.7 mM monobasic sodium phosphate, BioShop, cat# SPM 306; 150 mM sodium chloride, BioShop, cat# SOD001.10; ddH2O, pH 7.4); (v/w/w/v)) with protease inhibitors (1M NaF, Sigma, cat# S1504; 10 mg/ml PMSF, OmniPur, cat# 7110; 100 mM Na orthovanadate, Sigma, cat# S6508; and 10 mg/ml aprotinin, Sigma, cat# A6279). Cells were sheared using a syringe with a $26^{3/8}$ gauge needle (Becton Dickinson, cat# 309625), and protein was collected in Eppendorf tubes. Protein concentration was assayed using the Bio-Rad DC protein assay kit (BioRad, cat# 5000116). Where necessary, protein was concentrated using Amicon Ultra centrifugal filters (Millipore, cat# UFC501096).

Immunoblotting was performed as described previously[187], modified for use with Bio-Rad Mini-PROTEAN TGX Stain-Free Gels (BioRad, cat# 4568095). Briefly, cell protein extracts were diluted in 4x SDS sample buffer (225 µL 4x Laemmli Sample Buffer, Bio-Rad, cat# 161-0747; 25 µL ß-mercaptoethanol, Aldrich, cat# M6250-100ML; 0.002 g DTT, Sigma, cat# V3151; v/v/w), and boiled for 5 minutes, unless otherwise noted, to denature the protein, and incubated on ice until loaded onto gels. 30 µg of protein was loaded onto a 4-20% Bio-Rad Mini-PROTEAN TGX Stain-Free Gel (BioRad, cat# 4568095), and proteins were resolved under reducing/denaturing conditions. Proteins were then transferred onto Low Fluoro PVDF membrane (Bio-Rad, cat# 162-0264) at 100V for 60 min. Membranes were blocked in 5% skim milk powder (Carnation, cat# 5900011132) in 10 mM PBS (0.5M dibasic sodium phosphate; 0.5M monobasic sodium phosphate; 1.54M sodium chloride) (w/v) with 0.1% Tween-20 (Sigma, cat# P1379-500ML) (PBST; blocking buffer) for 1 hr at room temperature, and

incubated in primary antibody diluted in blocking buffer overnight at 4^{o}C (see Table 1 for antibody concentrations used). Membranes were rinsed twice in 0.1% PBST and twice in blocking buffer for 10 minutes prior to a one-hr incubation in horseradish peroxidase (HRP)-conjugated anti-mouse or anti-rabbit secondary antibody (see Table 1) diluted in blocking buffer. Blots were washed four times with 0.1% PBST, and signal was detected using a BioRad ChemiDoc XRS+ Imaging system with Image Lab software (BioRad, cat# 1708265) using Chemiluminescent substrate (Millipore, cat# WBKLS0500). Blots were stripped using a BME stripping buffer (100 mL 10% SDS stock, 62.5 mL 0.5M Tris HCl pH 6.8, 337.5 mL ddH20, 4 mL ß-mercaptoethanol, v/v/v/v), with a 30-minute incubation at 50^{o}C, washed five times with 0.1% PBST, and blocked in blocking buffer for an hour prior to incubation with primary antibodies.

Densitometry was performed in Fiji image analysis software[188]. Briefly, experimental blot and actin loading control blots were opened by Fiji, and a grey-scale standard curve was generated. Rectangular ROIs were selected to contain the maximum amount of the band of interest, while minimizing signal from nonspecific binding. Each lane in both the experimental and loading control lane were selected using the same size rectangular ROI, and the lane profile plots were collected. In the lane profiles, the background was removed for each lane analyzed, and the lane profile was bisected, and the area under the curve for one half of the lane was measured. The experimental band areas were normalized to the actin loading control signal and calculated as fold changes to CTRL.

Table 4.1: Antibodies, Concentrations, and Source

Epitope	Concentration	Host species	Source
Western Blotting			
ACER2	1/500	Rabbit	Aviva Systems Biology (ARP66122-P050)
Actin	1/2500	Mouse	Sigma (A4700)
ASAH1a	1/500	Rabbit	Gifted by Professor Sandhoff, Germany
ASAH1b	1/400	Rabbit	Sigma (HP005468)
ASAH2	1/1000	Rabbit	Abcam (ab113369)
CerS2	1/750	Rabbit	BethylLaboratories (A303-193A)
GBA1	1/2500	Rabbit	Sigma (G4171)
GCS	1/250	Rabbit	Abcam (ab98030)
Rb IgG-HRP	1/5000	Donkey	JacksonImmuno (711-035-152)
Mo IgG-HRP	1/2000	Goat	JacksonImmuno (115-035-146)
Immunofluorescence			
LAMP-1	1:100	Mouse	DSHB (H4A3-c)
Ceramide	1:500	Rabbit	Glycobiotech (MAB_0114)
Golgin-97	1:800	Mouse	Molecular Probes (A21270)
Mo IgM – Cy3	1:800	Donkey	JacksonImmuno
Mo IgG-Alexa 488	1:800	Goat	Life Technologies (A11001)
DRAQ5 stain	1:1000	N/A	Cell Signaling Technology (4084L)

4.5.3 HPLC-ESI-MS/MS Lipidomics

Fibroblasts were grown to confluency and extracted using a modified Bligh and Dyer protocol described previously[116, 125-127, 153, 189]. Briefly, cells were washed with tissue culture phosphate buffered saline (tcPBS, BioShop, cat# PBS404), counted, pelleted, and kept on ice until lipid extraction. Pellets were resuspended in 0.1 M Sodium Acetate (Sodium Acetate; Sigma, cat# S-2889, LC/MS grade water; J.T. Baker, cat# 9831-03), and transferred to a Kimble 10-ml glass threaded tube (VWR, cat# 21020-640) using a glass Pasteur pipette (Fisherbrand, Cat# 13-678-20C). Acidified methanol (2% acetic acid; Fisher, cat# A38-212, in methanol; Fisher, cat# BP1105 (v/v)) was added, along with 235 pmol of Cer(d18:1/16:0-D31) (Avanti Polar Lipids, cat# 868516), 470 pmol of GlcCer(d18:1/8:0) (Avanti Polar Lipids, cat# 860540) and 470 pmol of GalCer(d18:1/8:0) (Avanti Polar Lipids, cat# 860538) as internal standards. Lipids were extracted by addition of chloroform (Fisher, cat# C298) to a ratio of 1.6:2:1.9 Sodium acetate: acidified methanol: chloroform (v/v/v). The organic phase was collected, and the aqueous phase successively back-extracted using chloroform three times. The organic phases were collected and pooled. Samples were dried under a constant stream of nitrogen gas. Dried lipid extracts were re-dissolved in ethanol (Commercial Alcohols, cat# P016EAAN), and stored under nitrogen gas in amber glass vials (Chromatographic Specialties, cat# C779100AW) and kept at -80^{o}C.

Sphingolipid content was quantified as previously described[129]. Briefly, sphingolipids were quantified by HPLC-ESI-MS/MS using an Agilent 1290 Infinity II LC, equipped with a binary pump and autosampler, and a triple quadrupole-linear ion trap mass spectrometer QTRAP 5500, equipped with a Turbo V ion source (AB SCIEX, Concord, Canada). Samples were prepared for HPLC injection by diluting lipid extract with solvent A (LC/MS grade water with 0.1% formic acid (Fisher, cat# 56302) and 10 mM ammonium acetate (OmniPur, cat# 2145) and an external standard mixture containing 101.58 pmol of sphingomyelin standard SM(d18:1/18:1-d9) (Avanti Polar Lipids, cat# 791649) in ethanol. Reversed-phase HPLC separation was achieved on a 100 mm x 250 µm (i.d.) capillary column packed

with ReproSil-Pur 120 C8 beads (particle size of 3 µm and pore size of 120 Å, Dr. A. Maisch, Ammerbruch, Germany) with 5 µl sample injections by an autosampler maintained at 4°C with a flow rate of 10 µl/min. The binary solvent gradient consisted of solvent A, and solvent B (acetonitrile (J.T. Baker cat# 9829-03)/isopropanol (Fisher, cat# A416-4) (5:2; v/v) with 0.1% formic acid and 10 mM ammonium acetate). Gradient elution started with 30% solvent B, ramping to 100% solvent B over 5 minutes, and maintained for 30 minutes. After 30 minutes at 100% solvent B, the gradient dropped to 30% solvent B over the course of a minute, where it remained for the remaining 20 minutes remaining in the run to re-equilibrate and regenerate the column. A blank run wherein 5 µl of solvent A was injected, followed each sample run.

ESI-MS/MS acquisition and instrument control were performed using Analyst software (v 1.6.2, AB SCIEX). The ion source operated at 5500 V and at 250°C. Nitrogen was used as nebulizer/heated gas (GS1/GS2), curtain gas (CUR) and collision gas (CAD) with the source parameters of 20 psi GS1, 20 psi GS2, 20 psi CUR, and medium CAD. Compound parameters (declustering potential, entrance potential, collision energy, and collision cell exit potential) were individually optimized per transition. Transition lists were developed in discovery mode wherein the entire sphingolipidome was profiled using precursor ion scan (PIS) in positive ion mode monitoring the diagnostic product ion of the glycerophosphocholine headgroup at *m/z* 184.1 and again monitoring the *m/z* 264.3 corresponding to a didehydrated 18:1 sphingosine backbone as we have described[128]. Quantitative data acquisition was then performed in positive ion mode using selected reaction monitoring (SRM) mode monitoring transitions with product ions of *m/z* 184.1 corresponding to a phosphocholine headgroup for transitions corresponding to biological sphingomyelin species, and *m/z* 264.3 corresponding to a didehydrated 18:1 sphingosine backbone, for transitions corresponding to biological sphingolipids containing a d18:1, or t18:0 backbone[190]. Molecular identities were confirmed with a study specific pooled control in two HPLC-MRM information-dependent acquisition (IDA)-enhanced product ion (EPI) experiments, in which

MRM was used as a survey scan to identify target analytes, and an IDA of EPI spectra was acquired in the linear ion trap. The IDA method triggered EPI scans following analysis of MRM signals with dynamic background subtraction from the survey scan. The IDA criteria were set to select the one-to-three most intense peaks, and intensity threshold set to exceed 1000 cps. The EPI experiment operated in positive-ion mode, scanning mass range from *m/z* 200-1000 at a scan rate of 10,000 Da/s with dynamic fill in the ion trap. Two collision energies were applied, 35 eV and 50 eV with collision energy spread of 15 eV, to ensure a broad coverage of fragmentation for both low *m/z* and high *m/z* species. Following acquisition, the EPI spectra were examined for structural determination of the lipid species present in the samples. Processing of quantitative MRM data was performed using MultiQuant software (v 3.0.2, AB SCIEX). For quantification, raw peak areas were corrected for extraction efficiency, and instrument response by normalization to standards added at time of extraction or at time of mass spec. Lipid abundances were expressed as pmol equivalents of SM(d18:1/18:1-d9) per 1E6 cells for sphingomyelin species, or as pmol equivalents of Cer(d18:1/16:0-D31) per 1E6 cells for sphingolipid species. Percent ceramidase and hexosylceramidase activity was defined as the change in ceramide or hexosylceramide content in SMA-PME and FL fibroblasts relative to untreated age- and sex-matched controls.

4.5.4 Immunofluorescence

Immunofluorescence was performed as described previously[191, 192]. Briefly, patient and control fibroblasts were plated on Lab-Tek II square glass well chambers (Lab-Tek II #155379) in standard serum containing media and allowed to grow overnight under tissue culture conditions (see above). Cells were washed with 10mM PBS and fixed with 4% formaldehyde (Sigma-Aldrich, cat# F1635-500ML) in 10mM PBS for 10 minutes. Cells were washed with PBS and incubated with primary antibody (Table 1) diluted in antibody buffer (AB; 10 mM PBS; 0.1% Triton-X, Sigma, cat# T9284-500ML; 10% heat-inactivated Horse Serum, Wisent, cat# 06150). Following primary antibody incubation, samples were

washed with 10 mM PBS, and incubated with secondary antibodies for 1 hr at room temperature. Slides were washed with PBS, and if tertiary antibody was required, slides were incubated with tertiary antibody for 1 hr at room temperature. Samples requiring nuclear stain were incubated with DRAQ5 diluted in PBS for 5 minutes. Following the incubation, slides were washed with PBS, and coverslipped (Fisherscientific, cat# 10474379), and ProLong gold antifade reagent (Invitrogen, cat# P36930) was added. Slides were kept in the dark at room temperature until imaged. Slides were imaged by confocal laser scanning microscopy using a Leica TCS Sp5 (Leica Microsystems) microscope, captured with Leica LAS AF software (version 2.7.3.9723) using either an 20x objective (Leica, cat# 11506326) or a 63x objective (Leica, cat# 11506188).

4.5.5 Electron microscopy (EM)

Processing for EM was performed as described[193, 194].

4.5.6 Statistical Analysis

One-Way ANOVA, with Holm-Šidák post-hoc was used for experiments comparing three sets of data with alpha values set to 0.05. Error bars represent means ± SEM. Data were analyzed using GraphPad Prism version 10.0.2 for macOS (GraphPad Software, San Diego CA). Changes in the abundances of individual ceramide species were determined statistically by multiple t-tests with false discovery rate (FDR) set at 1% using two-stage linear step-up FDR procedure of Benjamini, Krieger and Yekutieli[134] assuming that standard deviations differed between groups.

Pathway activation scores for the reaction $j \rightarrow i$ with j as a reactant and i as a product for sample k were calculated using the following equations:

$$\textit{Equation 1}\; W_{ij,k} = \left(\frac{c_{ik}}{c_{jk}}\right) * A_{ij} * \left(-log\left(p_{ij}^{distc,k\in(1,N)}\right)\right) * c.v.\left(c_{j,k\in(1,N)}\right)$$

Where c_{ik} and c_{jk} are the concentrations for lipids *i* and *j* in sample *k*, A_{ij} is the element of the reaction adjacency matrix defined as:

$$\textit{Equation 2}\; A = \begin{cases} A_{ij} = 1, if\ i \to j\ and/or\ j \to i \\ A_{ij} = 0, else \end{cases},$$

$p_{ij}^{distc,k\in(1,N)}$, is the p-value of the distance correlation measure (distc) between *i* and *j* across all *N* samples, and $c.v.\left(c_{j,k\in(1,N)}\right)$ is the relative standard deviation of the concentration values for reactant *j* across *N* samples calculated as:

$$\textit{Equation 3}\; c.v\left(c_{j,k\in(1,N)}\right) = std\left(c_{j,k\in(1,N)}\right)/mean\left(c_{j,k\in(1,N)}\right)$$

4.6 Results

4.6.1 SMA-PME and FL ASAH1 variants significantly reduce aCDase protein levels.

Whole exome sequencing identified the following pathogenic variants in patient fibroblasts: FL#1 (c.413A>T, c.1099-1G>T); FL#2 (c.413A>T, c.413A>T); FL#3 (c.387_388del, c.665C>A); SMA-PME#1 (c.456A>C, c.850G>T); SMA-PME#2 (c.124A>G, c.536C>T); SMA-PME#3 (c.173+1G>A, c.456A>C); SMA-PME#4 (c.410A>G, c.456A>C); SMA-PME#5 (c.518A>T, c.594_599dup); SMA-PME#6 (c.456A>C, c.966-2A>G); SMA-PME#7 (c.109C>A, c.410_411del); (Figure 4.2A). Variants were converted to nomenclature corresponding to the NM_177924.5 transcript[161]. No overlapping mutations were detected (Figure 4.2A). There was no discernable pattern in the distribution of mutations across the protein that associated with SMA-PME or FL in the individuals in this study (Figure 4.2A). Western blot analysis (Figure 4.2B) showed significantly reduced protein levels of the α (14 kDa) and β (40 kDa) aCDase subunits in both SMA-PME and FL fibroblasts (Figure 4.2C).

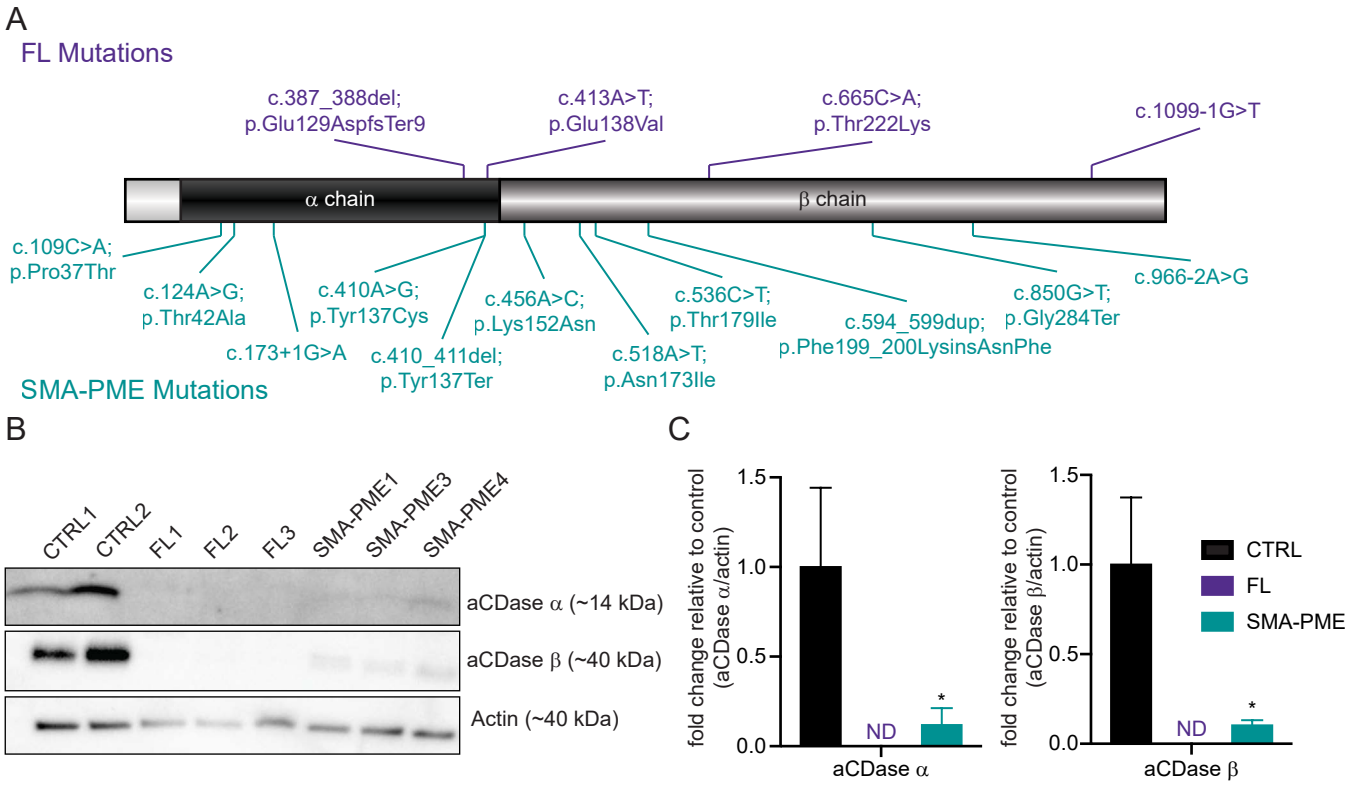

Figure 4.2: Pathogenic variations in *ASAH1* significantly reduce aCDase protein levels. A) Schematic (created using IBS[130]) of aCDase, with DNA and protein variants indicated. Positions of mutations are to scale. Missense mutations indicate the amino acid change. Nonsense mutations are indicated by amino acid change to Ter. B) Immunoblot analysis of aCDase α- and β- chains. Immunoblot is representative of three independent experiments. C) Quantification of immunoblots via densitometry. Data represent fold-change in protein levels relative to control ± SEM, normalized to actin. Statistics were one-way ANOVA with Holm-Šidák post-hoc, * $p \leq 0.05$. FL levels were below limit of detection (ND, not determined) and set to 0 for statistical analysis.

4.5.2 Intracellular sphingosine and hexosylsphingosine concentrations discriminate SMA-PME from FL

aCDase hydrolyzes Cers to Sph, GlcCers to GlcSph, and GalCers to GalSph (Figure 4.1). As species with a sphingosine (d18:1) backbone are the most abundant in higher order eukaryotes[195], we targeted the metabolism of ceramides and cerebrosides with this backbone. We first profiled all d18:1 species present in human fibroblasts by HPLC-ESI-MS/MS in precursor ion scan (PIS) mode wherein GlcCers and GalCers and GlcSph and GalSph were assessed collectively as hexosylceramides (HexCers) and hexosylsphingosines (HexSphs). We identified 17 Cer(d18:1) species and 18 HexCer(d18:1) species in addition to Sph(d18:1) and HexSph(d18:1). Structural identities were confirmed by IDA-EPI-LC-ESI-MS/MS. These species were then profiled in SRM mode.

In FL cells, Sph(d18:1) levels (aCDase product) were significantly depleted and total Cer content (aCDase substrates) significantly elevated compared to control (CTRL) (Figure 4.3A) consistent with the aCDase deficiency in Figure 4.2B. At the molecular level, the abundances of all 17 Cers detected in FL fibroblasts significantly increased (Figure 4.3A). Species with long chain fully saturated N-acyl chains (LC-SFAs) accumulated more (11-fold increase) than species with very long chain-SFAs (VLC-SFAs, 6-fold increase), VLC-monounsaturated N-acyl chains (VLC-MUFAs, 5-fold increase) or VLC-polyunsaturated N-acyl chains (VLC-PUFAs, 4-fold increase) (Figure 4.3A). This substrate-product profile was also expected given the reported preference of aCDase for ceramides with shorter N-acyl chains[196]. We further found that HexSph(d18:1) levels, the cerebroside products of aCDase, were mildly but not statistically significantly depleted in FL fibroblasts (Figure 4.3B). As with Cers, total cellular HexCer content (aCDase substrates) was significantly elevated (Figure 4.3B). Abundances of all 18 HexCers detected in fibroblasts significantly increased compared to CTRL (Figure 4.3B). The extent of HexCer accumulation (2-fold change) was not as pronounced as for Cers (6-fold change) again in keeping with the known aCDase substrate preference for ceramides over cerebrosides[197]. Interestingly, there were

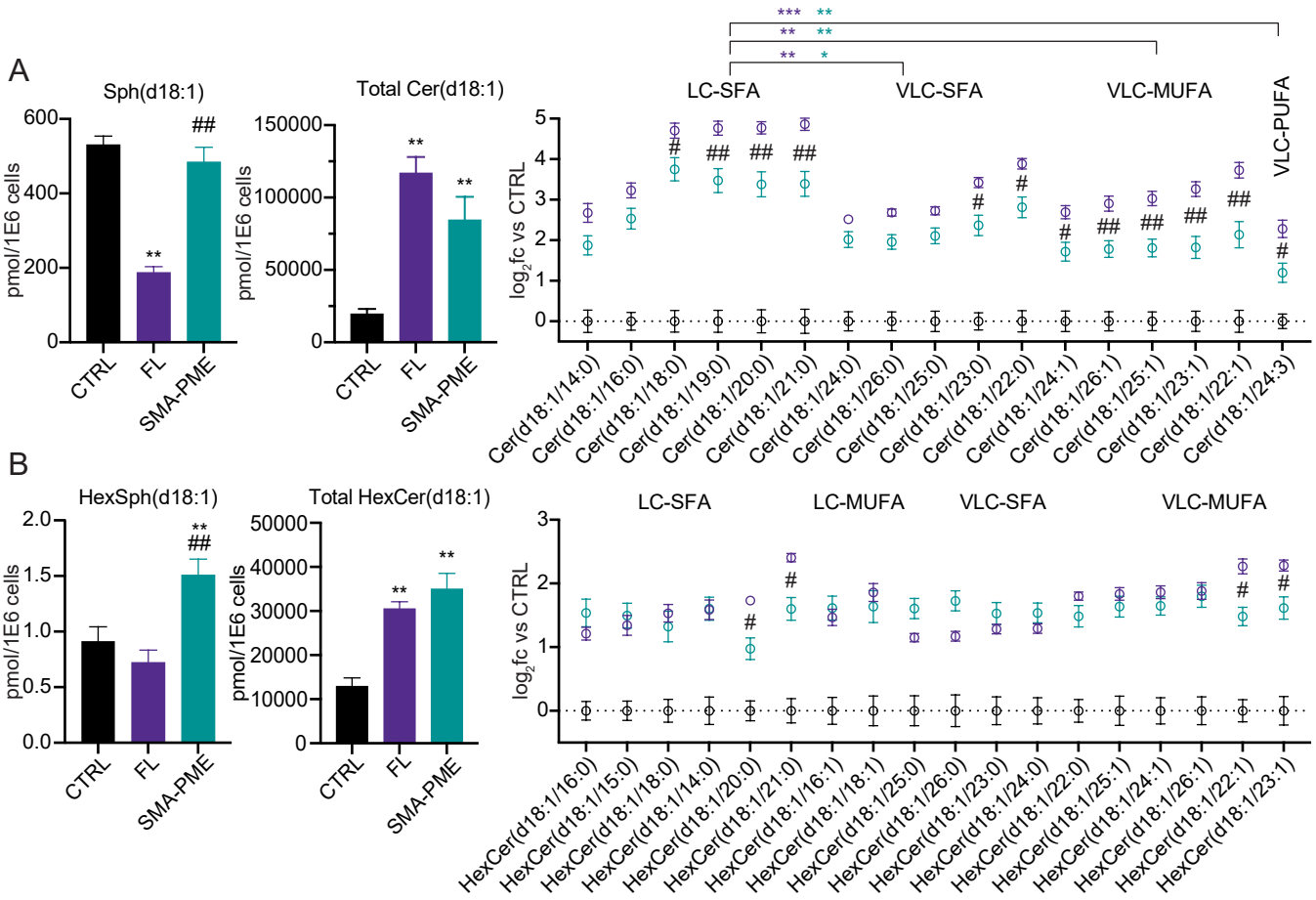

Figure 4.3: Sphingosine and hexosylsphingosine levels discriminate FL and SMA-PME. (A) Abundances of cellular Sph and total ceramide (Cer) content (bar graphs, left) or B) hexosylsphingosine (HexSph) and total hexosylceramide (HexCer) content (bar graphs, left). Data are expressed as pmol equivalents per 1E6 cells ± SEM. Right panels display individual Cer or HexCer species, separated by chain length and degree of unsaturation of their N-acyl chain. Data are expressed as $\log_2$ fold change relative to CTRL ± SEM. Statistics are one-way ANOVA with Holm-Šidák post hoc tests,*p < 0.05 vs CTRL or LC-SFA, ** p < 0.01 vs CTRL or LC-SFA, # p < 0.05 FL vs SMA-PME, ## p < 0.01 FL vs SMA-PME. In the right panels, the fold change of all species in FL and SMA-PME were statistically significantly elevated compared to CTRL at an alpha value of p=0.05 or lower. Statistically significant comparisons between FL and SMA-PME (#) are depicted or between summed abundances of N-acyl chain species. Abbreviations: LC – long chain, VLC – very long chain, SFA – saturated fatty acid, MUFA – monounsaturated fatty acid, PUFA – polyunsaturated fatty acid.

no statistically significant N-acyl chain differences in HexCer accumulation, suggesting no aCDase substrate preference in cerebroside hydrolysis (LC-SFA 2-fold increase; LC-MUFA, VLC-SFA, VLC-PUFA, 3-fold increase).

The SMA-PME substrate-product profile was markedly different from FL. As in FL, Cers and cerebrosides accumulated (Figure 4.3A, B); however, Sph(d18:1) and HexSph(d18:1) levels were not depleted rather they were significantly elevated compared to FL. As in FL, Cers (4-fold increase) accumulated to a greater extent than HexCers (3-fold increase). Like FL, levels of Cers with shorter N-acyl chains (LC-SFA 8-fold-increase) accumulated more than Cers with VLC-SFA (4-fold), VLC-MUFA or VLC-PUFA (3-fold) (Figure 4.3A). Again, as with FL cells, there was no HexCer substrate preference with respect to N-acyl chain length or degree of unsaturation (3-fold increase across all N-acyl chain subgroups). The striking difference between FL and SMA-PME was the significant and unexpected elevation in the levels of both aCDase products, Sph(d18:1) and HexSph(d18:1). In SMA-PME fibroblasts, Sph(d18:1) levels were not depleted (Figure 4.3A). HexSph(d18:1) levels were significantly elevated (Figure 4.3B). This product profile represented a unique SMA-PME lipid signature unexpected for an aCDase deficiency disorder.

4.5.3 Sphingolipid metabolism increases in SMA-PME and decreases in FL.

To identify the metabolic modifiers responsible for the Sph(d18:1) and HexSph(d18:1) enrichment in SMA-PMA, we combined unbiased lipidomics with bioinformatic network analysis of broader sphingolipid metabolism beyond reactions catalyzed by aCDase. We quantified not only the primary substrates and products of aCDase but also Cers with hydroxylated N-acyl chains (CerOH), phytoceramides Cer(t18:0), sphingomyelins (SM), lactosylceramides (LacCer), and globotriaosylceramides (Gb3) assessing changes in associations between lipid species at the molecular

level across conditions. In CTRL fibroblasts, lipid abundances were most strongly correlated within subclasses (i.e., Cer levels were strongly correlated with abundances of other Cers) as would be expected for a network at steady state (Figure 4.4A). There were 379 significant intra-subclass correlations as compared to 144 significant inter-subclass correlations (between lipid subclasses) (Figure 4.4B). In SMA-PME, the majority of significant correlations were also intra-subclass (Figure 4.4A). Specifically, there were 317 intra-subclass correlations, compared to 124 inter-subclass correlations (Figure 4.4B). Unique to SMA-PME, there were more *de novo* inter-subclass correlations between (a) HexCers and LacCers, HexCers and Sph(d18:1), and LacCers and Sph(d18:1) (Figure 4.4A). These associations highlighted a *de novo* relationship between HexCer and LacCer metabolism that correlated with elevated Sph(d18:1) and HexSph(d18:1) concentrations unique to SMA-PME. In FL, there were more significant inter-subclass correlations (n=271), than in intra-subclass correlations (n=210) (Figure 4.4B). The two inter-subclass pairs with the most *de novo* significant correlations were Cers correlating with SMs (63 significant correlations) and Cers correlating with HexCers (56 significant correlations) suggesting a change in the remodeling of SMs to Cers (sphingomyelin pathway) and HexCers to Cers (modification pathway).

Having identified differences at the network level in lipid homeostasis (Figure 4.4), we asked how these disruptions mechanistically altered intracellular Sph(d18:1), HexSph(d18:1), Cer(d18:1) and HexCer(d18:1) concentrations. For each bilateral metabolic reaction, pathway activation scores were calculated, quantifying the strength of metabolic pathway relative to CTRL (Figure 4.5A-C). Protein levels of enzymes mediating affected pathways were further quantified by immunoblotting (Figure 4.5D). Figure 4.5E summarizes the metabolic map of sphingolipids with an 18:0 N-acyl chain in both FL and SMA-PME. In FL, the primary metabolic deficit was one of hypometabolism resulting in a significant depletion of Sph(d18:1) and a significant accumulation of Cer(d18:1) relative to both CTRL and SMA-PME (Figure 4.3A, 4.5A-C, E). In FL, the salvage, sphingomyelin, and modification pathways

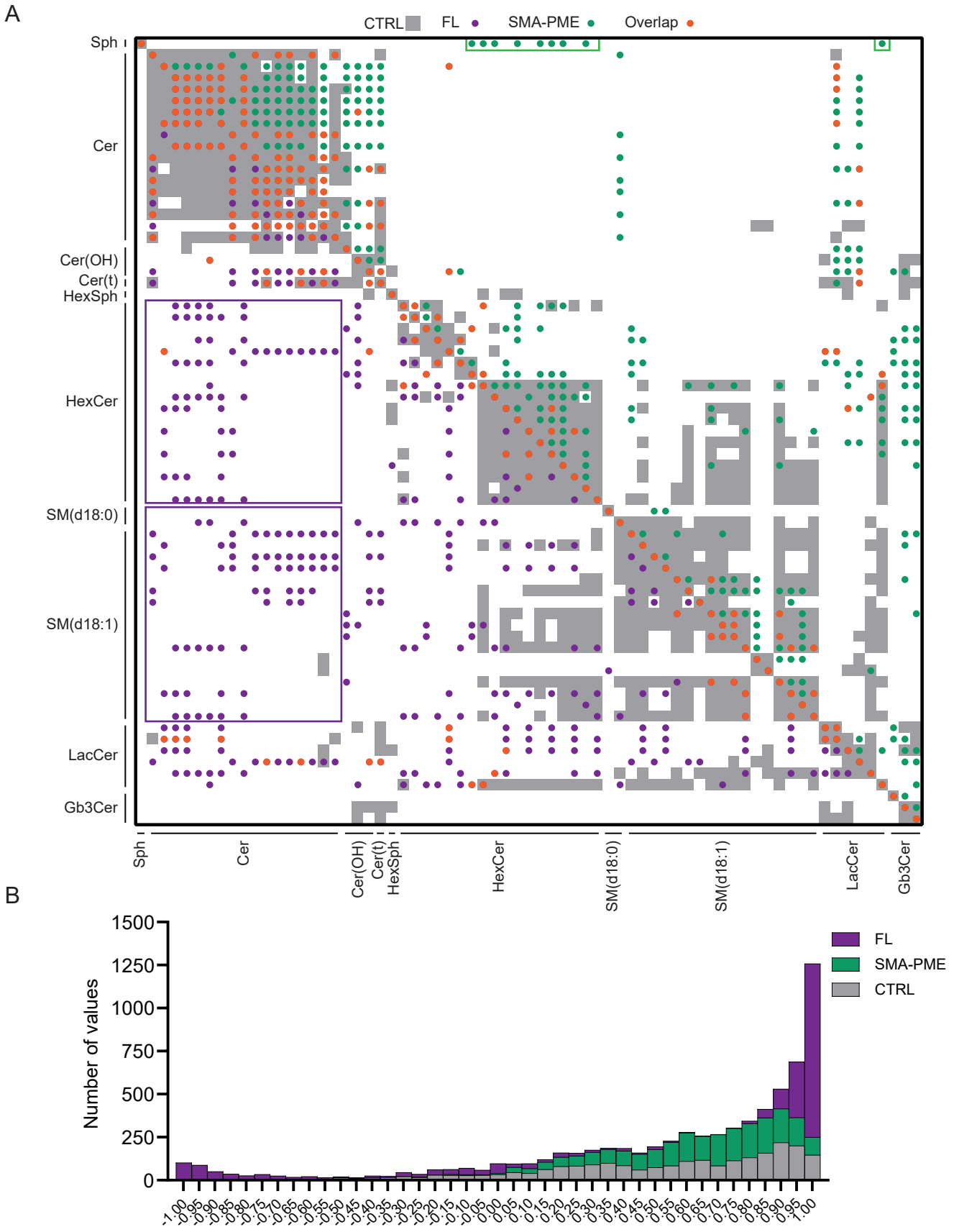

Figure 4.4: Sphingolipid metabolism is differentially disrupted in SMA-PME and FL. (A) Pearson r correlation matrix for statistically significant correlations ($p<0.05$) between lipid species. Data represent statistically significant associations between z-scores of sphingolipid abundances (pmol), thresholded to include only correlations greater than 0.9 or less than -0.9. Matrix is bisected displaying FL (purple circles) and CTRL (grey boxes) on bottom and SMA-PMA (green circles) and CTRL (grey boxes) on top. Correlations common to both FL and SMA-PME are indicated by orange circles. (B) Data represent the distribution and number of all statistically significant r values per condition.

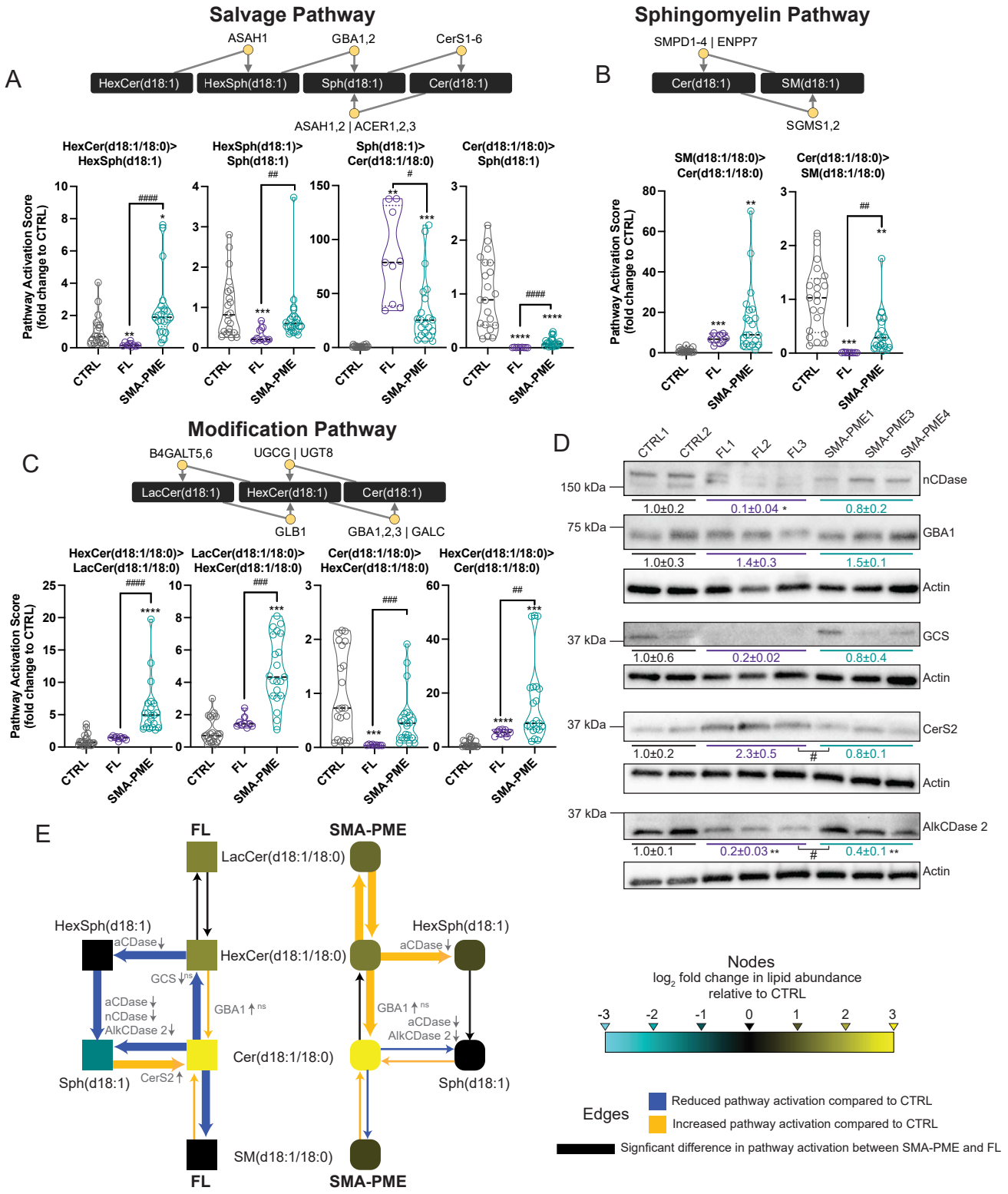

Figure 4.5. aCDase deficiency elicits sphingolipid hypometabolism in FL and hypermetabolism in SMA-PME. (A-C) Pathway activation scores quantifying the strength of each direct reaction in the salvage (A), sphingomyelin (B), and modification pathways (C). Statistics are one-way ANOVA with Holm-Šidák post hoc tests,*p < 0.05, **p<0.01, ***p<0.001, ****p<0.0001 vs CTRL; #p < 0.05, ##p<0.01, ###p<0.001, ###p<0.0001 FL vs SMA-PME. (D) Western analysis of enzyme levels mediating these pathways. (E) Summary of network level changes in sphingolipid metabolism for sphingolipids with 18:0 N-Acyl chains.

were significantly suppressed (Figure 4.5A-C, E). Hydrolysis of Cer(d18:1/18:0) to Sph(d18:1) was significantly reduced (Figure 4.5A, E), not only as a result of a loss of aCDase protein (Figure 4.2B, C) but also as a result of a decrease in *ASAH2* (neutral ceramidase, nCDase) and *ACER2* (alkaline ceramidase 2, AlkCDase) protein expression (Figure 4.5D). Hydrolysis of the of HexSph(d18:1) to Sph(d18:1) was also significantly reduced in FL, further contributing to the depletion of Sph(d18:1) (Figure 4.5A, E). Surprisingly, we found that the conversion of Sph(d18:1) to Cer(d18:1/18:0) *increased* in FL again enriching intracellular Cer(d18:1) content at the expense of Sph(d18:1) (Figure 4.5A, E). This conversion was associated with an increase in the expression of the CerS2 protein, one of six enzymes responsible for the synthesis of Cer(d18:1) from Sph(d18:1) (Figure 4.5, D). Finally, a decrease in the metabolism of Cer(d18:1) to either SM(d18:1) or HexCer(d18:1) via the sphingomyelin and modification pathways in FL further elevated intracellular Cer(d18:1) (Figure 4.5B, C, E). At the protein level, these changes in the Cer(d18:1) to HexCer(d18:1) modification pathway could be attributed to a reduction in glucosylceramide synthase (GCS) protein expression (Figure 4.5D).

In sharp contrast to FL, pathway analysis indicated that in SMA-PME, the metabolic outcome was one of Cer(d18:1) hypermetabolism, resulting in increased Sph(d18:1) and HexSph(d18:1) levels despite aCDase deficiency. Four metabolic differences distinguished SMA-PME from FL. First, the hydrolysis of Cer(d18:1) to Sph(d18:1) was not as severely reduced in SMA-PME compared to FL (Figure 4.5A). In SMA-PME, both aCDase and AlkCDase2 protein levels were reduced but, unlike FL, nCDase protein levels were maintained (Figure 4.5B). Second, and unexpectedly, the hydrolysis of cerebrosides by aCDase (HexCer(d18:1/18:0) to HexSph(d18:1)) *increased* in SMA-PME cells (Figure 4.5A, E). This pathway disruption was not anticipated for a canonical aCDase deficiency disorder yet was responsible for the elevation in HexSph(d18:1) levels compared to FL and CTRL (Figure 4.3B). Third, Sph(d18:1) levels were further supplemented and Cer(d18:1) levels further elevated by the shunting of rising HexSph(d18:1) concentrations to Sph(d18:1) and the increased conversion of HexCer(d18:1) to

Cer(d18:1) (Figure 4.5A, C). This hypermetabolic hydrolysis of the glucosyl/galactosyl headgroup could be attributed to an increase in protein expression of GBA1 (beta glucocerebrosidase) (Figure 4.5D).

4.5.4 Ceramides accumulate in the lysosome in FL and in vesicles fused to the plasma membrane in SMA-PME

Given these differences in ceramide metabolism, we asked whether both disorders were, in fact, lysosomal storage disorders. The number of Cer(d18:1)-positive LAMP-1+ inclusions were quantified by immunofluorescence in CTRL, FL, and SMA-PME cells (Figure 4.6A, B). We found that more cells presented with LAMP+/Cer(d18:1)+ inclusions in FL compared to SMA-PME or CTRL (Figure 4.6B). Moreover, the number of LAMP+/Cer(d18:1)+ inclusions per cell in FL were significantly higher and the area of the LAMP+/Cer(d18:1)+ inclusions significantly larger compared to SMA-PME or CTRL (Figure 4.6B). No differences were detected between SMA-PME and CTRL. Taken together, this cellular phenotype is consistent with FL but not SMA-PME being a lysosomal storage disorder.

Cer(d18:1) is synthesized from Sph(d18:1) salvaged in the lysosome following its translocation to ER. Newly synthesized Cer(d18:1) is then transported to the Golgi apparatus, and packaged in Golgin-97+ secretory vesicles for delivery to plasma membrane. We found that there were qualitatively more Golgin-97+/Cer(d18:1)+ vesicles in both SMA-PME and FL than CTRL by immunofluorescence (Figure 4.7). By electron microscopy, we found no indication of enlarged, lipid-rich lysosomes in SMA-PME fibroblasts (data not shown) but a marked increase in apparently aberrant vesicle fusion to plasma membrane. In CTRL fibroblasts, docked secretory vesicles, or early stage caveolae were detected adjacent to the plasma membrane (Figure 4.8A, sV). In SMA-PME fibroblasts, these vesicles appeared to be fused with, rather than docked to, the plasma membrane failing to exocytose (Figure 4.8B, sV) resulting in vacuoles or regions of plasma membrane expansion (Figure 4.8C, asterisks). Consistent with

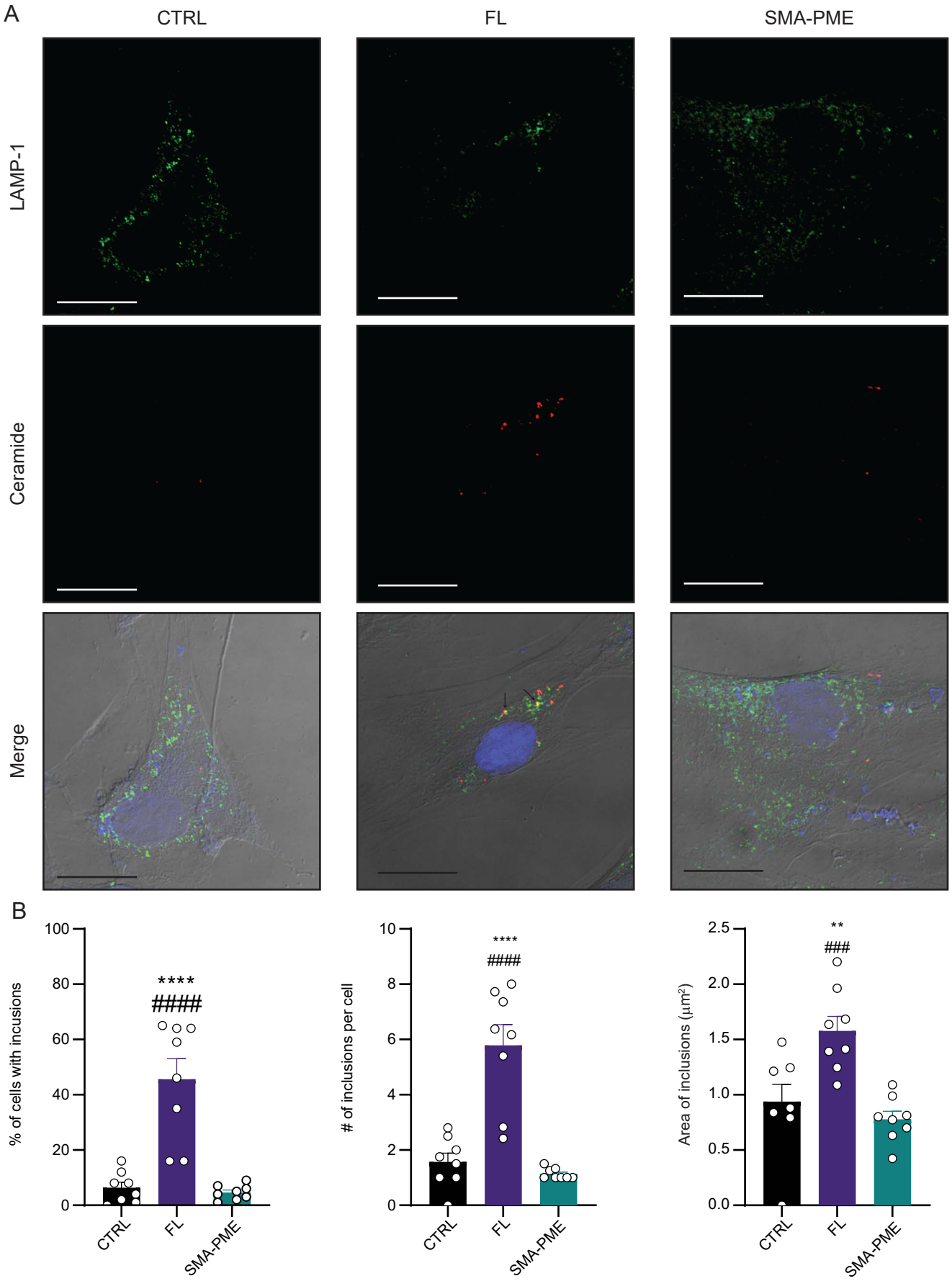

Figure 4.6: Ceramide accumulates FL but not SMA-PME lysosomes. (A) Immunofluorescent co-labelling of LAMP-1+ lysosomes (green) with anti-Ceramide antibodies (red). Nuclei were stained with DRAQ5 (blue). Merge includes differential interference contrast of cell structure. Scale bar represents 20 µm. Black arrows indicate regions of overlap of LAMP1 and Cer signal. (B) Percentage of cells with ceramide inclusions (left), number of inclusions per cell (middle), and area of inclusions (right). Bars represent mean ± SEM of N = 8 replicate measurements from 2 individual platings of cells from a CTRL, FL, and SMA-PME patient respectively. Statistics were one-way ANOVA with Holm-Šidák post hoc. ** $p < 0.01$, **** $p < 0.0001$ FL or SMA-PME compared to CTRL, ### $p < 0.001$, #### $p < 0.0001$ FL compared to SMA-PME.

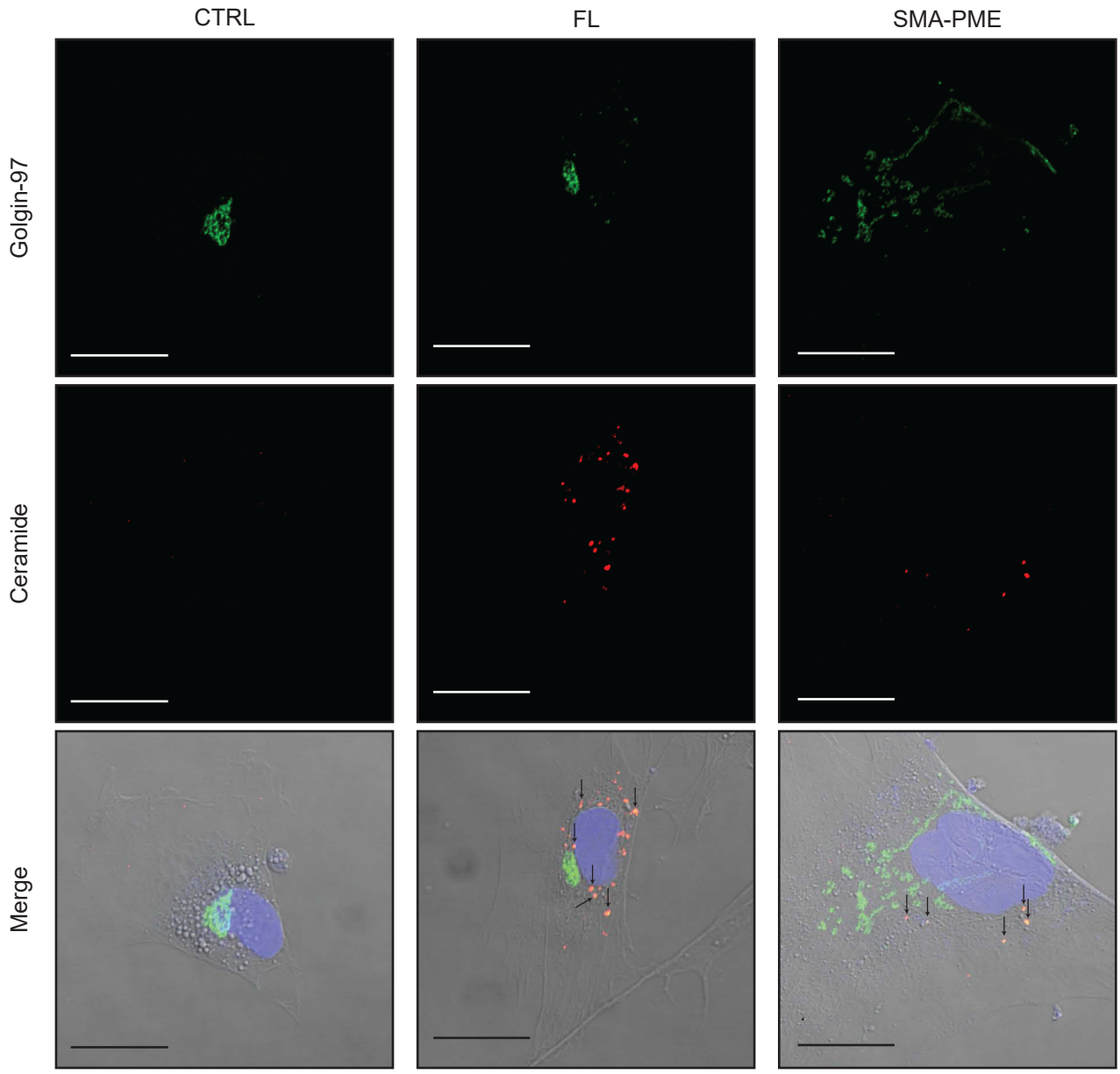

Figure 4.7: Co-localization of ceramide in Golgin-97 positive vesicles in both FL and SMA-PME. Immunofluorescence microscopy of CTRL, FL, and SMA-PME cells. Cells were co-labelled with anti-Golgin-97 (green), anti-ceramide (red) and DRAQ5 (blue). Merge includes differential interference contrast of cell structure. Scale bar represents 20 μm. Black arrows indicate regions of Golgin-97 and Cer signal overlap.

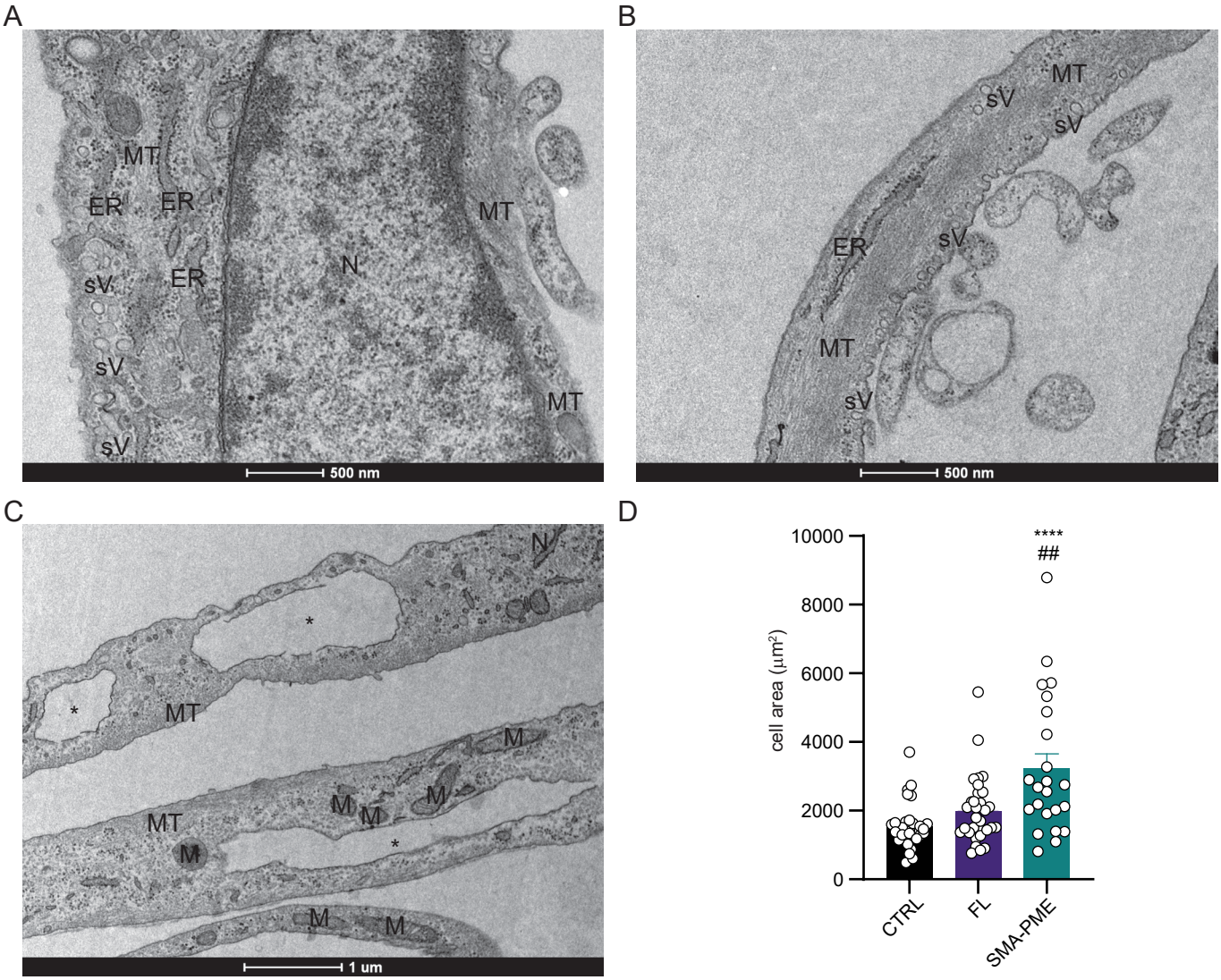

Figure 4.8: Fusion of secretary vesicles is increased in SMA-PME resulting in plasma membrane expansion and increased cell area. (A) In EM assessment of CTRL cells, secretory vesicles (sV) were observed docked to plasma membrane. (B) In SMA-PME, sVs appear fused to plasma membrane resulting in (C) large vacuoles (asterisks) that expanded the area of the plasma membrane. (D) SMA-PME cells were larger than FL or CTRL cells. Data represent mean cell area (in μm^2) ± SEM. Statistics were one-way ANOVA with Holm-Šidák post hoc. **** $p < 0.0001$ SMA-PME compared to CTRL. ## $p < 0.01$ SMA-PME compared to FL. Acronyms: N – nucleus; MT – microtubule (and/or fibers); sV – secretory vesicles; ER – endoplasmic reticulum; M – mitochondria.

an expansion in the plasma membrane as a result of lipid accumulation, there was a significant increase in total cell area in SMA-PME fibroblasts compared to CTRL and FL cells (Figure 4.8D).

4.7 Discussion

The rare childhood diseases, FL and SMA-PME, while both caused by mutations in *ASAH1*, have vastly different clinical presentations. Currently, little is known about the underlying biochemical pathology of these diseases, leading to these clinical presentations. We confirm in this study that FL is a canonical lysosomal storage disorder exacerbated by hypo-sphingolipid metabolism leading to the lysosomal accumulation of ceramides and cerebrosides and the depletion of sphingosine. By contrast, SMA-PME is metabolically distinct in that hyper-metabolic changes lead to both the accumulation of ceramides and cerebrosides, and sphingosine and hexosylspingosine, despite aCDase deficiency. This hyper-metabolism impairs secretary vesicle secretion leading to the expansion of vacuolized plasma membrane and an increase in cell size. Together, this study defines novel metabolic pathomechanisms, dubbed metabolic modifiers, that produce different cellular pathologies associated with the clinical presentation of SMA-PME and FL.

Loss of ceramidase activity along with the accumulation of ceramide within patient cells has been the defining, and thus diagnostic, biochemical feature for both FL and SMA-PME for quite some time[146, 173, 177, 178, 198]. Most studies, therefore, only report the levels of Cer(d18:1) to confirm the diagnosis of either of these diseases[18, 116, 146, 152, 153, 157, 160, 165, 176]. Thus there has been no insight into how *ASAH1* variants can produce either later onset isolated neurological symptoms (SMA-PME) or early onset peripheral pathology (FL). Here, we used unbiased lipidomic profiling and novel network analysis confirmed by molecular assessment of cell phenotype to identify a sphingolipid metabolic signature capable of distinguishing these diseases associated with different cellular pathologies. While there have been some

studies determining the effect of aCDase deficiency on the profile of lipids beyond ceramides[199-202], to our knowledge, this is the first exploration of wider sphingolipid subclasses in primary patient fibroblasts. Taken together, our sphingolipidome and protein expression assessment indicate that FL displays a broader hypometabolic network dysregulation, with more sphingolipid metabolic pathways supressed than in SMA-PME resulting in canonical lysosomal storage pathology whereas SMA-PME is a hypermetabolic disorder with more sphingolipid pathways activated in response to aCDase deficiency resulting in a plasma membrane pathology linked to neurological outcome. This later finding is consisting with other putative lysosomal storage disorders that present with defects in intracellular trafficking[203]. These include the aberrant transporting of endocytosed cholesterol in Neimann-Pick disease type C[204]; the aberrant processing and localization of lysosomal enzymes in Mucolipidosis type II and III[205]; the impaired cargo packaging and trafficking to the lysosome in Hermansky-Pudlak syndrome type 2[206]; or the aberrant vesicle formation and trafficking of Chediak-Higashi syndrome[207]. Taken together, our data suggest that the differential localization of ceramides and cerebrosides within the cells of FL and SMA-PME suggests very different disease mechanisms, leading to the differences in severity and symptoms of these disorders.

In summary, in this study we identified differences in the sphingolipidome, by examining the amount and distribution of various sphingolipids, and their metabolic enzymes, within FL and SMA-PME patient fibroblasts. This study helps to illuminate the different mechanisms of these two diseases, and we suggest that the differences detected indicate different disease mechanisms, which, in turn, could lead to two different treatment strategies for these diseases.

Chapter 5 : Enzyme replacement therapy normalizes sphingolipid dysregulation in SMA-PME fibroblasts

Graeme SV McDowell[1], Stephanie L Fowler[1], Mark Akins[1], Hongbin Xu[1], Irina Alecu[1], Yun Wang[1], Samantha Sherman[1], Thao Nguyen-Tran[1,2], Wendy Mears[3], Samuel F. Berkovic[4], Maria Spanou[5], Argirios Dinopoulos[5], Jodi Warman-Chardon[6,7], Edward H. Schuchman[8], Toni S. Pearson[9,10], Alexander Solyom[11], David A. Dyment*[3], and Steffany AL Bennett*[1,2]

[1]Neural Regeneration Laboratory, Ottawa Institute of Systems Biology, uOttawa Brain and Mind Research Centre, Department of Biochemistry, Microbiology, and Immunology; [2]Department of Chemistry and Biomolecular Sciences, Centre for Catalysis Research and Innovation, University of Ottawa, Ottawa, ON, Canada; [3]Department of Genetics, Children's Hospital of Eastern Ontario Research Institute, University of Ottawa, Ottawa, ON, Canada; [4]Epilepsy Research Center, Department of Medicine, University of Melbourne, Heidelberg, Victoria, Australia; [5]Pediatric Neurology Division, 3rd department of Pediatrics, Attikon University Hospital, Athens, Greece; [6]Department of Medicine (Neurology), Ottawa Hospital Research Institute, Ottawa, Ontario, Canada; [7]Children's Hospital of Eastern Ontario Research Institute, Ottawa, Ontario, Canada; [8]Department of Genetics and Genomic Sciences, Ichan School of Medicine at Mount Sinai, New York, NY, USA; [9]Department of Neurology, Washington University School of Medicine, St. Louis, Missouri, USA; [10]Departments of Neurology and Pediatrics, Columbia University Irving Medical Center, New York; [11]Aceragen, Basel, Switzerland.

* Joint corresponding authors: ddyment@cheo.on.ca (DAD); sbennet@uottawa.ca (SALB)

5.1 Objective of Study

In Chapter 3, I demonstrated that treatment with human recombinant aCDase could normalize ceramide levels *in vitro* in SMA-PME patient fibroblasts. In Chapter 4, I identified a hypermetabolic SMA-PME lipidomic phenotype that discriminated SMA-PME from FL. In this chapter, I asked whether with human recombinant aCDase could restore lipid homeostasis in SMA-PME patient fibroblasts and rescue the "metabolic modifier" pathology. As with Chapter 4, this work is being combined with studies performed by my lab colleagues using IPSC-derived neurons derived from these same fibroblast lines and additional bioinformatic analyses prior to submission for publication. Only studies I was directly involved in are included in this thesis.

5.2 Author Contributions

GSVM, DAD, and SALB conceived and designed the experiments and analyzed all data. Reagents, materials, and/or tools were provided by AS and WM. Cohorts, samples, and clinical history were provided by SFB, MS, AD, JW-D, EHS, TSP, AD, and DAD. HPLC-ESI-MS/MS was performed by GSVM, HX, SS, YW, TN-T, and IA. Cell culture experiments were performed by GSVM and MA. Western analyses were performed by SLF and GSVM.

5.3 Abstract

There is currently no cure for SMA-PME. The currently available treatments address the symptoms, and aim to improve patients' quality of life, but there are no available treatments which can address and fix the underlying pathology. The objective of this study was to determine if enzyme replacement therapy (ERT) would rescue the hypermetabolic pathology observed in previous chapters, and thus show promise as a treatment for SMA-PME. To determine this, we assessed the impact of rhAC treatment on

sphingolipid metabolism in SMA-PME patient fibroblasts, using high-performance liquid chromatography-differential mobility spectrometry-electrospray ionization-tandem mass spectrometry, quantifying various sphingolipid classes, including glucosyl and galactosylceramide levels. We found that levels of Cer could be rescued with treatment. Levels of cerebrosides were unaffected by rhAC treatment. By examining product-to-precursor ratios as a proxy for metabolic flux, we found that, despite levels of HexCers not being altered, the overall homeostatic metabolism was rescued. This proof-of-concept study shows that an ERT approach has the potential to be an effective treatment strategy for patients suffering from SMA-PME, and potentially other non-classical lysosomal storage disorders, given proper consideration of enzyme delivery to the central nervous system.

5.4 Introduction

Spinal muscular atrophy with progressive myoclonic epilepsy (SMA-PME, OMIM: 159950)[177] is a rare, autosomal recessive, pediatric disease caused by mutations in the N-acylsphingosine amidohydrolase 1 gene (*ASAH1*, MIM: 613468, GeneBank: NM_177924.5)[179, 180]. *ASAH1* encodes the lysosomal enzyme aCDase, responsible for the hydrolysis of ceramides and cerebrosides to sphingosine, glucosylsphingosine (GlcSph) and galactosylsphingosine (GalSph)[44, 45, 182, 183]. SMA-PME patients present with isolated neurological symptoms that include muscle weakness progressing to immobility and respiratory insufficiency as a result of lower motor neuron degeneration and progressive myoclonic epilepsy with seizures that include myoclonic, absence, and generalized tonic-clonic seizures[18, 116, 145, 146, 153, 154]. Onset of SMA-PME is late childhood/early adulthood and lasts 5-10 years with death due to myoclonic epilepsy and respiratory insufficiency[18, 145, 146, 149, 154, 184].

There is no specific treatment for SMA-PME and management is supportive. Patients are prescribed anti-epileptic drugs, for example valproic acid[116, 155], or put on dietary interventions, such as a ketogenic

diet, to help manage the myoclonus. SMA-PME seizures are, however, refractory to treatment, and these interventions deliver temporary relief at most or may even exacerbate clinical symptoms, as there are often periods of greater seizure activity following treatment[116, 155]. Similarly, there are no treatments for the spinal muscular atrophy. Physical therapy, or aids such as wheelchairs, are used to alleviate the burden of the symptoms, but without addressing the motor neuron degeneration, these only offer supportive relief with no cause-directed therapy available[18, 148, 159, 160].

There is a clear need for new cause-directed treatment strategies for patients with SMA-PME. One potential approach is enzyme replacement therapy (ERT). In ERT, recombinant enzymes are introduced to the patient, often by intravenous infusions, to compensate for enzyme deficiency (reviewed in [208, 209]). For lysosomal-localized targets like aCDase, recombinant enzymes are engineered with mannose-6-phosphate at the non-reducing ends of the sugar chains of the recombinant enzyme to facilitate lysosomal localization via the mannose 6-phosphate receptor pathway[208, 209]. ERT has been successfully used in multiple lysosomal storage disorders, and as of 2018 the FDA had approved ERT drugs for eight different diseases[210, 211]. Recently, He et al[172] explored the use of recombinant human aCDase (rhAC) as a potential therapy for Farber's disease (OMIM: 228000)[178]. In this study, the authors treated both Farber's disease patient cells, and a Farber's disease mouse model with rhAC, and found in the patient cells, the rhAC treatment was able to significantly reduce the amount of Cer buildup and increase the amount of Sph observed in the cells. In their mouse model, the authors found that rhAC was well tolerated and safe to administer to the animals, and also resulted in the reduction of Cer and increase in Sph in various tissues *in vivo*, increasing survival duration[172]. With respect to SMA-PME, we have shown that total intracellular content of Cer(d18:1) can be normalized in SMA-PME patient fibroblasts by treatment with rhAC and our activity analysis indicated that restoration to levels detected in cells with wild-type *ASAH1* required 58 h of treatment[18]. We have not yet determined whether rhAC treatment is sufficient to rescue all of the hypermetabolic defects in sphingolipid metabolism unique to SMA-PME.

To address this question, we assessed impact of rhAC treatment on sphingolipid metabolism in SMA-PME patient fibroblasts. Previously we evaluated cerebroside changes collectively. We asked here whether glucosylceramide (GlcCer) and galactosylceramide (GalCer) metabolism was equally affected. To drill down to the defect in these different cerebroside subclasses, we used high performance liquid chromatography-differential mobility spectrometry-electrospray ionization-tandem mass spectrometry (HPLC-DMS-ESI-MS/MS) wherein DMS is used as an orthogonal separation to HPLC to quantify GlcCers and GalCers[53]. We show here that ERT can rescue the hypermetabolic defect in SMA-PME cells, thereby indicating that ERT could be a beneficial technique, and should be explored further for the treatment of SMA-PME.

5.5 Materials and Methods

5.5.1 Cell culture

Primary dermal fibroblast lines were derived from punch biopsies from six SMA-PME patients by informed consent from their families according to CHEO REB #11/04 E research ethic board approval. The natural history of these patients has been described in[18, 116, 153, 184] and mutations/variants confirmed as we have described[116]. Apparently healthy controls (GM05400, GM05757, and GM00038) were obtained from the Coriell Institute. Fibroblasts were maintained in Dulbecco's Modified Eagle's Medium/Ham's Nutrient Mixture 12 (D-MEM/F-12) (Gibco, cat# 12400-016) supplemented with 10% fetal bovine serum (Sigma Aldrich, cat# F0926), and 2 mM L-glutamine (Gibco, cat# 25030-081 at 37^{o}C in a 5% CO_2 environment.

5.5.2 Treatment Paradigm

Treatments were performed as we have described[18]. Briefly, primary fibroblasts were cultured in D-MEM/F-12 supplemented with 10% fetal bovine serum, and 2 mM L-glutamine. Patient and control fibroblasts were plated at a density of $2.5x10^5$ cells in 10 cm^2 tissue culture dishes (VWR, cat# 10062-880), and maintained for 7 days until confluent, changing the media every 2-3 days. rhAC used for treatment was provided under material transfer agreement (MTA) with Enzyvant now Aceragen. Development for potential clinical use is continuing under Aceragen as ACG-801. Cultures were treated with 10 µg/ml of rhAC or vehicle (media) in complete media as previously described for Farber patient cells[172]. Media + rhAC was refreshed every 24 h and cells collected at 0, 24, and 48h post treatment.

5.5.3 HPLC-ESI-DMS-MS/MS Lipidomics

After treatment, lipids were extracted from the fibroblasts using a modified Bligh and Dyer protocol as described previously[116, 125-127, 153, 189] and in detail in Chapter 3.5.4 and 4.5.3. Sphingolipid content was quantified as we have previously described by HPLC-ESI-MS/MS[18, 129, 153] and in detail in Chapter 3.5.4 and 4.5.3. HPLC-DMS-ESI-MS/MS was performed as we have described[53]. Briefly, HPLC separation was performed as above (Chapter 3.5.4, 4.5.3), with an Agilent Infinity II system operating at a flow rate of 10 µl/min with 8 µl sample injection by an autosampler maintained at 4ºC. A 100 mm x 250 µm (inner diameter) capillary column packed with ReproSil-Pur 120 C8 beads (particle size of 3 µm and pore size of 120 Å) was used with a binary solvent gradient consisting of water with 0.1% formic acid and 10 mM ammonium acetate (solvent A) and acetonitrile-IPA (5:2, v/v) with 0.1% formic acid and 10 mM ammonium acetate (solvent B). The gradient started from 30% solvent B, and reached 100% solvent B within 5 min, where it was maintained for 30 min. The gradient was returned to 30% solvent B within 1 min and was maintained for 10 min to re-equilibrate the column prior to the next sample injection.

DMS separation was performed using a SelexION differential ion mobility device (SCIEX, Concord, Ontario) interfaced with a triple quadrupole-linear ion trap QTRAP 5500 mass spectrometer. The DMS cell was mounted in the atmospheric pressure region between the Turbo V ion source curtain and the orifice plate of the mass spectrometer, and nitrogen was used as a transport gas. DMS parameters were optimized previously[53], and the following DMS parameters were used: DMS cell temperature of 150ºC (low), modifier concentration of low (1.5% v/v in the transport gas, corresponding to a 173.8 µl/min flow rate for IPA), DMS resolution enhancement of 30 psi (medium) and a DMS offset of -3.0V, and nitrogen resolving gas at 30 psi. Isopropanol was used as chemical modifier. The optimal compensation voltage (CoV) and separation voltage (SepV) for each isomeric pair of standards was determined previously[53].

Data acquisition was performed in the positive ion mode using MRM with the optimized DMS parameters. Each duty cycle was 0.85 s, and the MRM data were acquired over the 45 min chromatography period. Instrument control and data acquisition were performed with Analyst software version 1.6.2, and MultiQuant software (v 3.0.2) was used for processing quantitative MRM data. For quantification, raw peak areas were corrected for extraction efficiency, and instrument response by normalization to standards added at time of extraction. Lipid abundances were expressed as pmol equivalents of either GalCer(d18:1/8:0) or GlcCer(d18:1/8:0) per 1E6 cells.

5.5.4 Statistics

Correlation matrices were generated by calculating Pearson r correlations for each pair of lipids within the individual sphingolipid subclasses. 3-4 biological replicates averaged for n = 7 patients were used to generate the matrix. Only values with a p value of < 0.05, and a Pearson r value of > 0.9, or $r < -0.9$ were included in the matrix. One-way Welch's ANOVA with false detection rate according to Benjamini, Krieger, and Yeukuteli[134] set to 0.05 was used when comparing lipid abundances and product-

to-precursor ratios (PtPrs). Data were analyzed using GraphPad Prism version 10.0.2 for macOS (GraphPad Software, San Diego CA).

5.6 Results

5.6.1 Panel selection for metabolic assessment

We selected a panel of six Cer and HexCer lipids to track metabolism by calculating the Pearson r correlations and generating correlation matrices from the Cer (Figure 5.1A) and HexCer (Figure 5.1B) pmol abundances reported in Chapter 4. We selected species that, when combined, produced the highest number of intra-subclass correlations such that all sub-species would be represented in our metabolic maps (Pearson $r > 0.9$, $p < 0.05$). Based on this panel prioritization, we tracked metabolism of 3 ceramides: Cer(d18:1/16:0), Cer(d18:1/23:1), and Cer(d18:1/24:1) and 6 cerebrosides: HexCer(d18:1/16:0) – GlcCer(d18:1/16:0) & GalCer(d18:1/16:0), HexCer(d18:1/18:0) – GlcCer(d18:1/18:0) & GalCer(d18:1/18:0), and HexCer(d18:1/25:0) – GlcCer(d18:1/25:0) & GalCer(d18:1/25:0).

5.5.2 rhAC treatment transiently alters GlcCer metabolism in wild-type fibroblasts

There were no changes in the combined abundances of Cer(d18:1/16:0), Cer(d18:1/23:1), and Cer(d18:1/24:1) after 24 or 48 h of rhAC treatment in wild-type (CTRL) fibroblasts (Figure 5.2A). HexCer(d18:1/16:0), HexCer(d18:1/18), and HexCer(d18:1/25:0) levels were elevated 24 and 48 h after treatment (Figure 5.2B). This increase was found to be the result of a statistically significant increase in GlcCer(d18:1) but not GalCer(d18:1) abundance that was restored by 48 h (Figure 5.2C, D). These data indicated that rhAC did not alter Cer(d18:1) or GalCer(d18:1) abundance in CTRL cells but transiently increased GlcCer(18:1) intracellular levels.

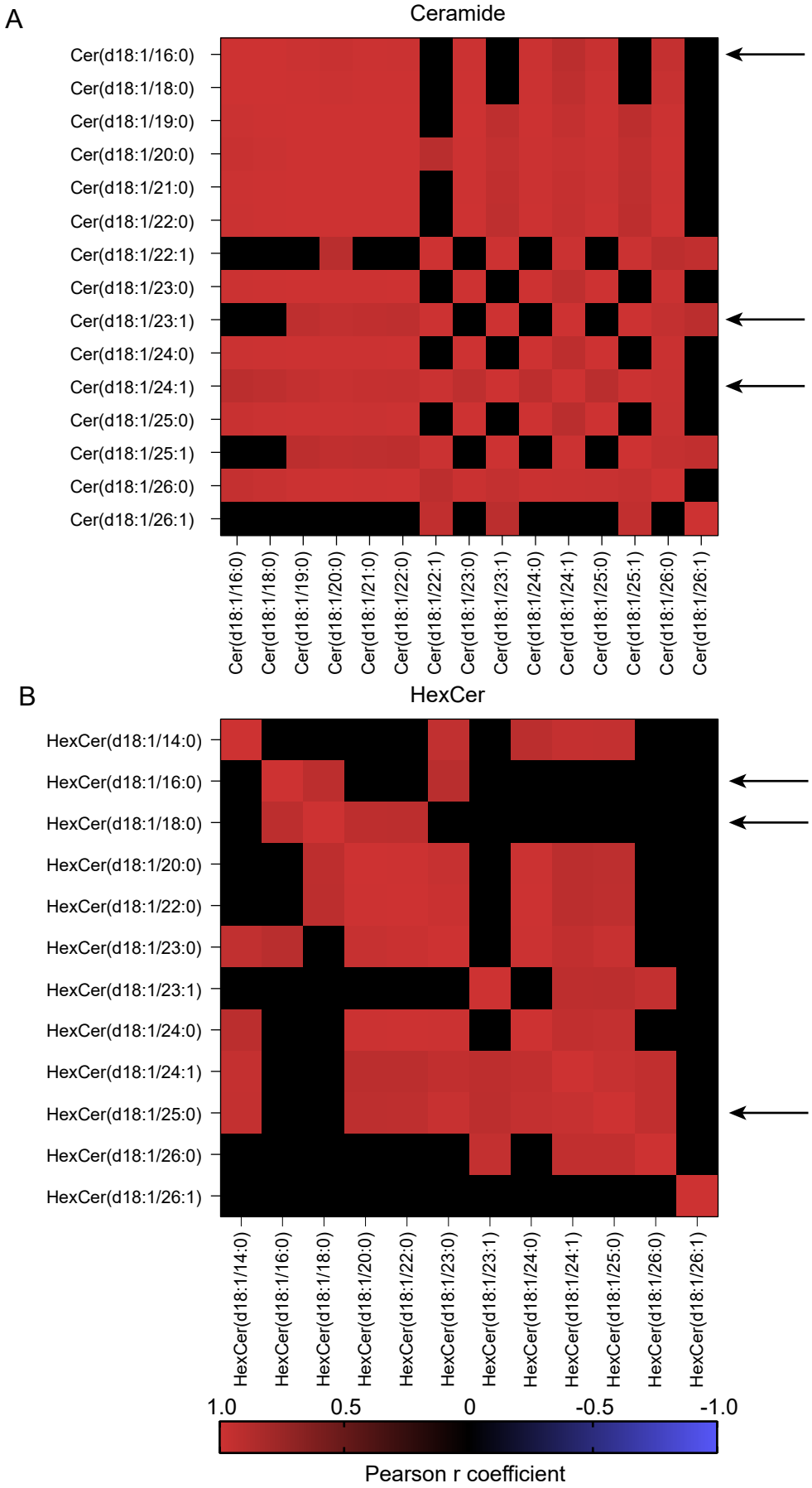

Figure 5.1: Selection of six Cer(d18:1) and six HexCer(d18:1) pairs for metabolic assessment. Pearson r correlation matrix for profiled A) Cer (d18:1) species, and B) HexCer(d18:1) species in SMA-PME patients. Pearson r values were calculated for each pair of lipids, generating each matrix. Significant Pearson r correlation values greater than 0.9, or less than -0.9, were included in the matrix. Arrows point to the species selected for the panel. Significance threshold of *p ≤ 0.05. n = 7 patients, with 3-4 biological replicates averaged per patient.

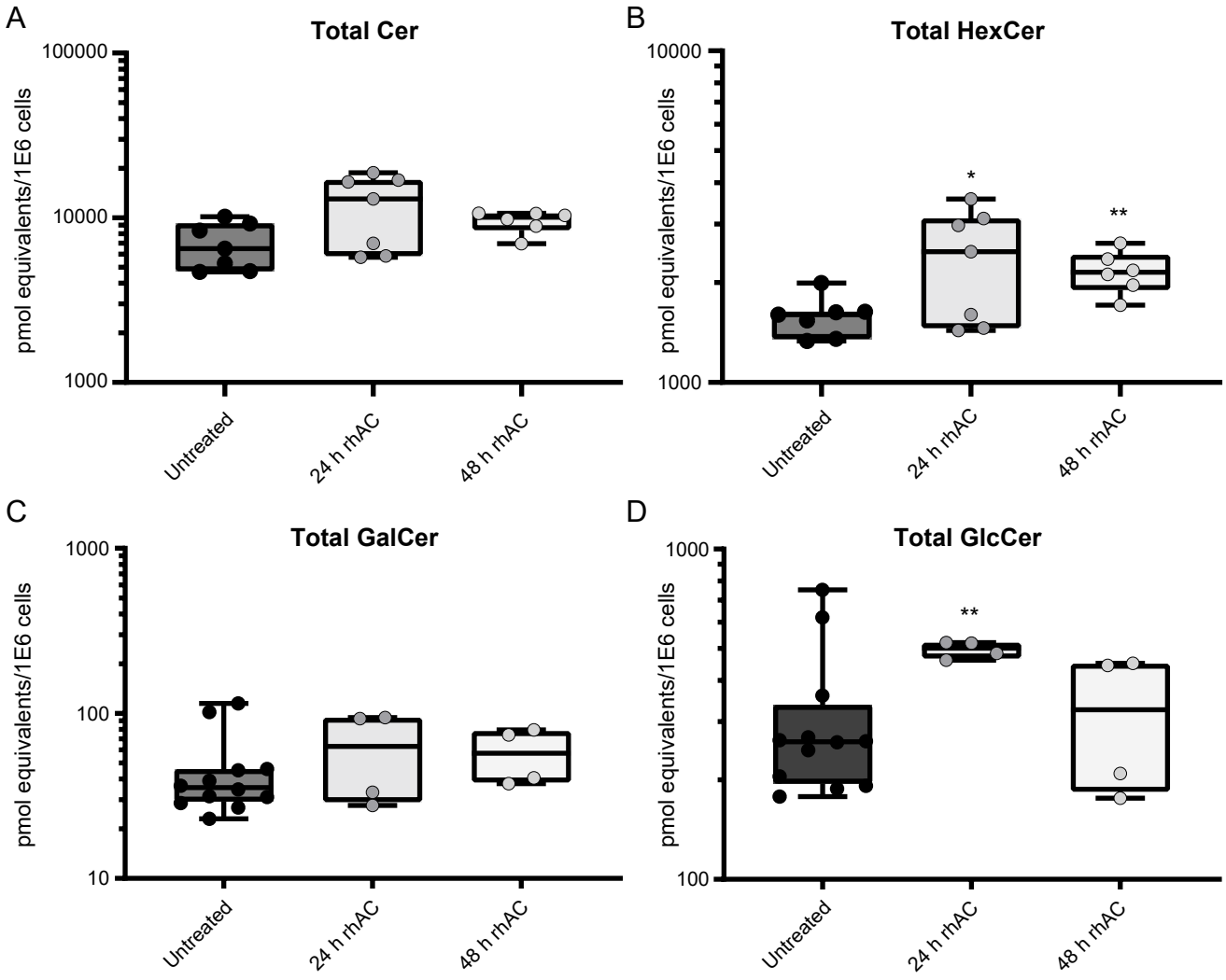

Figure 5.2: GlcCer levels, but not Cer or GalCer levels, are transiently elevated in CTRL cells following rhAC treatment. Box and whisker plots showing the combined abundance of A) the three Cers in the panel, B) the three HexCers in the panel, C) the GalCer component of the three panel HexCers, and D) the GlcCer component of the three panel HexCers. Data represent mean pmol equivalents (see methods) per 1E6 cells ± SEM from n = 2-4 replicate cultures of two or three different CTRL (wild-type) biopsies. Statistics were one-way Welch's ANOVA with post hoc tests of multiple comparisons performed using a false detection rate of 0.05% according to Benjamini, Krieger, and Yeukuteli[134]. * q ≤ 0.05, ** q < 0.01, compared to vehicle (complete-media)-reated cells.

5.5.3. rhAC treatment normalizes the levels of Cer, but not Glc or GalCer levels, in SMA-PME patient fibroblasts

We assessed Cer(d18:1), HexCer(d18:1), GalCer(d18:1) and GlcCer(d18:1) intracellular concentrations after 48 of rhAC treatment in fibroblasts derived from 6 SMA-PME patients and 2-3 CTRL lines (Figure 5.3). As reported in Chapter 3, ERT restored Cer(d18:1) levels in all SMA-PME patient cells (Figure 5.3A). We found here that rhAC did not affect cerebroside accumulation (Figure 5.3B). In SMA-PME patient-derived cells, accumulation of HexCer(d18:1) could be attributed to elevation in GlcCer(d18:1) not GalCer(d18:1) concentrations (Figure 5.3C, D). These aberrantly elevated GlcCer(d18:1) levels were not restored by ERT (Figure 5.3D).

5.5.4 rhAC treatment partially rescues Cer(d18:1) metabolism

To determine what the effect of rhAC supplementation was on overall sphingolipid metabolism, we calculated the product-to-precursor ratios (PtPrs) of each direct reaction as a proxy for enzyme activity. First, the Cer(d18:1) to HexCer(d18:1) PtPr was significantly elevated 2-fold in SMA-PME compared to CTRL yet restored to baseline after 48 h treated with rhAC (Figure 5.4A). Both Cer(d18:1) to GalCer(d18:1) and Cer(d18:1) to GlcCer(d18:1) PtPrs were significantly elevated in SMA-PME cells (Figure 5.4B, C) although only GlcCer(d18:1) abundances increased (Figure 5.3D). rhAC treatment rescued this product to precursor conversion (Figure 5.3B, C). Taken together, these data indicate that while rhAC treatment does not restore the levels of HexCer(d18:1), specifically GlcCer(d18:1) (Figure 5.3B, D) it does restore homeostatic balance by reducing intracellular Cer(d18:1) concentrations. Second, and importantly, ERT also restored the Sph(d18:1) to Cer(d18:1) ratio (Figure 5.4D) again by normalizing Cer(d18:1) levels. Third, rhAC reduced the Cer(d18:1) to SM(d18:1) conversion to near baseline (Figure 5.4E) presumably by eliminating the need to shunt rising Cer(d18:1) levels through the sphingomyelin pathway. Fourth, there was no change in GlcCer(d18:1) to LacCer(d18:1) PtPr

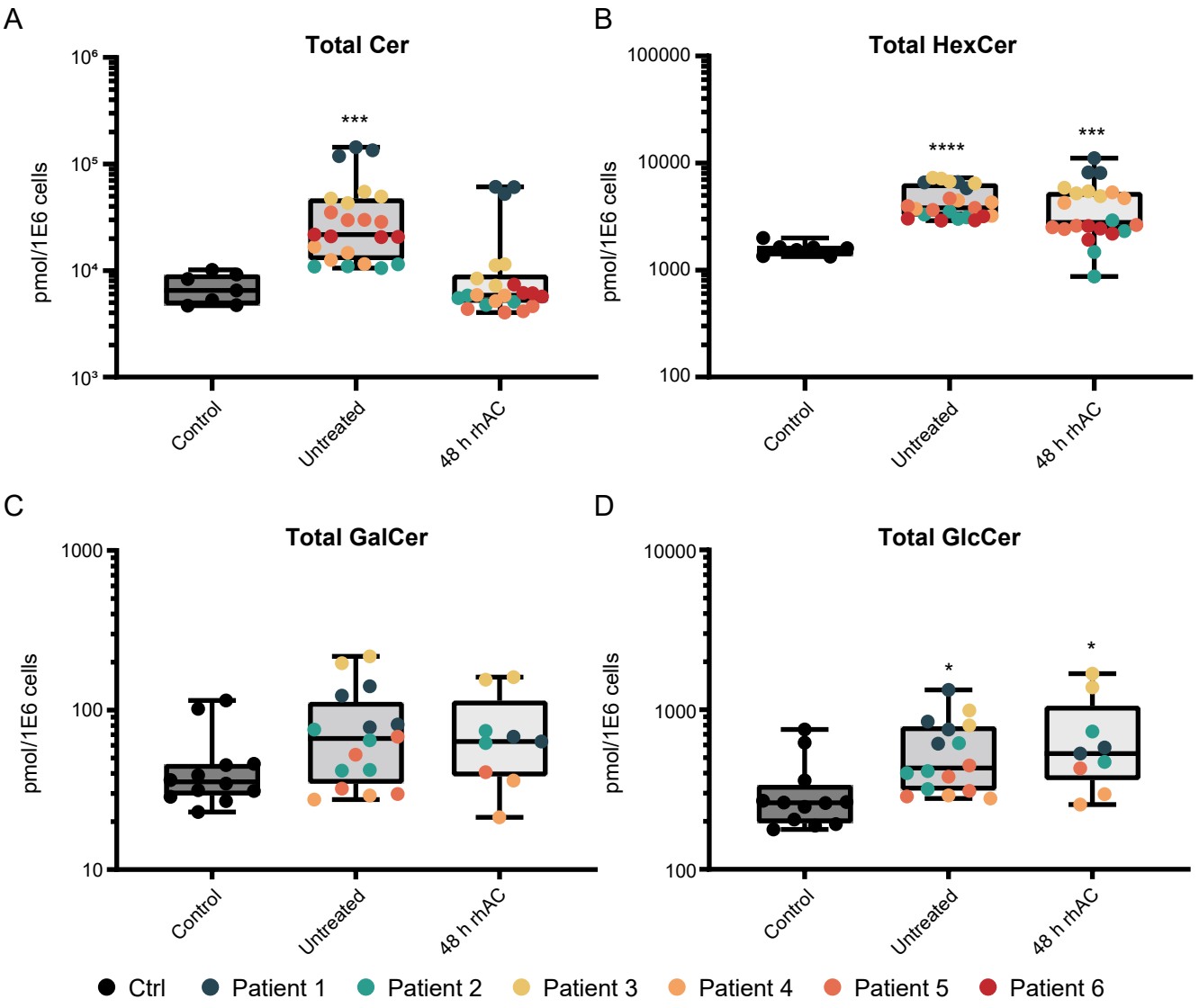

Figure 5.3: rhAC treatment for 48 h normalizes levels of Cer(d18:1) but not GlcCer(d18:1) in SMA-PME patient fibroblasts. Box and whisker plots showing the combined abundance of A) the three Cers in the panel, B) the three HexCers in the panel, C) the GalCer component of the three panel HexCers, and D) the GlcCer component of the three panel HexCers. Data represent mean pmol equivalents (see methods) per 1E6 cells ± SEM from n = 3-4 replicate cultures of two different CTRL and six different SMA-PME patients. Statistics were one-way Welch's ANOVA with post hoc tests of multiple comparisons performed using a detection rate of 0.05% according to Benjamini, Krieger, and Yeukuteli[134]. * q ≤ 0.05, *** q <0.001, **** q < 0.0001, compared to untreated cells.

modification pathway (Figure 5.4F) indicating that elevated GlcCer(d18:1) concentrations were not further shunted to more complex glycolipids and, as such, this pathway was not affected by rhAC such that GlcCer(d18:1) levels remained elevated in treated and untreated cells.

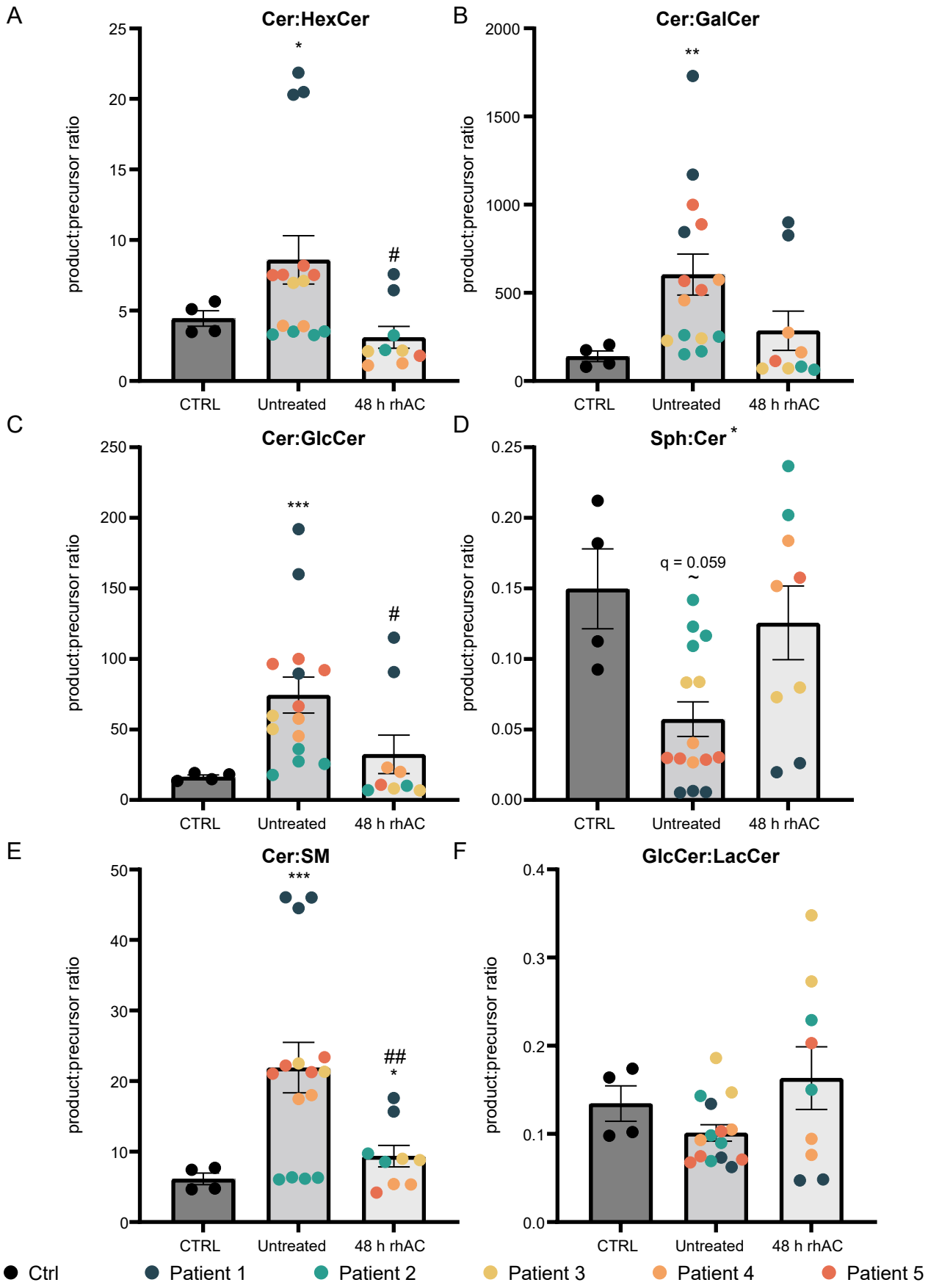

Figure 5.4: rhAC treatment normalizes Cer(d18:1) metabolic flux in SMA-PME fibroblasts. Product-to-precursor ratios (PtPrs) were calculated using the combined abundances of the three Cers, and the three HexCers in the panel compared to total Sph, SM and LacCer content. Bars represent mean ± SEM, each point depicts a biological replicate. In SMA-PME cultures, data represent 2-4 replicates of 5 patient cells, each colour-coded by patient. Statistics were one-way Welch's ANOVA and false detection rate of 0.05% according to Benjamini, Krieger, and Yeukutel[134]. * q ≤ 0.05, ** q < 0.01, *** q < 0.001 compared to Ctrl untreated cells. # q ≤ 0.05 compared to SMA-PME untreated cells. ~ q approaching significance.

5.7 Discussion

ERT is one of the major tools in combating rare lysosomal storage disorders, and for the past three decades, it has been used to treat Gaucher disease in 1991 and expanded to a handful of other rare diseases since then[210, 212]. To date, no-one has applied ERT to SMA-PME, and our aim in this study was to determine if ERT could normalize the aberrant sphingolipid metabolism detected in SMA-PME patient fibroblasts. We tracked metabolism using PtPrs as they have previously been used as both diagnostic[213] and predictive[214] factors in disease outcome. We found that treating SMA-PME patient fibroblasts with rhAC had the capacity to relieve the build-up of Cer(d18:1) but not GlcCer(d18:1), as well as normalize the sphingolipid metabolic network through normalizing PtPrs. These data suggest that ERT could have utility as a treatment for SMA-PME.

The most common conditions treated by ERT are lysosomal storage disorders, specifically those that are monogenetic. Our previous study demonstrated that while SMA-PME results from lysosomal aCDase deficiency, cellular pathology is extra-lysosomal with accumulation of ceramide expanding the plasma membrane and not sequestered in the lysosome. Despite this unique phenotype, we find that lysosomal targeted rhAC could reduce ceramide content and restore, in part, metabolic homeostasis. Recently, He et al examined the use of rhAC for ERT within Farber's disease[172] and demonstrated that ERT was well tolerated in animal and able to reverse the Cer storage in lysosomes[172]. Our data in SMA-PME cells is consistent with this study and expands the use of ERTs to extra-lysosomal lipid pathologies.

While the observed reduction of Cer in the SMA-PME patient cells was expected, the results surrounding HexCer were surprising. Previously, aCDase had been shown to have activity towards HexCer[44, 45, 182, 215], and therefore we expected that treatment with rhAC would reduce the build up of HexCer within the patient cells. While rhAC did not rescue the HexCer(d18:1), specifically GlcCer(d18:1) accumulation phenotype, ERT did restore Cer to GlcCer PtPrs to baseline levels. This

suggests that even though the rhAC treatment did not alter the GlcCer build up in patient fibroblasts, the treatment did correct the underlying metabolism within these cells by restoring Cer(d18:1) equilibrium.

While our results are promising in terms of the efficacy of ERT, there are still some questions to be answered. The most pressing of which, is what are the clinical implication of these results? The mechanism by which mutations in *ASAH1* result in the motor neuron degeneration at the core of the muscular atrophy, or the development of myoclonic epilepsy, is currently unknown. Studies involving kainic acid induced seizures, have demonstrated elevated levels of Cer associated with apoptotic neuronal loss[216, 217]. It has yet to be determined whether intraneuronal accumulation of Cer elicits neuronal death in SMA-PME and this question is being addressed by colleagues in the Bennett/Dyment laboratory using IPSC-derived patient neurons. It may be that it is the disruption of Cer synthesis that alters neuronal function. Previous studies have seen myoclonic seizures following the loss of Ceramide Synthase 1 and 2, and a resulting reduction of Cer species[218, 219]. It is suggested that this imbalance triggers an ER stress response, leading to neurodegeneration and thus myoclonic epilepsy[218], or by some other mechanism, such as myelin instability leading to degeneration[219] which will require investigation in SMA-PME. Further, the role of elevated HexCer(d18:1) or more specifically, GlcCer(d18:1), is also unclear. Wenger *et al* described a patient, who died of a neurologic disorder with myoclonic epilepsy as a symptom, who in post-mortem brain tissue was found to have elevated levels of GlcCer, which was not found in the brains of controls[220], implying that dysregulated GlcCer is also associated with myoclonic epileptic type symptoms. Thus, if it is the balance (or flux) between Cer and GlcCer that is the underlying cause of the symptoms, our PtPr data indicates that with rhAC treatment, the balance for most of these sphingolipid metabolic pathways is corrected. These data imply that ERT treatment could normalize the sphingolipid metabolism within these cells, thereby eliminating the metabolic cause of these symptoms.

Chapter 6 : General Discussion

In this thesis, I examined changes in lipid metabolism linked to genetic variation in lipid modifying genes that underlie three rare childhood diseases: *ANO6*-determined rare variant form of NPS, and *ASAH1*-determined FL and SMA-PME.

In Chapter 2, I followed the natural history of two NPS patients and identified novel *de novo* mutations in their *ANO6* gene, c.1414G>C, p.G472R and c.1830_1832delAAT, p.ΔI611, altering *ANO6* channel activity, scramblase activity, and glycerophosphoserine homeostasis. To provide insight into disease pathogenicity, I characterized a novel mouse model of this disease based on the G472R patient variant. I showed that this variant has an extremely low penetrance, with 90% of carriers unaffected and 10% lost to embryonic lethality or, rarely, presenting perinatally with NPS-like pathology (Figure 6.1).

In Chapter 3, I characterized the clinical presentation and phenotype:genotype relationships of six new patients with SMA-PME caused by *ASAH1* mutation, reporting that patients with the most common c.125C>T,p.Thr42Met variant develop proximal weakness in early childhood as their initial symptom whereas the heterozygous splicing variant c.456A>C is associated with sensorineural hearing loss, and the recurrent c.124A>G, p.Thr42Ala variant is linked to a less severe seizure presentation. In all cases, clinical severity was not linked to the extent of aCDase deficiency but rather to the pathogenic accumulation of ceramides that I show, for the first time, can be ameliorated *in vitro* by ERT (Figure 6.2).

Finally, in Chapters 4 and 5, I identified two distinct sphingolipid metabolic fingerprints that distinguished FL from SMA-PME. Specifically, I show that FL is, as expected, a classic lysosomal storage disorder, wherein Cer and HexCer accumulate and Sph is depleted in the lysosome whereas, in SMA-PME, accumulation of Cer, HexCer, are associated with maintenance of Sph and elevations in HexSph, unexpected in an aCDase deficiency disorder. In SMA-PME, lipids appear to accumulate not

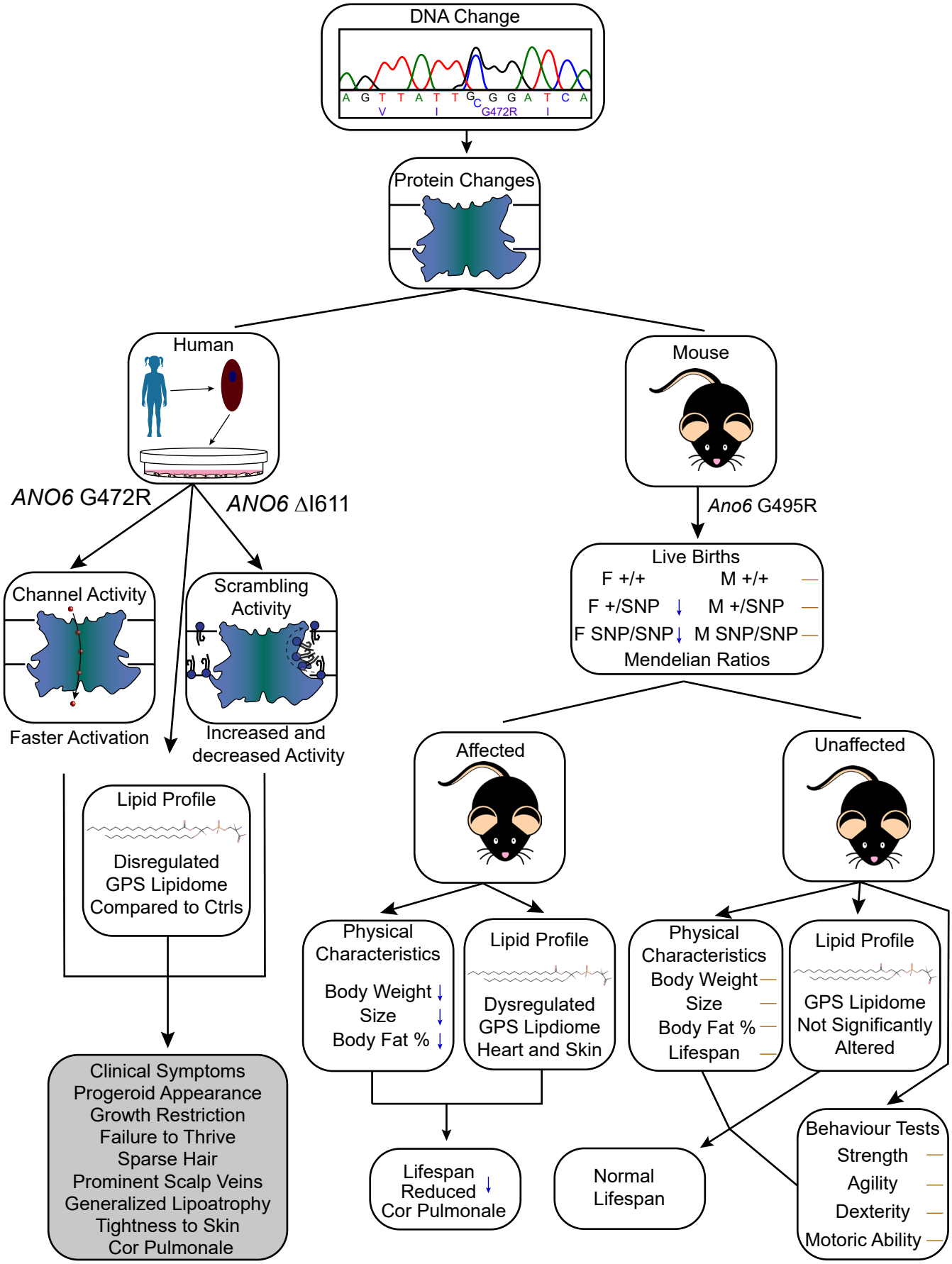

Figure 6.1: Summary of ANO6-NPS findings presented in this thesis. Mutations in ANO6 result in nucleotide changes in ANO6 protein. These mutations were studied in vitro using human cells, as well as in vivo using a CRISPR/Cas 9 mouse system. The mutations in human cells resulted in altered protein activity compared to wild-type, and alterations to the lipid profile in patient fibroblasts. It is currently unclear how these changes to ANO6 function result in the clinical symptoms of ANO6-NPS. In the mice, the mutations lead to two populations, with the affected population displaying similar features to the ANO6-NPS patients. More work is necessary to identify the mechanisms for these findings. Grey boxes represent what was known prior to this thesis, and white boxes represent new findings. Abbreviations: GPS – glycerophosphoserine; SNP – single nucleotide polymorphism.

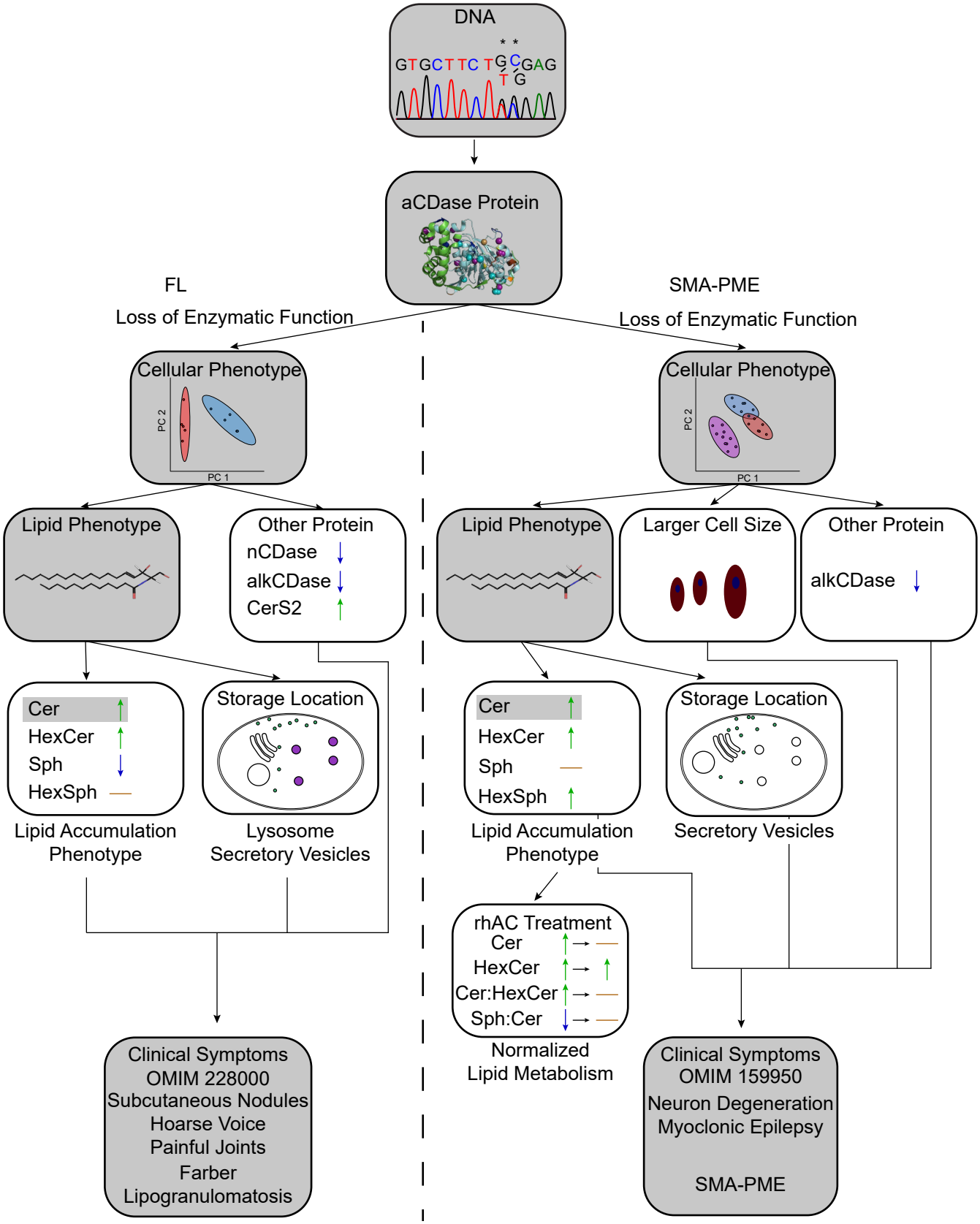

Figure 6.2: Summary of FL and SMA-PME findings from this thesis. Pathogenic genetic mutations in *ASAH1* result in mutant aCDase protein. FL and SMA-PME causing mutations result in loss of enzymatic function, leading to biochemical and cellular changes within these patient cells compared to control, and each other. We performed in vitro studies on FL and SMA-PME patient primary fibroblasts, examining characteristics of these cells. In these studies, we confirmed previously known changes to the lipid profile of these cells, as well as expanded upon the lipid phenotype by examining other sphingolipid subclasses, and examined the localization of ceramide within these cells. Further, we expanded upon the biochemical signature of these diseases discovering other enzymes affected, and found that SMA-PME cells were larger than their FL counterparts. Finally, we found that rhAC treatment normalized the sphingolipid metabolic network within SMA-PME cells. Abbreviations: FL – farbers disease/lipogranulomatosis. SMA-PME – spinal muscular atrophy with progressive myoclonic epilepsy. aCDase – acid ceramidase. nCDase – neutral ceramidase. alkCDase – alkaline ceramidase. CerS2 – ceramide synthase 2. Cer – ceramide. HexCer – hexosylceramide. HexSph – hexosylsphingosine. Sph – sphingosine. rhAC – recombinant human aCDase.

in the lysosome but at the plasma membrane expanding cell surface and increasing cell size. ERT was able to normalize much of the Cer content within the cells as well as the wider metabolic network specific to SMA-PME, as a proof of concept for ERT in the treatment of SMA-PME patients (Figure 6.2).

In this general discussion, I will discuss in more detail the findings presented throughout this thesis in context with what is known about these disorders. Further, I will indicate where gaps in knowledge still remain and speculate on potential next steps.

6.1 Insights into *ANO6*-driven Neonatal Progeroid Syndrome

The low penetrance of NPS symptoms in our G472R (murine G495R) mouse model suggested other genetic or metabolic modifiers capable of restoring the primary defect of GPS metabolic dysfunction. Thus, we have begun to look for other variants that might act with *Ano6* to increase penetrance. Two candidates are *POLR3A* and *LMNA.*

Since our identification of mutations in ANO6 associated with rare variant forms of NPS, it reported that variants in *POLR3A* gene are the genetic determinant of WRS[81-83, 221]. Specifically, the variants *POLR3A*:c.*18C>T, *POLR3A*:c.3G>T, p.M1*, *POLR3A*:c.490+1G>A, *POLR3A*:c.760C>T, p.R254*, *POLR3A:*c.1048+5G>T, *POLR3A*:c.1572+1G>A, *POLR3A:*c.1800C>T, p.I600I, *POLR3A*:c.1909+18G>A, *POLR3A:*c.1909+22G>A, *POLR3A*:c.2005C>T, p.R669*, *POLR3A:*c.2474C>G,p.S825*, *POLR3A*:c.2617-1G>A, *POLR3A*:c.2617C>T,p.R873*, *POLR3A:*c.2707G>A, p.G903R, *POLR3A:*c.3206G>A, p.R1069Q, *POLR3A*:c.3243-2A>G, *POLR3A*:c.3337-5T>A, *POLR3A*:c.3337-11T>C, *POLR3A:*c.3392A>G, p.K1131R, *POLR3A:*c.3772_3773delCT,p.L1258Gfs*12, *POLR3A:*c.3874G>A, p.D1292N, *POLR3A:*c.4003G>A, p.G1335R, and a deletion comprising exons 12-15, have all been identified within the *POLR3A* gene of WRS patients[81, 82, 221]. Interestingly, the majority of cases reported show compound mutations resulting

in WRS symptoms; only four patients developed symptoms with a single mutation, specifically the POLR3A:c.3772_3773delCT,p.L1258Gfs*12, POLR3A:c.3874G>A,p.D1292N, and POLR3A:c.2707G>A, p.G903R mutations[221] suggesting "two hits" are required for WRS to manifest. Mutations in POLR3A have also been associated with various other diseases, including sporadic and recessive spastic ataxia[222-225], hereditary spastic paraplegia[223, 224, 226-228], and POLR3-related leukodystrophy also referred to as 4H syndrome[229]. The POLR3A:c.1909+22G>A mutation is the most common[81, 82, 221-229]. Patient 2 in this study, with the ANO6:pΔI611 mutation, also carries a POLR3A:c.1909+22G>A mutation, but without any other *POLR3A* mutation, it was thus considered not to be pathogenic. One possibility is that harbouring both *ANO6* and *POLR3A* mutations are variants increase NPS penetrance although it has yet to be determined whether *POLR3A* has any impact on the glycerophosphoserine lipidome associated with pathology in this study. *POLR3A* encodes for the largest subunit of RNA Polymerase III, a polymerase which transcribes genes encoding ribosomal 5S RNA, tRNAs, mitochondrial RNA-processing RNA, and others[230], and the current theory is that loss of function mutations in *POLR3A* result in NPS (WRS)[231]. Loss of function mutations in this gene would result in an overall loss of protein transcription, beginning a cascade that leads to the symptoms of NPS. It would be interesting to test whether this includes GPS modifying enzymes.

Another form of progeria, HGPS, is caused by mutations in the *LMNA* gene, including LMNA:p.R471C in exon 8; LMNA:p.R527C in exon 9, and LMNA:p.G608S, LMNA:c.1824C>T, and LMNA:c.2036C>T in exon 11[232, 233]. Patient 1, with the ANO6:p.G472R mutation was found to harbour a LMNA:c.1698C>T p.H566H mutation, which had yet to be associated with any laminopathies[84]. *LMNA* encodes for both Lamin A and Lamin C, proteins that are found in the nuclear lamina and provide structure to the nuclear envelope, and the mutation found in LMNA which results in HGPS leads to an abnormal form of Lamin A known as progerin, which when integrated into the nuclear lamina disrupts the structure of the nucleus, leading to nuclear integrity failure resulting in premature cell death and the

clinical features of NPS[234]. Again, it remains to be determined how LMNA might influence lipid homeostasis.

It has yet to be determined how the variants in *ANO6* might directly impact on GPS metabolism beyond increasing scrambling to the outer leaflet in the gain of condition situation or accumulating lipid at the inner leaflet in the loss of function condition. Over the last few years, there has been a lot of interest in determining the structural-functional relationships in the activity of ANO6; how the activation by calcium allows for the transport of both ions and lipids to and from the cell, and what structural changes occur to facilitate these activities. While detailed discussions on the structure-function relationship of ANO6 is beyond the scope of this thesis, a basic discussion can provide some insights. One recent study, published by Arndt et al[235], may shed some light as to how GPS lipids may accumulate in our models. One of the structural features that has been identified in ANO6 appears to be a groove throughout the plasma membrane spanning face of the protein, formed by the positions of alpha helix 4, 5, and 6, where there are hydrophilic residues present[235]. It has long been suspected, that due to the presence of these hydrophilic residues embedded within the hydrophobic membrane-spanning domain of the protein, that this groove is where the lipids and ions travel during protein activation. In order to determine which residues within this groove are important for the scrambling or channel activities of this protein, Arndt et al performed a scanning mutagenesis of this groove region, mutating the residues to alanine, and measuring the scrambling and ion conductance of these mutants compared to wild type. Relevant to this work, the mutants I611A and I612A showed significant alterations in activity compared to wild-type. When either of these mutations were introduced, there were significant effects on the channel activity – in both cases the EC50 of the mutant was reduced compared to wild-type, meaning less calcium was required to produce the same activity and thus enhanced channel activity was observed, and in the I612A mutant an increase in scrambling was observed. With our patient mutation ΔI611, we observed an increase in channel activity, in line with this report, but we also observed an increase in scrambling

activity, which seems to be counter to what this paper observed. However, because the mutation in our patient was a deletion, one of the potential results of this, is the isoleucine at position 612 is effectively substituted with the methionine at position 613, resulting in a I612M mutation. While this mutation is not equivalent to the I612A mutation from Arndt *et al*, this could explain why in our patient we are seeing results more similar to the I612A mutation than the I611A mutation.

Throughout Arndt *et al.*'s report, they performed cryo-EM experiments of the mutant protein they generated, in order to visualize the structural changes occurring within these proteins. One point they found, is that during the activation of ANO6, they found that helix a3 had a large conformational change with the hinge point being Gly 473. Arndt *et al* wanted to determine what effect, if any, modifying this identified hinge residue on the activity of ANO6 would be. Generating a G473A mutant did not alter the activity of the protein, however, they found the G473P mutation resulted in a loss of activity in scrambling assays or in patch clamp recordings, thus restricting the movement potential of this residue seems to prevent the channel from opening. This finding is relevant to this thesis because of our other patient mutation, G472R. According to the canonical sequence of ANO6 as defined on uniprot[236], Gly473 should instead be Gly472, the mutated residue in our patient. In our results, the G472R mutant resulted in a mix of outcomes; evidence suggesting to a constitutively open ion channel, although with less maximal activity, and a slight reduction in scrambling activity compared to wild-type at all concentrations of A23187 ionophore. It is possible then, that the reason for this is in the arginine substitution. With this mutation, due to the size of arginine compared to glycine or alanine, it could limit the conformation of this part of the helix, preventing it from fully opening to wild-type levels, or fully closing. This could lead to seeing a constitutively open channel to allow ions to pass through, but not lipids, whereas when activated via the addition of calcium, the channel cannot fully open, resulting in a reduced amount of lipid transport out of the cell and thus the accumulation observed in this thesis. The interaction of the results presented in this thesis and the structural characteristics demonstrated by Arndt

et al, raise an interesting point; determining the structural effects of disease-causing mutations could lead to insights into protein function, and further mechanistic insights as to how these mutations are causing the observed results.

The embryonic lethality is consistent with reports that ANO/TMEM16 proteins impact on fertility. In a report by Zhang et al[237], they found that the genetic ablation of TMEM16F and the loss of scrambling activity resulted in the loss of trophoblast fusion, and thus placental development was affected. They also found that the TMEM16F knockout animals displayed impaired syncytiotrophoblast formation, abnormally enlarged maternal blood sinuses, and malformation of fetal blood vessels, resulting in intrauterine growth restriction and perinatal lethality[237]. Intrauterine growth restriction is one of the symptoms of NPS[238]. It could be argued that since the G472R mutation produced a loss of function in the scrambling ability of ANO6, as demonstrated in the HEK293 cells, perhaps the G495R mutation in our mouse model similarly produced a reduction in scrambling activity in the affected animals, which may be sufficient to provoke the same lethality described by Zheng *et al*, in these mice. In this study, we did not identify when or how embryos were lost thus it is possible that fertility also impacted on the observed Mendelian ratios. In a study by Gyobu et al[239], they discovered that the loss of another anoctamin protein, TMEM16E/ANO5, resulted in lower fertility due to a reduction in sperm motility, preventing fertilization of eggs. This opens the possibility that there are other pregnancy mechanisms affected by anoctamins, possibly including ANO6/TMEM16F.

6.2 Insights gained into SMA-PME and FL

In the second portion of this thesis, I examined the rare childhood diseases FL and SMA-PME. While these two diseases have been studied and compared before[160, 240, 241], this thesis expands these investigations into further lipidomic and metabolic network analysis. In doing so, I identified key

lipidomic and metabolic signatures of these diseases. In Chapter 4 I expanded the biochemical signature/features of these diseases, and in Chapter 5 I began exploring ERT as a potential treatment for SMA-PME.

Although in this thesis, I polarize the clinical presentations of FL and SMA-PME as being primary peripheral/systemic (FL) and isolated neurological (SMA-PME), it may also be that these two diseases represent the polar ends of a spectrum of aCDase deficiency disorders (Figure 6.3). One possible organization of this spectrum is described by theory 1 (Figure 6.3A). In this model, FL is strictly more severe than SMA-PME, which is more severe than control. This model came about with the initial indications that FL had lower reported levels of aCDase activity (<10% of control activity[186]), whereas SMA-PME had higher levels of aCDase activity (~30% of control activity[146]), and separately, the life expectancy for most FL cases was much lower than that for SMA-PME, with a life expectancy of approximately 2 years for the classical form of FL[178], whereas SMA-PME typically presents later in life, and the life expectancy is often into late childhood or early adulthood[177]. With this model, along with the further decrease in the aCDase activity, we would expect a significantly higher amount of Cer accumulation in FL cells than in SMA-PME cells. Some of the data presented in this thesis supports this model; mainly, we found that in FL there was a broader hypometabolic network dysregulation found than in SMA-PME, as we identified this network dysregulation occurring in more lipid species in FL than in SMA-PME, as well as seeing more of the sphingolipid metabolic enzymes affected. However, there are data refuting this model. Firstly, Patient 1 (described in Dyment 2014[116]) was identified as having SMA-PME with no FL like symptoms, but critically, had reported less aCDase activity than the reported FL patients. Further, some of the data presented in this thesis also refutes this model. Specifically, if this model is correct, we would expect a higher amount of Cer accumulation in FL than in SMA-PME. However, our data did not show this, as there was comparable amount of total Cer and total HexCer between FL and SMA-PME. The other major finding we had that refuted this model was

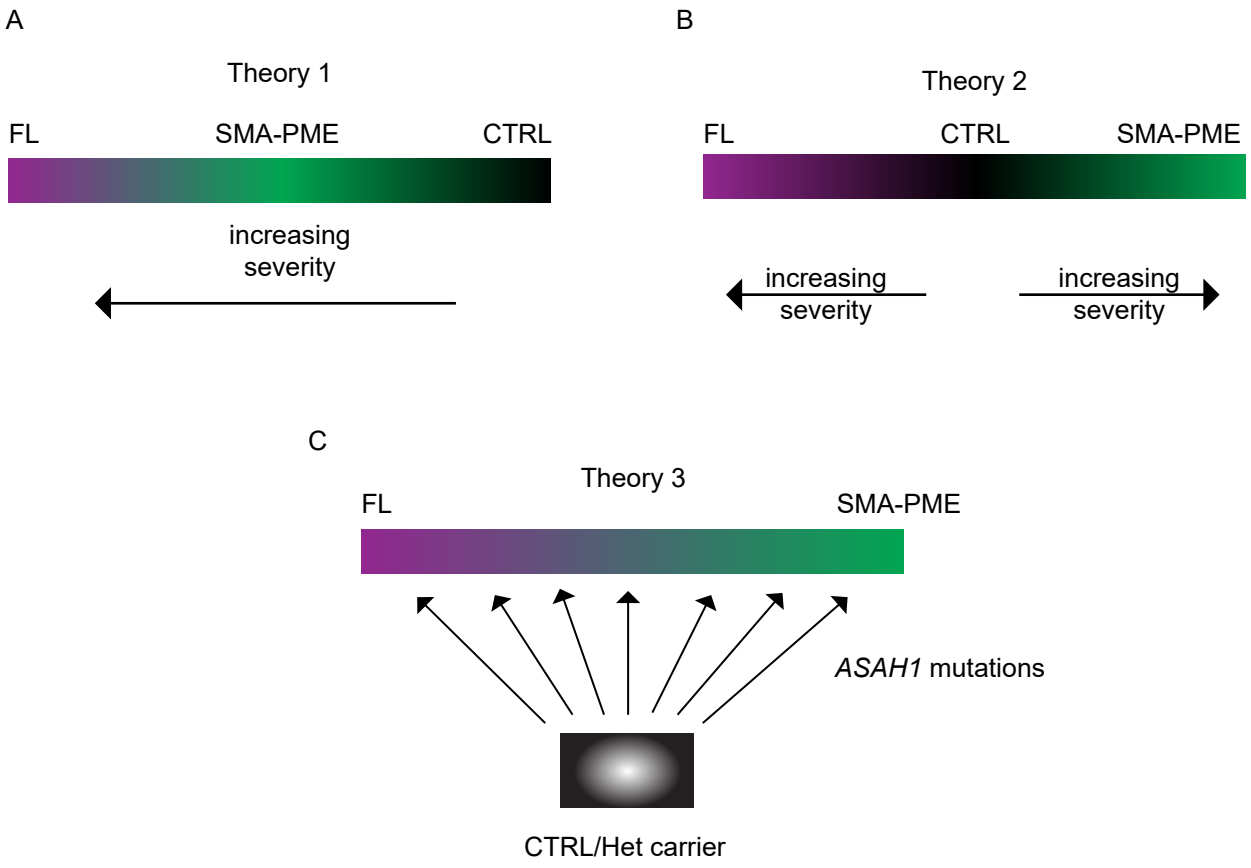

Figure 6.3: Proposed theories describing the FL-SMA-PME spectrum. A) Theory 1 depicts a model where FL is more a more severe form of aCDase deficiency. B) Theory 2 depicts a model where FL and SMA-PME are on opposite ends of the aCDase deficiency spectrum. C) Theory 3 depicts a combined model, where FL and SMA-PME are on opposite ends of the aCDase spectrum, and where control is on a different axis than the aCDase deficiency spectrum.

the subcellular localization of lipid accumulation, specifically that Cer did not accumulate in the same way in SMA-PME than in FL, implies that there may be fundamentally different disease mechanisms occurring, suggesting FL is not simply a more extreme version of SMA-PME, as this model suggests. Thus, a new model is needed.

In a second model (Figure 6.3B), FL and SMA-PME are at opposite ends of the spectrum, with CTRL in the middle. This suggests that while FL and SMA-PME are on a spectrum, they're effectively on opposite ends of this spectrum. This model represents the difference in disease mechanisms observed with the trafficking results, which is our main finding which supports this model. These data suggest that fundamental mechanisms occurring within these diseases are different; in FL there is substrate accumulation within the lysosome, showing a standard LSD disease mechanism, whereas in SMA-PME we did not see this lysosomal accumulation, instead evidence suggesting sequestering at the plasma membrane, indicating disordered trafficking or recycling, and thus a different disease etiology. Interestingly, a similar membrane accumulation does not appear to be occurring in FL; previous reports[242] did not report evidence of Cer accumulation at the membrane in FL cells, further indicating that these two diseases offer different mechanisms. However, while these data support this model, there are observations which are incompatible with it. First, while there are the above described differences in disease mechanism, there are features which overlap between the two diseases, including similar accumulation of total Cer and HexCer, but more importantly, patients have been identified with symptoms from both FL and SMA-PME[159, 173, 184]. This possibility of having a mixture of symptoms indicates that the diseases can't be completely different, which is what this model indicates. So, while this model demonstrates the difference in ceramide trafficking, it does not fully indicate how these diseases relate.

Thus, I propose a third, combination model of these two diseases (Figure 6.3C). In this model, FL and SMA-PME are on opposite ends of the spectrum, representing the differences in mechanisms

identified by the Cer localization, but crucially CTRL is on a different axis, where the presence of loss of function *ASAH1* mutations indicates if the patient is CTRL, or on the FL/SMA-PME spectrum. This model combines features of models 1 and 2; first, the two diseases are on a spectrum, where the different disease mechanisms are represented, but the spectrum of clinical presentations can also be depicted. Since CTRL is not on this axis, there is no direct comparison for severity of the two diseases, removing that weakness from model 1, but also allows for intermediate phenotypes, such as patients with clinical features of both diseases[159, 173, 184] , and shows that there are overlapping features of the diseases, such as similar levels of Cer accumulation, and potentially similar levels of aCDase loss of function. All together, this model fits our data, and the features of these diseases reported previously, better than does model 1 or 2.

6.2.1 SMA-PME and ERT treatment

The proposed combination model for the FL - SMA-PME spectrum in part relies on the observed differences in Cer accumulation within SMA-PME cells, which was one of the major findings from Chapter 4. This accumulation phenotype calls into question the major patho-mechanism for SMA-PME. The classical understanding of LSDs is that there is a deficit in one of the lysosomal acid hydrolases, resulting in a toxic build up of substrate in the lysosome. More recently, with the increasing view on lysosome function within the cell[203], other manifestations of LSDs are being explored, including abnormal storage of substrates unrelated to the defective enzyme, and aberrant trafficking of vesicles within the cell[203]. With this expanded view on LSDs, it becomes likely that SMA-PME falls under this extended definition of an LSD; it is a non-standard LSD wherein there is aberrant trafficking of vesicles containing substrate within the cell, similar to Niemann-Pick disease type C[243].

But what does this classification mean for potential treatment? ERT is well suited to treat the classical LSDs, as the substrate build up in the lysosome can be reduced by the introduction of a functional copy of the enzyme into the lysosome, as has been demonstrated in various LSDs, such as Gaucher disease, Fabry disease, Pompe disease, and MPS I, II, VI[210, 244] , and is undergoing trials for other diseases, such as FL, under ACG-801 with Aceragen. Recombinant enzymes when modified with a mannose-6-phosphate (M6P) tag are effectively taken up by cells and directed to the lysosome[208, 245], where they can then perform their function, and reduce the buildup of substrate within the patient cells. It is unclear, however, how ERT would fare as a treatment for a non-classical LSD, or if other types of treatments would be necessary. To examine this question, we used ERT as a proof-of-concept treatment for SMA-PME. This thesis, to our knowledge, is the first use of ERT on SMA-PME. Excitingly, we found that when treating SMA-PME patient cells with rhAC, that the metabolism was normalized/trending towards normalization, and the large excesses of Cer were reduced. While more studies will be required to determine proper dosing, enzyme concentration, and other factors to maximize the therapeutic capacity, this thesis shows that ERT could be used as a treatment for SMA-PME and excitingly, perhaps other non-classical LSDs as well. This discovery brings forward a question: if the Cer is not being localized to the lysosome, as our trafficking data implies, how does lysosomal targeting of the recombinant enzyme reduce the concentration of Cer within the cell?

My hypothesis for how this occurs has to do with the M6P receptor (M6PR) mechanism for delivering the enzyme to the lysosome (Figure 6.4). Prior to the presence of M6P tagged rhAC, the M6PR is at the plasma membrane along with an abundance of Cer – as we hypothesize that the Cer is accumulating at the plasma membrane (Figure 6.4A). Interaction of the M6P tagged rhAC with the M6PR induces endocytosis, wherein the enzyme is brought into the cell, but Cer is also brought into the cell through

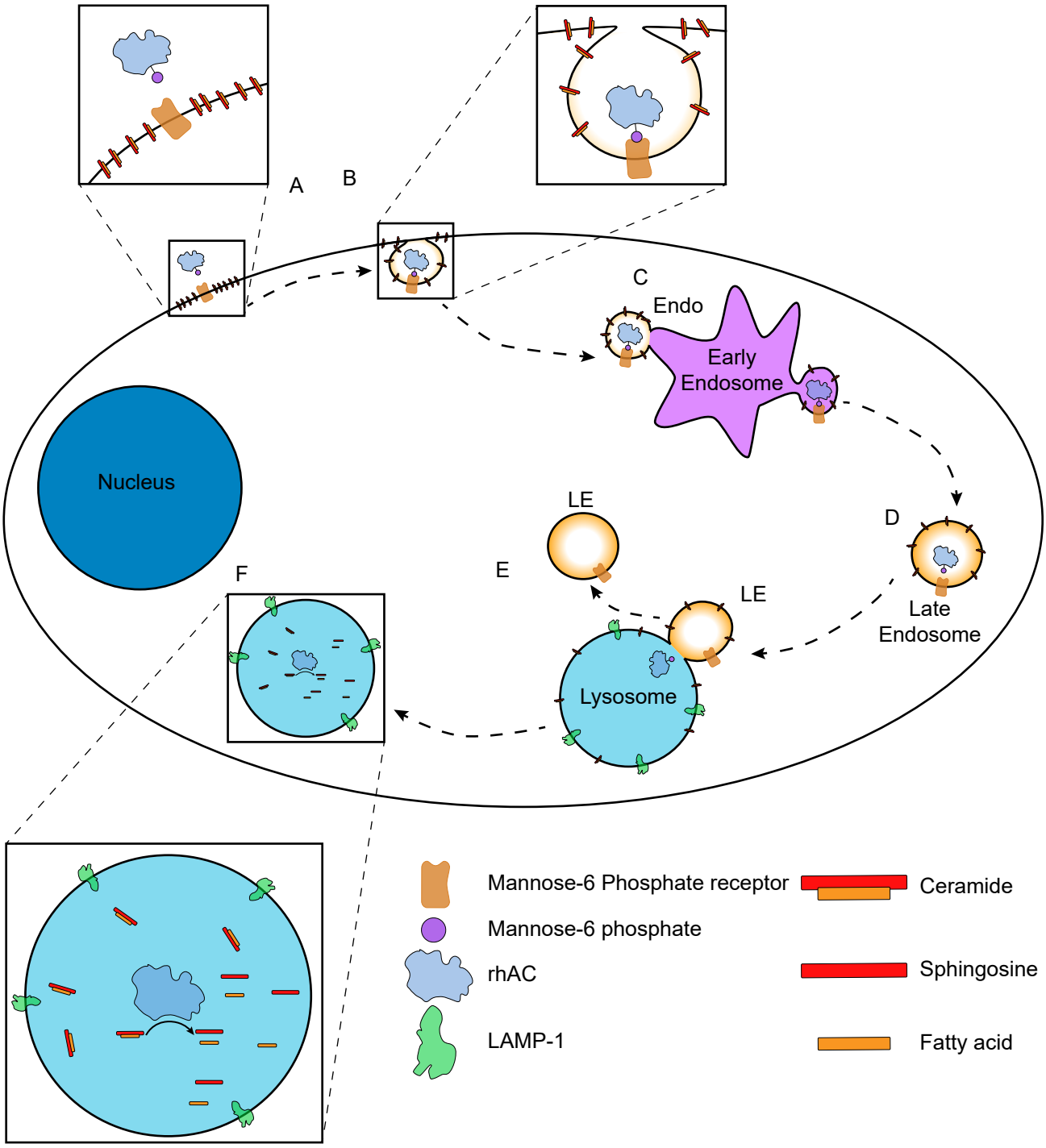

Figure 6.4: Proposed mechanism for Cer reduction upon rhAC treatment in SMA-PME cells. A) Mannose-6-Phosphate (M6P) tagged rhAC is recognized by and interacts with the M6P Receptor at the plasma membrane. B) M6P-tagged rhAC is endocytosed into the endo-lysosomal pathway after interaction with the M6P receptor. We hypothesize that excess Cer at the plasma membrane is also endocytosed with the rhAC. C) The endocytosed rhAC and Cer enter into the early endosome. D) Early endosome matures into late endosomes, where the rhAC dissociates with the M6P receptor. E) Late endosomes fuse with lysosomes, depositing the rhAC and the excess Cer into the lysosome, before recycling the M6P receptor to other cellular compartments. F) within the lysosome, rhAC performs its expected function, hydrolysing Cer into Sph and a free fatty acid.

Abbreviations: Cer – Ceramide; rhAC – recombinant human acid ceramidase; LAMP-1 – lysosomal associated membrane protein 1; LE – late endosome; M6P – Mannose-6 phosphate; Sph – sphingosine.

this endocytosis due to the excess build-up within the plasma membrane (Figure 6.4B). The endocytosed rhAC and Cer are transferred to the early endosome (Figure 6.4C) which mature into late endosomes. Due to the lower pH of the late endosomes (LE), the rhAC disassociates with the M6PR, allowing for transfer into lysosomes (Figure 6.4D). The LE fuses with the lysosome, depositing the rhAC, and in this hypothesis also the excess Cer, into the lysosome, before recycling the receptor back to the plasma membrane (Figure 6.4E). Once in the lysosome with the excess Cer, the rhAC is able to hydrolyse the Cer, thus reducing the build up, and allowing for the normalization of the sphingolipidome (Figure 6.4F).

This proposed mechanism also addresses why multiple treatments with rhAC were necessary; if only a portion of the Cer pool at the membrane is being endocytosed with each uptake event of rhAC, then perhaps the cells are exhausting the pool of Cer being brought to the lysosome, and the re-application of the rhAC is causing more Cer to be brought into the lysosome for hydrolysis. If the amount of Cer being brought into the lysosome with the rhAC is small in comparison to the amount of Cer the rhAC could hydrolyse, then perhaps further activation of the M6P pathway would further reduce the build up of Cer within the cells without requiring more rhAC infusions. This would reduce the amount of rhAC required for the same therapeutic effect. Further experimentation is required to fully elucidate the mechanism, half-life, and other features of this treatment to be able to move forward with potential preclinical and clinical trials.

This hypothesis could also explain why there was not a significant change in the amount of HexCer present within these patient cells. The proposed mechanism is based on Cer being carried with the rhAC to the lysosome, however, the fact that HexCer was not significantly altered raises the question: where is the increase in HexCer being stored? Since the addition of rhAC is not affecting the levels of HexCer, this implies that HexCer is not being stored in the lysosome, nor is it being stored at the plasma membrane; if it were, then the rhAC treatment would facilitate a reduction in the concentration of HexCer as well. Further study will be necessary to fully determine where each sphingolipid subclass is being

stored within these cells, to get a full picture as to the metabolic and trafficking changes within these cells.

6.4 Final summary

The initial aim of this thesis was to identify lipid-centric patho-mechanisms of ANO6-NPS, FL, and SMA-PME, and in doing so, enable new cause-directed therapeutic targeting for effective treatments of these diseases. Throughout this thesis, I have presented lipidomic data identifying changes to the lipid profiles of fibroblasts collected from patients with these diseases. In these lipidomic experiments, I identified fingerprints of these three diseases; First, I showed that not only is the distribution of lipids altered within ANO6-NPS patient fibroblasts, but the composition of the lipidome is also altered, perhaps indicating compensatory mechanisms occurring within these cells. Second, I showed differential accumulation and distribution profiles occurring within SMA-PME and FL patient fibroblasts. In this regard, this thesis was able to identify lipidomic alterations within patient cells, indicative both that FL and SMA-PME were different from healthy fibroblasts, but also that their lipidomes were different from each other. Along with these lipidomic experiments, this thesis also presented other metabolic features of these diseases. For example, in ANO6-NPS, we examined the consequences of the patient mutations on the channel and scrambling activities of ANO6/TMEM16F, and with FL and SMA-PME we identified alterations in the levels of other sphingolipid metabolic proteins, as well as differences in the distribution of Cer within FL and SMA-PME patient fibroblasts. Finally, within SMA-PME patient fibroblasts, as a proof of concept, we showed that ERT has the capacity to normalize the Cer accumulation, and potentially normalizing the overall lipid metabolism observed within the patient cells. Apart from demonstrating that ERT has the potential to be further developed into a treatment for SMA-PME, this experiment also addressed the second part of the aim of this thesis; using the lipid-centric patho-mechanisms identified in SMA-PME to enable new therapeutics for effective treatments.

Chapter 7 References

1. Casey B. Canadians Affected by Rare Diseases and Disorders: Improving Access to Treatment. Standing Committee on Health. 42nd parliament 1st session ed. Ottawa: House of Commons, 2019.
2. Drugs for Rare Diseases: Evolving Trends in Regulatory and Health Technology Assessment Perspectives. Ottawa: CADTH, 2013 Oct [updated 2016 Feb].
3. (NORD) NOfRD. Tay Sachs Disease - NORD (National Organization for Rare Disorders) [online]. Available at: https://rarediseases.org/rare-diseases/tay-sachs-disease/. Accessed 24-04-2022.
4. Lew RM, Burnett L, Proos AL, Delatycki MB. Tay-Sachs disease: current perspectives from Australia. Appl Clin Genet 2015;8:19-25.
5. Rozenberg R, Pereira Lda V. The frequency of Tay-Sachs disease causing mutations in the Brazilian Jewish population justifies a carrier screening program. Sao Paulo Med J 2001;119:146-149.
6. McDowell GA, Mules EH, Fabacher P, Shapira E, Blitzer MG. The presence of two different infantile Tay-Sachs disease mutations in a Cajun population. Am J Hum Genet 1992;51:1071-1077.
7. Sutton VR. Tay-Sachs disease screening and counseling families at risk for metabolic disease. Obstet Gynecol Clin North Am 2002;29:287-296.
8. Scriver CR. Human genetics: lessons from Quebec populations. Annu Rev Genomics Hum Genet 2001;2:69-101.
9. Haendel M, Vasilevsky N, Unni D, et al. How many rare diseases are there? Nat Rev Drug Discov 2020;19:77-78.
10. Boycott KM, Vanstone MR, Bulman DE, MacKenzie AE. Rare-disease genetics in the era of next-generation sequencing: discovery to translation. Nat Rev Genet 2013;14:681-691.
11. WHO. Rare diseases. Geneva, Switzerland: WHO, 2013: 148-151.
12. The Lancet Diabetes E. Spotlight on rare diseases. Lancet Diabetes Endocrinol 2019;7:75.
13. Aronson JK. Rare diseases and orphan drugs. Br J Clin Pharmacol 2006;61:243-245.
14. Ferreira CR. The burden of rare diseases. Am J Med Genet A 2019;179:885-892.
15. Baynam G, Bowman F, Lister K, et al. Improved Diagnosis and Care for Rare Diseases through Implementation of Precision Public Health Framework. Adv Exp Med Biol 2017;1031:55-94.
16. Stoller JK. The Challenge of Rare Diseases. Chest 2018;153:1309-1314.
17. University Health Network. Ehlers-Danlos Syndrome Clinic University Health Network [online]. Available at: https://www.uhn.ca/MCC/Clinics/Ehlers-Danlos_Syndrome_Clinic. Accessed Sept 25, 2020.
18. Lee MM, McDowell GSV, De Vivo DC, et al. The clinical spectrum of SMA-PME and in vitro normalization of its cellular ceramide profile. Ann Clin Transl Neurol 2022;9:1941-1952.
19. Shevchenko A, Simons K. Lipidomics: coming to grips with lipid diversity. Nat Rev Mol Cell Biol 2010;11:593-598.
20. Fahy E, Subramaniam S, Murphy RC, et al. Update of the LIPID MAPS comprehensive classification system for lipids. J Lipid Res 2009;50 Suppl:S9-14.
21. Fahy E, Subramaniam S, Brown HA, et al. A comprehensive classification system for lipids. J Lipid Res 2005;46:839-861.
22. Bennett SA, Valenzuela N, Xu H, Franko B, Fai S, Figeys D. Using neurolipidomics to identify phospholipid mediators of synaptic (dys)function in Alzheimer's Disease. Front Physiol 2013;4:168.
23. Casares D, Escriba PV, Rossello CA. Membrane Lipid Composition: Effect on Membrane and Organelle Structure, Function and Compartmentalization and Therapeutic Avenues. Int J Mol Sci 2019;20.

24. Vance JE, Tasseva G. Formation and function of phosphatidylserine and phosphatidylethanolamine in mammalian cells. Biochim Biophys Acta 2013;1831:543-554.
25. Bergo MO, Gavino BJ, Steenbergen R, et al. Defining the importance of phosphatidylserine synthase 2 in mice. J Biol Chem 2002;277:47701-47708.
26. Leventis PA, Grinstein S. The distribution and function of phosphatidylserine in cellular membranes. Annu Rev Biophys 2010;39:407-427.
27. Arikketh D, Nelson R, Vance JE. Defining the importance of phosphatidylserine synthase-1 (PSS1): unexpected viability of PSS1-deficient mice. J Biol Chem 2008;283:12888-12897.
28. Kim HY, Huang BX, Spector AA. Phosphatidylserine in the brain: metabolism and function. Prog Lipid Res 2014;56:1-18.
29. Kay JG, Fairn GD. Distribution, dynamics and functional roles of phosphatidylserine within the cell. Cell Commun Signal 2019;17:126.
30. Kannan M, Lahiri S, Liu LK, Choudhary V, Prinz WA. Phosphatidylserine synthesis at membrane contact sites promotes its transport out of the ER. J Lipid Res 2017;58:553-562.
31. Lenoir G, D'Ambrosio JM, Dieudonné T, Čopič A. Transport Pathways That Contribute to the Cellular Distribution of Phosphatidylserine. Frontiers in Cell and Developmental Biology 2021;9.
32. Burke JE, Dennis EA. Phospholipase A2 biochemistry. Cardiovasc Drugs Ther 2009;23:49-59.
33. Inoue A, Aoki J. Phospholipase A1: structure, distribution and function. Future Lipidology 2006;1:687-700.
34. Dennis EA, Cao J, Hsu YH, Magrioti V, Kokotos G. Phospholipase A2 enzymes: physical structure, biological function, disease implication, chemical inhibition, and therapeutic intervention. Chem Rev 2011;111:6130-6185.
35. Sato T, Aoki J, Nagai Y, et al. Serine phospholipid-specific phospholipase A that is secreted from activated platelets. A new member of the lipase family. J Biol Chem 1997;272:2192-2198.
36. Hishikawa D, Shindou H, Kobayashi S, Nakanishi H, Taguchi R, Shimizu T. Discovery of a lysophospholipid acyltransferase family essential for membrane asymmetry and diversity. Proc Natl Acad Sci U S A 2008;105:2830-2835.
37. Mozzi R, Buratta S, Goracci G. Metabolism and functions of phosphatidylserine in mammalian brain. Neurochem Res 2003;28:195-214.
38. Bartke N, Hannun YA. Bioactive sphingolipids: metabolism and function. J Lipid Res 2009;50 Suppl:S91-96.
39. Lone MA, Santos T, Alecu I, Silva LC, Hornemann T. 1-Deoxysphingolipids. Biochim Biophys Acta Mol Cell Biol Lipids 2019;1864:512-521.
40. Merrill AH. Sphingolipid Biosynthesis. In: Lennarz WJ, Lane MD, eds. Encyclopedia of Biological Chemistry. London, UK: Academic Press, 2013: 281-286.
41. Futerman AH. Sphingolipids. In: Ridgway ND, McLeod RS, eds. Biochemistry of Lipids, Lipoproteins and Membranes. Amsterdam, Netherlands: Elsevier, 2016: 297-326.
42. Hanada K. Serine palmitoyltransferase, a key enzyme of sphingolipid metabolism. Biochim Biophys Acta 2003;1632:16-30.
43. Tidhar R, Futerman AH. The complexity of sphingolipid biosynthesis in the endoplasmic reticulum. Biochim Biophys Acta 2013;1833:2511-2518.
44. Ferraz MJ, Marques AR, Appelman MD, et al. Lysosomal glycosphingolipid catabolism by acid ceramidase: formation of glycosphingoid bases during deficiency of glycosidases. FEBS Lett 2016;590:716-725.
45. Li Y, Xu Y, Benitez BA, et al. Genetic ablation of acid ceramidase in Krabbe disease confirms the psychosine hypothesis and identifies a new therapeutic target. Proc Natl Acad Sci U S A 2019;116:20097-20103.

46. Lucki NC, Li D, Bandyopadhyay S, Wang E, Merrill AH, Sewer MB. Acid ceramidase (ASAH1) represses steroidogenic factor 1-dependent gene transcription in H295R human adrenocortical cells by binding to the receptor. Mol Cell Biol 2012;32:4419-4431.
47. Coant N, Hannun YA. Neutral ceramidase: Advances in mechanisms, cell regulation, and roles in cancer. Adv Biol Regul 2019;71:141-146.
48. Abe A, Shayman JA. Sphingolipid Catabolism. In: Lennarz WJ, Lane MD, eds. Encyclopedia of Biological Chemistry, Second ed. London, UK: Academic Press, 2013: 287-292.
49. Bandhuvula P, Saba JD. Sphingosine-1-phosphate lyase in immunity and cancer: silencing the siren. Trends Mol Med 2007;13:210-217.
50. Kaltashov IA, Eyles SJ. Mass Spectrometry in Structural Biology and Biophysics, Second ed. Hoboken, New Jersey: John Wiley & Sons, Inc., 2012.
51. Fenn JB, Mann M, Meng CK, Wong SF, Whitehouse CM. Electrospray ionization for mass spectrometry of large biomolecules. Science 1989;246:64-71.
52. Han X. Lipidomics: Comprehensive Mass Spectrometry of Lipids, First ed. Hoboken, New Jersey: John Wiley & Sons, 2016.
53. Xu H, Boucher FR, Nguyen TT, et al. DMS as an orthogonal separation to LC/ESI/MS/MS for quantifying isomeric cerebrosides in plasma and cerebrospinal fluid. J Lipid Res 2019;60:200-211.
54. Waters. HPLC Separation Modes [online]. Available at: https://www.waters.com/waters/en_US/HPLC-Separation-Modes/nav.htm?cid=10049076&locale=en_US. Accessed March 30, 2022.
55. Harris DC. High-performance liquid chromatography. Quantitative Chemical Analysis, Seventh Ed, Seventh ed. New York, USA: W.H. Freeman and Company, 2007: 556-570.
56. Gross JH. Mass Spectrometry: A Textbook, 3 ed. Cham, Switzerland: Springer, 2017.
57. Kellogg MD. Measurement of Biological Materials. In: Robertson D, Williams GH, eds. Clinical and Translational Science. London, United Kingdom: Academic Press, 2017: 137-155.
58. Moldoveanu SC, David V. Essentials in Modern HPLC Separations: Elsevier, 2013.
59. Wilm M. Principles of electrospray ionization. Mol Cell Proteomics 2011;10:M111 009407.
60. Zhu X, Xu T, Peng C, Wu S. Advances in MALDI Mass Spectrometry Imaging Single Cell and Tissues. Frontiers in Chemistry 2022;9.
61. Faller R. UCD: Biophysics 241 - Membrane Biology. Available at https://phys.libretexts.org/@go/page/863. Accessed March 4, 2022, 2021.
62. de Hoffmann E, Stroobant V. Electrospray. Mass Spectrometry: Principles and Applications, Third ed. West Sussex, England: John Wiley & Sons, Ltd, 2013: 43-46.
63. Banerjee S, Mazumdar S. Electrospray ionization mass spectrometry: a technique to access the information beyond the molecular weight of the analyte. Int J Anal Chem 2012;2012:282574.
64. Konermann L, Ahadi E, Rodriguez AD, Vahidi S. Unraveling the mechanism of electrospray ionization. Anal Chem 2013;85:2-9.
65. Campbell JL, Le Blanc JC, Kibbey RG. Differential mobility spectrometry: a valuable technology for analyzing challenging biological samples. Bioanalysis 2015;7:853-856.
66. SCIEX A. Analyst 1.6.3 Software User Guide. Singapore: AB Sciex, 2015.
67. Safaei Z, Eiceman GA, Puton J, et al. Differential Mobility Spectrometry of Ketones in Air at Extreme Levels of Moisture. Sci Rep 2019;9:5593.
68. Dunnivant FM, Ginsbach JW. Basic Mass Spectrometry. Gas Chromatography, Liquid Chromatography, Capillary Electrophoresis - Mass Spectrometry: A basic Introduction. Washington, USA2011.
69. Clarke W. Mass Spectrometry in the clinical laboratory: determining the need and avoiding pitfalls. In: Nair H, Clarke W, eds. Mass Spectrometry for the Clinical Laboratory. London, United Kingdom: Academic Press, 2017.

70. Jabbour RE, Snyder AP. Mass spectrometry-based proteomics techniques for biological identification. In: Schaudies RP, ed. Biological Identification. Cambridge, United Kingdom: Woodhead Publishing, 2014: 370-430.
71. Gross JH. Tandem Mass Spectrometry. Mass Spectrometry A Textbook, Second ed. Heidelberg, Germany: Springer-Verlag Berlin Heidelberg, 2011: 416-478.
72. Sciex A. Powerful Scan Modes of QTRAP System Technology. In: Sciex A, ed.2019.
73. Mellon FA. Mass Spectrometry | Principles and Instrumentation. In: Caballero B, ed. Encyclopedia of Food Sciences and Nutrition, Second ed: Academic Press, 2003: 3739-3749.
74. Waddell Smith R. Mass Spectrometry. In: Siegel JA, Saukko PJ, Houck MM, eds. Encyclopedia of Forensic Sciences, Second ed: Academic Press, 2013: 603-608.
75. Rautenstrauch T, Snigula F. Progeria: a cell culture study and clinical report of familial incidence. Eur J Pediatr 1977;124:101-111.
76. Wiedemann HR. An unidentified neonatal progeroid syndrome: follow-up report. Eur J Pediatr 1979;130:65-70.
77. Rautenstrauch T, Snigula F, Wiedemann HR. [Neonatal progeroid syndrome (Wiedemann-Rautenstrauch). A follow-up study]. Klin Padiatr 1994;206:440-443.
78. Toriello HV. Wiedemann-Rautenstrauch syndrome. J Med Genet 1990;27:256-257.
79. Akawi N, Ali B, Al Gazali L. A progeroid syndrome with neonatal presentation and long survival maps to 19p13.3p13.2. Birth Defects Res A Clin Mol Teratol 2013;97:456-462.
80. Hou JW. Natural course of neonatal progeroid syndrome. Pediatr Neonatol 2009;50:102-109.
81. Jay AM, Conway RL, Thiffault I, et al. Neonatal progeriod syndrome associated with biallelic truncating variants in POLR3A. Am J Med Genet A 2016;170:3343-3346.
82. Wambach JA, Wegner DJ, Patni N, et al. Bi-allelic POLR3A Loss-of-Function Variants Cause Autosomal-Recessive Wiedemann-Rautenstrauch Syndrome. Am J Hum Genet 2018;103:968-975.
83. Beauregard-Lacroix E, Salian S, Kim H, et al. A variant of neonatal progeroid syndrome, or Wiedemann-Rautenstrauch syndrome, is associated with a nonsense variant in POLR3GL. Eur J Hum Genet 2019.
84. Kiraz A, Ozen S, Tubas F, Usta Y, Aldemir O, Alanay Y. Wiedemann-Rautenstrauch syndrome: report of a variant case. Am J Med Genet A 2012;158A:1434-1436.
85. Milenkovic VM, Brockmann M, Stohr H, Weber BH, Strauss O. Evolution and functional divergence of the anoctamin family of membrane proteins. BMC Evol Biol 2010;10:319.
86. Hahn Y, Kim DS, Pastan IH, Lee B. Anoctamin and transmembrane channel-like proteins are evolutionarily related. Int J Mol Med 2009;24:51-55.
87. Falzone ME, Malvezzi M, Lee BC, Accardi A. Known structures and unknown mechanisms of TMEM16 scramblases and channels. J Gen Physiol 2018;150:933-947.
88. Brunner JD, Lim NK, Schenck S, Duerst A, Dutzler R. X-ray structure of a calcium-activated TMEM16 lipid scramblase. Nature 2014;516:207-212.
89. Brunner JD, Schenck S, Dutzler R. Structural basis for phospholipid scrambling in the TMEM16 family. Curr Opin Struct Biol 2016;39:61-70.
90. Pedemonte N, Galietta LJ. Structure and function of TMEM16 proteins (anoctamins). Physiol Rev 2014;94:419-459.
91. Yu K, Whitlock JM, Lee K, Ortlund EA, Cui YY, Hartzell HC. Identification of a lipid scrambling domain in ANO6/TMEM16F. Elife 2015;4:e06901.
92. Duran C, Hartzell HC. Physiological roles and diseases of Tmem16/Anoctamin proteins: are they all chloride channels? Acta Pharmacol Sin 2011;32:685-692.
93. Whitlock JM, Hartzell HC. Anoctamins/TMEM16 Proteins: Chloride Channels Flirting with Lipids and Extracellular Vesicles. Annu Rev Physiol 2017;79:119-143.

94. Hankins HM, Baldridge RD, Xu P, Graham TR. Role of flippases, scramblases and transfer proteins in phosphatidylserine subcellular distribution. Traffic 2015;16:35-47.
95. Sahu SK, Gummadi SN, Manoj N, Aradhyam GK. Phospholipid scramblases: an overview. Arch Biochem Biophys 2007;462:103-114.
96. Bevers EM, Williamson PL. Phospholipid scramblase: an update. FEBS Lett 2010;584:2724-2730.
97. Contreras FX, Sanchez-Magraner L, Alonso A, Goni FM. Transbilayer (flip-flop) lipid motion and lipid scrambling in membranes. FEBS Lett 2010;584:1779-1786.
98. Suzuki J, Umeda M, Sims PJ, Nagata S. Calcium-dependent phospholipid scrambling by TMEM16F. Nature 2010;468:834-838.
99. Kay JG, Grinstein S. Sensing phosphatidylserine in cellular membranes. Sensors (Basel) 2011;11:1744-1755.
100. Kay JG, Koivusalo M, Ma X, Wohland T, Grinstein S. Phosphatidylserine dynamics in cellular membranes. Mol Biol Cell 2012;23:2198-2212.
101. Vance JE. Molecular and cell biology of phosphatidylserine and phosphatidylethanolamine metabolism. Prog Nucleic Acid Res Mol Biol 2003;75:69-111.
102. Bevers EM, Williamson PL. Getting to the Outer Leaflet: Physiology of Phosphatidylserine Exposure at the Plasma Membrane. Physiol Rev 2016;96:605-645.
103. Holthuis JC, Levine TP. Lipid traffic: floppy drives and a superhighway. Nat Rev Mol Cell Biol 2005;6:209-220.
104. Fadok VA, Voelker DR, Campbell PA, Cohen JJ, Bratton DL, Henson PM. Exposure of phosphatidylserine on the surface of apoptotic lymphocytes triggers specific recognition and removal by macrophages. J Immunol 1992;148:2207-2216.
105. Stuart MC, Damoiseaux JG, Frederik PM, Arends JW, Reutelingsperger CP. Surface exposure of phosphatidylserine during apoptosis of rat thymocytes precedes nuclear changes. Eur J Cell Biol 1998;76:77-83.
106. Brouckaert G, Kalai M, Krysko DV, et al. Phagocytosis of necrotic cells by macrophages is phosphatidylserine dependent and does not induce inflammatory cytokine production. Mol Biol Cell 2004;15:1089-1100.
107. Krysko DV, Denecker G, Festjens N, et al. Macrophages use different internalization mechanisms to clear apoptotic and necrotic cells. Cell Death Differ 2006;13:2011-2022.
108. Nagata S, Suzuki J, Segawa K, Fujii T. Exposure of phosphatidylserine on the cell surface. Cell Death Differ 2016;23:952-961.
109. Kloditz K, Fadeel B. Three cell deaths and a funeral: macrophage clearance of cells undergoing distinct modes of cell death. Cell Death Discov 2019;5:65.
110. Ehlen HW, Chinenkova M, Moser M, et al. Inactivation of anoctamin-6/Tmem16f, a regulator of phosphatidylserine scrambling in osteoblasts, leads to decreased mineral deposition in skeletal tissues. J Bone Miner Res 2013;28:246-259.
111. Verma SK, Leikina E, Melikov K, et al. Cell-surface phosphatidylserine regulates osteoclast precursor fusion. J Biol Chem 2018;293:254-270.
112. Yang H, Kim A, David T, et al. TMEM16F forms a Ca2+-activated cation channel required for lipid scrambling in platelets during blood coagulation. Cell 2012;151:111-122.
113. Su Y, Chen J, Dong Z, et al. Procoagulant Activity of Blood and Endothelial Cells via Phosphatidylserine Exposure and Microparticle Delivery in Patients with Diabetic Retinopathy. Cell Physiol Biochem 2018;45:2411-2420.
114. Lentz BR. Exposure of platelet membrane phosphatidylserine regulates blood coagulation. Prog Lipid Res 2003;42:423-438.

115. Reddy EC, Wang H, Christensen H, et al. Analysis of procoagulant phosphatidylserine-exposing platelets by imaging flow cytometry. Res Pract Thromb Haemost 2018;2:736-750.
116. Dyment DA, Sell E, Vanstone MR, et al. Evidence for clinical, genetic and biochemical variability in spinal muscular atrophy with progressive myoclonic epilepsy. Clin Genet 2014;86:558-563.
117. Cong L, Ran FA, Cox D, et al. Multiplex genome engineering using CRISPR/Cas systems. Science 2013;339:819-823.
118. Jordan M, Schallhorn A, Wurm FM. Transfecting mammalian cells: optimization of critical parameters affecting calcium-phosphate precipitate formation. Nucleic Acids Res 1996;24:596-601.
119. Williamson P, Christie A, Kohlin T, et al. Phospholipid scramblase activation pathways in lymphocytes. Biochemistry 2001;40:8065-8072.
120. Williamson P, Halleck MS, Malowitz J, et al. Transbilayer phospholipid movements in ABCA1-deficient cells. PLoS One 2007;2:e729.
121. Schneider CA, Rasband WS, Eliceiri KW. NIH Image to ImageJ: 25 years of image analysis. Nat Methods 2012;9:671-675.
122. Tang H, Vasselli JR, Wu EX, Boozer CN, Gallagher D. High-resolution magnetic resonance imaging tracks changes in organ and tissue mass in obese and aging rats. Am J Physiol Regul Integr Comp Physiol 2002;282:R890-899.
123. Caron AZ, He X, Mottawea W, et al. The SIRT1 deacetylase protects mice against the symptoms of metabolic syndrome. FASEB J 2014;28:1306-1316.
124. Berry DC, Stenesen D, Zeve D, Graff JM. The developmental origins of adipose tissue. Development 2013;140:3939-3949.
125. Ryan SD, Whitehead SN, Swayne LA, et al. Amyloid-beta42 signals tau hyperphosphorylation and compromises neuronal viability by disrupting alkylacylglycerophosphocholine metabolism. Proc Natl Acad Sci U S A 2009;106:20936-20941.
126. Whitehead SN, Hou W, Ethier M, et al. Identification and quantitation of changes in the platelet activating factor family of glycerophospholipids over the course of neuronal differentiation by high-performance liquid chromatography electrospray ionization tandem mass spectrometry. Anal Chem 2007;79:8539-8548.
127. Xu H, Valenzuela N, Fai S, Figeys D, Bennett SA. Targeted lipidomics - advances in profiling lysophosphocholine and platelet-activating factor second messengers. FEBS J 2013;280:5652-5667.
128. Granger MW, Liu H, Fowler CF, et al. Distinct disruptions in Land's cycle remodeling of glycerophosphocholines in murine cortex mark symptomatic onset and progression in two Alzheimer's disease mouse models. J Neurochem 2019;149:499-517.
129. Chitpin JG, Surendra A, Nguyen TT, et al. BATL: Bayesian annotations for targeted lipidomics. Bioinformatics 2022;38:1593-1599.
130. Liu W, Xie Y, Ma J, et al. IBS: an illustrator for the presentation and visualization of biological sequences. Bioinformatics 2015;31:3359-3361.
131. Grubb S, Poulsen KA, Juul CA, et al. TMEM16F (Anoctamin 6), an anion channel of delayed Ca(2+) activation. J Gen Physiol 2013;141:585-600.
132. Shimizu T, Iehara T, Sato K, Fujii T, Sakai H, Okada Y. TMEM16F is a component of a Ca2+-activated Cl- channel but not a volume-sensitive outwardly rectifying Cl- channel. Am J Physiol Cell Physiol 2013;304:C748-759.
133. van Engeland M, Nieland LJ, Ramaekers FC, Schutte B, Reutelingsperger CP. Annexin V-affinity assay: a review on an apoptosis detection system based on phosphatidylserine exposure. Cytometry 1998;31:1-9.
134. Benjamini Y, Kreiger A, Yekutieli D. Adaptive linear step-up procedures that control the false discovery rate. Biometrika 2006;93.

135. Millington-Burgess SL, Harper MT. Gene of the issue: ANO6 and Scott Syndrome. Platelets 2019:1-4.
136. Zwaal RF, Comfurius P, Bevers EM. Scott syndrome, a bleeding disorder caused by defective scrambling of membrane phospholipids. Biochim Biophys Acta 2004;1636:119-128.
137. Boisseau P, Bene MC, Besnard T, et al. A new mutation of ANO6 in two familial cases of Scott syndrome. Br J Haematol 2018;180:750-752.
138. Segawa K, Suzuki J, Nagata S. Constitutive exposure of phosphatidylserine on viable cells. Proc Natl Acad Sci U S A 2011;108:19246-19251.
139. Scudieri P, Caci E, Venturini A, et al. Ion channel and lipid scramblase activity associated with expression of TMEM16F/ANO6 isoforms. J Physiol 2015;593:3829-3848.
140. Le T, Jia Z, Le SC, Zhang Y, Chen J, Yang H. An inner activation gate controls TMEM16F phospholipid scrambling. Nat Commun 2019;10:1846.
141. Khaselev N, Murphy RC. Structural characterization of oxidized phospholipid products derived from arachidonate-containing plasmenyl glycerophosphocholine. J Lipid Res 2000;41:564-572.
142. Bader Lange ML, Cenini G, Piroddi M, et al. Loss of phospholipid asymmetry and elevated brain apoptotic protein levels in subjects with amnestic mild cognitive impairment and Alzheimer disease. Neurobiol Dis 2008;29:456-464.
143. Bennett SAL, Valenzuela N, Xu H, Franko B, Fai S, Figeys D. Using neurolipidomics to identify phospholipid mediators of synaptic (dys)function in Alzheimer's Disease. Frontiers in physiology 2013;4:168.
144. Lance JW, Evans WA. Progressive myoclonic epilepsy, nerve deafness and spinal muscular atrophy. Clin Exp Neurol 1984;20:141-151.
145. Haliloglu G, Chattopadhyay A, Skorodis L, et al. Spinal muscular atrophy with progressive myoclonic epilepsy: report of new cases and review of the literature. Neuropediatrics 2002;33:314-319.
146. Zhou J, Tawk M, Tiziano FD, et al. Spinal muscular atrophy associated with progressive myoclonic epilepsy is caused by mutations in ASAH1. Am J Hum Genet 2012;91:5-14.
147. Li CM, Park JH, He X, et al. The human acid ceramidase gene (ASAH): structure, chromosomal location, mutation analysis, and expression. Genomics 1999;62:223-231.
148. Giraldez BG, Guerrero-Lopez R, Ortega-Moreno L, et al. Uniparental disomy as a cause of spinal muscular atrophy and progressive myoclonic epilepsy: phenotypic homogeneity due to the homozygous c.125C>T mutation in ASAH1. Neuromuscul Disord 2015;25:222-224.
149. Rubboli G, Veggiotti P, Pini A, et al. Spinal muscular atrophy associated with progressive myoclonic epilepsy: A rare condition caused by mutations in ASAH1. Epilepsia 2015;56:692-698.
150. Gan JJ, Garcia V, Tian J, et al. Acid ceramidase deficiency associated with spinal muscular atrophy with progressive myoclonic epilepsy. Neuromuscul Disord 2015;25:959-963.
151. Oguz Akarsu E, Tekturk P, Yapici Z, Tepgec F, Uyguner ZO, Baykan B. Eyelid myoclonic status epilepticus: A rare phenotype in spinal muscular atrophy with progressive myoclonic epilepsy associated with ASAH1 gene mutation. Seizure 2016;42:49-51.
152. Filosto M, Aureli M, Castellotti B, et al. ASAH1 variant causing a mild SMA phenotype with no myoclonic epilepsy: a clinical, biochemical and molecular study. Eur J Hum Genet 2016;24:1578-1583.
153. Kernohan KD, Fresard L, Zappala Z, et al. Whole-transcriptome sequencing in blood provides a diagnosis of spinal muscular atrophy with progressive myoclonic epilepsy. Hum Mutat 2017;38:611-614.
154. Yildiz EP, Yesil G, Bektas G, et al. Spinal muscular atrophy with progressive myoclonic epilepsy linked to mutations in ASAH1. Clin Neurol Neurosurg 2018;164:47-49.
155. Shervin Badv R, Nilipour Y, Rahimi-Dehgolan S, Rashidi-Nezhad A, Ghahvechi Akbari M. A novel case report of spinal muscular atrophy with progressive myoclonic epilepsy from Iran. Int Med Case Rep J 2019;12:155-159.

156. Ame van der Beek N, Nelson I, Froissart R, et al. A new case of SMA phenotype without epilepsy due to biallelic variants in ASAH1. Eur J Hum Genet 2019;27:337-339.
157. Mahmoud IG, Elmonem MA, Zaki MS, et al. ASAH1-related disorders: Description of 15 novel pediatric patients and expansion of the clinical phenotype. Clin Genet 2020;98:598-605.
158. Puma A, Ezaru A, Cavalli M, et al. A case of ASAH1-related pure SMA evolving into adult-onset Farber disease. Clin Genet 2021;100:234-235.
159. Axente M, Shelby ES, Mirea A, et al. Clinical features and genetics in non-5q spinal muscular atrophy caused by acid ceramidase deficiency. J Med Life 2021;14:424-428.
160. Yu FPS, Amintas S, Levade T, Medin JA. Acid ceramidase deficiency: Farber disease and SMA-PME. Orphanet J Rare Dis 2018;13:121.
161. Elsea SH, Solyom A, Martin K, et al. ASAH1 pathogenic variants associated with acid ceramidase deficiency: Farber disease and spinal muscular atrophy with progressive myoclonic epilepsy. Hum Mutat 2020;41:1469-1487.
162. Dyment DA, Bennett SAL, Medin JA, Levade T. ASAH1-Related Disorders. In: Adam MP, Ardinger HH, Pagon RA, et al., eds. GeneReviews((R)). Seattle, USA2018.
163. Levade T, Sandhoff K, Schulze H, Medin JA. Acid ceramidase deficiency: Farber lipogranulomatosis. In: Valle D, Beaudet AL, Vogelstein B, Kinzler KW, Antonarakis SE, Ballabio A, eds. Online Metabolic & Molecular Bases of Inherited Disease (OMMBID: McGraw-Hill, 2009.
164. Bonafe L, Kariminejad A, Li J, et al. Brief Report: Peripheral Osteolysis in Adults Linked to ASAH1 (Acid Ceramidase) Mutations: A New Presentation of Farber's Disease. Arthritis Rheumatol 2016;68:2323-2327.
165. Levade T, Moser HW, Fensom AH, Harzer K, Moser AB, Salvayre R. Neurodegenerative course in ceramidase deficiency (Farber disease) correlates with the residual lysosomal ceramide turnover in cultured living patient cells. J Neurol Sci 1995;134:108-114.
166. Courage C, Oliver KL, Park EJ, et al. Progressive myoclonus epilepsies-Residual unsolved cases have marked genetic heterogeneity including dolichol-dependent protein glycosylation pathway genes. Am J Hum Genet 2021;108:722-738.
167. Sathe S, Pearson T. Phenotypic characterization of the spinal muscular atrophy with progressive myoclonus epilepsy syndrome caused by ASAH1 mutations. Molecular Genetics and Metabolism 2014;111:S93.
168. Cozma C, Iurascu MI, Eichler S, et al. C26-Ceramide as highly sensitive biomarker for the diagnosis of Farber Disease. Sci Rep 2017;7:6149.
169. He X, Li CM, Park JH, Dagan A, Gatt S, Schuchman EH. A fluorescence-based high-performance liquid chromatographic assay to determine acid ceramidase activity. Anal Biochem 1999;274:264-269.
170. Bedia C, Camacho L, Abad JL, Fabrias G, Levade T. A simple fluorogenic method for determination of acid ceramidase activity and diagnosis of Farber disease. J Lipid Res 2010;51:3542-3547.
171. Fowler SL, McLean AC, Bennett SAL. Tissue-specific cross-reactivity of connexin32 antibodies: problems and solutions unique to the central nervous system. Cell Commun Adhes 2009;16:117-130.
172. He X, Dworski S, Zhu C, et al. Enzyme replacement therapy for Farber disease: Proof-of-concept studies in cells and mice. BBA Clin 2017;7:85-96.
173. Lee BH, Mongiovi P, Levade T, Marston B, Mountain J, Ciafaloni E. Spinal muscular atrophy and Farber disease due to ASAH1 variants: A case report. Am J Med Genet A 2020;182:2369-2371.
174. Santos-Cortez RLP, Hu Y, Sun F, et al. Identification of ASAH1 as a susceptibility gene for familial keloids. Eur J Hum Genet 2017;25:1155-1161.
175. Alayoubi AM, Wang JC, Au BC, et al. Systemic ceramide accumulation leads to severe and varied pathological consequences. EMBO Mol Med 2013;5:827-842.

176. Ehlert K, Frosch M, Fehse N, Zander A, Roth J, Vormoor J. Farber disease: clinical presentation, pathogenesis and a new approach to treatment. Pediatr Rheumatol Online J 2007;5:15.
177. Online Mendelian Inheritance in Man (OMIM), McKusick VA, Kniffin CL. # 159950 - Spinal Muscular Atrophy with Progressive Myoclonic Epilepsy [online]. Available at: https://www.omim.org/entry/159950. Accessed July 02, 2020.
178. Online Mendelian Inheritance in Man (OMIM), McKusick VA, Kniffin CL. # 228000 - Farber Lipogranulomatosis [online]. Available at: https://www.omim.org/entry/228000. Accessed July 02, 2020.
179. Online Mendelian Inheritance in Man (OMIM), Gross MB, Converse PJ. * 613468 - N-Acylsphingosine amidohydrolase 1 [online]. Available at: https://www.omim.org/entry/613468. Accessed July 28, 2020.
180. NCBI Gene. ASAH1 N-acylsphingosine amidohydrolase 1 [online]. Available at: https://www.ncbi.nlm.nih.gov/gene?Db=gene&Cmd=DetailsSearch&Term=427. Accessed July 28, 2020.
181. Parveen F, Bender D, Law SH, Mishra VK, Chen CC, Ke LY. Role of Ceramidases in Sphingolipid Metabolism and Human Diseases. Cells 2019;8.
182. Yamaguchi Y, Sasagasako N, Goto I, Kobayashi T. The synthetic pathway for glucosylsphingosine in cultured fibroblasts. J Biochem 1994;116:704-710.
183. Kim MJ, Jeon S, Burbulla LF, Krainc D. Acid ceramidase inhibition ameliorates alpha-synuclein accumulation upon loss of GBA1 function. Hum Mol Genet 2018;27:1972-1988.
184. Teoh HL, Solyom A, Schuchman EH, et al. Polyarticular Arthritis and Spinal Muscular Atrophy in Acid Ceramidase Deficiency. Pediatrics 2016;138.
185. National Organization for Rare Disorders (NORD). ASAH1-Related Disorders - NORD [online]. Available at: https://rarediseases.org/rare-diseases/farbers-disease/. Accessed July 02, 2020.
186. Sands MS. Farber disease: understanding a fatal childhood disorder and dissecting ceramide biology. EMBO Mol Med 2013;5:799-801.
187. Fowler SL, McLean AC, Bennett SA. Tissue-specific cross-reactivity of connexin32 antibodies: problems and solutions unique to the central nervous system. Cell Commun Adhes 2009;16:117-130.
188. Schindelin J, Arganda-Carreras I, Frise E, et al. Fiji: an open-source platform for biological-image analysis. Nat Methods 2012;9:676-682.
189. Snider SA, Margison KD, Ghorbani P, et al. Choline transport links macrophage phospholipid metabolism and inflammation. J Biol Chem 2018;293:11600-11611.
190. Shaner RL, Allegood JC, Park H, et al. Quantitative analysis of sphingolipids for lipidomics using triple quadrupole and quadrupole linear ion trap mass spectrometers. J Lipid Res 2009;50:1692-1707.
191. Pettit AS, Desroches R, Bennett SA. The opiate analgesic buprenorphine decreases proliferation of adult hippocampal neuroblasts and increases survival of their progeny. Neuroscience 2012;200:211-222.
192. Tomlinson JJ, Shutinoski B, Dong L, et al. Holocranohistochemistry enables the visualization of alpha-synuclein expression in the murine olfactory system and discovery of its systemic anti-microbial effects. J Neural Transm (Vienna) 2017;124:721-738.
193. Griffith J, Mari M, De Maziere A, Reggiori F. A cryosectioning procedure for the ultrastructural analysis and the immunogold labelling of yeast Saccharomyces cerevisiae. Traffic 2008;9:1060-1072.
194. Kennedy MA, Gable K, Niewola-Staszkowska K, et al. A neurotoxic glycerophosphocholine impacts PtdIns-4, 5-bisphosphate and TORC2 signaling by altering ceramide biosynthesis in yeast. PLoS Genet 2014;10:e1004010.
195. Hannun YA, Obeid LM. Principles of bioactive lipid signalling: lessons from sphingolipids. Nat Rev Mol Cell Biol 2008;9:139-150.

196. Bernardo K, Hurwitz R, Zenk T, et al. Purification, characterization, and biosynthesis of human acid ceramidase. J Biol Chem 1995;270:11098-11102.
197. van Echten-Deckert G, Klein A, Linke T, Heinemann T, Weisgerber J, Sandhoff K. Turnover of endogenous ceramide in cultured normal and Farber fibroblasts. J Lipid Res 1997;38:2569-2579.
198. Sugita M, Dulaney JT, Moser HW. Ceramidase deficiency in Farber's disease (lipogranulomatosis). Science 1972;178:1100-1102.
199. Yu FPS, Sajdak BS, Sikora J, et al. Acid Ceramidase Deficiency in Mice Leads to Severe Ocular Pathology and Visual Impairment. Am J Pathol 2019;189:320-338.
200. Sikora J, Dworski S, Jones EE, et al. Acid Ceramidase Deficiency in Mice Results in a Broad Range of Central Nervous System Abnormalities. Am J Pathol 2017;187:864-883.
201. Yu FPS, Molino S, Sikora J, et al. Hepatic pathology and altered gene transcription in a murine model of acid ceramidase deficiency. Lab Invest 2019;99:1572-1592.
202. Kyriakou K, Lederer CW, Kleanthous M, Drousiotou A, Malekkou A. Acid Ceramidase Depletion Impairs Neuronal Survival and Induces Morphological Defects in Neurites Associated with Altered Gene Transcription and Sphingolipid Content. Int J Mol Sci 2020;21.
203. Parenti G, Medina DL, Ballabio A. The rapidly evolving view of lysosomal storage diseases. EMBO Mol Med 2021;13:e12836.
204. Vanier MT. Niemann-Pick disease type C. Orphanet J Rare Dis 2010;5:16.
205. Paik KH, Song SM, Ki CS, et al. Identification of mutations in the GNPTA (MGC4170) gene coding for GlcNAc-phosphotransferase alpha/beta subunits in Korean patients with mucolipidosis type II or type IIIA. Hum Mutat 2005;26:308-314.
206. Wei ML. Hermansky-Pudlak syndrome: a disease of protein trafficking and organelle function. Pigment Cell Res 2006;19:19-42.
207. Ward DM, Griffiths GM, Stinchcombe JC, Kaplan J. Analysis of the lysosomal storage disease Chediak-Higashi syndrome. Traffic 2000;1:816-822.
208. Beck M. Treatment strategies for lysosomal storage disorders. Dev Med Child Neurol 2018;60:13-18.
209. Parenti G, Pignata C, Vajro P, Salerno M. New strategies for the treatment of lysosomal storage diseases (review). Int J Mol Med 2013;31:11-20.
210. Li M. Enzyme Replacement Therapy: A Review and Its Role in Treating Lysosomal Storage Diseases. Pediatr Ann 2018;47:e191-e197.
211. Grunwald P. Lysosomal Storage Disorders and Enzyme Replacement Therapy. In: Grunwald P, ed. Pharmaceutical Biocatalysis: Important Enzymes, Novel Targets, and Therapies. Singapore: Jenny Stanford Publishing Pte. Ltd, 2021: 347-438.
212. Ries M. Enzyme replacement therapy and beyond-in memoriam Roscoe O. Brady, M.D. (1923-2016). J Inherit Metab Dis 2017;40:343-356.
213. Tieh PY, Yee JK, Hicks RA, Mao CS, Lee WN. Utility of a precursor-to-product ratio in the evaluation of presumptive positives in newborn screening of congenital adrenal hyperplasia. J Perinatol 2017;37:283-287.
214. Karsli T, Jain VG, Mhanna M, et al. Assessment of adrenal function at birth using adrenal glucocorticoid precursor to product ratios to predict short-term neonatal outcomes. Pediatr Res 2020;87:767-772.
215. Teranishi Y, Kuwahara H, Ueda M, et al. Sphingomyelin Deacylase, the Enzyme Involved in the Pathogenesis of Atopic Dermatitis, Is Identical to the beta-Subunit of Acid Ceramidase. Int J Mol Sci 2020;21.
216. Mikati MA, Abi-Habib RJ, El Sabban ME, et al. Hippocampal programmed cell death after status epilepticus: evidence for NMDA-receptor and ceramide-mediated mechanisms. Epilepsia 2003;44:282-291.

217. Mikati MA, Zeinieh M, Habib RA, et al. Changes in sphingomyelinases, ceramide, Bax, Bcl(2), and caspase-3 during and after experimental status epilepticus. Epilepsy Res 2008;81:161-166.
218. Vanni N, Fruscione F, Ferlazzo E, et al. Impairment of ceramide synthesis causes a novel progressive myoclonus epilepsy. Ann Neurol 2014;76:206-212.
219. Mosbech MB, Olsen AS, Neess D, et al. Reduced ceramide synthase 2 activity causes progressive myoclonic epilepsy. Ann Clin Transl Neurol 2014;1:88-98.
220. Wenger DA, Roth S, Kudoh T, et al. Biochemical studies in a patient with subacute neuropathic Gaucher disease without visceral glucosylceramide storage. Pediatr Res 1983;17:344-348.
221. Paolacci S, Li Y, Agolini E, et al. Specific combinations of biallelic POLR3A variants cause Wiedemann-Rautenstrauch syndrome. J Med Genet 2018;55:837-846.
222. Minnerop M, Kurzwelly D, Wagner H, et al. Hypomorphic mutations in POLR3A are a frequent cause of sporadic and recessive spastic ataxia. Brain 2017;140:1561-1578.
223. Di Donato I, Gallo A, Ricca I, et al. POLR3A variants in hereditary spastic paraparesis and ataxia: clinical, genetic, and neuroradiological findings in a cohort of Italian patients. Neurol Sci 2022;43:1071-1077.
224. Rydning SL, Koht J, Sheng Y, et al. Biallelic POLR3A variants confirmed as a frequent cause of hereditary ataxia and spastic paraparesis. Brain 2019;142:e12.
225. Morales-Rosado JA, Macke EL, Cousin MA, Oliver GR, Dhamija R, Klee EW. Interpretation challenges of novel dual-class missense and splice-impacting variant in POLR3A-related late-onset hereditary spastic ataxia. Mol Genet Genomic Med 2020;8:e1341.
226. D'Amore A, Tessa A, Casali C, et al. Next Generation Molecular Diagnosis of Hereditary Spastic Paraplegias: An Italian Cross-Sectional Study. Front Neurol 2018;9:981.
227. Ruggiero L, Iovino A, Dubbioso R, et al. Multimodal evaluation of an Italian family with a hereditary spastic paraplegia and POLR3A mutations. Ann Clin Transl Neurol 2020;7:2326-2331.
228. de Assis Pereira Matos PCA, Gama MTD, Bezerra MLE, da Rocha AJ, Barsottini OGP, Pedroso JL. POLR3A-Related Disorder Presenting with Late-Onset Dystonia and Spastic Paraplegia. Mov Disord Clin Pract 2020;7:467-469.
229. La Piana R, Cayami FK, Tran LT, et al. Diffuse hypomyelination is not obligate for POLR3-related disorders. Neurology 2016;86:1622-1626.
230. (OMIM) OMIiM, Hartz PA, Kniffin CL. *614258 - Polymerase III, RNA, Subunit A; POLR3A [online]. Available at: https://www.omim.org/entry/614258. Accessed April 15, 2023.
231. MedlinePlus. POLR3A gene: MedlinePlus Genetics [online]. Available at: https://medlineplus.gov/genetics/gene/polr3a/#conditions. Accessed 2023-03-29.
232. Cao H, Hegele RA. LMNA is mutated in Hutchinson-Gilford progeria (MIM 176670) but not in Wiedemann-Rautenstrauch progeroid syndrome (MIM 264090). J Hum Genet 2003;48:271-274.
233. Gonzalo S, Kreienkamp R, Askjaer P. Hutchinson-Gilford Progeria Syndrome: A premature aging disease caused by LMNA gene mutations. Ageing Res Rev 2017;33:18-29.
234. MedlinePlus. LMNA gene: MedlinePlus Genetics [online]. Available at: https://medlineplus.gov/genetics/gene/lmna/#conditions. Accessed 2023-03-29.
235. Arndt M, Alvadia C, Straub MS, Clerico Mosina V, Paulino C, Dutzler R. Structural basis for the activation of the lipid scramblase TMEM16F. Nat Commun 2022;13:6692.
236. UniProt C. UniProt: the Universal Protein Knowledgebase in 2023. Nucleic Acids Res 2023;51:D523-D531.
237. Zhang Y, Le T, Grabau R, et al. TMEM16F phospholipid scramblase mediates trophoblast fusion and placental development. Sci Adv 2020;6:eaba0310.
238. NIH, GARD. Neonatal progeroid syndrome - About the Disease [online]. Available at: https://rarediseases.info.nih.gov/diseases/330/neonatal-progeroid-syndrome. Accessed 2023-05-10.

239. Gyobu S, Miyata H, Ikawa M, et al. A Role of TMEM16E Carrying a Scrambling Domain in Sperm Motility. Mol Cell Biol 2016;36:645-659.
240. Schuchman EH. Acid ceramidase and the treatment of ceramide diseases: The expanding role of enzyme replacement therapy. Biochim Biophys Acta 2016;1862:1459-1471.
241. Kleynerman A, Rybova J, Faber ML, McKillop WM, Levade T, Medin JA. Acid Ceramidase Deficiency: Bridging Gaps between Clinical Presentation, Mouse Models, and Future Therapeutic Interventions. Biomolecules 2023;13.
242. Eviatar L, Sklower SL, Wisniewski K, Feldman RS, Gochoco A. Farber lipogranulomatosis: an unusual presentation in a black child. Pediatr Neurol 1986;2:371-374.
243. Sun A. Lysosomal storage disease overview. Ann Transl Med 2018;6:476.
244. Mechler K, Mountford WK, Hoffmann GF, Ries M. Pressure for drug development in lysosomal storage disorders - a quantitative analysis thirty years beyond the US orphan drug act. Orphanet J Rare Dis 2015;10:46.
245. Coutinho MF, Prata MJ, Alves S. Mannose-6-phosphate pathway: a review on its role in lysosomal function and dysfunction. Mol Genet Metab 2012;105:542-550.